ISSN - 0571 - 7132

ԱՍՏՂԱՖԻԶԻԿԱ
АСТРОФИЗИКА

ТОМ 67 АВГУСТ, 2024 ВЫПУСК 3

АСТРОФИЗИКА ТОМ 67 ВЫПУСК 3 2024

(Продолжение на 4-й стр. обложки)

ЕРЕВАН

Выходит с 1965г.
на русском и английском языках

"АСТРОФИЗИКА" - научный журнал, издаваемый Национальной академией наук Республики Армения. Журнал печатает оригинальные статьи по физике звезд, физике туманностей и межзвездной среды, по звездной и внегалактической астрономии, а также статьи по областям науки, сопредельным с астрофизикой. Журнал предназначается для научных работников, аспирантов и студентов старших курсов.

"ԱՍՏՂԱՖԻԶԻԿԱ"-ն գիտական հանդես է, որը հրատարակում է Հայաստանի Հանրապետության Գիտությունների Ազգային Ակադեմիան: Հանդեսը տպագրում է ինքնատիպ հոդվածներ աստղերի ֆիզիկայի, միգամածությունների և միջաստղային միջավայրի ֆիզիկայի, աստղաբաշխության և արտագալակտիկական աստղագիտության, ինչպես նաև աստղաֆիզիկային սահմանակից բնագավառների գծով: Հանդեսը նախատեսված է գիտական աշխատակիցների, ասպիրանտների և բարձր կուրսերի ուսանողների համար:

Адрес редакции: Республика Армения, Ереван 19, пр. Маршала Баграмяна 24г
Редакция ж. "Астрофизика", тел. 56 81 38
e–mail: astrofiz@sci.am

ISSN - 0571 - 7132

ԱՍՏՂԱՖԻԶԻԿԱ
АСТРОФИЗИКА

ТОМ 67 АВГУСТ, 2024 ВЫПУСК 3

2024 ВЫПУСК 3 ТОМ 67 АСТРОФИЗИКА

(Продолжение на 4-й стр. обложки)

ЕРЕВАН

CONTENTS

Индекс 70022

СОДЕРЖАНИЕ (продолжение)

АСТРОФИЗИКА

ТОМ 67 АВГУСТ, 2024 ВЫПУСК 3

DOI: 10.54503/0571-7132-2024.67.3-279

LARGE DIFFUSE DWARFS IN THE DYNAMICALLY COLD TRIPLE GALAXY SYSTEMS

I.D.KARACHENTSEV[1], A.E.NAZAROVA[1], V.E.KARACHENTSEVA[2]
Received 30 May 2024

We report on the discovery of three large diffuse dwarf (LDD) galaxies located in isolated triple systems. They have effective diameters of $3.6 \div 10.0$ kpc and effective surface brightness of $26.2 \div 27.3$ ^{m}/sq. arcsec. We note that the LDD galaxies tend to occur in small groups with a very low dispersion of radial velocities. The total (orbital) mass of the triplets approximately equals to their integral stellar mass within velocity measurement errors. The presence of LDD galaxies in cold multiple systems seems mysterious.

Keywords: *galaxies - dwarf galaxies - low surface brightness galaxies*

1. *Introduction*. Over a wide range of luminosities, the average surface brightness (SB) of galaxies, and their integral absolute magnitude, *M*, follow a relation $SB = (1/3)M + \text{const}$, which corresponds to an approximate constancy of the average volumetric stellar density for major and dwarf galaxies [1]. However, with the advent of deep sky surveys, a specific population of low surface brightness galaxies has been discovered, whose luminosity is typical of dwarf systems and whose sizes are comparable to those of normal galaxies. These objects are called "ultradiffuse galaxies" (UDG). As defined by van Dokkum et al. [2], these include galaxies with a central surface brightness in the *g*-band $SB_g(0) > 24$ ^{m}/sq. arcsec and a linear effective diameter $A_{50} > 3.0$ kpc, within which half of the galaxy's luminosity is contained.

Many UDG galaxies have been discovered in the nearby clusters: Virgo [3], Fornax [4] and Coma [5], and a small number have been also found in nearby groups around NGC 253, Cen A, NGC 5485 [6-8]. A catalog of 7070 UDG candidates selected over 20000 sq. degr. of sky was recently published by Zaritsky et al. [9]. According to [10], about 40% of UDG objects are found in clusters, about 20% are located in groups, and the remaining 40% occur in scattered filaments, avoiding common field regions. No isolated UDG galaxies have yet been discovered. This arrangement of diffuse galaxies relative to the elements of the cosmic web indicates that the structure of UDG galaxies is determined not so much by features of their internal evolution as by the influence of external environment. The disperse stellar structure of UDG galaxies is obviously a sensitive indicator of the tidal influence of their neighbors.

Studying the closest examples of UDG galaxies helps to advance our understanding of their specifics. In the Local Volume with a radius of 10 Mpc, 15 objects were noted [11] that meet the criterion of an ultradiffuse galaxy. All of these UDG objects are located in the known nearby groups. Among them, some (Sag dSph, KK 208, Scl-MM-Dw2, And XIX) have an elongated structure with an apparent axial ratio $b/a < 0.5$, which is caused by gravitational disturbance from a massive neighbor. Others (Garland, NGC 3521sat, d0226+3325) have an irregular shape and a young stellar population, indicating that these dwarfs likely formed from tidal tails and bridges on the outskirts of major galaxies. We consider it appropriate to strengthen the criterion for a large diffuse dwarf (LDD) galaxy, selecting into this category objects of even lower surface brightness, having a round smooth shape and lack of young stellar population. As a criterion for a galaxy to belong to a LDD object, we use the following conditions:

i. The effective diameter of a galaxy in the g-band is $A_{50,\,g} > 3.0$ kpc;

ii. Effective surface brightness in the g-band $SB_{50,\,g} > 26.0\,^{m}$/sq. arcsec;

iii. Apparent axial ratio $b/a > 0.5$;

iv. Morphological type dSph with a smooth shape and an old population ($g - r > 0.50$).

Of the thousand galaxies in the Local Volume, only five known galaxies satisfy these conditions: CenMM-dw1, IKN, KK 77, Cen-MM-dw3 and NGC 4631dw1 with distances in the range (3.6 - 7.4) Mpc, effective diameters $A_{50} = (3.1 - 5.6)$ kpc, effective surface brightness $SB_{50} = (26.2 - 28.1)\,^{m}$/sq. arcsec and absolute magnitudes $M_B = (-11^m.6 - -12^m.6)$. The names of the galaxies are indicated as they are presented in the Updated Nearby Galaxy Catalog [1], a regularly updated version of which is available on-line[1]. It is likely that the Local Volume contains other LDD galaxies that have not yet been discovered due to the incompleteness of deep sky surveys.

2. *A LDD galaxy in the NGC 3056 triplet*. While searching for new nearby dwarf galaxies in DESI Legacy Imaging Surveys, DR10 [12], we discovered a low surface brightness object at coordinates RA = 09:54:43.9 DEC = -28:30:54 (J2000). Its image is shown on the left panel of Fig.1. To the north of it at a distance of 13', there is a galaxy of type S0a with a radial velocity $V_{LG} = 674$ km s^{-1} relative to the centroid of the Local Group. This galaxy with its two satellites: ESO 435-016 and ESO 435-020 forms a triple system, presented in the list of nearby isolated triplets of galaxies [13]. The parameters of this system are shown in Table 1. Its columns contain: galaxy name; its coordinates; morphological type; apparent B-magnitude; radial velocity in km s^{-1}; projection separation

[1] *http://www.sao.ru/lv/lvgdb*

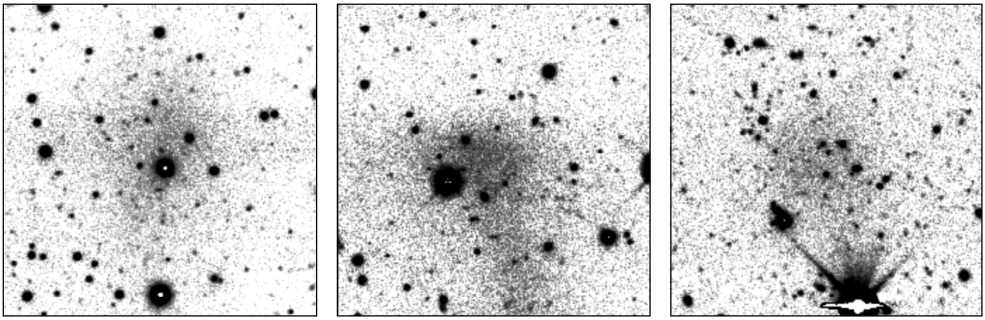

Fig. Images of three large diffuse dwarf galaxies from the DESI Legacy Imaging Surveys: LDD 0954-28, LDD 0911-14 and LDD 0852-02 from the left ro right. Each image size is $2' \times 2'$. North is to the top, East is to the left.

from the main galaxy, R_p, in kpc; estimate of the orbital (projected) mass $M_p = (16/\pi G)\Delta V^2 R_p$ in units of $10^{10} M_\odot$, where ΔV is the difference in radial velocities of the satellite and the host galaxy, and G is the gravitational constant [14]. The irregular galaxy ESO 435-020 has a peculiar structure with signs of recent merging. A feature of the triplet is the small dispersion of the radial velocities of galaxies, comparable to the errors in velocity measurements. The reason for this may be the projection effect, when the velocity vectors of both satellites are almost perpendicular to the line of sight. The observed low velocity dispersion may also be a consequence of the low total mass of the galaxy triplet.

The last row of the table corresponds to the LDD galaxy we noted with a very low surface brightness. We assume that this object is a physical member of the triplet. The analysis undertaken by Karachentseva et al. [15], showed that isolated dSph galaxies are extremely rare. In the volume of the Local Supercluster with a radius of approximately 40 Mpc, only a dozen such putative cases have been noted. Radial velocity measurements in dSph galaxies are very difficult due to the absence of a noticeable amount of neutral hydrogen in them and due to the low optical surface brightness. In those rare cases when such measurements were

Table 1

PROPERTIES OF NGC 3056 TRIPLET OF GALAXIES

Name	RA(2000.0) deg	DEC(2000.0) deg	Type	B mag	V_{LG} km s^{-1}	R_p kpc	M_p 10^{10}
NGC 3056	148.637	-28.298	S0a	12.6	674±5	0	-
ESO 435-016	149.691	-28.622	Im	13.5	678±4	209	0.4
ESO 435-020	149.838	-28.133	Irr-p	14.4	673±2	227	0.03
LDD 0954-28	148.683	-28.515	Sph	17.8	-	47	-

possible, the radial velocities of spheroidal dwarfs turned out to be close to the velocities of neighboring normal galaxies [16], making the assumption of their isolation unlikely.

3. *Other examples of LDD in triplets of galaxies*. The catalog of isolated galaxy triplets in the Local Supercluster [17] contains data on 168 triple systems with radial velocities $V_{LG} < 3500\,\mathrm{km\,s^{-1}}$. The sample of these triplets is characterized by the following median parameters: member radial velocity dispersion of $40\,\mathrm{km\,s^{-1}}$, projected harmonic radius of 155 kpc, projection (orbital) mass of $5\cdot 10^{11} M_\odot$, and orbital mass-to-stellar mass ratio $M_p/M_* = 25$.

We assumed that a low velocity dispersion in a multiple galaxy system may be a favorable factor for the presence of very diffuse objects in it. Among 168 nearby triplets, there are 17 systems with the small ratio $M_p/M_* < 2$, located in the Legacy Imaging Surveys area. Looking at these cases, we found two more triple systems with major members NGC 2781 and UGC 4640, containing candidate LDD objects. Their images are shown in the middle and right panels of Fig.1. Data on these triplets are presented in Tables 2, 3, the parameters of which are similar to those in Table 1. Radial velocities of galaxies and their errors are taken from Lyon Extragalactic Database = LEDA [18]. The distances to NGC 2781 (30.6 Mpc) and UGC 4640 (49.0 Mpc) were estimated from their radial velocities taking into account local cosmic flows in the Numerical Action Method model [19]. The

Table 2

PROPERTIES OF NGC 2781 TRIPLET OF GALAXIES

Name	RA(2000.0) deg	DEC(2000.0) deg	Type	B mag	V_{LG} km s^{-1}	R_p kpc	M_p 10^{10}
NGC 2781	137.864	-14.817	S0a	12.5	1766±22	0	-
DDO 57	137.832	-15.051	Im	14.8	1784±2	94	3.6
MCG-02-24-03	138.028	-15.432	Sm	15.2	1794±6	101	9.3
LDD 0911-14	137.856	-14.703	Sph	18.2	-	46	-

Table 3

PROPERTIES OF UGC 4640 TRIPLET OF GALAXIES

Name	RA(2000.0) deg	DEC(2000.0) deg	Type	B mag	V_{LG} km s^{-1}	R_p kpc	M_p 10^{10}
UGC 4640	132.933	-02.134	Sc	13.8	3091±3	0	-
Arp 257a	132.909	-02.367	Sm	14.4	3103±4	200	3.4
Arp 257b	132.908	-02.354	Im	16.8	3106±6	189	5.0
LDD 0852-02	133.148	-02.177	Sph	19.2	-	184	-

distance to NGC 3056 (12.2 Mpc) was determined from surface brightness fluctuations [20].

As a control sample, we searched for LDD galaxies in the virial zones of 17 triplets with an $M_p/M_* > 100$ and didnot find a single LDD object. Since triplets of galaxies with $M_p/M_* < 2$ constitute only 10 percent of their total number (17/168), the probability of three triplets with LDD members falling into this category is 0.001.

4. *Surface photometry of LDD galaxies*. We performed surface photometry of three new very low surface brightness galaxies, absent in [9] catalog, to estimate their structural parameters. For this purpose, data from DESI Legacy Imaging Surveys, DR10 in the g and r bands were used. The photometry of the galaxies was carried out by measuring photometric curves of growth using standard ellipse-fitting and aperture photometry techniques in photutils[2]. This was preceded by background subtraction. Also, foreground and bright background objects were masked and then the corresponding pixels were replaced by the mean flux in the aperture rings contained in the mask. We fit the resulting curve of growth, $f(r)$, using the following modified exponential law:

$$f(r) = f(r_0) + f^{\exp}(r), \quad r > r_0, \tag{1}$$

where $f^{\exp}(r)$ - the flux corresponding to the standard exponential law and $f(r_0)$ - the additional flux from the inner part ($r < r_0$) of the galaxy. This leads to:

$$f(r) = f_{tot}\left(1 - \frac{f_{tot}^{exp}}{f_{tot}}\left(1 + \frac{r}{h}e^{-r/h}\right)\right), \tag{2}$$

where f_{tot}, f_{tot}^{exp} and h - fitting parameters of the model: total flux, total flux (without adding $f(r_0)$) from the standard exponential law and the exponential scale from the standard exponential law.

The results of measuring the integral magnitudes of galaxies g and r, effective radii $r_{50,g}$ and $r_{50,r}$ are presented in Table 4. It also shows $B = g + 0.542(g - r) + 0.141$ and $V = g - 0.496(g - r) - 0.015$ integral magnitudes of galaxies in B and V system [21].

As one can see, the integrated color indices $B - V$, taking into account the color excess $E(B - V)$ due to extinction, turns out to be typical for dSph galaxies with old stellar population. The effective linear diameters $A_{50} > 3.0$ kpc of all three diffuse galaxies and their effective surface brightness $SB_{50} > 26.0^{\mathrm{m}}$/sq. arcsec satisfy the conditions formulated above for LDD galaxies. The assumption that these LDD galaxies are physical members of the triplets under consideration looks very plausible, given that such diffuse objects have not yet been discovered in the general

[2] *https://photutils.readthedocs.io/en/stable/*

Table 4

PHOTOMETRIC PARAMETERS OF THE LDD GALAXIES

Name	g mag	r mag	B mag	V mag	$r_{50,g}$ "	$r_{50,r}$ "	$SB_{50,g}$ mag/sq.arcsec	$A_{50,g}$ kpc	$B-V$ mag	$E(B-V)$ mag	M_B mag
LDD0954-28	17.31	16.75	17.75	17.02	30.77	31.96	26.74	3.64	0.73	0.065	-12.95
LDD0911-14	17.76	17.12	18.25	17.43	19.83	19.65	26.24	5.88	0.64	0.046	-14.37
LDD0852-02	18.70	18.08	19.18	18.38	21.10	21.15	27.31	10.02	0.62	0.016	-14.34

field. The absolute magnitudes of these LDD galaxies, indicated in the last column of Table 4, are 1-3 mag brighter than similar objects in the Local Volume.

5. *Brief discussion*. We estimated the stellar mass of galaxy triplets M_* using the ratio $M_*/M_\odot = 0.6(L_K/L_\odot)$ according to Lelli et al. [22]. The values of the total luminosity of triplets in the K-band are taken from the catalog [17] with correction for the adjusted distance. Data on Table 5 show that the estimate of the total (projected) mass of triplets turned out to be approximately equal to their stellar mass within the M_p errors due to the velocity measurement errors. From this we can conclude that the "cold" kinematics of the triplets under consideration does not require the presence of a noticeable amount of dark matter in them. It remains unclear how such a feature of triplets can be related to the presence in their volume of very diffuse galaxies with old stellar populations.

In general, various possible scenarios for the formation of LDD galaxies have been discussed in the literature: a high angular momentum of the LDD [22], a stellar feedback from the host galaxy [23], and "failed Milky Way" mechanism [24].

Note that the average projection separation of LDD galaxies, 92 kpc, is about half the average distance of late-type satellites, 170 kpc. The same effect of segregation of dSph and dIrr galaxies is also well known in other groups and clusters of galaxies.

The diffuse satellite LDD 0911-14 exhibits a strong shape distortion in the form of a tidal tail directed towards the massive host galaxy NGC 2781. Our photometry of this satellite was limited to the main body of the object. Taking into account the tidal tail almost doubles the integral luminosity and effective

Table 5

TRIPLE SYSTEMS OF GALAXIES WITH LDD

Name	D Mpc	$\log(M_*)$ 10^{10}	$\log(M_p)$ 10^{10}
NGC 3056	12.2	0.87	0.22±0.20
NGC 2781	30.6	5.11	6.45±2.85
UGC 4640	49.0	2.51	4.20±0.80

diameter of this galaxy.

It is obvious that galaxy systems with cold kinematics and the presence of very diffuse members can also be found among groups with a larger population. As an example, we note a group of four satellites around the galaxy NGC 660. At a projection distance of 13' east of NGC 660 there is an extremely low surface brightness galaxy (01:43:55.2 + 13:38:42), discovered by Karachentsev & Kaisina [25]. The spiral galaxy NGC 660 itself has a very peculiar shape in the form of two merging galaxies. With its low ratio $M_p/M_* \simeq 3$, this group stands out among other groups in the Makarov & Karachentsev [13] catalog.

Recently, Okamoto et al. [26] discovered an extremely low surface brightness satellite near the nearby spiral galaxy NGC 253 using deep stellar photometry with the Hyper Suprime-Cam on the Subaru telescope. According to the authors, this "ghost" galaxy has an effective diameter of 6.7 ± 0.7 kpc, an effective surface brightness of $SB_{50} \sim 30^{m}$/sq. arcsec, an apparent axial ratio of $b/a = 0.94$, and old stellar population. This satellite, NGC 253-SNFC-dw1, is located at a projection separation of $R_p = 75$ kpc from the center of NGC 253 and shows weak signs of tidal disruption. In its size and extremely low surface brightness, this dim satellite of NGC 253 is similar to the Milky Way satellite, Antlia 2, with $A_{50} = 5.8 \pm 0.6$ kpc, $SB_{50} = 31.9^{m}$/sq. arcsec [27] and the satellite of M 31, And XIX, with $A_{50} = 6.2 \pm 2.0$ kpc, $SB_{50} = 31.0^{m}$/sq. arcsec [28]. Such objects are undetectable by conventional photometry, since their surface brightness is 5-6 mag fainter than that of the UDG galaxies discussed by [3].

It is interesting to note that the galaxy NGC 253, along with NGC 2683 and NGC 2903, has the minimum radial velocity dispersion of satellites ($\sigma_v < 45$ km s^{-1}) among the 25 brightest galaxies in the Local Volume with a luminosity similar to that of the Milky Way. This fits with the trend that the cold kinematics of the satellites (or the deficiency of dark matter in the group) favors the survival in the group of "fragile" satellites with very low stellar density.

We did not consider here the possible reasons for the observed correlation between the presence of LDD galaxies in a group and the deficiency of dark matter in it. Apparently, it is necessary to accumulate richer statistics of such cases, as well as perform dynamic modeling of tidal destruction of diffuse satellites under different assumptions about the shape of the satellites' orbits and the amount of dark matter in the LDD galaxy. According to Penarrubia et al. [29], the tidal influence of the dark halo of the main galaxy in a group reduces the central surface brightness of a satellite and shortens its size. Torrealba et al. [27] noted that *N*-body modeling a strong tidal stripping of a diffuse companion can explain the observed properties of Antlia 2-type galaxies.

More in-depth observations of the mentioned triplets of galaxies both in the optical range and in the neutral hydrogen line could clarify the problem of the supposed connection between the cold kinematics of the group's satellites and the presence of LDD galaxies in it.

Acknowledgements. This work has made use of the DESI Legacy Imaging Surveys, the Lyon Extragalactic Database and the revised version of the Local Volume database. IDK and AEN are supported by the Russian Science Foundation grant 24-12-00277.

[1] Special Astrophysical Observatory of the Russian Academy of Sciences, Russia, e-mail: idkarach@gmail.com
[2] Main Astronomical Observatory, National Academy of Sciences of Ukraine, Kiev, Ukraine, e-mail: valkarach@gmail.com

БОЛЬШИЕ ДИФФУЗНЫЕ КАРЛИКИ В ДИНАМИЧЕСКИ ХОЛОДНЫХ ТРОЙНЫХ СИСТЕМАХ ГАЛАКТИК

И.Д.КАРАЧЕНЦЕВ[1], А.Е.НАЗАРОВА[1], В.Е.КАРАЧЕНЦЕВА[2]

Мы сообщаем об обнаружении трех больших диффузных карликовых (LDD) галактик, расположенных в изолированных тройных системах. Они имеют эффективные диаметры (3.6 - 10.0) кпк и эффективные поверхностные яркости (26.2 - 27.3) зв. вел. с квадратной секунды. Отмечено, что LDD галактики имеют тенденцию встречаться в мелких группах с очень малой дисперсией лучевых скоростей. Суммарная (орбитальная) оценка массы этих триплетов примерно равна их суммарной звездной массе в пределах ошибок измерения лучевых скоростей галактик. Наличие LDD галактик в холодных кратных системах представляется загадочным.

Ключевые слова: *галактики - карликовые галактики - галактики низкой поверхностной яркости*

REFERENCES

1. *I.D.Karachentsev*, *D.I.Makarov*, *E.I.Kaisina*, Astron. J., **145**, 101, 2013.
2. *P. van Dokkum*, *R.Abraham*, *A.Merritt et al.*, Astrophys. J., **798L**, 45, 2015.
3. *J.C.Mihos*, *P.Harding*, *J.J.Feldmeier et al.*, Astrophys. J., **834**, 16, 2017.

4. *R.P.Munoz*, *P.Eigenthaler*, *T.H.Puzia et al.*, Astrophys. J., **813**, L15, 2015.
5. *J.Koda*, *M.Yagi*, *H.Yamanoi et al.*, Astrophys. J., **807**, L2, 2015.
6. *D.Crnojevic*, *D.J.Sand*, *K.Spekkens et al.*, Astrophys. J., **823**, 19, 2016.
7. *E.Toloba*, *D.J.Sand*, *K.Spekkens et al.*, Astrophys. J., **816**, L5, 2016.
8. *A.Merritt*, *P. van Dokkum*, *S.Danieli et al.*, Astrophys. J., **833**, 168, 2016.
9. *D.Zaritsky*, *R.Donnerstein*, *A.Dey et al.*, Astrophys. J. Suppl., **267**, 27, 2023.
10. *J.Roman*, *I.Trujillo*, Mon. Not. Roy. Astron. Soc., **468**, 4039, 2017.
11. *I.D.Karachentsev*, *L.N.Makarova*, *M.E.Sharina et al.*, Astrophys. Bull., **72**, 376, 2017.
12. *A.Dey*, *D.J.Schlegel*, *D.Lang et al.*, Astron. J., **157**, 168, 2019.
13. *D.Makarov*, *I.Karachentsev*, Mon. Not. Roy. Astron. Soc., **412**, 2498, 2011.
14. *I.Karachentsev*, *O.Kashibadze*, Astron. Nachr., **342**, 999, 2021.
15. *V.E.Karachentseva*, *I.D.Karachentsev*, *M.E.Sharina*, Astrophysics, **53**, 462, 2010.
16. *M.E.Sharina*, *I.D.Karachentsev*, *V.E.Karachentseva*, in The Zeldovich Universe: Genesis and Growth of the Cosmic Web, ed. R. van de Weygaert, S.Shandarin, E.Saar, J.Einasto, **308**, 473, 2016.
17. *D.I.Makarov*, *I.D.Karachentsev*, Astrophys. Bull., **64**, 24, 2009.
18. *D.Makarov*, *P.Prugniel*, *N.Terekhova et al.*, Astron. Astrophys., **570**, A13, 2014.
19. *E.J.Shaya*, *R.B.Tully*, *Y.Hoffman et al.*, Astrophys. J., **850**, 207, 2017.
20. *J.L.Tonry*, *A.Dressler*, *J.P.Blakeslee et al.*, Astrophys. J., **546**, 681, 2001.
21. *T.M.C.Abbott*, *M.Adamów*, *M.Aguena et al.*, Astrophys. J. Suppl., **255**, 20, 2021.
22. *N.C.Amorisco*, *A.Loeb*, Mon. Not. Roy. Astron. Soc., **459**, L51, 2016.
23. *A. Di Cintio*, *C.B.Brook*, *A.Dutton et al.*, Mon. Not. Roy. Astron. Soc., **466**, L1, 2017.
24. *P. van Dokkum*, *R.Abraham*, *J.Brodie et al.*, Astrophys. J., **828**, L6, 2016.
25. *I.D.Karachentsev*, *E.I.Kaisina*, Astrophys. Bull., **77**, 372, 2022.
26. *S.Okamoto*, *A.M.N.Ferguson*, *N.Arimoto et al.*, Astrophys. J., **967L**, 240, 2024.
27. *G.Torrealba*, *V.Belokurov*, *S.E.Koposov et al.*, Mon. Not. Roy. Astron. Soc., **488**, 2743, 2019.
28. *N.F.Martin*, *R.A.Ibata*, *G.F.Lewis et al.*, Astrophys. J., **833**, 167, 2016.
29. *J.Peñarrubia*, *J.F.Navarro*, *J.A.W.McConnachie*, Astrophys. J., **673**, 226, 2008.

А С Т Р О Ф И З И К А

ТОМ 67 АВГУСТ, 2024 ВЫПУСК 3

DOI: 10.54503/0571-7132-2024.67.3-289

PROBING PSEUDOSCALARS WITH PULSAR POLARISATION DATA SETS

K.CHAND[1], S.MANDAL[2]

Received 25 June 2024
Accepted 26 August 2024

Recently a data set containing linear and circular polarisation information of a collection of six hundred pulsars has been released. The operative radio wavelength for the same was 21 cm. Pulsars radio emission process is modelled either with synchroton/superconducting self-Compton route or with curvature radiation route. These theories fall short of accounting for the circular polarisation observed, as they are predisposed towards producing, solely, linear polarisation. Here we invoke (pseudo)scalars and their interaction with photons mediated by colossal magnetic fields of pulsars, to account for the circular part of polarisation data. This enables us to estimate the pseudoscalar parameters such as its coupling to photons and its mass in conjunction as product. To obtain these values separately, we turn our attention to recent observation on 47 pulsars, whose absolute polarisation position angles have been made available. Except, a third of the latter set, the rest of it overlaps with the expansive former data set on polarisation type and degree. This helps us figure out, both the pseudoscalar parameters individually, that we report here.

Keywords: *ALP-γ (14.80.Va) mixing:pulsar (97.60.Gb):polarisation (42.25.Ja)*

1. *Introduction.* In the last two decades, scenarios in which pseudoscalar [1-6] particles and photons couple and subsequently mix (Fig.1) in the presence of magnetic fields. There are many ways in which photon can interact with axion like particles (ALPs). And these interaction can change the polarisation properties of electromagnetic radiations through different phenomena [7,8]. First may be, since the axions alter the photon dispersion relation, EM wave propagation in the presence of an axion backdrop can modify the polarisation of the wave. Different photon polarisation modes propagate through an axion cloud at different phase velocities. [9,10] provides the modified dispersion relation of photon polarisation modes. Second may be, the axion photon scattering process at the second level of coupling $O(g_{a\gamma}^2)$ can also produce circular polarisation by converting linear polarisation through Faraday conversion. The development of the Stokes parameters at the second order of $g_{a\gamma}$ is then computed using the quantum Boltzmann method. In third we study the scattering process of photons from a magnetic field by exchanging virtual axions in the intermediate states as a second order phenomena in terms of $O(g_{a\gamma}^2)$ using the quantum Boltzmann approach, i.e. when

plane polarized light coming from a source it's parallel component which is parallel to magnetic field may interact with magnetic field and convert into axion like particles (ALPs) and these ALPs may again interact with magnetic field and reconvert back to the photons, while perpendicular component of plan polarized light will go as it is. Because ALPs have very little non zero mass so its velocity is smaller than photons. So, due to this conversion parallel component of plan polarized light will moves slowly and a phase difference will come in the parallel and perpendicular components of plane polarized light which will induce circular component in the incident light. This mixing have received a lot of attention [11-17], both phenomenologically [18-25] and observationally [26-33]. This is of particular interest in astrophysics, where this mixing of photons with pseudoscalars could make the universe transparent [34], change the polarisation properties of light [35] and is be potentially responsible for effects such as "Supernovae dimming" [34] or "Large-scale coherent orientation" [35] of the universe, also known as "Hutsemekers" effect. The best-known light pseudoscalar particle, the axion, was introduced long ago [36] to explain the absence of CP violation in Quantum Chromodynamics (QCD) [37]. One postulated the existence of a new spontaneously broken continuous Peccei-Quinn symmetry, so that the axion was a pseudo Goldstone boson. It was soon realised that one needed to introduce a very large scale in the theory in order to suppress the interactions of the axion, while preserving the Peccei-Quinn mechanism. The invisible axion [38] emerges at a unification scale, and the effective coupling is suppressed by this scale. The invisible axion, being closely related to QCD, has definite and interrelated expressions for its mass [39] and coupling strength [40] to other particles, given

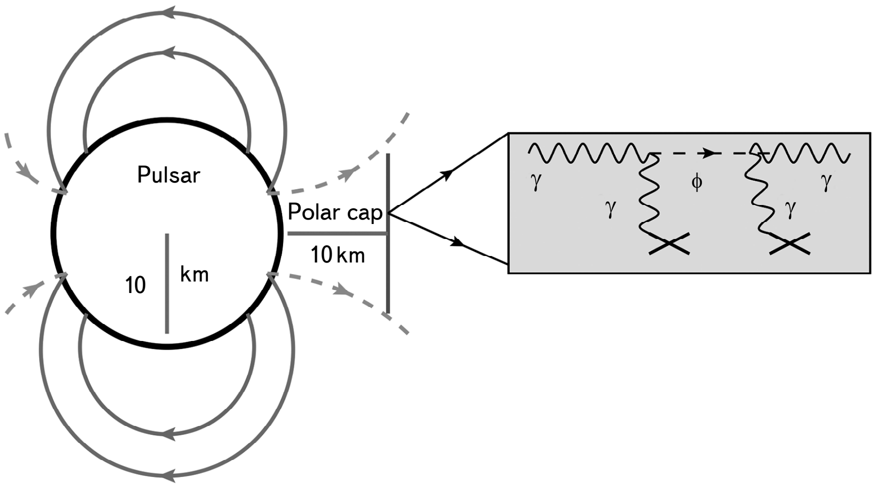

Fig.1. Axion photon mixing in the polar cap region.

a specific model [41,42]. Various cosmological and astrophysical bounds can be used to further constrain the parameters [40], and the allowed parameters do not lead to observable effects over cosmological scales. The mass of the pseudoscalar particle needs to be very close to the photon effective mass in order to mix in the rather weak magnetic fields of the extra galactic space. However, generic pseudoscalars or axion-like particles (ALP's) have been hypothesized by many extensions of the standard model of particle physics. Theories such as supergravity [43] and superstring theory [44] contain many broken U(1) symmetries, that can lead to very light scalar, or pseudoscalar, particles.

Pulsars, discovered fifty years back [45], are a fusion fuel less state of a two to three solar mass $M_{\odot}$ star [46], wherein surmounting inward gravitational pull [47], in absence of a commensurate radiation pressure from fusion, makes it collapse [48], into a tiny object [49]. Two effects follow: the protons and neutrons coalesce together making the pulsars synonymous with neutron stars [50]; and, also during this compression phase the the magnetic flux is conserved, thereby promoting the magnetic induction field inside it to a colossal [50] value. Other effects such as the "pulsating" nature of the "star" in its last phase of stellar evolution, leading to the nomenclature and discovery of the same [50], won't be pursued here.

Pulsars have been harnessed to estimate the coloumn density [51], by observing pulsar dispersion measure. Also, the magnetic field of the interstellar medium (henceforth ISM) along the line of sight can be estimated by observing its rotation measure [51]. Pulsars were traditionally, observed on earth inside the radio frequency window specifically, from 100 MHz - 100 GHz [50]. However, over time, pulsars became known for emission in other wavebands like X-ray, γ -ray, etc. [52]. Despite, half a century of efforts, the mechanisms for such types of radiation and properties thereof, such as polarisation, are not very well understood [53]. This in turn banks heavily on the fact that pulsar atmosphere or its magnetosphere models are still in its infancy [54]. There are competing contenders as preferred models for pulsed emission and continuum radiation. Curvature radiation, synchroton radiation, inverse Compton radiation, superconducting self Compton radiation, etc. are at the forefront, but none fits all observational features of pulsars [53]. We shall, however, restrict ourselves, polarisation properties of radiation inside the pulsar atmosphere without looking into the radiation origin. Here we shall harness the two pulsar properties the size, and magnetic field which in turn is deduced from period and associated derivative, to estimate the pseudoscalar parameters like the mass and its coupling to photons, with the help of 21 cm observations.

In section 2 we describe the polarimetric data set on six hundred pulsars [55], along with the quantities that can be derived from these observed parameters

Table 1

PULSAR POLARISATION PROPERTIES AT 1.4 GHz (sample)

Jname	P (ms)	$\dot{P}$ unitless	log($\dot{E}$) (ergs^{-1})	L/I %	V/I %	$\lvert V\rvert/I$ %	err %	B Gev^2	χ rad
J0034-0721	943	4.24E-16	31.3	10.7	7.7	7.5	3	4.44E-08	0.303493832023204
J0051+0423	354.7	7.14E-18	30.8	13.1	-2.3	11.2	3.3	3.53E-09	0.287272232961884
J0108-1431	807.6	8.43E-17	30.8	76.7	15.5	13.1	3.1	1.83E-08	0.085016451375219
J0134-2937	137	8.21E-17	33.1	45.3	-17.2	16.9	3	7.44E-09	0.178538083464964
J0151-0635	1464.7	3.99E-16	30.7	29.1	-1.7	4.2	3.3	5.36E-08	0.070948527302082
J0152-1637	832.7	1.16E-15	31.9	15.1	1.1	6	3	6.90E-08	0.190253188556182
J0206-4028	630.6	1.27E-15	32.3	10.6	9.3	9.9	3.1	6.27E-08	0.366407550893253
J0211-8159	1077.3	3.17E-16	31	17	11.7	15.4	5.5	4.10E-08	0.502033554635695
J0255-5304	447.7	2.86E-17	31.1	7.3	-4.1	5.5	3	7.94E-09	0.329545023167104
J0304+1932	1387.6	1.35E-15	31.3	33.4	15.1	14.8	3	9.60E-08	0.209112164789615
J0343-3000	2597	5.59E-17	29.1	14.3	3.1	3.9	3.2	2.67E-08	0.107846382092558
J0401-7608	545.3	1.64E-15	32.6	28.6	-0.1	4.7	3	6.63E-08	0.08060916072996
J0448-2749	450.4	1.46E-16	31.8	23.9	-13.3	11.8	3	1.80E-08	0.225223527837328
J0450-1248	438	1.07E-16	31.7	25.3	2.5	6	3.4	1.52E-08	0.126047990334037
J0452-1759	548.9	5.28E-15	33.1	18.9	3.6	4.2	3	1.19E-07	0.109334472936971
J0459-0210	1133.1	1.47E-15	31.6	10.4	-12.9	9.6	3.8	9.05E-08	0.337370471111776
J0520-2553	241.6	2.84E-17	31.9	18.2	-4.3	5	3.6	5.81E-09	0.129970070094264
J0525+1115	354.4	7.12E-17	31.8	10.6	12.5	15.5	3	1.11E-08	0.478954335502063
J0528+2200	3745.5	4.21E-14	31.5	36.9	-4.9	4.6	3	8.81E-07	0.062683228726001
J0533+0402	963	1.8E-16	30.9	13.3	4	5.5	3.2	2.92E-08	0.211767678516289
J0536-7543	1245.9	6.17E-16	31.1	48.8	-11.1	11	3	6.15E-08	0.110852247980192
J0540-7125	1286	8.55E-16	31.2	14.2	3.1	15.8	4.8	7.35E-08	0.391121799864486
J0543+2329	246	1.5E-14	34.6	45.2	-8.2	7.9	3	1.35E-07	0.086515496781741
J0601-0527	396	1.25E-15	32.9	30.9	4.4	11.3	3	4.94E-08	0.175294355633881
J0614+2229	335	6.01E-14	34.8	72	20.3	20.1	3	3.15E-07	0.135938275210493

assuming a basic pulsar model [50]. The observation of circular polarisation is hitherto unexplained by radiation models, theoretical [56-58] and statistical [59] alike, so far. Thereafter, in the section 3, we invoke the light quanta to pseudoscalar interaction to step wise calculate the correlators, ab initio, between the three degrees of freedom. Thereby, in section 4 we digress to Stokes parameters; the experimental interface with theoretical quantities like ellipticity parameter and polarisation position angle, using the definition of correlators. In the next section 5, we discuss the extraction process of pseudoscalar parameters, for mixing case only, discarding another two cases and leaving the general case open that might arise, naturally. Also in this segment we estimate the values of regression parameters derived from statistical analysis of the data set tables. In the next section we present our results. Thereafter, we conclude by projecting the feasibility of our result and scope in future directions.

2. *Observation*. The following data shown in Table 1 is a small part of the data obtained from [55]. It contains the spin down luminosity $\dot{E}$ [48] and pulsar spin period P [49] all six hundred of them. Following the basic pulsar model [50,60] we may derive pulsar parameters such as spin period time derivative $\dot{P}$ and the magnetic field B_s.

$$B_s = 3.2 \cdot 10^{19} \sqrt{P\dot{P}}\,, \quad \dot{P} = \frac{\dot{E}P^3}{4\pi^2 I}. \tag{1}$$

Also, from the ratio between the percentage of circular to linear polarisation provides us with the ellipticity parameter χ.

$$\tan(2\chi) = \frac{V}{p_{lin}}. \tag{2}$$

We have extracted and separately tabulated these derived values for further use in section 5.

3. *Pseudoscalar photon mixing*. We begin our discussion with a derivation of the equations of motion for the axion-photon system [61] where the term "axion" stands generically for any light pseudoscalar particle. A suitable Lagrangian density is given by

$$\begin{aligned}\mathcal{L} = &-\frac{1}{4}F_{\mu\nu}F^{\mu\nu} + \frac{1}{2}\partial_\mu\, a\,\partial^\mu\, a - \frac{1}{2}m_a^2 a^2 + \frac{1}{4M}F_{\mu\nu}\tilde{F}^{\mu\nu} a \\ &+ \frac{a^2}{90\, m_e^4}\left[\left(F_{\mu\nu}F^{\mu\nu}\right)^2 + \frac{7}{4}\left(F_{\mu\nu}\tilde{F}^{\mu\nu}\right)^2\right],\end{aligned} \tag{3}$$

where a is the axion field, m_a its mass, $F_{\mu\nu}$ the electromagnetic field tensor, and $\tilde{F}^{\mu\nu} = \varepsilon^{\mu\nu\rho\sigma} F_{\rho\sigma}/2$ its dual. The third term describes the CP-conserving interaction between the pseudoscalar and the electromagnetic field where the energy scale M is a phenomenological parameter to characterize the interaction strength i.e. $g_{\alpha\gamma} = 1/M$, $g_{\alpha\gamma}$ is coupling constant. The last term in Eq. (3) is the Euler-Heisenberg effective Lagrangian' arising from the vacuum polarizability. It describes photon-photon interactions in the limit where the photon frequencies are small in comparison with the electron mass m_e, and all field strengths are weak in comparison with the critical field strengths. In our case last term is negligible. We will solve equation of motion for above Lagrangian.

The following mixing matrix (4) provides for the necessary ingredient of photon pseudoscalar mixing mediated by a magnetic field [61]. Also this reference assumes a free space, for calculation, hence there are no Faraday effect (M_{21}, M_{12} entries) terms coupling the two photon polarisations. Inside pulsar magnetosphere this could hardly be the case. However, we may still ignore the Faraday terms. The reason being the smallness of it inside spaces with large magnetic fields; as shown in by one of the coauthors [62], by deriving the limiting propagation frequency, below which Faraday effect holds significance.

$$\omega_L = \frac{\omega_p^2 \omega_B \left(\omega_p^2 - m_a^2\right)}{|\mathcal{B}|^2} \frac{\cos\Theta}{\sin^2\Theta},$$

for the values derived from the pulsar database, such as the magnetic field, and the plasma frequency from literature [63], which is much smaller than the pseudoscalar mass, we see that Faraday effect can safely be neglected at the operating frequency of 1.4 GHz ($>> \omega_L$), with which the observations were made.

$$M = \begin{pmatrix} A_1 & 0 & 0 \\ 0 & A_2 & T \\ 0 & T & -B \end{pmatrix}, \tag{4}$$

The symbols in the matrix (4) stands for

$$A_1 = 4\omega^2 \xi \sin^2\Theta + \omega_p^2, \quad A_2 = 7\omega^2 \xi \sin^2\Theta + \omega_p^2, \quad B = m_a^2, \quad T = g\mathcal{B}\omega. \tag{5}$$

where, $\mathcal{B}$ is the magnetic field, Θ is the angle between the $\vec{k}$ and the magnetic field $\mathcal{B}$, m_a the axion mass, and $\xi = (\alpha/45\pi)\left(e\mathcal{B}/m_f^2\right)^2$, with m_f [61] the lightest Fermion mass.

The non-diagonal 2×2 matrix, in Eq. (4) is given by,

$$M_2 = \begin{pmatrix} A_2 & T \\ T & -m_a^2 \end{pmatrix}. \tag{6}$$

One can solve for the eigen values of the Eq. (7), from the determinant equation,

$$\begin{vmatrix} A_2 - \lambda & T \\ T & -m_a^2 - \lambda \end{vmatrix} = 0, \tag{7}$$

and the roots are,

$$M_\pm = \frac{A_2 - m_a^2}{2} \pm \frac{1}{2}\sqrt{\left[\left(A_2 + m_a^2\right)^2 + 4T^2\right]}. \tag{8}$$

3.1. *Equation of motion*. The equation of motion for the axion photon mixing, in the non-diagonal basis gets decoupled and can be written in the matrix from as:

$$\left[\left(\omega^2 + \partial_z^2\right)\mathbf{I} + \mathbf{M}\right]\begin{pmatrix} A_\perp \\ A_\parallel \\ a \end{pmatrix} = 0. \tag{9}$$

where $\mathbf{I}$ is a 3×3 identity matrix and $\mathbf{M}$ is the mixing matrix.

The uncoupled and the coupled equations can further be written as,

$$\left[\left(\omega^2 + \partial_z^2\right) + A_1\right]\left(A_\perp\right) = 0 \tag{10}$$

and

$$\left[\left(\omega^2 + \partial_z^2\right)\mathbf{I} + M_2\right]\begin{pmatrix} A_{||} \\ a \end{pmatrix} = 0\,. \tag{11}$$

It is possible to diagonalise Eq. (11) by a similarity transformation (we would denote the diagonalising matrix by O), leading to the form,

$$\left[\left(\omega^2 + \partial_z^2\right)\mathbf{I} + M_D\right]\begin{pmatrix} \overline{A}_{||} \\ \overline{a} \end{pmatrix} = 0\,. \tag{12}$$

when the diagonal matrix M_D is given by:

$$M_D = \begin{pmatrix} M_+ & 0 \\ 0 & M_- \end{pmatrix}. \tag{13}$$

3.2. *Dispersion relations*. Defining the wave vectors in terms of k_i's, as:

$$k_\perp = \sqrt{\omega^2 + A_1}\,, \quad k_+ = \sqrt{\omega^2 + M_+}\,, \quad k_- = -\sqrt{\omega^2 + M_+} \tag{14}$$

and

$$k'_+ = \sqrt{\omega^2 + M_-}\,, \quad k'_- = -\sqrt{\omega^2 + M_-}\,. \tag{15}$$

3.3. *Solutions*. The solutions for the gauge field and the axion field, given by (12) as well as the solution for eqn. for $A_\perp$ in k space can be written as,

$$\overline{A}_{||}(z) = \overline{A}_{||+}(0)e^{ik_+z} + \overline{A}_{||-}(0)e^{-ik_-z}\,, \tag{16}$$

$$\overline{a}(z) = \overline{a}_+(0)e^{ik'_+z} + \overline{a}_-(0)e^{-ik'_-z}\,, \tag{17}$$

$$A_\perp(z) = A_{\perp+}(0)e^{ik_\perp z} + A_{\perp-}(0)e^{-ik_\perp z}\,. \tag{18}$$

The diagonal matrix can be written as

$$M_D = O^T M_2 O \tag{19}$$

when

$$O = \begin{pmatrix} \cos\theta & -\sin\theta \\ \sin\theta & \cos\theta \end{pmatrix} \equiv \begin{pmatrix} c & -s \\ s & c \end{pmatrix} \tag{20}$$

in short hand notation.

3.4. *Similarity transformation*. The diagonal matrix

$$M_D = \begin{pmatrix} c & -s \\ -s & c \end{pmatrix}\begin{pmatrix} M_{11} & M_{12} \\ M_{21} & M_{22} \end{pmatrix}\begin{pmatrix} c & -s \\ s & c \end{pmatrix}, \tag{21}$$

With $M_{11} = A_2$, $M_{12} = T$, $M_{21} = T$ lastly $M_{22} = -B$.

The value of the parameter θ, is fixed from the equality,

$$M_D = \begin{pmatrix} c & s \\ -s & c \end{pmatrix} \begin{pmatrix} M_{11} & M_{12} \\ M_{21} & M_{22} \end{pmatrix} \begin{pmatrix} c & -s \\ s & c \end{pmatrix} = \begin{pmatrix} M_+ & 0 \\ 0 & M_- \end{pmatrix}, \tag{22}$$

leading to,

$$\begin{pmatrix} c^2 M_{11} + s^2 M_{22} + 2csM_{12} & M_{12}\left(c^2 - s^2\right) + cs\left(M_{22} - M_{11}\right) \\ M_{12}\left(c^2 - s^2\right) + cs\left(M_{22} - M_{11}\right) & s^2 M_{11} + c^2 M_{22} - 2csM_{12} \end{pmatrix} = \begin{pmatrix} M_+ & 0 \\ 0 & M_- \end{pmatrix}. \tag{23}$$

Equating the components of the matrix equation (23), one arrives at:

$$\tan(2\theta) = \frac{2M_{12}}{M_{11} - M_{22}} = \frac{T}{A_2 - m_a^2}. \tag{24}$$

3.5. *Correlation functions*. The solutions for propagation along the +ve z axis, is given by,

$$\overline{A}_{||}(z) = \overline{A}_{||}(0)e^{ik_+ z} \tag{25}$$

$$\overline{a}(z) = \overline{a}(0)e^{ik'_+ z} \tag{26}$$

that can further be written in the following form,

$$\begin{pmatrix} \overline{A}_{||}(z) \\ \overline{a}(z) \end{pmatrix} = \begin{pmatrix} e^{ik_+ z} & 0 \\ 0 & e^{ik'_+ z} \end{pmatrix} \begin{pmatrix} \overline{A}_{||}(0) \\ \overline{a}(0) \end{pmatrix}. \tag{27}$$

Since,

$$\begin{pmatrix} \overline{A}_{||}(z/0) \\ \overline{a}(z/0) \end{pmatrix} = O^T \begin{pmatrix} A_{||}(z/0) \\ a(z/0) \end{pmatrix} \tag{28}$$

it follows from there that,

$$\begin{pmatrix} A_{||}(z) \\ a(z) \end{pmatrix} = O \begin{pmatrix} e^{ik_+ z} & 0 \\ 0 & e^{ik'_+ z} \end{pmatrix} O^T \begin{pmatrix} A_{||}(0) \\ a(0) \end{pmatrix}. \tag{29}$$

Using Eq. (29) we arrive at the relation,

$$A_{||}(z) = \left[e^{ik_+ z}\cos^2\theta + e^{ik'_+ z}\sin^2\theta\right]A_{||}(0) + \left[e^{ik_+ z} - e^{ik'_+ z}\right]\cos\theta\sin\theta\, a(0) \tag{30}$$

$$a(z) = \left[e^{ik_+ z} - e^{ik'_+ z}\right]\cos\theta\sin\theta\, A_{||}(0) + \left[e^{ik_+ z}\sin^2\theta + e^{ik'_+ z}\cos^2\theta\right]a(0). \tag{31}$$

If the axion field is zero to begin with, i.e

$$a(0) = 0. \tag{32}$$

Then the solution for the gauge fields take the following form,

$$A_{||}(z) = \left[e^{ik_+ z}\cos^2\theta + e^{ik'_+ z}\sin^2\theta\right]A_{||}(0) \tag{33}$$

$$A_\perp(z) = e^{ik_\perp z}A_\perp(0). \tag{34}$$

The correlations of different components take the following form:

$$\left\langle A_{\|}^{*}(z)A_{\|}(z)\right\rangle = \left[\cos^{4}\theta + \sin^{4}\theta + 2\sin^{2}\theta\cos^{2}\theta\cos[(k_{+}-k_{+}')z]\right]\left\langle A_{\|}^{*}(0)A_{\|}(0)\right\rangle \tag{35}$$

$$\left\langle A_{\|}^{*}(z)A_{\perp}(z)\right\rangle = \left[\cos^{2}\theta\, e^{i(k_{\perp}-k_{+})z} + \sin^{2}\theta\, e^{i(k_{\perp}-k_{+}')z}\right]\left\langle A_{\|}^{*}(0)A_{\perp}(0)\right\rangle \tag{36}$$

$$\left\langle A_{\perp}^{*}(z)A_{\perp}(z)\right\rangle = \left\langle A_{\perp}^{*}(0)A_{\perp}(0)\right\rangle . \tag{37}$$

4. *Stokes parameters*. Using the definitions of the Stokes parameters, in terms of the correlators:

$$I = \left\langle A_{\|}^{*}(z)A_{\|}(z)\right\rangle + \left\langle A_{\perp}^{*}(z)A_{\perp}(z)\right\rangle , \tag{38}$$

$$Q = \left\langle A_{\|}^{*}(z)A_{\|}(z)\right\rangle - \left\langle A_{\perp}^{*}(z)A_{\perp}(z)\right\rangle , \tag{39}$$

$$U = 2\mathrm{Re}\left\langle A_{\|}^{*}(z)A_{\perp}(z)\right\rangle , \tag{40}$$

$$V = 2\mathrm{Im}\left\langle A_{\|}^{*}(z)A_{\perp}(z)\right\rangle . \tag{41}$$

Using the relations for the corresponding correlators, the Stokes parameters turn out to be

$$\begin{aligned} I &= \left[\cos^{4}\theta + \sin^{4}\theta + 2\sin^{2}\theta\cos^{2}\theta\cos[(k_{+}-k_{+}')z]\right]\left\langle A_{\|}^{*}(0)A_{\|}(0)\right\rangle + \left\langle A_{\perp}^{*}(0)A_{\perp}(0)\right\rangle \\ Q &= \left[\cos^{4}\theta + \sin^{4}\theta + 2\sin^{2}\theta\cos^{2}\theta\cos[(k_{+}-k_{+}')z]\right]\left\langle A_{\|}^{*}(0)A_{\|}(0)\right\rangle - \left\langle A_{\perp}^{*}(0)A_{\perp}(0)\right\rangle \\ U &= 2\left(\left[\cos^{2}\theta\cos[(k_{\perp}-k_{+})z]\right] + \sin^{2}\theta\cos[(k_{\perp}-k_{+}')z]\right)\left\langle A_{\|}^{*}(0)A_{\perp}(0)\right\rangle \\ V &= 2\left(\left[\cos^{2}\theta\sin[(k_{\perp}-k_{+})z]\right] + \sin^{2}\theta\sin[(k_{\perp}-k_{+}')z]\right)\left\langle A_{\|}^{*}(0)A_{\perp}(0)\right\rangle . \end{aligned} \tag{42}$$

The Stokes parameters are also expressed as such

$$I = I_{p} , \tag{43}$$

$$Q = I_{p}\cos 2\psi \cos 2\chi , \tag{44}$$

$$U = I_{p}\sin 2\psi \cos 2\chi , \tag{45}$$

$$V = I_{p}\sin 2\chi . \tag{46}$$

where χ , ψ are are usual ellipticity parameter and the polarisation position angle. The degree of (linear /) polarisation is given by,

$$p = \frac{\sqrt{Q^{2}+U^{2}+V^{2}}}{I_{p}} , \quad p_{lin} = \frac{\sqrt{Q^{2}+U^{2}}}{I_{p}} \tag{47}$$

and the linear polarisation angle is given by

$$\tan 2\psi = \frac{U}{Q} , \quad \tan 2\chi = \frac{V}{p_{lin}} . \tag{48}$$

It has been noted in [64], that in case, we make any coordinate transformation around the axis of photon propagation the two linear polarisation become mixed. Hence, we need to be careful, as our solution process entails a similarity transformation. To see this we define the density matrix

$$\rho(z)=\begin{pmatrix}\left\langle A_{\|}^{*}(z)A_{\|}(z)\right\rangle & \left\langle A_{\|}(z)A_{\perp}^{*}(z)\right\rangle\\ \left\langle A_{\|}^{*}(z)A_{\perp}(z)\right\rangle & \left\langle A_{\perp}^{*}(z)A_{\perp}(z)\right\rangle\end{pmatrix}=\frac{1}{2}\begin{pmatrix}I(z)+Q(z) & U(z)-iV(z)\\ U(z)+iV(z) & I(z)-Q(z)\end{pmatrix}, \tag{49}$$

if we rotate the density matrix by an amount α about an axis perpendicular the plane containing $A_{\|}(z)$, $A_{\perp}(z)$, the density matrix transforms as $\rho(z)\rightarrow\rho'(z)$ given such to be

$$\rho'(z)=\frac{1}{2}R(\alpha)\begin{pmatrix}I(z)+Q(z) & U(z)-iV(z)\\ U(z)+iV(z) & I(z)-Q(z)\end{pmatrix}R^{-1}(\alpha), \tag{50}$$

where,

$$R(\alpha)=\begin{pmatrix}\cos\alpha & -\sin\alpha\\ \sin\alpha & \cos\alpha\end{pmatrix}. \tag{51}$$

Under such transformation the $I(z)$ and $V(z)$ remains unaltered. However, the $Q(z)$ and $U(z)$ starts mixing with each other by the following

$$\begin{pmatrix}Q'(z)\\ U'(z)\end{pmatrix}=\begin{pmatrix}\cos 2\alpha & \sin 2\alpha\\ -\sin 2\alpha & \cos 2\alpha\end{pmatrix}\begin{pmatrix}Q(z)\\ U(z)\end{pmatrix}. \tag{52}$$

We conclude this section by mentioning that in such a case the ellipticity parameter remains unaltered but the polarisation position angle changes by 2α as given below

$$\tan(2\chi')=\tan(2\chi),\quad \tan(2\psi')=\tan(2\alpha+2\psi). \tag{53}$$

5. *Ellipticity parameter and polarization position angle*. As a follow-up to the analytical expressions given in the previous section/s, we consider two special case of the Stokes parameter where either one of the two effects, namely, the mixing effect or, the vacuum birefringence effect would be absent. Thereafter we shall consider the general formula. In each case, we would like to obtain the value of the ellipticity angle χ after propagation a fixed distance z of light and determine it's frequency dependence. For all the three cases we shall assume the light to be completely plane polarised in the transverse direction, or U polarised. This is common observance in pulsar polarisation cases.

5.1. *Case - I: Mixing only*. Here we assume that the vacuum birefringence terms (i.e. ξ term inside the diagonal ones A_1, A_2) are absent. We also assume a pseudoscalar mass which is much less than the plasma frequency here. This greatly simplifies calculation without being much deviant from the reality, if we consider the parameters of the pulsar environment. Next we consider how the circular polarisation varies in this case. Assuming $\theta << 1$ one have

$$V = \left(\sin\left[\left(k_{\perp} - k_{+}\right)z\right] + \left[\frac{g\mathfrak{B}\omega}{\omega_p^2 + m_a^2}\right]^2 \sin\left[\left(k_{\perp} - k'_{+}\right)z\right] \right) \left\langle A_{\|}^{*}(0) A_{\perp}(0) \right\rangle . \tag{54}$$

Following the set of Eqs. (14)-(15) we can simplify the arguments of the remaining sinusoids of Eq. (54) as given below:

$$k_{\perp} - k_{+} = -\left\{ \frac{\left(g\mathfrak{B}\omega\right)^2}{2\left(\omega_p^2 + m_a^2\right)\omega} \right\}, \quad k_{\perp} - k'_{+} = +\left\{ \frac{\left(g\mathfrak{B}\omega\right)^2}{2\left(\omega_p^2 + m_a^2\right)\omega} + \frac{m_a^2}{2\omega} \right\}. \tag{55}$$

So, if $\xi = 0$, then the ellipticity parameter to its lowest order ($\propto \theta^2$) is found to be as follows, which matches well with [64,65], though the later most probably has a typo(1).

$$\chi \approx \frac{1}{96\omega} \left(g\mathfrak{B} m_a\right)^2 z^3 . \tag{56}$$

Similarly, we may now turn our attention to two linear polarisation degrees of freedom, where the mixing angle $\theta << 1$, is small, to figure out the polarisation position angle.

$$\tan(2\psi) = \frac{U}{Q} . \tag{57}$$

However, in the beginning of this section we have already mentioned that $U \simeq 1$. This is true for the parameters of interest used here and the observational cases to be discussed later. This makes the polarisation position angle inversely proportional to Q. But before we evaluate the expression for Q, we note that in the case of mixing the beam is assumed to propagate at an angle $\pi/4$ as compared to the magnetic field of the pulsar. Hence we need to change our expression for polarisation position angle accordingly. As discussed during derivation of Eq. (53), we have;

$$\tan\left(2\psi + \frac{\pi}{2}\right) = \frac{1}{Q} . \tag{58}$$

Next, we evaluate Q keeping in mind the approximations made before. Keeping terms up to order θ^2 in the expression for Q, we have,

$$Q = -2\theta^2 \left[\sin^2\left(\frac{\left\langle k_{\perp} - k'_{+} \right\rangle z}{2} \right) \right] . \tag{59}$$

Again, following the set of Eqs. (14)-(15), we have

---

(1) *It claimed concurrence with the former but is actually at variance, with it*

$$\langle k_+ - k'_+ \rangle \simeq \frac{m_a^2}{2\omega}. \tag{60}$$

Substituting, one gets, in conjuntion with [65]

$$\psi = \frac{1}{16}(g\mathfrak{B}z)^2. \tag{61}$$

However, unlike the circular polarisation, which was attributed to its entirety, to the mixing effect, one can not ascribe the entire pulsar linear polarisation [66] to this tiny mixing effect, where the mixing angle $\theta \ll 1$. So, we note that the pulsar radio emission is inherently linearly polarised to a large degree, due to curvature, synchroton and superconducting self Compton effects thereof. We use $U \simeq 1$ and only the Q part is modelled via pseudoscalar photon mixing; where

$$Q = \frac{1}{8}(g\mathfrak{B}z)^2 \tag{62}$$

along with the definitive couple of Eq. (48) to note that the linear polarisation observed is equal to

$$p_{lin} = Q\sec\left(2\psi + \frac{\pi}{2}\right). \tag{63}$$

We note that the determination process of absolute pulsar polarisation [67] position

Table 2

REGRESSION RESULT FOR THE COUPLING OF THE PSEUDOSCALAR

Coefficients	Mean	Std.-Error	*F*-statistics	*t*-value	Pr(> |*t*|)
Slope	2.404e-25	4.567e-26	27.7196	5.265	1.21e-05

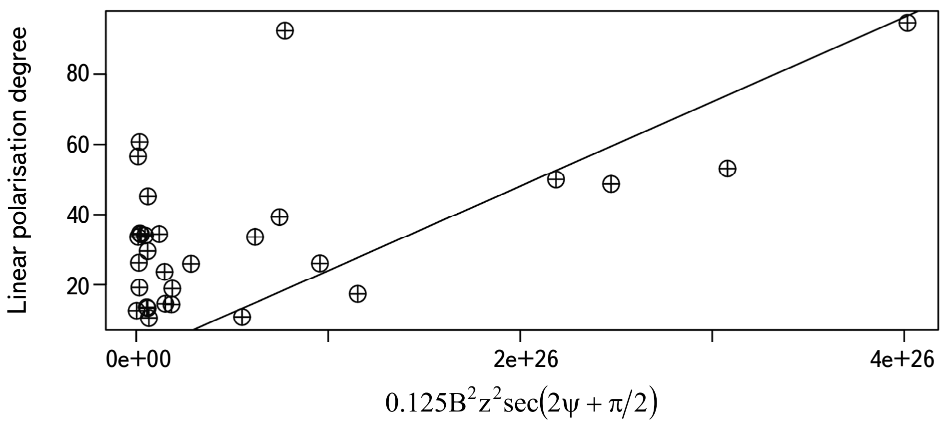

Fig.2. Linear regression between PPAs and Lin. Pol. Abscissa is in GeV^2 units and the ordinate is dimensionless.

Table 3

SMALL SAMPLE OF ABSOLUTE PULSAR POLARISATION POSITION ANGLES, FROM [68]

Pulsar	PA_V , deg	PA_0	Ψ , deg
B0011+47	+136(3)	43(7)	-87(8)
B0136+57	-131(0)	43(3)	6(3)
B0329+54	119(1)	20(4)	99(4)
B0355+54	48(1)	-41(4)	89(5)
B0450+55	108(0)	-23(16)	-94(16)
B0450-18	40(5)	47(3)	-7(6)
B0540+23	58(19)	-85(3)	-37(19)
B0628-28	294(2)	26(2)	88(3)
B0736-40	227(5)	-44(5)	91(7)

angles, is now experimentally feasible and the same values have already been scraped out for 30 odd pulsars. The literature contains a little less than fifty absolute PPAs from [68], out of which only 30 cross matched with that of our old set of 537 data, used to calculate the ellipticity parameter.

The expression for Q has only one unknown, the coupling of pseudoscalar with photons. Hence, we may do a regression analysis here, too, to estimate the same. The summary table is given in Table 2.

For the sake of brevity, we post a small segment of total 47 pulsar given in [68] in Table 3. The pulsar names here are catalogued in B1950 almanac standard, which were then converted to J2000 almanac standard and cross matched with the original and usable 537 strong population data on pulsar polarisation. 30 odd

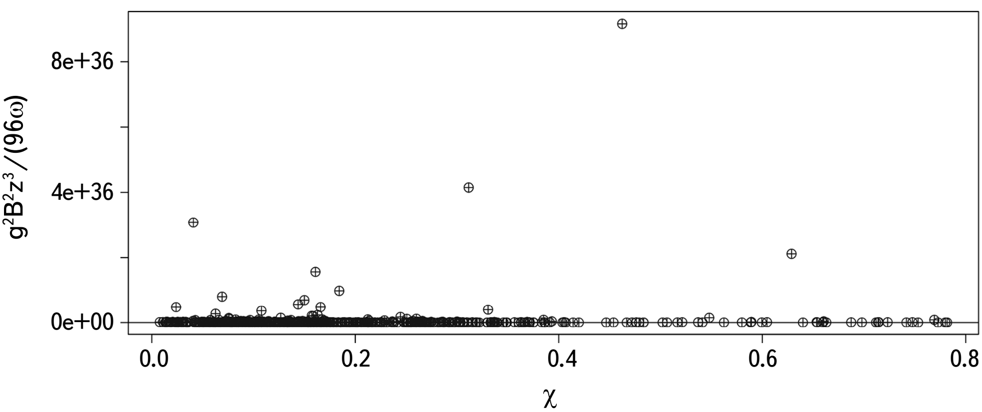

Fig.3. Linear regression between observed and (scaled) theoretical ellipticity parameter. Abscissa is dimensionless and the ordinate is in GeV^{-2} units.

Table 4

REGRESSION RESULT FOR THE MASS OF THE PSEUDOSCALAR

Coefficients	Mean	Std. error	F-statistics	t-value	Pr(>|t|)
Slope	7.471e-38	2.251e-38	11.0164	3.319	0.000964

samples of them were found to be common in both.

Now, we turn our attention back to the ellipticity parameter given in Eq. (56). Being a small angle, we have relegated the tangent as equivalent to its angular argument. The regression analysis thus to be undertaken is between circular and linear random variables, lying on LHS (ellipticity parameter) and RHS (magnetic field) respectively. Suffice it to say that the LHS is readily read off from the Table 1. The result of correlation study is given in the Table 4.

5.2. *Case - II: Vacuum birefringence only*. Here if we assume the mixing to be absent then we get $\theta = 0$ and hence we get the circular polarisation as

$$V = 2\left(\sin\left[\left(k_{\perp} - k_{+}\right)z\right]\right)\left\langle A_{\parallel}^{*}(0)A_{\perp}(0)\right\rangle. \tag{64}$$

Here, we need to evaluate only one argument and it is the same as given above:

$$k_{\perp} - k_{+} = \frac{1}{2\omega}\{-3\xi\}. \tag{65}$$

We note, that, the mass of the pseudoscalar cancels and the mixing term is assumed zero. We see, that, the circular polarisation has now become inversely proportional to frequency assuming the argument to be considerably small as in the other case. Given that no circular polarisation would be produced in this case, it would be uninteresting to ponder over here.

5.3. *Case III: Limiting case*. We note the essential non-linearity resulting from the two effect taken in conjunction. Since we can not just add the two effects separately, even if they both are small and perturbative, to obtain the final result. We also note that the two effects shall be competing with each other when the following condition is met

$$\omega\xi \approx g\mathcal{B}.$$

Leaving aside the numerical prefactors - tentatively we see that, unless the value of magnetic field is much larger than normal pulsars (as in magnetars) and the beam frequency used in experiment is quite high (unlike the present case), even the modest values coming from astronomical bounds on pseudoscalar may not be comparable with the vacuum birefringence effect and the former is in fact larger in effect.

5.4. *Case IV: General case [69].* Here in this subsection we calculate the amount of circular polarisation, vide the Stokes parameter V, without resorting to any of the approximations made in the preceding two subsections, for completeness. Here the expression for the V becomes

$$V = \left\{ \cos^2\left[\frac{g\mathfrak{B}\omega}{7\xi\omega^2\sin^2\alpha + \omega_p^2 + m_a^2}\right]\sin\left[(k_\perp - k_+)z\right] \right.$$
$$\left. + \sin^2\left[\frac{g\mathfrak{B}\omega}{7\xi\omega^2\sin^2\alpha + \omega_p^2 + m_a^2}\right]\sin\left[(k_\perp - k'_+)z\right]\right\}\left\langle A_\parallel^*(0)A_\perp(0)\right\rangle. \tag{66}$$

Hence at lowest order the first term, in ($\theta << 1$) limit, would not change anything from what the first term, for the case of the pure mixing effect, did. But the second term, even at the lowest order shall render the expression for V qualitatively different from what is was then at pure mixing effect. Needless to say that pure vacuum birefringence effect does not match, even qualitatively, with any of them, either. For completeness, we write down the values of the wave vectors again.

$$k_\perp - k_+ = \frac{1}{2\omega}\left\{\xi\left(4\cos^2\alpha - 7\sin^2\alpha\right) + \left[\frac{(g\mathfrak{B}\omega)^2}{7\xi\omega^2\sin^2\alpha + m_a^2}\right]\right\}$$
$$k_\perp - k'_+ = \frac{1}{2\omega}\left\{4\xi\cos^2\alpha + m_a^2 - \left[\frac{(g\mathfrak{B}\omega)^2}{7\xi\omega^2\sin^2\alpha + m_a^2}\right]\right\}. \tag{67}$$

Thus far we have only shown the difference of results of all three separate cases in terms of the V parameters depicting circular polarisation. This can be done with other two linear polarisation degrees of freedom, too. We leave this for a future endeavour.

6. ***Result.*** By the careful analysis of [55], containing 600 Pulsar polarisation data, of which 537 are used here and that of [68], containing 47 absolute PPAs for pulsars, 30 of which are common to the above, we came to the following result given in Table 5. We however note that more data samples on absolute PPAs are required to obtain a more statistically significant result on the coupling, which is deduced, from this parameter. Currently a little over fifty pulsars are

Table 5

THE RESULT OF THIS ANALYSIS

Results Obtained		
Parameters	Values	Significance level
$g_{\phi\gamma}$ m_a	$4.903 \cdot 10^{-13}$ GeV^{-1} $2.733 \cdot 10^{-10}$ eV	≃0.001% < 0.1%

amenable to this type of absolute PPA studies. The second quantity, namely the mass, has the numbers (>500) on its side. Nonetheless, its extraction from the ellipticity parameter, in turn, hinges on the coupling value, indirectly affecting the confidence interval found from the population. Also, for the sake of thoroughness we mention that the degree of linear polarisation is claimed to be dependent on frequencies in which they are observed [70]. The PPAs that are quoted in [68], are for various radio frequencies, e.g. 327 MHz, 691 MHz, 3.1 GHz etc., including that of 1.4 GHz, which corresponds to 21 cm. Since, there has been no connection to PPAs are made with frequency, to our knowledge to this date, we did not investigate this further.

7. *Discussion and outlook*. Taking advantage of new age of data explosion arising out from newer observational techniques and that of machine tools, we tried to estimate pseudoscalar particle mass and its coupling to photons. The results thus obtained do not match any standard axion models such as DFSZ or KSVZ etc. Hence these finding must be accommodated in the fold of axion like particles (ALPs) outside of the QCD realm. Surprisingly, our bottom up study, has automatically, led us to values, that are comparable and between the contemporary theories on cosmic axion background radiation (CAB), leading to soft X-ray excesses observed from Coma cluster [71] and that of the extra-galactic background light (EBL) to ALPs conversion and oscillation, leading to an observed anomalous γ ray transparency of the universe [72]. Fortunately, the previous constraints set on the mass and coupling of pseudoscalars, either by the changes in of quasar polarisation, hypothetically by ALPs [73], or by the γ ray burst SN1987A [74], occurring through a so called ALPs burst, are not in conflict with our results, either.

As mentioned in section 5 a future incorporation of vacuum birefringence effect into this study, may be performed, so as to see how the result on these estimates may change, for better or worse. These parameters may also be harnessed for devising CDM/WDM models and to obtain their relic densities.

Acknowledgements. The authors acknowledge the software R [75] for easing out the statistical analysis. SM is thankful of the help of K.Bhattyacharya regarding the same.

[1] Physics Department, Parul University, Vadodara, Gujarat-391760, India, e-mail 2015rpy9054@mnit.ac.in

[2] Physics Department, Malaviya National Institute Of Technology, Jaipur, Rajasthan-302017, India, e-mail: smandal.phy@mnit.ac.in

ИССЛЕДОВАНИЕ ПСЕВДОСКАЛЯРОВ С ПОМОЩЬЮ НАБОРОВ ДАННЫХ О ПОЛЯРИЗАЦИИ ПУЛЬСАРОВ

К.ЧАНДА, С.МАНДАЛ

Недавно был опубликован новый набор данных, содержащий информацию о линейной и круговой поляризации 600 пульсаров на радиоволне 21 см. Существующие модели радиоизлучения пульсаров, такие как синхротонное/автокомптоновое или искривленное излучение, не могут объяснить наблюдаемую круговую поляризацию, поскольку они предсказывают только линейную поляризацию. Чтобы решить эту проблему, мы предлагаем использовать (псевдо)скалярные частицы, взаимодействующие с фотонами в присутствии интенсивных магнитных полей пульсаров, для объяснения круговой поляризации. Это позволяет нам оценить псевдоскалярные параметры, такие как связь с фотонами и массу в виде их произведения. Чтобы получить эти значения по отдельности, мы воспользовались недавними наблюдениями 47 пульсаров, для которых определены абсолютные позиционные углы поляризации. Две трети этого нового набора наблюдений пересекается с обширным предыдущим набором данных о типе и степени поляризации. Это позволило определить оба псевдоскалярных параметра индивидуально.

Ключевые слова: *ALP-γ (14.80.Va)смешение: пульсар (97.60.Gb): поляризация (42.25.Ja)*

REFERENCES

1. *L.Maiani*, *S.Petrozenio*, *E.Zavattini*, Phys. Lett. B, **175**, 359, 1986.
2. *R.D.Peccei*, *H.Quinn*, Phys. Rev. Lett., **38**, 1440, 1977.
3. *F.Wilczek*, Phys. Rev. Lett., **40**, 279, 1978.
4. *S.Weinberg*, Phys. Rev. Lett., **40**, 223, 1978.
5. *J.E.Kim*, Phys. Rev. Lett., **43**, 103, 1979.
6. *L.Abbott*, *P.Sikivie*, Phys. Lett. B, **120**, 133, 1983.
7. *S.Evans*, *J.Rafelski*, Phys. Lett. B, **791**, 331, 2019.
8. *S.Shakeri*, *F.Hajkarim*, J. Cosmol. Astropart. Phys., **2023**(04), 017, 2023.
9. *F.Finelli*, *M.Galaverni*, Phys. Rev. D, **79**, 063002, 2009.
10. *S.Alexander*, *E.McDonough*, *A.Pullen et al.*, J. Cosmol. Astropart. Phys., **2020**(01), 032, 2020.
11. *S.Das et al.*, J. Cosmol. Astropart. Phys., **06**(002), 2005.

12. *P.Jain*, *G.Narain*, *S.Sarala*, Mon. Not. Roy. Astron. Soc., **347**, 394, 2004.
13. *N.Agarwal*, *A.Kamal*, *P.Jain*, Phys. Rev. D, **83**, 065014, 2011.
14. *N.Agarwal*, *P.K.Aluri*, *P.Jain et al.*, The European Physical Journal C, **72**, 1928, 2012.
15. *P.Tiwari*, *P.Jain*, International Journal of Modern Physics D, **22**, 50089, 2013.
16. *P.Tiwari.*, Phys. Rev. D, **86**, 115025, 2012.
17. *P.Jain*, *P.Tiwari*, Mon. Not. Roy. Astron. Soc., **460**(3), 2698, 2016.
18. *S.Das et al.*, Pramana, **70**, 439, 2008.
19. *A.Payez*, Phys. Rev., **85**, 087701, 2012.
20. *A.Payez*, *J.R.Cudell*, *D.Hutsemékers*, Phys. Rev. D, **84**, 085029, 2011.
21. *G.Raffelt*, *H.Vogel*, *A.Kartavtsev*, JCAP01(2017)024, 01, 024, 2017.
22. *V.Pelgrims*, *D.Hutsemekers*, arxiv:1503.03482.
23. *V.Pelgrims*, *D.Hutsemekers*, arxiv:1604.03937.
24. *A.Payez*, Patras Workshop on Axions, WIMPs and WISPs. In arXiv:1309.6114, 2013.
25. *A.Payez*, *C.Evoli*, *T.Fischer et al.*, J. Cosmol. Astropart. Phys., **1502**(006), 2014.
26. *D.Hutsemékers*, *H.Lamy*, arXiv:astro-ph/0012182, 2000.
27. *D.Hutsemekers*, Astron. Astrophys., **332**, 410, 1998.
28. *D.Hutsemekers*, *H.Lamy*, Astron. Astrophys., **367**, 381, 2001.
29. *D.Hutsemekers*, *R.Cabanac*, *H.Lamy et al.*, Astron. Astrophys., **441**, 915, 2005.
30. *D.Hutsemekers*, *L.Braibant*, Astron. Astrophys., 572(A18), 2014.
31. *D.Hutsemekers*, *B.Borguet*, *D.Sluse et al.*, Astron. Astrophys., **520**(L7), 2010.
32. *N.Jackson*, *R.A.Battye*, *I.W.A.Browne et al.*, Mon. Not. Roy. Astron. Soc., **376**, 371, 2007.
33. *A.R.Jagannathan*, *P.Taylor*, Mon. Not. Roy. Astron. Soc., **459**(1), L36, 2016.
34. *C.Csaki et al.*, J. Cosmol. Astropart Phys., **0305**(005), 2003.
35. *D.Hutsemékers*, *J.R.Cudell*, *A.Payez*, Invisible Universe International Conference. In AIP Conf. Proc., **1038**, 211, 2008. arXiv:0805.3946.
36. *R.D.Peccei*, *H.Quinn*, Phys. Rev. D, **16**, 1791, 1977.
37. *A.Pich*, arXiv:hep-ph/9505231v1, 1995.
38. *M.Dine*, arXiv:hep-ph/0011376v2, 2000.
39. *P.Sikivie*, Phys. Rev. D, **32**, 2988, 1985.
40. *E.Kolb*, *M.S.Turner*, The Early Universe. Westview Press, 2nd ed. edition, 1994. Chap 10.
41. *W.Fischler*, *M.Srednicki*, *M.Dine*, Phys. Lett. B, **104**, 199, 1981.
42. *M.A.Shifman*, *A.I.Vainshtein*, *V.I.Zakharov*, Nucl. Phys. B, **166**, 493, 1980.
43. *P.Majumdar*, *S.Sengupta*, Class. Quant. Grav., **16**, L89, 1999.
44. *A.Sen*, Int. Jour. Mod. Phys. A, **16**, 4011, 2001.
45. *A.Hewish*, *S.J.Bell*, *J.D.H.Pilkington et al.*, Nature, **217**, 709, 1968.
46. *M.S.Longair*, High energy astrophysics, volume 2. Cambridge University Press, 1994, p.99.
47. *M.S.Longair*, Our evolving universe. CUP Archive, 1996. p.72.

48. Pulsar Properties. Webpage - https://www.cv.nrao.edu/course/astr534/PDFnewfiles/Pulsars.pdf.
49. *A.Lohfink*, Pulsars. webpage - https://www.astro.umd.edu/ alohfink/seminar.pdf, 2008.
50. *D.R.Lorimar*, M.Kramer, Handbook of Pulsar Astronomy. Cambridge University Press, 2005.
51. *W.M.Yan et al.*, Mon. Not. Roy. Astron. Soc., **414**, 2087, 2011.
52. *A.K.Harding*, *C.Kalapotharakos*, Multiwavelength Polarization of Rotation-Powered Pulsars. 2017, arXiv:1704.06183.
53. New Advances in Pulsar Magnetosphere Modelling, PoS. SISSA, 2017. arXiv:1702.00732.
54. *V.Beskin*, Pulsar Magnetospheres and Pulsar Winds, 2016. arXiv:1610.03365.
55. *S.Johnston*, *M.Kerr*, Mon. Not. Roy. Astron. Soc., **474**(4), 4629, 2018.
56. *P.F.Wang*, *C.Wang*, *J.L.Han*, Mon. Not. Roy. Astron. Soc., **423**(1), 2464, 2012.
57. *R.T.Gangadhara*, Astrophys. J., **710**, 29, 2010.
58. *H.Ardavan*, *A.Ardavan*, *J.Fasel et al.*, POS, **78**, 16, 2008.
59. *M.M.McKinnon*, Astrophys. J., **568**, 302, 2002.
60. *P.Jaroenjittichai*, PhD thesis, Physics and Astronomy (UoM), 2013.
61. *G.Raffelt*, *L.Stodolsky*, Phys. Rev. D, **37**(5), 1237, 1988.
62. *A.K.Ganguly*, *P.Jain*, *S.Mandal*, Phys. Rev. D, **79**, 115014, 2009.
63. *D.B.Melrose*, *M.Z.Rafat*, J. Phys., Conf. Ser., **932**, 012011, 2017. doi: 10.1088/1742-6596/932/1/012011.
64. *A.K.Ganguly*, Introduction to Axion Photon Interaction in Particle Physics and Photon Dispersion in Magnetized Media. In Eugene Kennedy, editor, Particle Physics, chapter 3, p.49-74. InTech, April 2012.
65. *R.Cameron et al*, Phys. Rev. D, **47**(9), 3707, 1993.
66. *M.Gedalin*, *E.Gruman*, *D.B.Melrose*, Phys. Rev. Lett., **88**, 121101, 2002.
67. *M.M.Force*, *P.Demorest*, *J.M.Rankin*, Mon. Not. Roy. Astron. Soc., **453**, 4485, 2015.
68. *J.M.Rankin*, Astrophys. J., **804**, 112, 2015.
69. *R.P.Mignani et al.*, Mon. Not. Roy. Astron. Soc., **465**, 492, 2017.
70. *P.F.Wang*, *C.Wang*, *J.L.Han*, Mon. Not. Roy. Astron. Soc., **448**(1), 771, 2015.
71. *J.P.Conlon*, *M.C.D.Marsh*, Phys. Rev. Lett., **111**(15), 151301, 2013.
72. *M.Meyer*, *D.Horns*, *M.Raue*, Phys. Rev. D, **87**, 035027, 2013.
73. *A.Payez*, *J.R.Cudell*, *D.Hutsemékers*, J. Cosmol. Astropart. Phys., **1207**(041), 2012.
74. *A.Payez*, *C.Evoli*, *T.Fischer et al.*, J. Cosmol. Astropart. Phys., **006**(02), 2015.
75. *R.C.Team*, R: A Language and Environment for Statistical Computing. R Foundation for Statistical Computing, Vienna, Austria, 2013.

АСТРОФИЗИКА

ТОМ 67 АВГУСТ, 2024 ВЫПУСК 3

DOI: 10.54503/0571-7132-2024.67.3-309

BSN: FIRST PHOTOMETRIC LIGHT CURVE ANALYSIS OF TWO W-TYPE CONTACT BINARY SYSTEMS OP Boo AND V0511 Cam

A.PORO[1], M.TANRIVER[2,3], A.KESKIN[2], A.BULUT[4,5], S.RABIEEFAR[6], M.M.GHARGHABI[6], F.WALTER[7], S.HOLY[7]

Received 21 May 2024
Accepted 26 August 2024

This study presented the first light curve analysis of the OP Boo and V0511 Cam binary stars, which was conducted in the frame of the Binary Systems of South and North (BSN) Project. Photometric ground-based observations were conducted with standard filters at two observatories in the Czech Republic. We computed a new ephemeris for each of the systems using our extracted times of minima, TESS data, and additional literature. Linear fits for O-C diagrams of both systems were considered using the Markov Chain Monte Carlo (MCMC) method. The light curves were analyzed using the Wilson-Devinney (WD) binary code combined with the Monte Carlo (MC) simulation. The light curve solutions of both target systems required a cold starspot. The absolute parameters of the systems were calculated by using a $P-M$ parameter relationship. The positions of the systems were also depicted on the Hertzsprung-Russell (HR), $P-L$, $\log M_{tot}-\log J_0$, and $T-M$ diagrams. The hotter component in both systems is determined to be a more massive star. Therefore, it can be concluded that both systems are W-type contact binary systems.

Keywords: *binaries: eclipsing - methods: observational - stars: individual (OP Boo and V0511 Cam)*

1. *Introduction*. The component stars in a contact binary system overfill their own Roche lobes [1]. It indicates their surfaces' potentials are equal. The W Ursae Majoris (W UMa) system belongs to a type known as Low-Temperature Contact Binaries (LTCBs), and their stars' temperatures are close to each other [2,3]. Contact binary systems are divided into two categories, A and W, according to the companions' masses and temperatures [4]. In the A-subtype, the more massive component has a higher effective temperature; otherwise, the system is classified as the W-subtype.

In addition, the estimation of absolute parameters in contact systems using orbital period has been the goal of many investigations [5-8]. Mass transfer between two stars can also be determined by analyzing variations in the orbital period over time. There are also theories about the upper and lower limits of the orbital period in contact systems, which indicate that it is less than 0.6 days [8]. Although these systems are very important in terms of the formation, stellar structure, and evolution of stars, there are still many ambiguities and questions. It seems that observing and studying more contact systems can help by creating a larger sample to answer the questions [9].

The first light curve analysis of the OP Boo and V0511 Cam binary systems from the northern hemisphere of the sky was provided in this work. These two binary systems were discovered by the ASAS-SN survey and Khruslov [10]. OP Boo and V0511 Cam are introduced as contact binary systems in catalogs and databases.

The OP Boo (GSC 03861-00642) binary system's coordinates are RA = 225°.80046 and Dec = 53°.56501 from the Gaia DR3. This system's apparent magnitude is reported as $V = 12.78$ in the ASAS-SN catalog. OP Boo's orbital period is reported as 0.3114482 day in the ZTF catalog, 0.311447 day in the ATLAS catalog, and 0.3114445 day in the ASAS-SN catalog.

V0511 Cam (GSC 04548-01797) is a binary system with coordinates RA = 151°.47734 and Dec = 81°.98326 from Gaia DR3. The ASAS-SN variable stars catalog reported an apparent magnitude of $V = 12.59$ for V0511 Cam. The orbital period of the V0511 Cam system is reported to be 0.4046236 day in the ASAS-SN catalog, and 0.404615 day in the VSX database.

The first light curve study of binary stars is important to create larger samples for deeper parameter investigations of these types of systems. The paper is organized as follows: Specifications on photometric observations and the data reduction process are given in Section 2. For each of the systems, the new ephemeris and extracted minima times are presented in Section 3. The light curve solutions for the systems are contained in Section 4. Section 5 presents the estimation of the absolute parameters. Finally, the conclusion is included in Section 6.

2. *Observation and data reduction*. Two observatories in the Czech Republic observed the binary systems V0511 Cam and OP Boo in an expanse of two nights.

OP Boo was observed using a GSO Newton 200/1000 telescope and a ZWO ASI 178MM CCD. The observation was performed at a private observatory (49°.645N, 14°.755E) in April 2019. This observation was carried out with a V filter and a 60-second exposure time. We reduced the raw CCD images, and the basic data reduction was performed for dark and flat-field images using Muniwin 2.1.31 software. During the observation, we used UCAC4 718-055116 ($V^{mag} = 12.95$) as a comparison star, UCAC4 718-055147 ($V^{mag} = 12.65$) for the first check star, and UCAC4 718-055152 ($V^{mag} = 12.51$) for the second check star.

V0511 Cam was observed in September 2021 at the Štefánik Observatory (50°.081N, 14°.398E). We applied a 16-inch F/10 Schmidt-Cassegrain telescope and a SBIG ST10XME CCD. In this observation, the Johnsons-Cousins R_c filter was used, and the exposure time was 60 seconds. We employed PCs that were online synchronized with stratum 0 NTP servers using Dimension 4 software. The CCD image processing and data reduction were done with dark and flat-field images, relative aperture photometry by Muniwin 2.1 software, and artificial comparison stars from three sources. Therefore, UCAC4 861-006287 ($V^{mag}=$ 12.26), UCAC4 860-006752 ($V^{mag}=12.29$), and UCAC4 861-006284 ($V^{mag}=$ 11.97) are used as comparison stars. UCAC4 860-006775 ($V^{mag}=13.37$) was our check star in this observation.

The apparent magnitudes reported in this section for comparison and check stars are from the AAVSO Photometric All Sky Survey (APASS) DR9 catalog.

TESS data were used in this study for both target systems. TESS observed the OP Boo system in sector 50 with a 600-second exposure. For the V0511 Cam system, we also utilized sector 60 with a 200-second exposure time. The data is available at the Mikulski Space Telescope Archive (MAST).

3. *Orbital period variations*. The orbital period of contact systems is known to have changed over time. It is an important parameter obtained from observations to understand some characteristics of these kinds of systems. Orbital period analysis and a new ephemeris computation are important for those systems whose orbital period variations and light curve analysis have not yet been investigated.

We have extracted a primary and a secondary minimum for each of the OP Boo and V0511 Cam systems. All minima are given in the Barycentric Julian Date and Barycentric Dynamical Time (BJD_{TDB}). Table 1 contains the times of minima extracted in this study and collected from the literature. Appendix tables 4 and 5 listed the primary and secondary times of minima extracted from TESS data.

For OP Boo, we used a primary minimum (2456191.62078) from the Paschke [11] study and an orbital period (0.3114445 day) reported by the ASAS-SN catalog as a reference ephemeris. For V0511 Cam, a primary minimum (2451470.67123) from the Khruslov [12] study and orbital period (0.4046236 day) come from the ASAS-SN catalog, used for the reference ephemeris. So, the epoch and O-C values of all minima were computed using the reference ephemeris of each system.

The number of observed minima and their time intervals are important for O-C analysis. There have been few ground-based observations of the two systems in the study, and linear fits have been taken into consideration for O-C diagrams (Fig.1). We used 20 walkers and 10000 iterations for each walker in the MCMC process to determine new ephemeris for each system. Thus, we carried out the MCMC sampling using the PyMC3 package [13]. The new ephemeris for each system is presented in Equations 1 and 2:

$$\text{OP Boo}: \quad \text{Min.}I(\text{BJD}_{\text{TDB}}) = 2456191.61897(37) + 0.311446559(33)E \tag{1}$$

$$\text{V0511 Cam}: \quad \text{Min.}I(\text{BJD}_{\text{TDB}}) = 2451470.67123(1) + 0.4046225292(16)E\,. \tag{2}$$

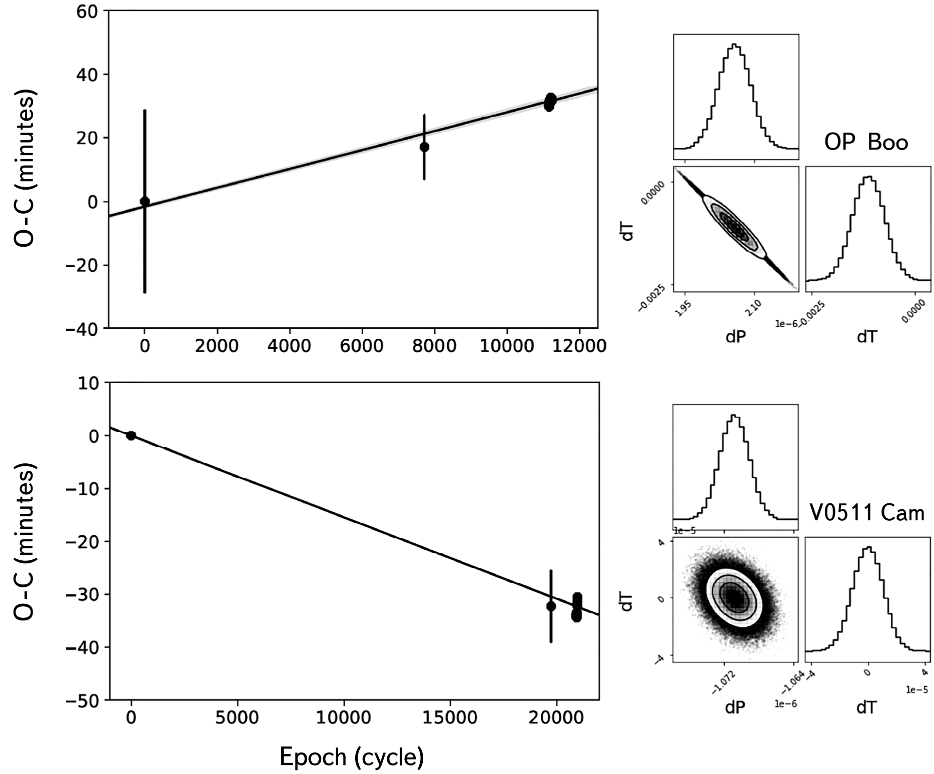

Fig.1. The O-C diagrams of OP Boo and V0511 Cam eclipsing binaries with linear fits and corner plots.

Table 1

GROUND-BASED OBSERVATIONS' AVAILABLE CCD TIMES OF MINIMA

System	Min.(BJD_{TDB})	Error	Filter	Epoch	O-C	Reference
OP Boo	2456191.62078	0.02000	CCD	0	0	Paschke [11]
	2457471.49608	0.00050	CCD	4109.5	-0.0059	Lehký et al. [14]
	2458595.36130	0.00700	*V*	7718	0.0119	This study
	2458595.50872	0.00660	*V*	7718.5	0.0036	This study
V0511 Cam	2451470.67123		*R*	0	0	Khruslov [12]
	2456043.51046	0.00300	*-Ir*	11301.5	-0.0144	Hubscher et al. [15]
	2459459.33503	0.00052	R_c	19743.5	-0.0223	This study
	2459459.53719	0.00470	R_c	19744	-0.0224	This study

Table 2

PHOTOMETRIC SOLUTIONS OF THE OP Boo AND V0511 Cam SYSTEMS

Parameter	OP Boo	V0511 Cam	Parameter	OP Boo	V0511 Cam
T_c (K)	4852(27)	5809(38)	$r_c(mean)$	0.356(5)	0.306(5)
T_h (K)	5388(32)	5908(38)	$r_h(mean)$	0.402(7)	0.487(7)
$q = M_2/M_1$	1.233(41)	2.856(65)	*Phase shift*	0.069(1)	-0.056(1)
$\Omega_c = \Omega_h$	4.100(15)	6.298(22)	$Col._{spot}$ (deg)	87	107
i°	59.57(23)	59.19(39)	$Long._{spot}$ (deg)	344	305
f	0.035(4)	0.206(33)	$Rad._{spot}$ (deg)	21	20
l_c/l_{tot}	0.359(1)	0.278(1)	T_{spot}/T_{star}	0.95	0.90
l_h/l_{tot}	0.641(2)	0.722(2)	$Component_{spot}$	Hotter	Hotter

4. *Light curve solutions*. Photometric light curve analysis of the OP Boo and V0511 Cam system was performed by the WD (Wilson-Devinney) code and MC simulation [16].

We assumed the bolometric albedo and gravity-darkening coefficients were $A_1 = A_2 = 0.5$ [17] and $g_1 = g_2 = 0.32$ [18], respectively. We used the limb darkening coefficients from the van Hamme [19] study. Also, we considered the reflection effect in our contact binary systems [20,21].

In this study, we considered the initial system temperature from Gaia. Then, we estimated the components' temperature ratio from the depth difference of the primary and secondary minima. We set the temperature reported from the Gaia DR2 and Gaia DR3 on the hotter stars of OP Boo and V0511 Cam, respectively.

Then, using MC simulation, we performed a mass ratio and other parameters search with large ranges. So, we searched for a mass ratio between 0.1 and 9, inclination between 40 and 90, surface potentials between 1.5 and 9, and temperatures between 4000 and 7000 for both stars Poro et al. [22].

After searching and ensuring a suitable theoretical fit, we did the MC simulations with the five main parameters i, q, Ω, T_c, and T_h. It should be noted that the error rate of normalized flux in the TESS data was high (about 0.1), and the analysis was carried out regardless.

According to the asymmetry in the maximum of the light curve, we added a cold starspot on the hotter component of the OP Boo and V0511 Cam systems. This can be described by the O'Connell effect that contact systems are known for their magnetic activity [23]. Fig.3 shows that OP Boo's starspot is located near the contact region, which is to find the best synthetic fit on the light curve. Furthermore, the starspot on the V0511 Cam system has a lower temperature than the OP Boo due to the difference in light curve maxima.

The results of the light curve analysis are shown in Table 2. The observed and synthetic light curves of the V0511 Cam and OP Boo binary systems are displayed in Fig.2. Furthermore, the geometric structures of the systems are shown in Fig.3.

5. *Estimation of absolute parameters*. There is a method to estimate the absolute parameters through Gaia's parallax [8]. This method can be accurate if the values of a_1 ($R_\odot$) and a_2 ($R_\odot$) are close together. The values of a_1 ($R_\odot$) and a_2 ($R_\odot$) are derived during the process of estimating absolute parameters using

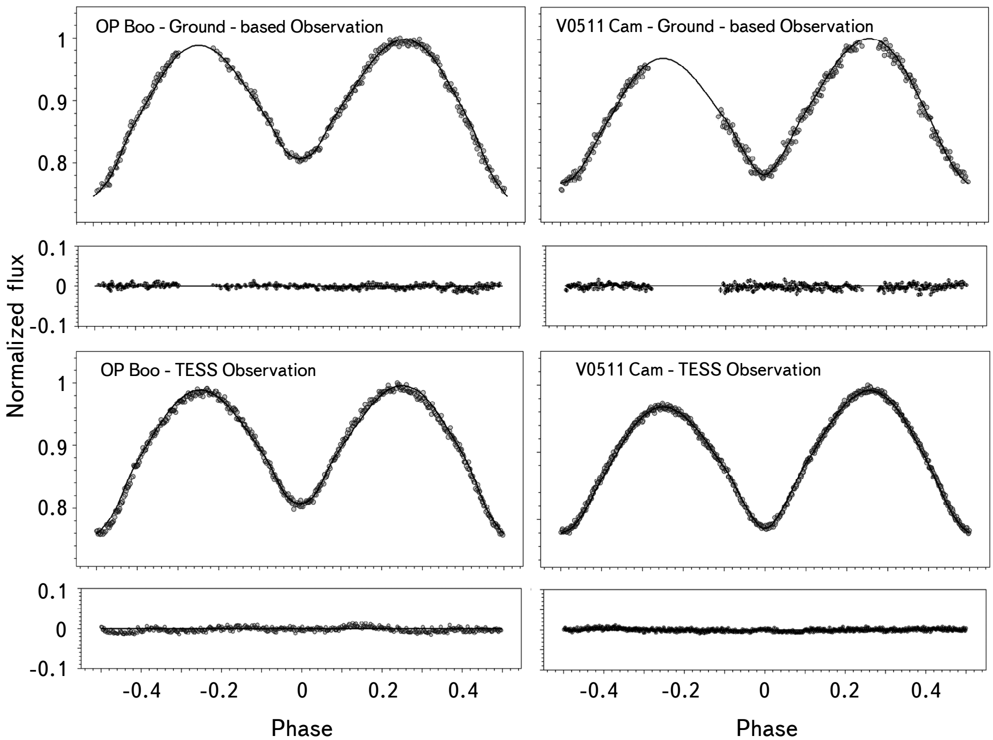

Fig.2. The photometric light curves of the systems, and synthetic light curves obtained from light curve solutions and residuals are plotted.

Gaia DR3 parallax, and they should be the same in theory [24,25]. However, their values require that they be found relatively close to each other in computations. a ($R_\odot$) is calculated using the average of a_1 ($R_\odot$) and a_2 ($R_\odot$) in the Gaia DR3 method for estimating absolute parameters.

Additionally, the possibility of using this method is dependent on V_{max} from the observation and the appropriate A_V. The precision of computations, including parallax, is reduced with increasing values of A_V [26]. Regarding the OP Boo

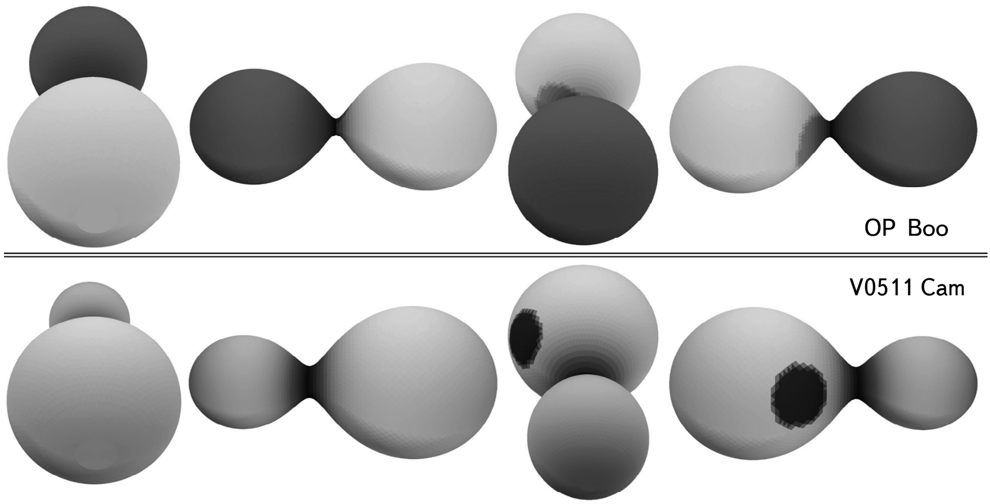

Fig.3. 3D view of the binary systems in 0, 0.25, 0.5, and 0.75 phases.

binary system, in Gaia DR3 the value of the parallax error (0.5880) exceeds that of the parallax (0.4216) and this causes a large error in the distance value (d(pc) $= 2371.99 \pm 990.48$). However, we can also look at the Re-normalized Unit Weight Error (RUWE) in Gaia DR3, whose value for this system is 54.94 but should be less than 1.4 [27]. On the other hand, values of d(pc) $= 634.17 \pm 4.35$ and RUWE $= 1.02$ are acceptable and appropriate for the V0511 Cam system. So, Gaia DR3 parallax is not a good way to estimate the absolute parameters of the OP Boo system.

There are other methods for estimating absolute parameters, most of which use sample-based statistical analysis. So, we employed the $P-M_1$ relation from the Poro et al. [8] study (Equation 3). This relation is related to a more massive component.

$$M_1 = (2.924 \pm 0.075)P + (0.147 \pm 0.029). \qquad (3)$$

This relation comes from a sample of 118 systems, and for all of them, the Gaia parallax was used to estimate absolute parameters. Therefore, its output may closely resemble that of the Gaia Parallax used directly.

First, we estimated the mass of the more massive star using the $P-M_1$ relation. The mass ratio is then employed to determine the mass of the other star. $a(R_\odot)$ was calculated using the system's total mass and orbital period, and the radius of each star can be found using r_{mean}. Additionally, the stars' luminosity was determined using each star's radius and temperature. Finally, we calculated the absolute bolometric M_{bol} of the stars using the well-known Pogson's relation [28],

Table 3

THE ABSOLUTE PARAMETERS OF OP Boo AND V0511 Cam

Parameter	OP Boo		V0511 Cam	
	Cooler star	Hotter star	Cooler star	Hotter star
$M/M_{\odot}$	0.858(13)	1.058(52)	0.463(12)	1.323(66)
$R/R_{\odot}$	0.855(84)	0.965(99)	0.854(107)	1.360(167)
$L/L_{\odot}$	0.365(85)	0.708(173)	0.750(224)	2.032(595)
M_{bol} (mag.)	5.824(228)	5.105(237)	5.043(284)	3.960(279)
log(*g*) (cgs)	4.508(75)	4.493(64)	4.240(91)	4.292(79)
a ($R_{\odot}$)	2.401(200)		2.793(298)	

where $M_{bol\odot}$ is taken as 4.73-mag. The estimation of absolute parameters of OP Boo and V0511 Cam systems is presented in Table 3.

6. *Conclusion*. Photometric observations of the OP Boo and V0511 Cam systems were carried out at two observatories in the Czech Republic. Data reduction processes were done according to the standard method, and light curves were prepared for analysis. We also used TESS data for both binary systems.

We extracted the times of minima from our observations and TESS data. Then, we collected mid-eclipse times from the literature as well. Using the reference ephemeris, the epoch and O-C values were calculated. We used the MCMC method for linear fits in the O-C diagrams and presented a new ephemeris for each system.

We presented the first light curve analysis for both target binary systems in this study. Light curve analysis was done with the WD code and MC simulation.

The temperature obtained from the light curve solutions shows that in both systems, the secondary minimum is deeper and hotter than the primary. The temperature difference between the two stars in the OP Boo system is 536 K, and in the V0511 Cam system, it is 99 K. According to the temperature of each star obtained from the light curve analysis and the Cox [29] study, it is possible to determine their spectral type. Therefore, for the OP Boo system, the cooler star is K2 and the hotter star is K0 in the spectral type; this is for V0511 Cam's cooler star which is G3, and G2 is for the hotter star. The solution of the light curve for the OP Boo and V0511 Cam systems required the addition of a cold starspot on the hotter component, representing the O'Connell effect [23].

We estimated the absolute parameters of the systems using the relationship between the orbital period and the mass of the more massive component [8] and the results of the light curve analysis. The positions of OP Boo and V0511 Cam

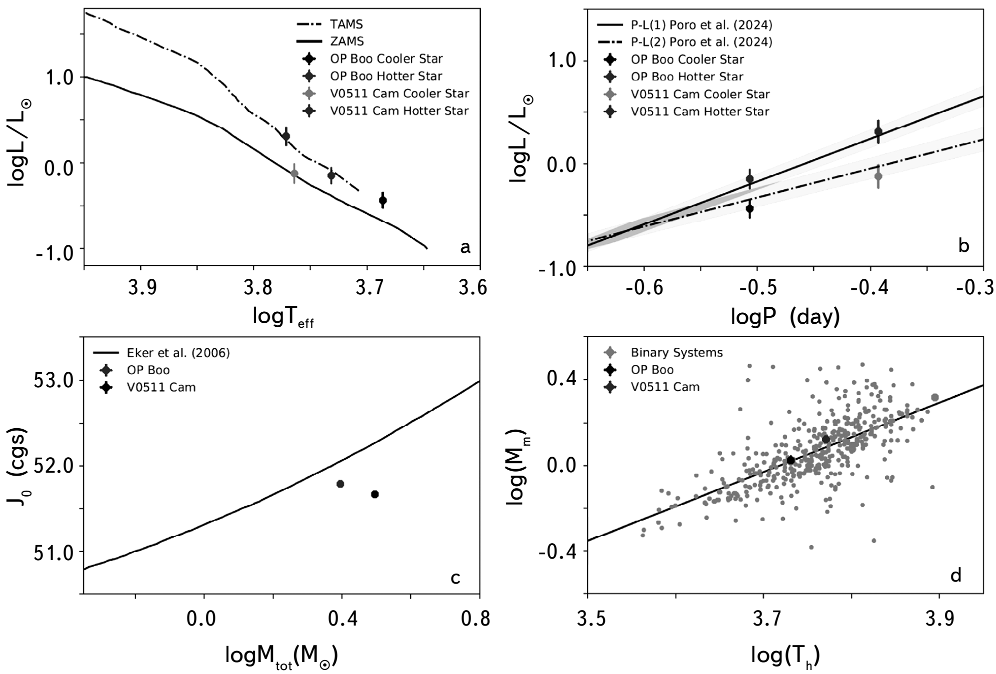

Fig.4. (a) HR, (b) P - L, and (c) logM_{tot} - logJ_0 (d) T_h - M_m diagrams, respectively.

stars on the HR diagram are presented (Fig.4a). So, the HR diagram shows the hotter stars are on the Terminal-Age Main Sequence (TAMS) line, and the cooler components lie between the Zero-Age Main Sequence (ZAMS) and TAMS. Fig.4b shows the position of the stars of the two systems compared to the P-$L_{1,2}$ theoretical fit obtained from the Poro et al. [9] study, which is in good agreement. As expected, hotter and more massive stars are on the P-L_1 theoretical fit, and cooler and less massive stars are on the P-L_2 theoretical fit.

Based on computations, the orbital angular momentum of OP Boo is 51.778 $\pm$0.023, and the value of V0511 Cam is 51.666$\pm$0.026. So, OP Boo and V0511 Cam are located in a contact binary systems region, as shown by the logM_{tot} - logJ_0 diagram (Fig.4c). The parabolic curve is shown in Fig.4c, and the results are based on the Eker et al. [30] study.

The Poro et al. [31] study used 428 contact binary systems and presented the T_h-M_m relationship. The position of the target systems is shown in this relationship. In Fig.4d, the horizontal axis shows the effective temperature of the hotter component, and the vertical axis shows the more massive star of each system. As Fig.4d shows, the positions of the stars are in good agreement with the theoretical fit.

We obtained a mass ratio, fillout factor, inclination, and stars' temperature from the light curve solution and MC simulation. The light curve analysis and absolute parameters of both systems suggest that OP Boo and V0511 Cam are W UMa contact and W-subtype binary systems.

Acknowledgements. This manuscript has been prepared based on a multilateral collaboration between the BSN project, the Raderon AI Lab (https://raderonlab.ca), and Erciyes University (https://www.erciyes.edu.tr). "This study was supported by the Scientific Research Projects Coordination Unit of Erciyes University (project number FBA-2022-11737)". The authors thank the Astronomical Society of the Czech Republic; data is available in http://var2.astro.cz/. We made use of information from the Gaia mission of the European Space Agency (http://www.cosmos.esa.int/gaia). Data from the TESS mission observations are used in this paper. The NASA Explorer Program provides funding for the TESS project. We are grateful to Ehsan Paki and Somayeh Soomandar for their help.

[1] Astronomy Department of the Raderon AI Lab., BC., Burnaby, Canada, e-mail: atilaporo@bsnp.info
[2] Department of Astronomy and Space Science, Faculty of Science, Erciyes University, Kayseri TR-38039, Türkiye
[3] Erciyes University, Astronomy and Space Science Observatory Application and Research Center, Kayseri TR-38039, Türkiye
[4] Department of Physics, Faculty of Arts and Sciences, Çanakkale Onsekiz Mart University, Terzioğlu Kampüsü, TR-17020, Çanakkale, Türkiye
[5] Astrophysics Research Center and Observatory, Çanakkale Onsekiz Mart University, Terzioğlu Kampüsü, TR-17020, Çanakkale, Türkiye
[6] Department of Physics, Khayyam University, Mashhad, Iran
[7] Variable Star and Exoplanet Section of Czech Astronomical Society, Prague, Czech Republic

APPENDIX

The appendix tables contain a list of the primary and secondary times of minima for the OP Boo and V0511 Cam systems, extracted from TESS observations.

Table 4

THE EXTRACTED PRIMARY TIMES OF MINIMA FROM TESS SECTOR 50 DATA FOR OP Boo

Min.	Error	Epoch	O-C	Min.	Error	Epoch	O-C
1	2	3	4	1	2	3	4
2459665.3400	0.0002	11153.5	0.0230	2459670.9454	0.0002	11171.5	0.0224
2459665.4938	0.0002	11154	0.0211	2459671.1003	0.0002	11172	0.0215
2459665.6513	0.0002	11154.5	0.0228	2459671.2570	0.0002	11172.5	0.0226
2459665.8055	0.0002	11155	0.0213	2459671.4119	0.0001	11173	0.0217
2459665.9631	0.0002	11155.5	0.0232	2459671.5686	0.0003	11173.5	0.0227
2459666.1163	0.0002	11156	0.0207	2459671.7233	0.0001	11174	0.0217
2459666.2748	0.0002	11156.5	0.0234	2459671.8800	0.0002	11174.5	0.0227
2459666.4280	0.0002	11157	0.0210	2459672.0347	0.0002	11175	0.0217
2459666.5859	0.0002	11157.5	0.0231	2459672.1915	0.0001	11175.5	0.0227
2459666.7394	0.0003	11158	0.0209	2459672.5029	0.0002	11176.5	0.0227
2459666.8971	0.0003	11158.5	0.0228	2459672.6579	0.0002	11177	0.0220
2459667.0513	0.0003	11159	0.0214	2459672.8144	0.0002	11177.5	0.0227
2459667.2085	0.0002	11159.5	0.0228	2459672.9695	0.0002	11178	0.0221
2459667.3628	0.0002	11160	0.0214	2459673.1259	0.0002	11178.5	0.0227
2459667.5201	0.0003	11160.5	0.0230	2459673.2810	0.0001	11179	0.0222
2459667.6745	0.0003	11161	0.0216	2459673.4372	0.0002	11179.5	0.0227
2459667.8316	0.0003	11161.5	0.0230	2459673.5922	0.0002	11180	0.0219
2459667.9857	0.0002	11162	0.0214	2459673.7488	0.0002	11180.5	0.0228
2459668.1432	0.0002	11162.5	0.0232	2459673.9036	0.0002	11181	0.0219
2459668.2973	0.0003	11163	0.0216	2459674.0604	0.0002	11181.5	0.0229
2459668.4541	0.0002	11163.5	0.0226	2459674.2150	0.0001	11182	0.0219
2459668.6080	0.0003	11164	0.0208	2459674.3716	0.0001	11182.5	0.0227
2459668.7659	0.0002	11164.5	0.0230	2459674.5267	0.0002	11183	0.0220
2459668.9199	0.0002	11165	0.0212	2459674.6832	0.0001	11183.5	0.0228
2459669.0771	0.0001	11165.5	0.0228	2459674.8380	0.0001	11184	0.0220
2459669.2314	0.0003	11166	0.0213	2459674.9948	0.0001	11184.5	0.0230
2459669.3883	0.0001	11166.5	0.0225	2459675.1495	0.0002	11185	0.0220
2459669.5429	0.0002	11167	0.0214	2459675.3062	0.0001	11185.5	0.0230
2459669.6998	0.0002	11167.5	0.0226	2459675.4606	0.0002	11186	0.0216
2459669.8543	0.0003	11168	0.0213	2459675.6178	0.0002	11186.5	0.0231
2459670.0113	0.0002	11168.5	0.0226	2459675.7722	0.0001	11187	0.0218
2459670.1660	0.0001	11169	0.0216	2459675.9291	0.0002	11187.5	0.0230
2459670.3227	0.0001	11169.5	0.0226	2459676.0834	0.0001	11188	0.0216
2459670.4773	0.0002	11170	0.0215	2459676.2405	0.0001	11188.5	0.0230
2459670.6341	0.0002	11170.5	0.0226	2459676.3950	0.0001	11189	0.0217
2459670.7890	0.0002	11171	0.0217	2459676.5522	0.0002	11189.5	0.0232

Table 4 (The end)

1	2	3	4	1	2	3	4
2459676.7064	0.0001	11190	0.0217	2459683.5588	0.0002	11212	0.0223
2459676.8634	0.0001	11190.5	0.0230	2459683.7156	0.0001	11212.5	0.0234
2459677.0180	0.0002	11191	0.0218	2459683.8703	0.0001	11213	0.0224
2459677.1749	0.0002	11191.5	0.0230	2459684.0269	0.0003	11213.5	0.0233
2459677.3294	0.0001	11192	0.0218	2459684.1819	0.0001	11214	0.0225
2459677.4863	0.0001	11192.5	0.0229	2459684.3384	0.0001	11214.5	0.0233
2459677.6408	0.0001	11193	0.0217	2459684.4930	0.0002	11215	0.0222
2459677.7979	0.0002	11193.5	0.0231	2459684.6497	0.0001	11215.5	0.0232
2459677.9527	0.0001	11194	0.0221	2459684.8046	0.0001	11216	0.0223
2459678.1095	0.0002	11194.5	0.0233	2459684.9612	0.0001	11216.5	0.0232
2459678.2638	0.0001	11195	0.0219	2459685.1162	0.0002	11217	0.0225
2459679.3550	0.0008	11198.5	0.0230	2459685.2727	0.0002	11217.5	0.0233
2459679.5098	0.0002	11199	0.0221	2459685.4275	0.0002	11218	0.0223
2459679.6673	0.0002	11199.5	0.0239	2459685.5841	0.0002	11218.5	0.0232
2459679.8213	0.0003	11200	0.0222	2459685.7390	0.0002	11219	0.0224
2459679.9781	0.0002	11200.5	0.0232	2459685.8956	0.0002	11219.5	0.0233
2459680.1331	0.0002	11201	0.0224	2459686.0503	0.0001	11220	0.0223
2459680.2894	0.0003	11201.5	0.0230	2459686.2072	0.0001	11220.5	0.0234
2459680.4440	0.0003	11202	0.0220	2459686.3618	0.0001	11221	0.0222
2459680.6011	0.0002	11202.5	0.0233	2459686.5183	0.0002	11221.5	0.0231
2459680.7562	0.0002	11203	0.0227	2459686.6731	0.0001	11222	0.0222
2459680.9126	0.0002	11203.5	0.0233	2459686.8298	0.0001	11222.5	0.0231
2459681.0673	0.0002	11204	0.0224	2459686.9848	0.0002	11223	0.0224
2459681.2238	0.0002	11204.5	0.0231	2459687.1412	0.0002	11223.5	0.0230
2459681.3788	0.0002	11205	0.0224	2459687.2962	0.0002	11224	0.0224
2459681.5354	0.0002	11205.5	0.0233	2459687.4528	0.0001	11224.5	0.0232
2459681.6901	0.0002	11206	0.0223	2459687.6074	0.0002	11225	0.0221
2459681.8469	0.0003	11206.5	0.0233	2459687.7642	0.0001	11225.5	0.0231
2459682.0013	0.0003	11207	0.0220	2459687.9186	0.0002	11226	0.0219
2459682.1582	0.0003	11207.5	0.0232	2459688.0756	0.0002	11226.5	0.0232
2459682.3131	0.0003	11208	0.0224	2459688.2305	0.0002	11227	0.0223
2459682.4697	0.0002	11208.5	0.0232	2459688.3873	0.0002	11227.5	0.0234
2459682.6245	0.0002	11209	0.0223	2459688.5417	0.0001	11228	0.0221
2459682.7809	0.0002	11209.5	0.0230	2459688.6987	0.0002	11228.5	0.0233
2459682.9359	0.0003	11210	0.0222	2459688.8531	0.0001	11229	0.0220
2459683.0925	0.0002	11210.5	0.0232	2459689.0100	0.0002	11229.5	0.0232
2459683.2475	0.0003	11211	0.0224	2459689.1650	0.0002	11230	0.0225
2459683.4040	0.0001	11211.5	0.0232				

Table 5

THE EXTRACTED PRIMARY TIMES OF MINIMA FROM TESS SECTOR 60 DATA FOR V0511 Cam

Min.	Error	Epoch	O-C	Min.	Error	Epoch	O-C
2459939.6259	0.0002	20930.5	-0.0196	2459948.5276	0.0002	20952.5	-0.0196
2459939.8241	0.0003	20931	-0.0237	2459948.7260	0.0003	20953	-0.0235
2459940.0310	0.0002	20931.5	-0.0191	2459948.9321	0.0002	20953.5	-0.0197
2459940.2289	0.0002	20932	-0.0235	2459949.1306	0.0003	20954	-0.0235
2459940.4357	0.0002	20932.5	-0.0191	2459949.3371	0.0002	20954.5	-0.0194
2459940.6335	0.0002	20933	-0.0235	2459949.5353	0.0002	20955	-0.0235
2459940.8402	0.0002	20933.5	-0.0191	2459949.7404	0.0002	20955.5	-0.0207
2459941.0380	0.0002	20934	-0.0237	2459955.2014	0.0002	20969	-0.0221
2459941.2451	0.0002	20934.5	-0.0189	2459955.4054	0.0002	20969.5	-0.0204
2459941.4426	0.0003	20935	-0.0236	2459955.6058	0.0002	20970	-0.0223
2459941.6498	0.0002	20935.5	-0.0189	2459955.8098	0.0001	20970.5	-0.0206
2459941.8473	0.0003	20936	-0.0236	2459956.0106	0.0002	20971	-0.0222
2459942.0543	0.0002	20936.5	-0.0190	2459956.2137	0.0002	20971.5	-0.0214
2459942.2520	0.0002	20937	-0.0236	2459956.6185	0.0002	20972.5	-0.0212
2459942.4587	0.0003	20937.5	-0.0191	2459956.8197	0.0002	20973	-0.0223
2459942.6565	0.0002	20938	-0.0236	2459957.0231	0.0002	20973.5	-0.0212
2459942.8635	0.0002	20938.5	-0.0190	2459957.2245	0.0002	20974	-0.0221
2459943.0611	0.0003	20939	-0.0237	2459957.4275	0.0002	20974.5	-0.0214
2459943.2679	0.0002	20939.5	-0.0192	2459957.6290	0.0002	20975	-0.0222
2459943.4659	0.0003	20940	-0.0235	2459957.8326	0.0002	20975.5	-0.0209
2459943.6718	0.0002	20940.5	-0.0199	2459958.0340	0.0002	20976	-0.0219
2459944.0775	0.0002	20941.5	-0.0188	2459958.2369	0.0001	20976.5	-0.0212
2459944.2748	0.0003	20942	-0.0239	2459958.4389	0.0002	20977	-0.0216
2459944.4821	0.0002	20942.5	-0.0189	2459958.6411	0.0001	20977.5	-0.0217
2459944.6796	0.0002	20943	-0.0237	2459958.8434	0.0002	20978	-0.0217
2459944.8867	0.0002	20943.5	-0.0189	2459959.0459	0.0001	20978.5	-0.0215
2459945.0841	0.0002	20944	-0.0238	2459959.2482	0.0002	20979	-0.0215
2459945.2912	0.0002	20944.5	-0.0190	2459959.4502	0.0002	20979.5	-0.0218
2459945.4888	0.0003	20945	-0.0237	2459959.6527	0.0002	20980	-0.0217
2459945.6958	0.0002	20945.5	-0.0190	2459959.8548	0.0001	20980.5	-0.0219
2459945.8937	0.0002	20946	-0.0235	2459960.0578	0.0002	20981	-0.0212
2459946.1001	0.0002	20946.5	-0.0193	2459960.2595	0.0001	20981.5	-0.0218
2459946.2985	0.0002	20947	-0.0232	2459960.4621	0.0002	20982	-0.0215
2459946.5051	0.0002	20947.5	-0.0190	2459960.6638	0.0001	20982.5	-0.0221
2459946.7029	0.0002	20948	-0.0235	2459960.8669	0.0002	20983	-0.0214
2459946.9095	0.0002	20948.5	-0.0192	2459961.0687	0.0002	20983.5	-0.0219
2459947.1076	0.0003	20949	-0.0234	2459961.2716	0.0001	20984	-0.0213
2459947.3139	0.0002	20949.5	-0.0194	2459961.4730	0.0001	20984.5	-0.0221
2459947.5123	0.0002	20950	-0.0234	2459961.6763	0.0002	20985	-0.0212
2459947.7188	0.0002	20950.5	-0.0192	2459961.8775	0.0002	20985.5	-0.0223
2459947.9169	0.0002	20951	-0.0234	2459962.0808	0.0001	20986	-0.0213
2459948.1230	0.0002	20951.5	-0.0196	2459962.2822	0.0001	20986.5	-0.0223
2459948.3216	0.0002	20952	-0.0233				

BSN: ПЕРВОЕ ИССЛЕДОВАНИЕ КРИВЫХ БЛЕСКА КОНТАКТНЫХ ДВОЙНЫХ СИСТЕМ OP Boo И V0511 Cam

А.ПОРО[1], М.ТАНРИВЕР[2,3], А.КЕСКИН[2], А.БУЛУТ[4,5], С.РАБИЕФАР[6], М.М.ГАРГАБИ[6], Ф.ВАЛЬТЕР[7], С.ХОЛИ[7]

Впервые, используя фотометрические данные, выполнен анализ кривых блеска двойных системы OP Boo и V0511 Cam. Наблюдения и анализ были проведены в рамках проекта BSN (Binary Systems of South and North). Наземные фотометрические наблюдения со стандартными фильтрами были проведены в двух обсерваториях Чешской республики. Новые эфемериды для каждой из этих систем вычислены, используя извлеченные нами моменты минимумов кривых блеска, данные TESS, а также имеющуюся в литературе информацию. Линейные аппроксимации O-C диаграмм были рассмотрены с помощью метода марковских цепей Монте-Карло (MCMC). Анализ кривых блеска был выполнен с использованием программы моделирования двойных звезд Уилсона-Девинни (WD) и Монте-Карло симуляцией (MC). Для обеих систем полученные решения предполагают наличие холодного звездного пятна. Абсолютные значения параметров систем рассчитывались с использованием соотношения параметров $P-M$. Представлены положения систем на диаграммах Герцшпрунга-Рассела (HR), $P-L$, $\log M_{tot}-\log J_0$ и $T-M$. Горячий компонент в обеих системах определяется как более массивная звезда. Следовательно, можно сделать вывод, что обе системы являются контактными двойными системами W-типа.

Ключевые слова: *двойные звезды - затмение-метод: наблюдения - звезды: индивидуальные (OP Boo и V0511 Cam)*

REFERENCES

1. *L.B.Lucy*, Astrophys. J., **151**, 1123, 1968. doi:10.1086/149510.
2. *S.M.Rucinski*, Contact Binaries of the W UMa Type. Publisher: Springer, 1993.
3. *K.Yakut*, *P.P.Eggleton*, Astrophys. J., **629**, 1055, 2005. doi:10.1086/431300.
4. *L.Binnendijk*, Vistas in Astronomy, **12**, 217, 1970.
5. *S.Qian*, Mon. Not. Roy. Astron. Soc., **342**, 1260, 2003. doi:10.1046/j.1365-8711.2003.06627.x.

6. *S.Kouzuma*, PASJ, **70**, 90, 2018. doi:10.1093/pasj/psy086.
7. *O.Latković*, *A.Čeki*, *S.Lazarević*, Astrophys. J. Suppl., **254**, 10, 2021. doi:10.3847/1538-4365/abeb23.
8. *A.Poro*, *S.Sarabi*, *S.Zamanpour et al.*, Mon. Not. Roy. Astron. Soc., **510**, 5315, 2022. doi:10.1093/mnras/stab3775
9. *A.Poro*, *E.Paki*, *A.Alizadehsabegh et al.*, RAA, **24**, 015002, 2024. doi:10.1088/1674-4527/ad0866.
10. *A.V.Khruslov*, PZP, **7**, 6, 2007.
11. *A.Paschke*, OEJV, **162**, 1, 2014.
12. *A.V.Khruslov*, PZP, **8**, 52, 2008.
13. *J.Salvatier*, *T.V.Wieckiâ*, *C.Fonnesbeck*, Astrophysics Source Code Library, ascl-1610, 2016.
14. *M.Lehký*, *K.Hoňková*, *L.Šmelcer et al.*, OEJV, **211**, 1, 2021.
15. *J.Hubscher*, *W.Braune*, *P.B.Lehmann*, IBVS, **6048**, 1, 2013.
16. *R.E.Wilson*, *E.J.Devinney*, Astrophys. J., **166**, 605, 1971.
17. *S.M.Ruciński*, AcA, **19**, 245, 1969.
18. *L.B.Lucy*, ZA, **65**, 89, 1967.
19. *W. van Hamme*, Astron. J., **106**, 2096, 1993. doi:10.1086/116788.
20. *R.E.Wilson*, Astrophys. J., **356**, 613, 1990.
21. *A.Prša*, *K.E.Conroy*, *M.Horvat et al.*, Astrophys. J. Suppl., **227**, 29, 2016. doi:10.3847/1538-4365/227/2/29.
22. *A.Poro*, *S.Zamanpour*, *M.Hashemi et al.*, New Astron., **86**, 101571, 2021. doi:10.1016/j.newast.2021.101571.
23. *D.J.K.O.Connell*, Mon. Not. Roy. Astron. Soc., **111**, 642, 1951. doi:10.1093/mnras/111.6.642.
24. *A.Poro*, *E.Fernández-Lajús*, *M.Madani et al.*, RAA, **23**, 095011, 2023. doi:10.1088/1674-4527/ace027.
25. *A.Poro*, *M.Hedayatjoo*, *M.Nastaran et al.*, New Astron., **110**, 102227, 2024. doi:10.1016/j.newast.2024.102227.
26. *A.Poro*, *M.Tanriver*, *R.Michel et al.*, Publ. Astron. Soc. Pacif., **136**, 024201, 2024. doi:10.1088/1538-3873/ad1ed3.
27. *L.Lindegren*, Gaia Technical Note: GAIA-C3-TN-LU-LL-124-01, 2018.
28. *N.Pogson*, Mon. Not. Roy. Astron. Soc., **17**, 12, 1856. doi:10.1093/mnras/17.1.12.
29. *A.N.Cox*, Allen's Astrophysical Quantities, AIP Press, Springer, New York, 2000.
30. *Z.Eker*, *O.Demircan*, *S.Bilir et al.*, Mon. Not. Roy. Astron. Soc., **373**, 1483, 2006. doi:10.1111/j.1365-2966.2006.11073.x.
31. *A.Poro*, *S.Baudart*, *M.Nourmohammad et al.*, RAA, **24**, 055001, 2024. doi:10.1088/1674-4527/ad3a2c

А С Т Р О Ф И З И К А

ТОМ 67 АВГУСТ, 2024 ВЫПУСК 3

DOI: 10.54503/0571-7132-2024.67.3-325

REANALYZING THE LIGHT CURVES AND ABSOLUTE PARAMETERS OF TWENTY CONTACT BINARY STARS USING TESS DATA

E.PAKI, A.PORO

Received 28 May 2024
Accepted 26 August 2024

Reanalyzing contact binaries with space-based photometric data and investigating possible parameter changes can yield accurate samples for theoretical studies. We investigated light curve solutions and fundamental parameters for twenty contact binary systems. The most recent Transiting Exoplanet Survey Satellite (TESS) data is used to analyze. The target systems in the investigation have an orbital period of less than 0.58 days. Light curve solutions were performed using the PHysics Of Eclipsing BinariEs (PHOEBE) Python code version 2.4.9. The results show that systems had various mass ratios from $q = 0.149$ to $q = 3.915$, fillout factors (the degree of contact) from $f = 0.072$ to $f = 0.566$, and inclinations from $i = 52^{\circ}.8$ to $i = 87^{\circ}.3$. The effective temperature of the stars was less than 7016 K, which was expected given the features of most contact binary stars. Twelve of the target systems' light curves were asymmetrical in the maxima, showing the O'Connell effect, and a starspot was required for light curve solutions. The estimation of the absolute parameters of the binary systems was presented using the a - P empirical relationship and discussed. The orbital angular momentum J_0 of the systems was calculated. The positions of the systems were also depicted on the M - L, M - R, q - L_{ratio}, M_{tot} - J_0, and T - M diagrams.

Keywords: *binaries: eclipsing - binaries: close - data analysis*

1. *Introduction.* Eclipsing binaries are important in investigating stellar formation and structure, examining stellar evolution theories, and determining stars' physical properties. Binary systems were first classified into three types based on the light curves' shapes: Algol (EA), β Lyrae (EB), and W Ursae Majoris (W UMa, EW). Then, a more precise classification was provided by Kopal [1], which was based on Roche geometry, binary systems were classified as detached, semi-detached, and contact. Contact binary systems are one of the most interesting kinds of stellar binaries among observers and researchers. Contact systems' stars have filled their Roche lobes [1], and the temperature difference between these stars is close to each other [2]. Some of them are known as low-mass and Low-Temperature Contact Binaries (LTCBs) systems [3].

According to the Binnendijk [4] study, contact binaries can be divided into A and W subtypes. The more massive component has a higher effective temperature in the A-subtype, and if the less massive component has a higher effective temperature, it is classified as a W-subtype. These subtypes are still being discussed, and for a better understanding, it is necessary to determine and analyze a large number of contact systems in terms of fundamental parameters.

The stars of contact systems are transferring mass to each other [5], and in this process, their orbital periods can be changed. The orbital period of contact systems plays a role in relations with absolute parameters, and they are effective in the evolutionary process of these systems [6,7]. There have been several studies conducted on the upper and lower cut-offs of these systems' orbital periods [8]. The investigations show that contact systems' orbital periods usually lie between 0.2 and 0.6 days.

One of the prominent features in many contact systems is the presence of starspot(s) induced by the stars' magnetic activities. Hot or cold starspots, which are required for the light curve solution, are explained by the O'Connell effect [9]. The effect of starspots can be seen on the asymmetric maxima of the light curve.

There are unsolved issues related to contact binary systems, parameter relationships, and the evolution of stars [10]. This requires precisely defined elements from further contact binary samples [11]. Even in the case of well-studied systems, it will be important to carry out investigations due to issues with phasing, challenging novel discoveries, and evolutionary status.

In the following sections, we present the general specifications of target systems in catalogs and literature (Section 2), light curve solutions of 20 contact binary systems (Section 3), estimating absolute parameters (Section 4), and finally a discussion and conclusion (Section 5).

2. *Tartget systems and dataset.*

2.1. *Systems' selection.* We considered twenty contact binary systems for light curve analysis and estimation of absolute parameters. The selected studies for these target systems have considered the mass ratio based on spectroscopic results. We used these mass ratios as the initials for the light curve analysis. Due to the passage of time compared to some selected studies and spectroscopic quality, the final mass ratios may change slightly in this study.

Except for DY Cet [12], which has performed light curve analysis using TESS Sector 4 data, other systems have been studied previously using just ground-based data. Some parameters can be obtained from spectroscopic data analysis; however, most of the light curve elements are determined from photometric data. Therefore, the accuracy of photometric data has a significant impact on the results of the light curve solutions and then on the estimation of absolute parameters. Therefore, by using suitable quality TESS data, parameters may be obtained with more appropriate accuracy.

An introduction to the target systems is available in the online version of this study: https://doi.org/10.48550/arXiv.2405.18618.

2.2. *TESS observations*. TESS provides high accuracy and high time resolution light curves of contact binary stars that promote scientific studies. The main goal of the TESS mission is to detect and classify exoplanets, and each observation sector takes about 28 days. We used TESS data for light curve analysis in this study [13-14]. TESS data are available at the Mikulski Archive for Space Telescopes (MAST). If each of the systems had several sectors in TESS, we selected the most recent available sector with good-quality data for the light curve analysis. The sector used for each system is listed in Table 1, and all of them were observed at a 120-second exposure time.

2.3. *General features*. The selected contact binary systems have orbital periods ranging from 0.22 to 0.58 days, their apparent magnitude is $8^m.14$ to $11^m.26$, and the effective temperature of star 1 (T_1) is 4300 to 6980 K in the reference studies.

Table 1 contains the names of the selected systems along with their general characteristics. Therefore, in Table 1, the RA and DEC of the systems from the SIMBAD database, the distance obtained from the Gaia DR3 parallax, the apparent magnitude of the system from the All Sky Automated Survey (ASAS) catalog, the time of minima (BJD_{TDB}) and the orbital period from the Variable Star indeX (VSX) database, and the last column, the used TESS sector, were given. We used Schlafly, Finkbeiner [15] study, and the DUST-MAPS Python package developed by Green et al. [16] to determine the extinction coefficient A_V along with its uncertainty.

3. *Light curve analysis*. The PHOEBE Python code version 2.4.9 [17] and TESS filter were used to perform light curve analysis on 20 binary systems. Based on the appearance of the light curve, the short orbital period, and the results of previous studies, we selected contact mode for the systems' light curve solutions.

Assumed values for the bolometric albedo and gravity-darkening coefficients were $A_1 = A_2 = 0.5$ (Ruciński [18]) and $g_1 = g_2 = 0.32$ (Lucy [19]). We used the Castelli, Kurucz [20] method to model the stellar atmosphere, and the limb darkening coefficients were from the PHOEBE tables. The reflection effect in contact binary systems refers to the component's irradiation of each other. We considered this effect in the light curve analysis.

We set initial effective temperatures for stars and mass ratio from reference studies and analyzed the light curves of 20 target systems (Table 2). Parameter input values were taken from studies including spectroscopic data for these target systems. The optimization tool in PHOEBE was then utilized to improve the output of light curve solutions and obtain the final results. The five main

Table 1

COORDINATES AND OTHER CHARACTERISTICS OF TARGET BINARY SYSTEMS

System	RA J2000	DEC J2000	d pc	V mag	A_V	t_0 BJD_{TDB}	P day	TESS Sector
AC Boo	14 56 28.3364	+46 21 44.0691	155.42(36)	10.27(21)	0.029(1)	2452499.9507	0.35245	50
AQ Psc	01 21 03.5557	+07 36 21.6178	133.27(37)	8.55(18)	0.079(1)	2453653.7169	0.47560	43
BI CVn	13 03 16.4093	+36 37 00.6406	221.26(2.11)	10.41(22)	0.031(1)	2444365.2503	0.38416	49
BX Dra	16 06 17.3670	+62 45 46.0898	520.27(4.65)	10.68(22)	0.048(1)	2449810.5906	0.57902	58
BX Peg	21 38 49.3911	+26 41 34.2134	149.34(56)	10.88(23)	0.076(1)	2455873.3966	0.28042	55
CC Com	12 12 06.0379	+22 31 58.6828	71.38(11)	11.21(23)	0.035(1)	2453012.8637	0.22069	49
DY Cet	02 38 33.1803	-14 17 56.7219	186.88(49)	9.47(20)	0.046(1)	2453644.7385	0.44079	4
EF Boo	14 32 30.5386	+50 49 40.6868	160.93(34)	9.63(20)	0.021(1)	2452500.2238	0.42052	50
EX Leo	10 45 06.7720	+16 20 15.6771	97.10(24)	8.91(19)	0.037(1)	2448500.0087	0.40860	46
FU Dra	15 34 45.2133	+62 16 44.3332	159.56(50)	10.68(22)	0.030(1)	2448500.2637	0.30672	51
HV Aqr	21 21 24.8100	-03 09 36.8855	154.24(2.32)	9.85(21)	0.090(1)	2452500.2191	0.37446	55
LO And	23 27 06.6850	+45 33 22.0263	290.62(3.82)	11.26(23)	0.213(2)	2456226.6800	0.38044	57
OU Ser	15 22 43.4748	+16 15 40.7337	53.29(7)	8.14(17)	0.024(1)	2448500.2787	0.29677	51
RW Com	12 33 00.2840	+26 42 58.3618	107.60(25)	11.05(23)	0.026(1)	2454918.7048	0.23735	49
RW Dor	05 18 32.5451	-68 13 32.7780	123.57(17)	11.00(23)	0.087(1)	2453466.5302	0.28546	67
RZ Com	12 35 05.0595	+23 20 14.0278	208.26(1.70)	10.34(22)	0.032(1)	2458253.6304	0.33851	49
TW Cet	01 48 54.1435	-20 53 34.5917	152.71(46)	10.40(22)	0.022(1)	2454476.6173	0.31685	3
UV Lyn	09 03 24.1259	+38 05 54.5972	143.65(36)	9.60(20)	0.036(1)	2453407.3606	0.41498	21
UX Eri	03 09 52.7437	-06 53 33.5110	237.40(1.00)	11.15(23)	0.142(1)	2454828.6698	0.44529	4
VW Boo	14 17 26.0325	+12 34 03.4469	150.05(38)	10.49(22)	0.037(1)	2452840.6121	0.34232	50

parameters (T_1, T_2, q, f, l_1) were then processed for the optimization.

The well-known O'Connell effect [9] appears by the asymmetry in the brightness of maxima in the light curve of eclipsing binary stars. The most probable reason for this phenomenon is the existence of starspot(s) caused by the components' magnetic activity [21]. Eight systems had symmetrical light curves and 12 systems needed a cold starspot for light curve analysis.

The parameters i, q, f, $T_{1,2}$, Ω, l_1/l_{tot}, and $r_{(mean)1,2}$ are estimated by modeling the TESS light curves. Table 3 presents the light curve analysis results. Fig.1 shows TESS data and synthetic light curves of the binary systems. The geometric structure of the systems in phases 0.25 or 0.75 is shown in Fig.2. The color in Fig.2 indicates the differences in temperature on the star's surface.

4. *Estimation of the absolute parameters*. There are various methods to derive absolute parameters, particularly when photometric data is utilized. In some investigations, empirical relationships or the Gaia DR3 parallax method are used to estimate absolute parameters [37,6,38]. Using Gaia DR3 parallax to

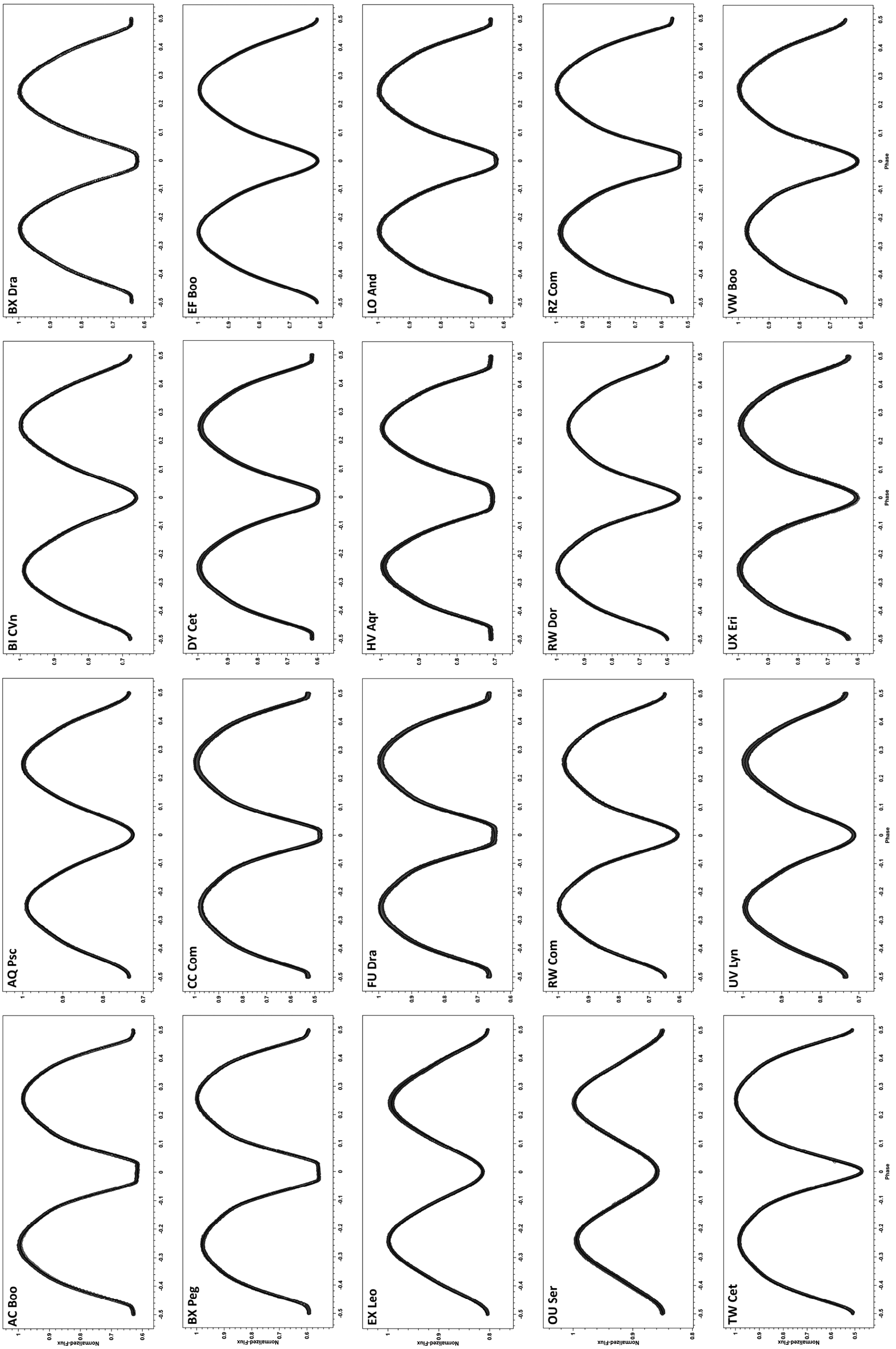

Fig.1. TESS data and synthetic light curves for the target binary systems.

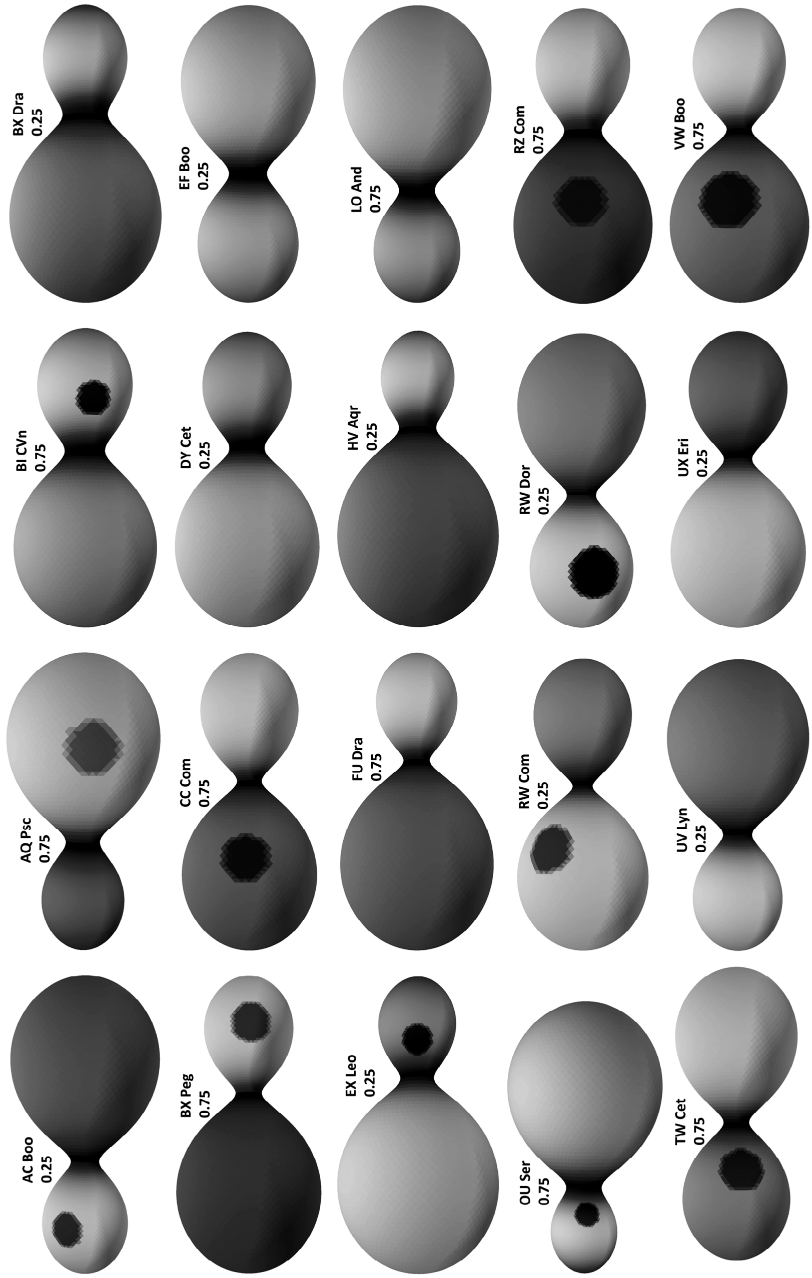

Fig.2. Three-dimensional view of the systems in phases 0.25 or 0.75.

estimate absolute parameters can have good accuracy, but there are challenges to obtaining proper accuracy. Challenges make this method unsuitable for some binary systems investigations. For example, the parameter that is obtained from the observational data and plays an important role in the calculation process is the maximum apparent magnitude V_{max}. In the first step of the calculation process using Gaia DR3 parallax, V_{max} is used to estimate the absolute magnitude M_V. Therefore, this may not be an appropriate method for calculating the absolute parameters in ground-based observations if the light curve's maxima display more dispersion. On the other hand, the extinction coefficient A_V should also be reasonable and low value (Table 1). In some cases, the large error for the Gaia DR3 parallax is associated with a large A_V value, although either alone can overshadow the accuracy of the absolute parameter estimates. Large parallax errors usually come in systems with galactic coordinates b between +5 and -5, making it challenging to determine A_V with good accuracy [39]. Also, the initial temperature chosen for the analysis can completely affect the accuracy of the results. The study published by the Poro et al. [40] study discusses the limitations of this method. In this study, due to the lack of a reliable value of V_{max} for all target systems, we preferred not to use this method.

The mass ratio is one of the most crucial factors in the estimation of the absolute parameters. There are several methods to test or obtain mass ratios from

Table 2

LIGHT CURVE SOLUTIONS' RESULTS IN REFERENCE STUDIES OF THE SYSTEMS

System	i °	$q = M_2/M_1$	f	T_1 (K)	T_2 (K)	$\Omega_1 = \Omega_2$	Reference
AC Boo	86.3(5)	3.340(4)	0.046	6250	6241(6)	7.034(4)	[22]
AQ Psc	69.06(80)	0.266(2)	0.35	6250(157)	6024(150)	2.253(12)	[23]
BI CVn	71.30(10)	2.437(4)	0.146(11)	6125(2)	6093	5.698(4)	[24]
BX Dra	80.63(6)	0.2884(5)	0.515	6980	6979(2)	2.3475(16)	[25]
BX Peg	87.2(6)	2.66	0.171(12)	5887(7)	5300	6.057(8)	[26]
CC Com	89.8(6)	1.90(1)	0.17	4300	4200(60)	5.009	[27]
DY Cet	82.48(34)	0.356(9)	0.24	6650(178)	6611(176)	2.529(5)	[23]
EF Boo	75.7(2)	1.871	0.18	6450	6425(14)	4.921(12)	[28]
EX Leo	60.8(2)	0.2	0.35	6340	6110(14)	2.186(12)	[29]
FU Dra	80.4(2)	3.989	0.190(12)	6100	5842(6)	7.778	[30]
HV Aqr	79.186(183)	0.145	0.569(10)	6460	6669(7)	2.036	[31]
LO And	80.1(6)	0.305(4)	0.4	6650	6690(24)	2.401(9)	[32]
OU Ser	50.47(2.24)	0.173(17)	0.68	5940(144)	5759(283)	2.090(17)	[23]
RW Com	72.43(29)	0.471(6)	0.15	4830(115)	4517(98)	5.319(9)	[23]
RW Dor	77.2(1)	1.587	0.115(67)	5560	5287(10)	4.64(4)	[33]
RZ Com	86.8(6)	2.179(9)	0.11(1)	6276(200)	6070	5.393(10)	[34]
TW Cet	81.18(10)	0.75(3)	0.06	5865(152)	5753(147)	3.308(2)	[23]
UV Lyn	67.6(1)	2.685	0.18	6000	5770(5)	6.080(1)	[35]
UX Eri	75.70(23)	0.373(21)	0.18	6093(153)	6006(150)	6.065(8)	[23]
VW Boo	73.81(5)	2.336	0.108(5)	5560	5198(3)	5.626(3)	[36]

Table 3

THE RESULTS OF THE LIGHT CURVE ANALYSIS OF THE SYSTEMS IN THIS STUDY

System	i °	$q = M_2/M_1$	f	T_1 (K)	T_2 (K)	$\Omega_1 = \Omega_2$	l_1/l_{tot}	$r_{(mean)1}$	$r_{(mean)2}$	Spot
AC Boo	84.05(50)	3.364(22)	0.199(10)	6378(77)	6091(75)	6.970(34)	0.289(17)	0.292(1)	0.500(1)	1
AQ Psc	68.60(65)	0.255(27)	0.314(24)	6299(58)	5969(51)	2.314(60)	0.794(9)	0.519(2)	0.287(2)	1
BI CVn	69.36(36)	2.437(137)	0.356(12)	6186(48)	6010(46)	5.643(193)	0.345(22)	0.332(6)	0.483(5)	1
BX Dra	79.85(27)	0.259(4)	0.566(20)	6944(46)	7016(44)	2.281(11)	0.744(11)	0.531(1)	0.304(1)	0
BX Peg	87.30(39)	2.861(20)	0.154(6)	5822(73)	5357(63)	6.337(30)	0.354(21)	0.303(1)	0.484(1)	1
CC Com	85.83(56)	1.991(46)	0.113(11)	4369(60)	4154(47)	5.172(71)	0.422(7)	0.330(2)	0.450(2)	1
DY Cet	81.05(65)	0.345(8)	0.287(13)	6666(52)	6569(45)	2.503(17)	0.721(14)	0.493(2)	0.311(2)	0
EF Boo	74.77(23)	1.882(35)	0.261(9)	6412(48)	6452(48)	4.929(54)	0.363(15)	0.347(2)	0.456(2)	0
EX Leo	59.22(41)	0.172(26)	0.467(108)	6200(72)	6245(68)	2.110(71)	0.808(35)	0.556(11)	0.262(12)	1
FU Dra	78.74(29)	3.915(30)	0.164(7)	6090(46)	5848(43)	7.700(43)	0.261(11)	0.278(1)	0.511(1)	0
HV Aqr	79.35(45)	0.168(2)	0.516(21)	6495(46)	6649(53)	2.095(6)	0.802(10)	0.560(1)	0.263(1)	0
LO And	79.24(51)	0.304(8)	0.315(13)	6716(53)	6622(62)	2.415(17)	0.741(15)	0.505(2)	0.301(3)	0
OU Ser	52.82(51)	0.149(37)	0.565(192)	5852(61)	5836(67)	2.046(105)	0.829(46)	0.570(18)	0.257(21)	1
RW Com	74.14(59)	0.540(80)	0.072(11)	4779(57)	4586(49)	2.929(153)	0.669(51)	0.441(14)	0.333(13)	1
RW Dor	76.08(30)	1.590(99)	0.144(12)	5506(48)	5318(51)	4.576(152)	0.426(3)	0.352(6)	0.433(6)	1
RZ Com	85.66(16)	2.348(21)	0.293(8)	6359(60)	6004(54)	5.559(33)	0.373(16)	0.330(1)	0.476(1)	1
TW Cet	83.62(36)	0.762(56)	0.103(9)	5899(51)	5708(52)	3.307(97)	0.589(3)	0.413(6)	0.366(6)	1
UV Lyn	65.77(12)	2.696(62)	0.187(7)	5993(34)	5792(38)	6.096(87)	0.323(14)	0.310(2)	0.481(2)	0
UX Eri	75.62(42)	0.508(50)	0.146(13)	6214(69)	5878(66)	2.847(97)	0.685(35)	0.452(9)	0.333(9)	0
VW Boo	73.38(13)	2.377(85)	0.127(10)	5504(54)	5267(50)	5.700(123)	0.360(23)	0.316(3)	0.466(3)	1

photometric data [41,42]. In this study, the initial mass ratio of target systems was obtained using different qualities of spectroscopic data from reference studies. The analysis of light curves showed that the mass ratio did not change significantly compared to the reference studies.

We used the semi-major axis and orbital period (a - P) relationship for estimating absolute parameters from the study Poro et al. [39] (Eq. (1)). Considering that the uncertainties reported in Eq. (1) have upper and lower limits, we used their average for calculations.

$$a = \left(0.372^{+0.113}_{-0.114}\right) + \left(5.914^{+0.272}_{-0.298}\right) P . \tag{1}$$

Then, using the well-known equation of Kepler's third law (Eq. (2)), we obtained the total mass ($M_1 + M_2$) of the components. Since $q = M_2/M_1$, the values of each star's mass were estimated.

$$\frac{a^3}{G\left(M_1 + M_2\right)} = \frac{P^2}{4\pi^2} . \tag{2}$$

The values of r_{mean} obtained from light curve solutions (Table 3) and the radius R of each star were calculated (Eq. (3)).

$$a = \frac{R}{r}. \tag{3}$$

According to the effective temperature obtained from the light curve analysis and the calculated radius, the luminosity L was calculated (Eq. (4)).

$$L = 4\pi R^2 \sigma T^4. \tag{4}$$

The absolute bolometric magnitude of stars was calculated and $M_{bol\odot}$ considered 4.73 from the Torres [43] throughout this estimating process (Eq. (5)).

$$M_{bol} - M_{bol\odot} = -2.5\log\frac{L}{L_\odot}. \tag{5}$$

The surface gravity of each star was also calculated based on its mass and radius (Eq. (6)).

$$g = G_\odot \frac{M}{R^2}. \tag{6}$$

The uncertainties of the absolute parameters were calculated using the errors determined by the PHOEBE code for the light curve elements used in the process, such as $T_{1,2}$, $r_{mean1,2}$, and q. Table 4 contains the results of the estimated absolute parameters.

5. *Discussion and conclusion*. We selected 20 contact binary systems and one of the latest published studies for each of them. The target systems have or used spectroscopic results. Except for DY Cet, none of them have used TESS data for analysis. Quality photometric data, like space-based data, is important for obtaining accurate light curve parameters and then estimating absolute parameters.

We conducted the light curve analysis using the PHOEBE Python code and TESS observations. We considered the effective temperature and mass ratio reported in the studies as input values. The results of the light curve analysis showed that the mass ratio of the systems has changed slightly. The minimum difference between the mass ratio of our results and reference studies is related to the BI CVn system with 0%, and the maximum difference is for the BX Peg system with 7%. The elapsed times from the reference studies and precise TESS data rather than ground-based observations can account for some of the discrepancies in the light curve analysis results.

The stars in contact binary systems have a small temperature difference due to mass and energy transfer [6]. The difference in effective temperature between the two stars in the BX Peg system had the maximum value at 465 K among the target systems, while the OU Ser system with 16 K had the lowest. Table 5 lists the temperature difference between companions. Based on the stars' effective temperatures, we estimated the spectral type of the stars using Cox [44] study (Table 5). We also checked the results of the effective temperature in this study

Table 4

ESTIMATED ABSOLUTE PARAMETERS OF 20 CONTACT BINARY SYSTEMS USING Gaia DR3 PARALLAX

System	$M_1(M_\odot)$	$M_2(M_\odot)$	$R_1(R_\odot)$	$R_2(R_\odot)$	$L_1(L_\odot)$	$L_2(L_\odot)$	M_{bol1}	M_{bol2}	$\log(g)_1$	$\log(g)_2$	$a(R_\odot)$
AC Boo	0.37(10)	1.23(35)	0.72(7)	1.23(11)	0.77(19)	1.87(46)	5.02(24)	4.05(24)	4.29(3)	4.35(4)	2.46(21)
AQ Psc	1.53(35)	0.39(14)	1.65(14)	0.91(8)	3.88(84)	0.96(21)	3.26(21)	4.78(22)	4.19(2)	4.11(6)	3.18(25)
BI CVn	0.49(11)	1.19(35)	0.88(9)	1.28(12)	1.02(26)	1.92(46)	4.71(25)	4.02(23)	4.24(1)	4.30(3)	2.64(22)
BX Dra	1.74(41)	0.45(11)	2.02(15)	1.15(9)	8.52(60)	2.91(55)	2.40(19)	3.57(19)	4.07(3)	3.97(3)	3.80(28)
BX Peg	0.37(11)	1.06(34)	0.62(6)	0.98(10)	0.39(11)	0.72(19)	5.75(26)	5.09(25)	4.43(3)	4.48(4)	2.03(19)
CC Com	0.43(14)	0.87(31)	0.55(6)	0.75(8)	0.10(3)	0.15(4)	7.22(29)	6.77(28)	4.59(3)	4.62(4)	1.68(18)
DY Cet	1.36(34)	0.47(13)	1.47(12)	0.93(8)	3.84(82)	1.44(31)	3.27(21)	4.33(21)	4.24(3)	4.17(4)	2.98(24)
EF Boo	0.62(15)	1.16(32)	0.99(9)	1.30(11)	1.50(33)	2.66(57)	4.29(22)	3.67(21)	4.23(2)	4.27(3)	2.86(23)
EX Leo	1.49(36)	0.26(11)	1.55(16)	0.73(10)	3.20(89)	0.73(25)	3.47(27)	5.07(32)	4.23(1)	4.12(5)	2.79(23)
FU Dra	0.30(9)	1.19(36)	0.61(6)	1.12(11)	0.46(11)	1.32(31)	5.58(23)	4.43(23)	4.35(3)	4.42(4)	2.19(20)
HV Aqr	1.42(39)	0.24(7)	1.45(13)	0.68(6)	3.37(73)	0.82(18)	3.41(21)	4.95(22)	4.27(3)	4.15(4)	2.59(22)
LO And	1.28(34)	0.39(12)	1.32(12)	0.79(8)	3.22(72)	1.08(27)	3.46(22)	4.65(24)	4.30(3)	4.23(4)	2.62(22)
OU Ser	1.28(34)	0.19(11)	1.21(16)	0.55(10)	1.55(51)	0.31(15)	4.25(31)	5.99(41)	4.38(1)	4.24(5)	2.13(20)
RW Com	0.87(24)	0.47(22)	0.78(11)	0.59(9)	0.29(10)	0.14(5)	6.08(33)	6.87(34)	4.59(1)	4.56(5)	1.78(18)
RW Dor	0.56(15)	0.88(30)	0.73(8)	0.89(10)	0.44(12)	0.57(16)	5.63(27)	5.33(27)	4.46(1)	4.48(4)	2.06(20)
RZ Com	0.47(13)	1.10(32)	0.78(7)	1.13(10)	0.90(22)	1.50(35)	4.84(23)	4.29(23)	4.32(3)	4.37(4)	2.37(21)
TW Cet	0.86(22)	0.66(23)	0.93(10)	0.82(9)	0.94(25)	0.65(18)	4.80(26)	5.20(26)	4.44(1)	4.42(4)	2.25(20)
UV Lyn	0.48(12)	1.28(35)	0.88(8)	1.36(12)	0.89(19)	1.87(40)	4.85(21)	4.05(21)	4.23(2)	4.28(3)	2.83(23)
UX Eri	1.22(27)	0.62(21)	1.36(14)	1.00(11)	2.48(67)	1.08(31)	3.74(26)	4.65(27)	4.26(1)	4.23(4)	3.01(24)
VW Boo	0.47(12)	1.11(34)	0.76(7)	1.12(11)	0.47(12)	0.87(21)	5.54(25)	4.89(24)	4.35(2)	4.39(4)	2.40(21)

with the reports of Gaia and TESS, so that the difference is less than 5%.

Additionally, EX Leo, HV Aqr, and OU Ser are low mass ratio contact systems with values of 0.172(28), 0.168(23), and 0.149(24), respectively. Although these three systems have a low mass ratio, they are not close to the extremely low mass ratio cutoff, which is less than 0.1 [45]. On the other hand, we have three systems (BX Dra, HV Aqr, OU Ser) with fillout factors greater than 50% and mass ratios less than 0.25. These specifications relate to deep overcontact binaries suggested by the Qian et al. [46] study, which found that this type of star is likely to be the progenitor of a blue straggler/FK Com-type star [47,45].

We estimated the absolute parameters using the semi-major axis and orbital period relationship. So, some values from the light curve solutions ($T_{1,2}$, q, $r_{mean1,2}$), and the orbital period used in the calculation process.

The positions of the stars were displayed using the Zero-Age Main Sequence (ZAMS) and the Terminal-Age Main Sequence (TAMS) on the Mass-Luminosity ($M - L$) and Mass-Radius ($M - R$) diagrams, based on the absolute parameters (Fig.3a, b). Additionally, the outcomes have been compared with the theoretical fits from the study Poro et al. [10], and as expected the $M - L$ and $M - R$

Table 5

THE SPECTRAL TYPE (Sp) OF STARS, TEMPERATURE DIFFERENCE OF COMPANIONS, TOTAL MASS, ORBITAL ANGULAR MOMENTUM, AND SUBTYPE OF THE TARGET BINARY SYSTEMS

System	Sp Star1	Sp Star2	ΔT (K)	M_{tot} ($M_\odot$)	J_0	Subtype
AC Boo	F5	F8	287	1.60(46)	51.53(18)	W
AQ Psc	F6	G1	330	1.92(49)	51.67(19)	A
BI CVn	F8	G0	176	1.68(46)	51.65(17)	W
BX Dra	F1	F1	72	2.19(52)	51.80(16)	W
BX Peg	G3	K0	465	1.43(45)	51.45(20)	W
CC Com	K5	K5	215	1.30(46)	51.41(21)	W
DY Cet	F3	F3	97	1.83(48)	51.69(17)	A
EF Boo	F5	F5	40	1.77(47)	51.74(17)	A
EX Leo	F7	F7	45	1.74(47)	51.46(21)	W
FU Dra	G0	G3	242	1.49(45)	51.42(19)	W
HV Aqr	F5	F3	154	1.66(46)	51.41(18)	W
LO And	F2	F3	94	1.67(46)	51.58(18)	A
OU Ser	G3	G3	16	1.47(45)	51.25(26)	A
RW Com	K3	K3	193	1.33(45)	51.45(23)	A
RW Dor	G8	K0	188	1.44(45)	51.55(19)	W
RZ Com	F5	G0	355	1.57(45)	51.58(18)	W
TW Cet	G2	G6	191	1.51(45)	51.62(19)	A
UV Lyn	G0	G3	201	1.76(47)	51.67(17)	W
UX Eri	F7	G2	336	1.84(48)	51.77(18)	A
VW Boo	G8	K0	237	1.58(46)	51.59(18)	W

connections are weak. Fig.3c shows the position of the systems compared to the q - L_{ratio} theoretical fit obtained from the study Poro et al. [10], with which they are in good agreement. We utilized the following equation from the study Eker et al. [48] to calculate the orbital angular momentum J_0 of the systems:

$$J_0 = \frac{q}{(1+q)^2} \sqrt[3]{\frac{G^2}{2\pi} M^5 P}, \tag{7}$$

where q is the mass ratio, M is the total mass of the system, P is the orbital period, and G is the gravitational constant. The results of estimating the J_0 are listed in Table 5 along with the total mass of the systems. We also determined the subtype of each system (Table 5). Therefore, we considered the systems where the more massive star has a hotter effective temperature than the companion as A-type and otherwise as W-type. Additionally, the target systems' position is depicted in the $\log M_{tot}$ - $\log J_0$ diagram (Fig.3d), which indicates that they are in a contact binary systems region.

The temperature-mass relationship for contact binary systems was presented

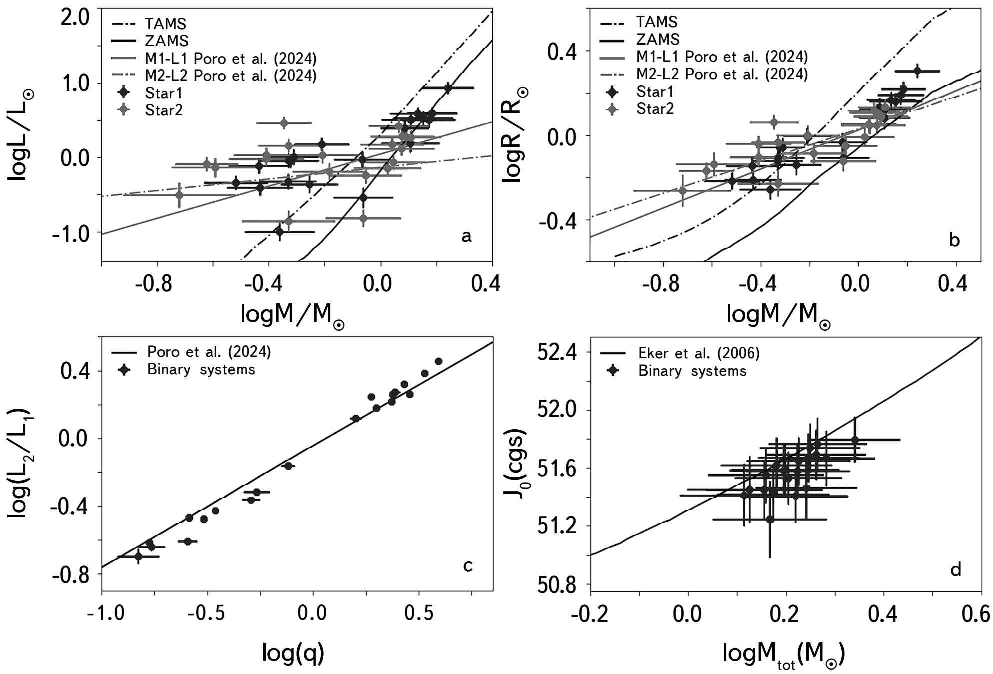

Fig.3. (a) $M_{1,2}$ - $L_{1,2}$, (b) $M_{1,2}$ - $R_{1,2}$, (c) q - L_{ratio}, and (d) M_{tot} - J_0 diagrams.

by Poro et al. [49] with a linear fit. They made use of 428 contact systems from the study [6] sample. The hotter component T_h and the mass of the more massive star M_m were considered for this relation by Poro et al. [49]. Our target systems are positioned on the T_h - M_m diagram (Fig.4), which indicates good agreement with the theoretical fit and uncertainty.

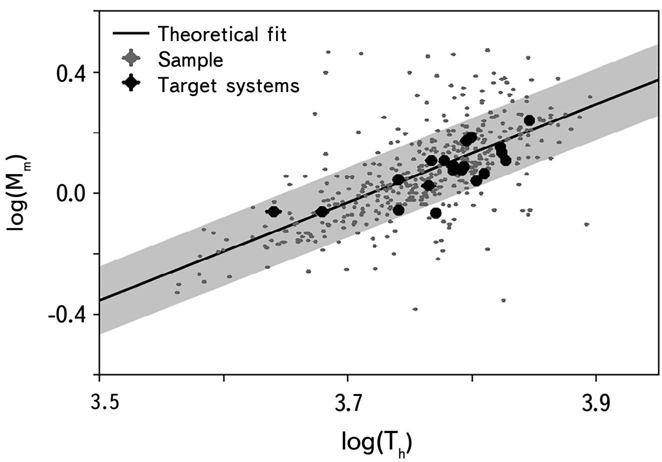

Fig.4. The diagram of the relationship between the effective temperature T_h and the mass M_m of the primary component in contact binary stars in which the studied systems are displayed.

Acknowledgements. This manuscript was prepared by the BSN project (https://bsnp.info/). We used data from the European Space Agency's mission Gaia (http://www.cosmos.esa.int/gaia). We made use of the SIMBAD database, which is operated by CDS in Strasbourg, France (http://simbad.u-strasbg.fr/simbad/). This work includes data from the TESS mission observations. Funding for the TESS mission is provided by the NASA Explorer Program. We acknowledge the TESS team for its support of this study.

Binary Systems of South and North (BSN) Project, Tehran, Iran, e-mail: atilaporo@bsnp.info

АНАЛИЗ КРИВЫХ БЛЕСКА И АБСОЛЮТНЫХ ПАРАМЕТРОВ ДВАДЦАТИ КОНТАКТНЫХ ДВОЙНЫХ ЗВЕЗД С ИСПОЛЬЗОВАНИЕМ ДАННЫХ TESS

Э.ПАКИ, А.ПОРО

Анализ контактных двойных звезд с использованием фотометрических данных космических телескопов и исследование возможных изменений параметров могут дать точную картину для теоретических исследований. Мы исследовали решения световых кривых и фундаментальные параметры для двадцати контактных двойных систем. Для анализа использовались самые последние данные спутника для исследования транзитных экзопланет (TESS). Исследованные в данной работе системы имеют орбитальный период менее 0.58 дня. Решения световых кривых были получены с использованием Python-кода PHOEBE версии 2.4.9. Результаты показывают, что системы имели различные соотношения масс от $q=0.149$ до $q=3.915$, коэффициенты заполнения (степень контакта) от $f=0.072$ до $f=0.566$ и наклоны от $i=52^{\circ}.8$ до $i=87^{\circ}.3$. Эффективная температура звезд была менее 7016 K, как и ожидалось, учитывая особенности большинства контактных двойных звезд. Кривые блеска двенадцати из целевых систем были асимметричны в максимумах, показывая эффект О'Коннелла, и для решений световых кривых требовалось наличие звездного пятна. Были представлены и обсуждены оценки абсолютных параметров двойных систем с использованием эмпирической зависимости a - P. Рассчитаны орбитальные угловые моменты J_0 систем. Положения систем представлены на диаграммах M - L, M - R, q - L_{ratio}, M_{tot} - J_0 и T - M.

Ключевые слова: *двойная звезда: затмение - двойные звезды: близкие - анализ данных*

REFERENCES

1. *Z.Kopal*, Close binary systems. The International Astrophysics Series, London: Chapman & Hall, 1959.
2. *G.P.Kuiper*, Astrophys. J., **93**, 133, 1941.
3. *K.Yakut*, *P.P.Eggleton*, Astrophys. J., **629**, 1055, 2005. doi:10.1086/431300.
4. *L.Binnendijk*, Vistas in Astronomy, **12**, 217, 1970.
5. *L.B.Lucy*, *R.E.Wilson*, Astrophys. J., **231**, 502, 1979. doi:10.1086/157212.
6. *O.Latković*, *A.Čeki*, *S.Lazarević*, Astrophys. J. Suppl., **254**, 10, 2021. doi:10.3847/1538-4365/abeb23.
7. *G.A.Loukaidou*, *K.D.Gazeas*, *S.Palafouta et al.*, Mon. Not. Roy. Astron. Soc., **514**, 5528, 2022. doi:10.1093/mnras/stab3424.
8. *X.-D.Zhang*, *S.-B.Qian*, Mon. Not. Roy. Astron. Soc., **497**, 3493, 2020. doi:10.1093/mnras/staa2166.
9. *D.J.K.O'Connell*, PRCO, **2**, 85, 1951.
10. *A.Poro*, *E.Paki*, *A.Alizadehsabegh et al.*, RAA, **24**, 015002, 2024. doi:10.1088/1674-4527/ad0866.
11. *K.Li*, *Q.-Q.Xia*, *C.-H.Kim et al.*, Astron. J., **162**, 13, 2021. doi:10.3847/1538-3881/abfc53.
12. *M.F.Yıldırım*, 2022, RAA, 22, 055013. doi:10.1088/1674-4527/ac5ee8.
13. *G.R.Ricker*, *D.W.Latham*, *R.K.Vanderspek et al.*, AAS, 2010.
14. *K.G.Stassun*, *R.J.Oelkers*, *J.Pepper et al.*, Astron. J., **156**, 102, 2018. doi:10.3847/1538-3881/aad050.
15. *E.F.Schlafly*, *D.P.Finkbeiner*, Astrophys. J., **737**, 103, 2011. doi:10.1088/0004-637X/737/2/103.
16. *G.M.Green*, *E.Schlafly*, *C.Zucker et al.*, Astrophys. J., **887**, 93, 2019. doi:10.3847/1538-4357/ab5362.
17. *A.Prša*, *K.E.Conroy*, *M.Horvat et al.*, Astrophys. J. Suppl., **227**, 29, 2016. doi:10.3847/1538-4365/227/2/29.
18. *S.M.Ruciński*, AcA, **19**, 245, 1969.
19. *L.B.Lucy*, ZA, **65**, 89, 1967.
20. *F.Castelli*, *R.L.Kurucz*, arXiv preprint astro-ph/0405087.
21. *K.Sriram*, *S.Malu*, *C.S.Choi*, Astron. J., **153**, 231, 2017. doi:10.3847/1538-3881/aa6893.
22. *R.H.Nelson*, IBVS, **5951**, 1, 2010.
23. *S.Deb*, *H.P.Singh*, Mon. Not. Roy. Astron. Soc., **412**, 1787, 2011. doi:10.1111/j.1365-2966.2010.18016.x.
24. *R.H.Nelson*, *H.V.Şenavci*, *Ö.BaŞtürk et al.*, NewA, **29**, 57, 2014. doi:10.1016/j.newast.2013.11.006.
25. *J.-H.Park*, *J.W.Lee*, *S.-L.Kim et al.*, PASJ, **65**, 1, 2013. doi:10.1093/pasj/65.1.1.
26. *K.Li*, *S.Hu*, *D.Guo et al.*, NewA, **41**, 17, 2015. doi:10.1016/j.newast.2015.04.010.
27. *O.Köse*, *B.Kalomeni*, *V.Keskin et al.*, Astron. Nachr., **332**, 626, 2011. doi:10.1002/

asna.201011566.
28. *K.D.Gazeas*, *A.Baran*, *P.Niarchos et al.*, AcA, **55**, 123, 2005.
29. *S.Zola*, *K.Gazeas*, *J.M.Kreiner et al.*, Mon. Not. Roy. Astron. Soc., **408**, 464, 2010. doi:10.1111/j.1365-2966.2010.17129.x.
30. *L.Liu*, *S.-B.Qian*, *J.-J.He et al.*, PASJ, **64**, 48, 2012. doi:10.1093/pasj/64.3.48.
31. *K.Li*, *S.-B.Qian*, NewA, **21**, 46, 2013. doi:10.1016/j.newast.2012.11.003.
32. *R.H.Nelson*, *R.M.Robb*, IBVS, **6134**, 1, 2015.
33. *T.Sarotsakulchai*, *S.-B.Qian*, *B.Soonthornthum et al.*, PASJ, **71**, 34, 2019. doi:10.1093/pasj/psy149.
34. *R.H.Nelson*, *K.B.Alton*, IBVS, **6266**, 1, 2019. doi:10.22444/IBVS.6266.
35. *S.Zola*, *J.M.Kreiner*, *B.Zakrzewski et al.*, AcA, **55**, 389, 2005.
36. *L.Liu*, *S.-B.Qian*, *L.-Y.Zhu et al.*, Astron. J., **141**, 147, 2011. doi:10.1088/0004-6256/141/5/147.
37. *F.Tavakkoli*, *A.Hasanzadeh*, *A.Poro*, New Astron., **37**, 64, 2015. doi:10.1016/j.newast.2014.12.004.
38. *A.Poro*, *E.Ferńandez-Lajús*, *M.Madani et al.*, RAA, **23**, 095011, 2023. doi:10.1088/1674-4527/ace027.
39. *A.Poro*, *M.Tanriver*, *R.Michel et al.*, Publ. Astron. Soc. Pacif., **136**, 024201, 2024. doi:10.1088/1538-3873/ad1ed3.
40. *A.Poro*, *M.Hedayatjoo*, *M.Nastaran et al.*, New Astron., **110**, 102227, 2024. doi:10.1016/j.newast.2024.102227.
41. *A.Poro*, *S.Zamanpour*, *M.Hashemi et al.*, New Astron., **86**, 101571, 2021. doi:10.1016/j.newast.2021.101571.
42. *S.Kouzuma*, Astrophys. J., **958**, 84, 2023. doi:10.3847/1538-4357/ad03e1.
43. *G.Torres*, Astron. J., **140**, 1158, 2010. doi:10.1088/0004-6256/140/5/1158.
44. *A.N.Cox*, Allen's Astrophysical Quantities, AIP Press, Springer, New York, 2000.
45. *K.Li*, *Q.-Q.Xia*, *C.-H.Kim et al.*, Astrophys. J., **922**, 122, 2021. doi:10.3847/1538-4357/ac242f.
46. *S.-B.Qian*, *Y.-G.Yang*, *B.Soonthornthum et al.*, Astron. J., **130**, 224, 2005. doi:10.1086/430673.
47. *Y.-G.Yang*, *S.-B.Qian*, *L.-Y.Zhu et al.*, Astron. J., **138**, 540, 2009. doi:10.1088/0004-6256/138/2/540.
48. *Z.Eker*, O.Demircan, *S.Bilir et al.*, Mon. Not. Roy. Astron. Soc., **373**, 1483, 2006. doi:10.1111/j.1365-2966.2006.11073.x.
49. *A.Poro*, *S.Baudart*, *M.Nourmohammad et al.*, RAA, **24**, 055001, 2024. doi:10.1088/1674-4527/ad3a2c.

А С Т Р О Ф И З И К А

ТОМ 67 АВГУСТ, 2024 ВЫПУСК 3

DOI: 10.54503/0571-7132-2024.67.3-341

A SIMPLE ANALYTICAL METHOD USING FOKKER-PLANCK EQUATION FOR MODELING PARTICLE ACCELERATION AT ASTROPHYSICAL SHOCKS

J.-H.HA

Received 19 June 2024
Accepted 26 August 2024

Shocks are ubiquitous in astrophysical environments, and particle acceleration at such astrophysical shocks is related to high-energy phenomena. In particular, the acceleration mechanism and the time evolution of the particle distribution function have been extensively examined. This paper describes a simple analytic method using the one-dimensional Fokker-Planck equation in the test-particle regime. We aim to investigate the evolution of the particle distribution function in the shock upstream, which could be streaming toward Earth along the open magnetic field geometry. The behavior of the analytical solution is examined over a wide range of parameters representing shock structure, such as the shock Mach number, plasma beta, injection fraction into diffusive shock acceleration, and the scale of the upstream magnetic field. The behavior is associated with upstream turbulence for diffusive shock acceleration, as expected. Additionally, pre-accelerated particles could affect the time evolution of the particle distribution only when the radiative or advection losses are small enough for the pre-accelerated distribution to have a flatter power-law slope than the power-law slope based on shock acceleration theory. We also provide a formula for a spherically expanding shock and its relevant application to calculate high-energy emission due to hadronic interactions. We suggest that the simple analytic method could be applied to examine astrophysical shocks with a wide range of plasma parameters.

Keywords: *particle acceleration: high-energy radiation: astrophysical shocks: Fokker-Planck equation*

1. *Introduction.* Shocks are induced in various astrophysical environments due to supersonic flow motions such as coronal mass ejections in the interplanetary medium [1-3], supernova remnants in the interstellar medium [4-6], and gravitational collapse in the large-scale structure of the universe [7-10]. While the properties of shocks can be affected by the characteristics of the medium, it has been demonstrated that such shocks efficiently accelerate particles. Particle acceleration at shocks has been explained by first-order Fermi acceleration, which states that particles can gain energy through multiple interactions with the converging waves near the shocks (i.e., diffusive shock acceleration (DSA, hereafter)) [11,12]. Modeling particle acceleration at astrophysical shocks has been examined by previous studies using numerical approaches, including plasma kinetic simulations [13-18], hydrodynamic simulations [19,20], and models for the advection-diffusion

of particle distribution functions in spatial and momentum space based on the Fokker-Planck equation [1,20-23].

Using plasma kinetic simulations, the physical mechanisms for magnetic field amplification and wave generation for scattering off particles in both the upstream and downstream regions have been extensively studied [13-18]. Although the properties of plasma waves for particle acceleration can depend on the characteristics of the medium, such as supersonic flow properties (i.e., nonrelativistic, relativistic) and magnetic field strength (i.e., unmagnetized, weakly magnetized, and strongly magnetized plasmas), it has been shown that plasma waves can be induced by various instabilities due to the plasma beam distribution causing velocity space anisotropy [16,17]. According to simulation results, such waves can be self-excited due to particle reflection at the shock surface during the evolution of collisionless shocks, and evidence of particle acceleration through multiple wave-particle interactions has been observed [13-15,18]. While plasma kinetic simulations are a powerful tool for investigating the microphysics of particle acceleration through first-principle calculations, they are limited in their ability to observe the full DSA process, which occurs over longer timescales than the growth timescale of plasma instabilities.

Considering the effects of particle acceleration at shocks and their observational implications beyond the kinetic scales, theoretical modeling has been conducted, including DSA-produced cosmic-ray populations (i.e., cosmic-ray populations following a power-law distribution) and the physics of advection and diffusion in spatial and momentum spaces. To obtain the particle spectral evolution as a stationary shock structure, a test-particle approach has been employed, assuming that the evolution of the shock structure is independent of the dynamical feedback of cosmic-ray particles [1,23]. Moreover, hydrodynamic simulations, including magnetohydrodynamics, have been used to model the dynamical evolution of shocks in astrophysical media more sophisticatedly [9,10,24,25]. Based on such modeling, multi-wavelength emissions due to particle acceleration at shocks have also been examined [24-29].

As a follow-up to the previous studies summarized above, this study aims to describe simplified analytic method using the one-dimensional Fokker-Planck equation. The effects of shock upstream conditions on particle spectral evolution were also examined to demonstrate the robustness of the analytical solution in various astrophysical environments. Additionally, we provide a potential application for calculating high-energy radiation due to particle acceleration at shocks, showing that our simple model can be used as a tool for rapidly estimating observable radiation flux. Moreover, the simple analytical approach described in this work has the advantage of being flexibly expandable. In particular, it would be possible to extend our simple model to incorporate detailed physics, including diffusion models and the microphysics of particle injection into DSA.

2. *Basic physics*. This section describes the basic physics, including the particle distribution function and relevant plasma physics, for particle acceleration at collisionless shocks. The importance of the characteristics of the particle distribution function for estimating the efficiency of particle acceleration at shocks is also discussed.

2.1. *Particle distribution function*. The particle distribution of thermal plasma is commonly modeled as Maxwellian, given by

$$f_{MW}(p)=\frac{n_{0i}}{\pi^{3/2}}\,p_{th}^{-3}\exp\left[-\left(\frac{p}{p_{th}}\right)^{2}\right], \tag{1}$$

where $p_{th}=\sqrt{2mk_BT}$ is the thermal momentum and n_{0i} is the plasma density, defined as

$$n_{i0}\equiv\int 4\pi p^2 f_{MW}(p)dp\,. \tag{2}$$

While the Maxwellian distribution is reasonable for describing the medium in the absence of nonlinear processes such as plasma and magnetohydrodynamic (MHD) waves, shocks, and turbulence, it has been demonstrated that plasma processes associated with such phenomena can accelerate particles. This particle energization results in a particle distribution that deviates from the Maxwellian, known as the kappa distribution [30-32]. The kappa distribution is defined as:

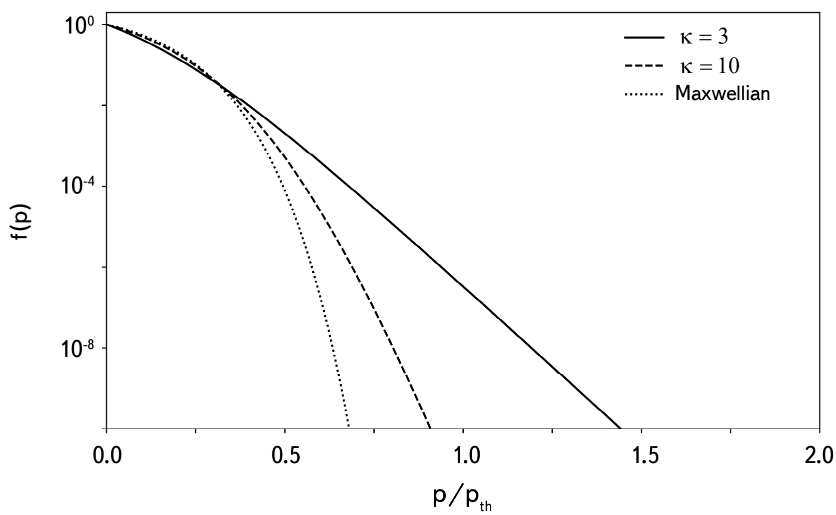

Fig.1. Examples of Maxwellian and kappa distribution functions.

$$f_\kappa(p) = \frac{n_{0i}}{\pi^{3/2}} p_{th}^{-3} \frac{\Gamma(\kappa+1)}{(\kappa-3/2)^{3/2}\Gamma(\kappa-1/2)} \left[1 + \frac{1}{(\kappa-3/2)}\left(\frac{p}{p_{th}}\right)^2\right]^{-(\kappa+1)}, \quad (3)$$

where $\Gamma(x)$ is the Gamma function and the parameter, κ, determines the slope of the supra-thermal distribution. For $p >> p_{th}$, the kappa distribution follows a power-law form, $f_\kappa(p) \propto p^{-2(\kappa+1)}$. Fig.1 shows examples of particle distribution functions. A smaller value of κ results in a flatter particle distribution, whereas a larger value of κ makes the kappa distribution closer to the Maxwellian. It has been shown that the kappa distribution modulates the nature of plasma waves [33], and thus the presence of such suprathermal populations could affect the efficiency of shock acceleration.

2.2. *Plasma physics for particle acceleration at collisionless shocks*. To understand particle acceleration at shocks mediated by waves in the shock upstream and downstream, the evolution of shock structure and the plasma instabilities responsible for generating plasma waves that scatter off particles should be considered. When examining plasma processes associated with electrostatic waves, plasma frequencies ($\omega_{pe} = \sqrt{4\pi ne^2/m_e}$, $\omega_{pi} = \sqrt{4\pi ne^2/m_i}$) and skin depths ($c/\omega_{pe}$ and c/ω_{pi}) are employed. Electromagnetic interactions, on the other hand, are characterized using gyrofrequencies ($\Omega_e = eB/m_e c$, $\Omega_i = eB/m_i c$) and gyroradii of thermal electrons and ions ($r_{th,e} = v_{th,e}/\Omega_e$, $r_{th,i} = v_{th,i}/\Omega_i$). Particularly, the characteristic scales of ions (i.e., Ω_i^{-1}, $r_{th,i}$) are employed to describe the dynamics of shock evolution, where the shock thickness is a few times the gyroradius of downstream thermal ions, $r_{th,i2}$. This indicates that particle energization through multiple crossings of the shock structure (i.e., diffusive shock acceleration, DSA) is feasible only for particles with momenta greater than the so-called injection momentum, $p_{inj} \sim 3p_{th,i2} = 3\sqrt{2m_i k_B T_2}$ [16,19,34-35]. It has been demonstrated that particles with momenta beyond p_{inj} drive plasma instabilities in the shock upstream and downstream, and these self-excited plasma waves can further accelerate particles [13-18]. Plasma kinetic simulations have provided evidence that such plasma processes can extend to DSA [13-15,18].

When modeling the distribution of shock-accelerated particles, the number of particles with $p \geq p_{inj}$ is parameterized as the so-called injection fraction, ε_{inj}. It is important to note that this injection fraction can strongly depend on the distribution of the background medium. If shock acceleration and particle transport associated with MHD waves are active in the medium, the thermal particle distribution may deviate from the Maxwellian distribution and instead follow the kappa distribution. Specifically, the presence of a kappa distribution could enhance the injection fraction, as illustrated in Fig.2.

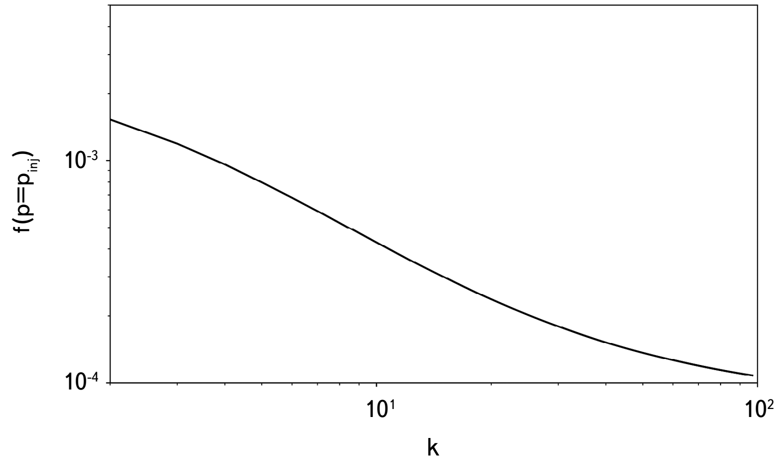

Fig.2. The normalization of the particle distribution function at $p = p_{inj}$ with different kappa values ranging from $\kappa = 2$ to $\kappa = 10^2$.

In the modeling described in the following section, two main factors of the kappa distribution were considered: (1) the injection fraction into DSA, which changes the efficiency of shock acceleration; and (2) the effects of the momentum distribution of pre-accelerated particles following a power-law form.

3. *Simple analytic model based on Fokker-Planck equation.*

3.1. *Shock structure and one-dimensional Fokker-Planck equation.* In this work, we solve the Fokker-Planck equation to study the time evolution of shock-accelerated particles due to diffusive shock acceleration (DSA). Throughout the paper, we use formulas in the shock rest frame. Considering the scale length of the magnetized medium, $L_B = B(\partial B/\partial r)^{-1}$ with an open field geometry in the shock upstream $B_1(r) = B_0 \exp(-r/L_B)$, we assume the shock structure as follows:

$$
\begin{aligned}
U(r) &\approx \begin{cases} U_1, & r > 0, \\ U_2 = U_1/\rho_c, & r < 0, \end{cases} \\
n(r) &\approx \begin{cases} n_1 = n_{i0} \exp(-2r/L_B), & r > 0, \\ n_2 = \rho_c\, n_{i0}, & r < 0, \end{cases} \\
B(r) &\approx \begin{cases} B_1 = B_0 \exp(-r/L_B), & r > 0, \\ B_2 = \rho_c\, B_0, & r < 0, \end{cases} \\
T(r) &\approx \begin{cases} T_1, & r > 0, \\ T_2, & r < 0, \end{cases}
\end{aligned}
\tag{4}
$$

where $U(r)$, $n(r)$, $B(r)$ and $T(r)$ represent the velocity, density, magnetic field, and temperature profiles, respectively, and ρ_c denotes the shock compression ratio. The subscripts 1 and 2 denote upstream and downstream quantities, respectively. The sonic and Alfvenic Mach numbers are then calculated as follows:

$$M_s = \frac{U_1}{c_s}, \quad M_A = \frac{U_1}{V_A} = \sqrt{\frac{\gamma\beta}{2}} M_s, \tag{5}$$

where $c_s = \sqrt{2\gamma n_i k_B T_1 / m_i}$ and $V_A = B_0 \big/ \sqrt{4\pi n_i m_i}$ are the sound and Alfven speeds, respectively, with the adiabatic index, $\gamma = 5/3$. According to the shock jump condition, the temperature jump can be computed using the sonic Mach number:

$$\frac{T_2}{T_1} = \frac{\left(5M_s^2 - 1\right)\left(M_s^2 + 3\right)}{16 M_s^2}. \tag{6}$$

In the finite shock upstream and downstream, the spatial diffusion coefficients associated with the plasma waves are defined as:

$$D(r) = \begin{cases} D_1(p), & L_1 > r > 0, \\ D_2(p), & -L_2 < r < 0, \end{cases} \tag{7}$$

where L_1, and L_2 represent the finite sizes of the shock upstream and downstream, respectively.

Since the DSA process can be explained in a one-dimensional system, we solved the one-dimensional Fokker-Planck equation. To account for the advection and diffusion of particle distribution into the interplanetary and interstellar medium, characterized by an open field geometry, we solved the one-dimensional Fokker-Planck equation in the shock upstream, as follows:

$$\begin{aligned} &\frac{\partial f(r,p,t)}{\partial t} + \frac{\partial}{\partial r}\left(U_1 + \frac{D_1(p)}{L_B}\right) f(r,p,t) - \left(\frac{\partial U_1}{\partial r} + \frac{U_1}{L_B}\right)\frac{\partial}{\partial p}\frac{p}{3} f(r,p,t) \\ &\qquad - \frac{\partial}{\partial r}\left(D_1(p)\frac{\partial f(r,p,t)}{\partial r}\right) = s(r,p,t), \end{aligned} \tag{8}$$

where $f(r,p,t)$ and $s(r,p,t)$ denote the particle distribution function and the source function, respectively. Based on the DSA theory and assuming steady injection, the initial particle distribution $f_0(r,p,t=0)$, and the source term $s(r,p,t)$ are assumed as follows:

$$\begin{aligned} Q_{inj}(r) &= \varepsilon_{inj}\, n_{i,0} U_1 \exp\left(-\frac{2r}{L_B}\right), \\ f_0(r,p,t=0) &= \frac{Q_{inj}(r)}{4\pi U_1 p_{inj}^3}\left(\frac{p}{p_{inj}}\right)^{-q} = \frac{\varepsilon_{inj}\, n_{i,0}}{4\pi\, p_{inj}^3}\exp\left(-\frac{2r}{L_B}\right)\left(\frac{p}{p_{inj}}\right)^{-q}\exp\left(-\frac{p}{p_{max}}\right), \\ s(r,p,t) &= Q_{inj}(r)\delta(r)\delta\left(p - p_{inj}\right) = \varepsilon_{inj}\, n_{1,0} U_1 \exp\left(-\frac{2r}{L_B}\right)\delta(r)\delta\left(p - p_{inj}\right), \end{aligned} \tag{9}$$

where p_{inj} and p_{max} are the injection and maximum momentum, respectively. As described in the section 2.2, the injection momentum is approximately a few times of the downstream thermal momentum, $p_{inj} \sim 3\,p_{th,i2} = 3\sqrt{2\,m_i k_B T_2}$. Considering the gyroradius of particles, the maximum momentum can be constrained by the size of the magnetic field of the system, $p_{max}c/eB_0 \approx L_B$. In addition, ε_{inj} denotes the injection fraction into DSA.

We here derive a simplified analytic form of $\partial f/\partial t$ at the shock front based on the shock structure described above in the test-particle limit. Adopting the exponential shock precursor defined in Eqs. (4) and (7), we obtained the following derivatives of $f \propto n_{i0}\exp(-2r/L_B)$ in the spatial domain:

$$\frac{\partial f}{\partial r} \approx -\frac{2}{L_B} f\,, \quad \frac{\partial^2 f}{\partial r^2} \approx \frac{4}{L_B^2} f\,, \quad \frac{\partial U_1}{\partial r} \approx 0\,, \quad \frac{\partial D_1}{\partial r} \approx 0\,. \tag{10}$$

We also obtain the following derivative of $f \propto p^{-q}$,

$$\frac{\partial (pf)}{\partial p} = (1-q)f\,. \tag{11}$$

Using Eqs. (10)-(11), the partial derivative terms of Eq. (8) can be simplified at the shock front as follows:

$$\begin{gathered}
\frac{\partial}{\partial r}\left(U_1 + \frac{D_1(p)}{L_B}\right) f(r,p,t) \approx \left(U_1 + \frac{D_1(p)}{L_B}\right)\frac{\partial f(r,p,t)}{\partial r} = -\left(\frac{2U_1}{L_B} + \frac{2D_1(p)}{L_B^2}\right) f(r,p,t), \\
\left(\frac{\partial U_1}{\partial r} + \frac{U_1}{L_B}\right)\frac{\partial}{\partial p}\frac{p}{3} f(r,p,t) \approx \frac{U_1}{L_B}\frac{\partial}{\partial p}\frac{p}{3} f(r,p,t) = \frac{U_1}{L_B}\frac{1-q}{3} f(r,p,t), \\
\frac{\partial}{\partial r}\left(D_1(p)\frac{\partial f(r,p,t)}{\partial r}\right) \approx D_1(p)\frac{\partial^2 f(r,p,t)}{\partial r^2} = \frac{4D_1(p)}{L_B^2} f(r,p,t).
\end{gathered} \tag{12}$$

Based on Eqs. (12), $\partial f/\partial t$ can be simplified as

$$\frac{\partial f(r,p,t)}{\partial t} \approx -\left(\frac{7-q}{3}\frac{U_1}{L_B}\right) f(r,p,t) + \frac{6D_1(p)}{L_B^2} f(r,p,t) + s(r,p,t). \tag{13}$$

Here, the first and second terms denote the contributions of advection and diffusion, respectively. The time evolution of $f(r,p,t)$ is then computed numerically as follows,

$$\begin{aligned}
f(r,p,t_{i+1}) = f(r,p,t_0) + \int_0^{t_i}\left(\frac{\partial f(r,p,t)}{\partial t}\right)_{t_i} dt = f(r,p,t_0) \\
+ \sum_{t_i \in \{0,\,\tau_{acc}\}} \Delta t\left(\frac{\partial f(r,p,t)}{\partial t}\right)_{t_i}.
\end{aligned} \tag{14}$$

Here, time interval Δt satisfies $\Delta t << \tau_{acc}$ and is normalized in units of Ω_i^{-1}, since the acceleration timescale depends on Ω_i^{-1}.

3.2. *Characteristic scales*. To calculate the accumulated particle distribution function, the following characteristic timescales are employed:

$$
\begin{aligned}
&\tau_{AD} \approx \frac{L_1}{U_1}, \\
&\tau_{acc}(p) \approx \frac{1}{U_1 - U_2}\left[\frac{D_1(p)}{U_1} + \frac{D_2(p)}{U_2}\right] \approx \frac{D_1(p)}{U_1^2}\left(\frac{1}{1-\rho_c^{-1}}\right)\left(\frac{1}{1+\rho_c^2}\right), \\
&\tau_{diff}(p) \approx \frac{D_1(p)}{U_1^2} \approx \frac{2}{\pi}\frac{1}{q}\left(\frac{M_A - 1}{\varepsilon_{inj} M_A^2}\right)\left(\frac{p}{p_{inj}}\right)^{q-3} \Omega_i^{-1}, \\
&D_1(p) \approx \frac{1}{3}\nu\lambda_1(p) \approx \frac{2}{\pi}\frac{1}{q}\left(\frac{M_A - 1}{\varepsilon_{inj} M_A^2}\right)\left(\frac{p}{p_{inj}}\right)^{q-3} U_1^2\, \Omega_i^{-1}.
\end{aligned}
\tag{15}
$$

Here, τ_{AD} is the adiabatic deceleration timescale of a supersonic ejecta, τ_{acc} is the shock acceleration timescale, and τ_{diff} is the turbulent diffusion timescale associated with waves generated by shock-accelerated particles [3]. In 2-nd Eq. of (15), the acceleration timescale satisfies $\tau_{acc} < \tau_{diff}$ since the shock compression ratio ρ_c is always larger than 1. This is consistent with the physical requirement that the timescale for particle acceleration should be shorter than the diffusion timescale; otherwise, particles would diffuse away from the shock surface before undergoing significant acceleration. Additionally, adiabatic losses typically occur more slowly than diffusion and acceleration processes. The relationship between characteristic timescales and length scales (i.e., $L_{diff} \approx U_1 \tau_{diff}$, $L_{acc} \approx U_1 \tau_{acc}$ and $L_1 \approx U_1 \tau_{AD}$) can be summarized as follows, particularly for particles with $p \le p_{max}$:

$$
\tau_{acc}(p) < \tau_{diff}(p) << \tau_{AD}, \quad L_{acc}(p) < L_{diff}(p) << L_1. \tag{16}
$$

In panel (a) of Fig.3., we plot the characteristic length scales with the following parameters: $\beta = 1$, $M_s = 5$, $M_A = 4.56$, $c_s/c = 10^{-4}$, $V_A/c = 1.09\cdot 10^{-4}$, $\varepsilon_{inj} = 10^{-2}$. Throughout the entire momentum domain, L_{acc} exceeds L_{diff}. Given the finite system size where $L_1 \approx L_B$, particle momentum can reach up to p_{max}. Beyond p_{max}, particles cannot be further energized through DSA due to the absence of plasma waves with wavelengths larger than $\lambda_w \approx L_B$. In the remaining panels of Fig.3, we analyze the diffusion length scale by varying the sonic Mach number, M_s (panel (b)), the injection fraction into DSA, ε_{inj} (panel (c)) and plasma beta, β (panel (d)). As shown in panel (b), the diffusion length is longer for smaller M_s, reflecting a steeper slope of $f(x, p, t)$ beyond p_{inj}, which can reduce instabilities associated with high-energy particle streaming [11,36,37]. Similarly, panel (c) shows that the diffusion length depends on ε_{inj}. In panel (d), we observe that the diffusion length scale increases with β because higher β values indicate lower magnetic energy in plasma waves. Notably, the diffusion length converges at sufficiently high β

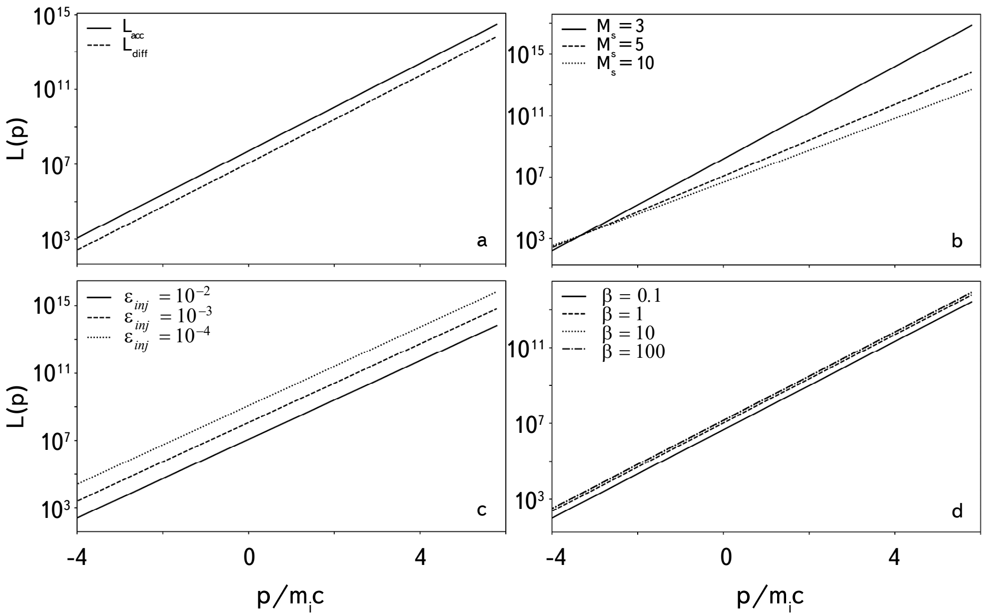

Fig.3. (a) Acceleration length scale (solid line) and diffusion length scale (dashed line) using the parameters with $\beta = 1$, $M_s = 5$, $M_A = 4.56$, $c_s / c = 10^{-4}$, $V_A / c = 1.09 \cdot 10^{-4}$, $\varepsilon_{inj} = 10^{-2}$; (b) Diffusion length scales with different sonic Mach numbers; (c) Diffusion length scales with different injection rates; (d) Diffusion length scales with different plasma betas. In panels (b) - (d), the same parameters used in panel (a) were employed except for the parameter being investigated for dependency.

($\beta >> 1$). This convergence occurs because in very weakly magnetized plasma, particle dynamics are largely influenced by self-excited magnetic fields due to high-energy particle streaming. This behavior aligns with 3-rd Eq. of (15), where for $\beta >> 1$, the diffusion length $L_{diff}(p)$ approximates:

$$L_{diff}(p) \sim \frac{D_1(p)}{U_1} \propto \frac{\Omega_i^{-1}}{M_A}. \tag{17}$$

Given $\Omega_i^{-1} \to \infty$ and $M_A \to \infty$ as $\beta \to \infty$, $L_{diff}(p)$ converges accordingly.

3.3. *Effects of shock parameters on the particle distribution function*. In this section, we present the analytic solution of the one-dimensional equation, including the time evolution of the particle distribution and its parameter dependencies such as the sonic Mach number M_s, the injection fraction ε_{inj}, plasma beta β, and the scale length L_B (or p_{max}). Such an investigation across the parameter space provides reliability to the analytic solution in tracking the time evolution of shock-accelerated particles. Table 1 summarizes the parameters used in this paper. Velocities are expressed in units of the speed of light c, and the scale length L_B, is normalized by $10^2\, r_{i,th}$, considering that plasma processes at the shock structure could pre-accelerate particles up to $pc/eB_0 \sim 10^2\, r_{i,th}$ [13-15].

Table 1

PARAMETERS USED IN THIS WORK.

Case 1 is the fiducial case and the remaining cases are performed for comparison. Groups for particular parameter dependence are summarized as follows: (L_B: Case1, Case2, Case3); (M_s: Case1, Case4, Case5); (ε_{inj} : Case1, Case6, Case7); (β: Case1, Case8, Case9, Case10).

	β	M_s	M_A	c_s/c	V_A/c	ε_{inj}	$L_B/(10^2 r_{i,th})$
Case1	1	5	4.56	10^{-4}	$1.09 \cdot 10^{-4}$	10^{-2}	10^3
Case2	1	5	4.56	10^{-4}	$1.09 \cdot 10^{-4}$	10^{-2}	10^5
Case3	1	5	4.56	10^{-4}	$1.09 \cdot 10^{-4}$	10^{-2}	10^{10}
Case4	1	3	2.74	10^{-4}	$1.09 \cdot 10^{-4}$	10^{-2}	10^{10}
Case5	1	10	9.13	10^{-4}	$1.09 \cdot 10^{-4}$	10^{-2}	10^{10}
Case6	1	5	4.56	10^{-4}	$1.09 \cdot 10^{-4}$	10^{-3}	10^{10}
Case7	1	5	4.56	10^{-4}	$1.09 \cdot 10^{-4}$	10^{-4}	10^{10}
Case8	0.1	5	1.44	10^{-4}	$3.45 \cdot 10^{-4}$	10^{-2}	10^3
Case9	10	5	14.42	10^{-4}	$3.45 \cdot 10^{-5}$	10^{-2}	10^3
Case10	100	5	45.64	10^{-4}	$1.09 \cdot 10^{-5}$	10^{-2}	10^3

We first examine the time evolution of the particle distribution function at the shock front shown in Fig.4. Each line in the plot represents a time interval of 250 Ω_i^{-1}, which is sufficient to capture the plasma processes of DSA [13,14]. While the slope of the distribution function remains constant, momentum diffusion is observed as a consequence of continuous energy injection from the source term, $s(r,p,t)$. At $t = t_3$, particles accumulate near $p/m_i c \sim 10^3$ due to the limited scale of the magnetic field size L_B in the shock upstream. Such particles could escape from the shock structure and be observed as galactic or extragalactic cosmic rays.

We next investigate how the particle distribution function at the shock front depends on the parameters (i.e., M_s, ε_{inj} , β, L_B). Fig.5 displays the momentum distribution functions at the shock front at $t = t_1 = 500\Omega_i^{-1}$ with a wide range of parameters. The panels illustrate that M_s and ε_{inj} affect the slope and normalization of the particle distribution function, respectively, as shown in panels (a) and (b), especially when the magnetic scale L_B is sufficiently large. The dependence on L_B shown in panel (c) indicates that the spectra with larger L_B can extend to higher momenta. We particularly focus on the dependence of β with the same L_B. With the same system size, the maximum momentum gained via DSA is proportional to the magnetic field because the gyroradius of particles increases with decreasing magnetic field strength. The time-evolved spectra with different values of plasma beta shown in panel (d) are consistent with this interpretation. If the system size and the wavelength of upstream waves were infinite, such beta dependence would not be observed.

3.4. *Effects of pre-accelerated particles*. We now expand the analytic solution to include pre-accelerated particles influenced by shocks or turbulence. These pre-accelerated particles, following power-law distribution, can undergo

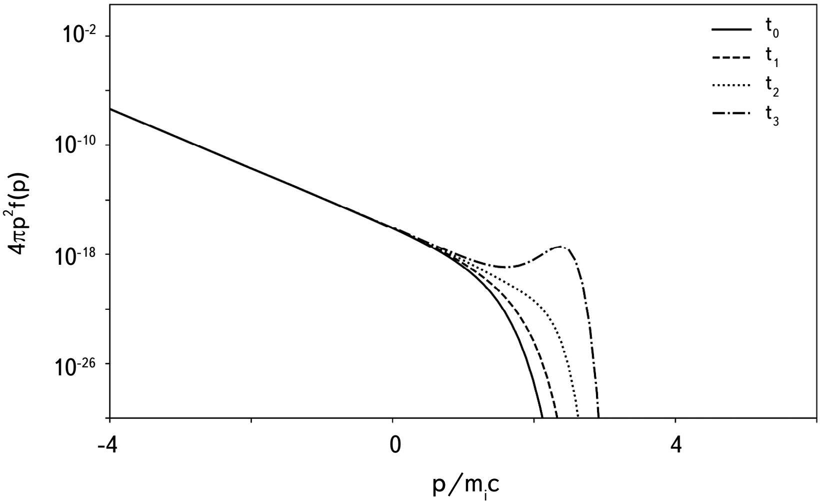

Fig.4. Time evolution of the particle distribution function at the shock front (Case 1 in Table 1). The plots are shown from $t_0 = 250\,\Omega_i^{-1}$ to $t_3 = 1000\,\Omega_i^{-1}$ with a time interval of $250\,\Omega_i^{-1}$.

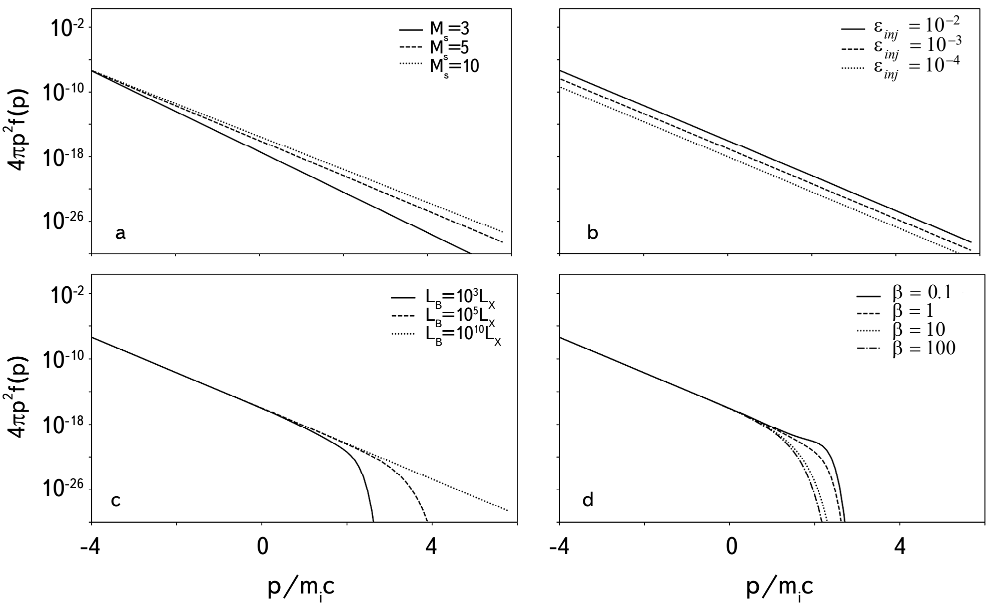

Fig.5. (a) Dependence on the sonic Mach number; (b) Dependence on the injection fraction; (c) Dependence on the magnetic field size; (d) Dependence on the plasma beta. The model information is provided in Table 1. Note that the particle distribution functions are measured at the shock front.

further acceleration through DSA [39,40]. The initial particle distribution, including the shock-accelerated particle distribution, $\tilde{f}(r, p, t=0)$, can be summarized as follows:

$$
\begin{aligned}
&Q_{pre}(r) = \varepsilon_{pre}\, n_{i,0} U_1 \exp\left(-\frac{2r}{L_B}\right), \\
&f_{pre}(r, p, t=0) = \frac{Q_{pre}(r)}{4\pi U_1 p_{inj}^3}\left(\frac{p}{p_{inj}}\right)^{-\tilde{q}} = \frac{\varepsilon_{pre}\, n_{i,0}}{4\pi\, p_{inj}^3}\exp\left(-\frac{2r}{L_B}\right)\left(\frac{p}{p_{inj}}\right)^{-\tilde{q}}, \\
&\tilde{f}(r, p, t=0) = \frac{Q_{inj}(r)}{4\pi U_1 p_{inj}^3}\left(\frac{p}{p_{inj}}\right)^{-q} + qp^{-q}\int_{p_{inj}}^{p} p'^{q-1} f_{pre}(r, p, t=0)\, dp' \\
&= \frac{Q_{inj}(r)}{4\pi U_1 p_{inj}^3}\left(\frac{p}{p_{inj}}\right)^{-q} + \frac{q}{(q-\tilde{q})}\left(1-\left(\frac{p}{p_{inj}}\right)^{-(q-\tilde{q})}\right)\frac{Q_{pre}(r)}{4\pi U_1 p_{inj}^3}\left(\frac{p}{p_{inj}}\right)^{-\tilde{q}},
\end{aligned}
\tag{18}
$$

where ε_{pre} is a parameter that determines the normalization of the pre-accelerated distribution, $f_{pre}(r, p, t=0)$. We particularly consider the cases where $q \neq \tilde{q}$. For $q < \tilde{q}$, the pre-accelerated distribution is steeper than the DSA slope, indicating that radiative or advection losses dominate over diffusion processes in confining particles near the shock surface. For $q > \tilde{q}$, on the other hand, strong turbulence exists to confine the pre-accelerated particles.

Using the parameter set from Case 1 in Table 1, we examined the impact of pre-accelerated particles on the time evolution of the particle distribution function at the shock front by varying the parameters, $\tilde{q}$, and ε_{pre}. For reference, the particle distribution function generated by the shock with $M_s = 5$ exhibits the slope, $q = 4.17$. The dependence on the slope of pre-accelerated particles, $\tilde{q}$, is shown in Fig.6 for four different timesteps ($t = [t_0,\ t_3]$). Here, the normalization factor is assumed as $\varepsilon_{pre}/\varepsilon_{inj} = 10^{-1}$. The results demonstrate that the effects of pre-accelerated particles are significant when the pre-accelerated distribution has a flatter slope than the DSA slope ($q > \tilde{q}$). Conversely, when $q < \tilde{q}$, the contribution of pre-accelerated particles appears negligible. Consistently, the time-evolved particle distribution function exhibits a power-law slope q, independent of $\tilde{q}$, as shown in previous studies [40]. Furthermore, the dependence on the number density of pre-accelerated particles, $\varepsilon_{pre}/\varepsilon_{inj}$, ranging from 10^{-3} to 10^{-1} with $\tilde{q} = 4$, is shown in Fig.7. As expected, $\varepsilon_{pre}/\varepsilon_{inj}$ influences the slope of the time-evolved distribution function.

The effects of pre-accelerated particles can be applied to analyze various astrophysical environments. For instance, in galaxy clusters, multiple shocks with different Mach numbers M_s are continuously induced due to gravitational collapse, enabling particle acceleration through these shocks. Ha et al. [24], for example,

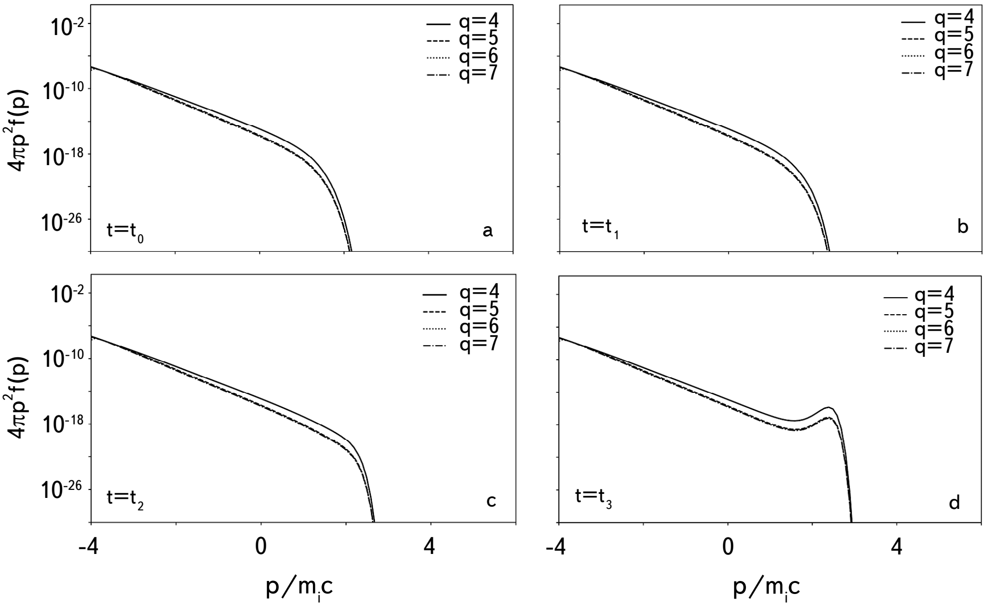

Fig.6. Time evolution of the particle distribution function at the shock front for different values of $\tilde{q}$, ranging from 4 to 7.

calculated accumulated cosmic ray spectra without considering the detailed time evolution of particle spectra. Furthermore, in star-forming galaxies, numerous shocks are generated by stellar winds and supernova remnants. We interpret that multiple acceleration processes could be active in such environments.

3.5. *Applications*. We interpret that the simple solution of the Fokker-Planck equation could be applicable to typical astrophysical shocks propagating in interplanetary, interstellar, and intracluster media. It is shown that this simple solution demonstrates reliable parameter dependence regarding particle acceleration via DSA. Once the shock parameters are obtained from observational data, the averaged particle distribution function over time and spatial domains can be computed. We provide an example assuming a spherically expanding shock with the shock surface, $A_s(t) \approx \Theta_s (r_s(t))^2$, where Θ_s is the solid angle and $r_s(t)$ is the mean shock propagation length at time t. Using the volume that the shock passed through, the volume-averaged distribution function, $\bar{f}(p)$, can be calculated as follows:

$$\bar{f}(p) \approx \frac{\sum_{t_i \in \{0, \tau_{acc}\}} A_s(t_i) U_2 f(r, p, t_i) \Delta t}{\sum_{t_i \in \{0, \tau_{acc}\}} A_s(t_i) U_2 \Delta t}. \tag{19}$$

For shocks in the interplanetary medium, for example, the shock parameters

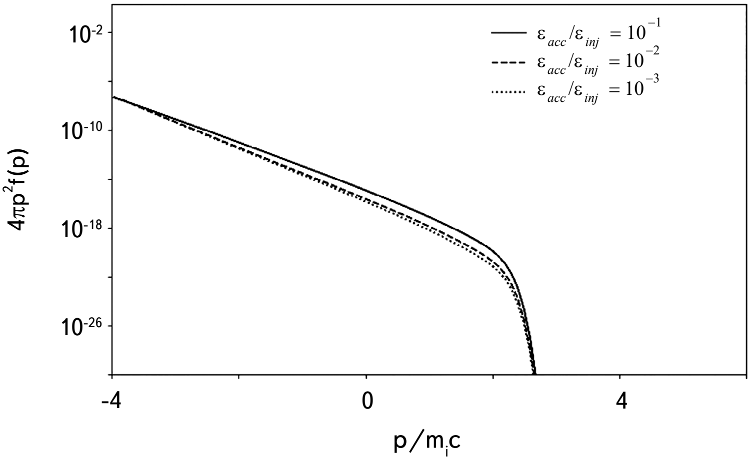

Fig.7. Effect of the fraction of pre-accelerated particles at the shock front, $\varepsilon_{pre}/\varepsilon_{inj}$ at $t = t_2$.

associated with coronal mass ejections (CME) can be obtained using publicly available IDL tools (such as the CME Analysis Tool; see [38]). By adopting the solid angle and speed of CME along with solar wind parameters such as density and magnetic fields, it is possible to estimate the averaged particle flux that could impact space weather.

The analytic solution can be also used to calculate high-energy radiation. For instance, hadronic γ-rays resulting from inelastic collisions between shock-accelerated protons and background thermal protons have been observed from supernova remnants [41,42] and star-forming galaxies [43-46]. Using the volume-averaged particle distribution function, $\bar{f}(p)$, with the dynamical timescale of the shock, τ_{dyn}, the number density of shock-accelerated particles, $N_i(E)$, can be computed as follows:

$$\frac{N_i(p)}{\tau_{dyn}} \sim \bar{f}(p), \quad N_i(E) = 4\pi p^2 N_i(p)\frac{dp}{dE}. \tag{20}$$

The pion source function is computed using the following equation proposed by Kelner et al. [47]:

$$\begin{aligned} N_\pi(E_\pi) &= \frac{cn_m}{K_\pi}\sigma_{pp}\left(m_i c^2 + \frac{E_\pi}{K_\pi}\right)N_i\left(m_i c^2 + \frac{E_\pi}{K_\pi}\right), \\ \sigma_{pp}(E) &= \left(34.3 + 1.88\theta + 0.25\theta^2\right)\left[1 - \left(\frac{E_{th}}{E}\right)^4\right]^2 mb, \end{aligned} \tag{21}$$

where $K_\pi \sim 0.17$ is the fraction of kinetic energy transferred from a proton to a pion, n_m is the number density of the background medium, and $\sigma_{pp}(E)$ is the cross-section of proton-proton collisions with $\theta = \ln(E/\mathrm{TeV})$, and the threshold energy, $E_{th} = 1.22\,\mathrm{GeV}$. Using the pion source function, the γ-ray production rate is then calculated as:

$$N_\gamma\left(E_\gamma\right) = 2\int_{E_{min}}^{\infty} \frac{N_\pi\left(E_\pi\right)}{\sqrt{E_\pi^2 - m_\pi^2 c^4}}\,dE_\pi\,, \tag{22}$$

where $E_{min} = E_\gamma + m_\pi^2 c^4 / \left(4E_\gamma\right)$ is the minimum energy of the produced γ-ray. Previous studies for estimating hadronic γ-ray from extragalactic sources typically assume a steady-state particle distribution function produced at shock to calculate the accumulated cosmic-ray flux during the system's dynamical timescales [26-29]. Since the simple model formulated in this paper includes the time evolution of the particle distribution function, it would be possible to improve such models by incorporating this time evolution. We will leave these investigations for future work.

4. *Summary*. In this study, we developed an analytic method using the one-dimensional Fokker-Planck equation to examine the time evolution of particle distribution functions at the shock front in the context of diffusive shock acceleration (DSA). We explored the impact of various shock parameters, including the sonic Mach number M_s, injection fraction ε_{inj}, plasma beta β, and scale length L_B. Our findings demonstrated the reliability of the analytic solution in capturing the time-dependent behavior of shock-accelerated particles, highlighting the interplay between advection, diffusion, and injection processes. The results showed that the momentum diffusion and particle accumulation are significantly influenced by these parameters, providing valuable insights into the particle acceleration mechanisms in astrophysical environments.

Additionally, we extended our model to include the effects of pre-accelerated particles, revealing that the initial distribution of these particles can alter the subsequent DSA process. We applied our model to various astrophysical scenarios, such as galaxy clusters and star-forming galaxies, where multiple shocks and turbulence are prevalent. Furthermore, the analytic solution was utilized to calculate high-energy radiation, specifically hadronic γ-rays produced by inelastic collisions between shock-accelerated protons and background thermal protons. By incorporating the time evolution of the particle distribution function, our model offers improvements over traditional steady-state approaches, laying the foundation for more accurate predictions of cosmic-ray spectra and high-energy radiation in diverse astrophysical contexts.

Acknowledgements. We thank to anonymous referees for providing constructive comments to improve the manuscript.

Korea Space Weather Center, Korea AeroSpace Administration, South Korea,
e-mail: hjhspace223@gmail.com

ПРОСТОЙ АНАЛИТИЧЕСКИЙ МЕТОД МОДЕЛИРОВАНИЯ УСКОРЕНИЯ ЧАСТИЦ В АСТРОФИЗИЧЕСКИХ УДАРНЫХ ВОЛНАХ С ИСПОЛЬЗОВАНИЕМ УРАВНЕНИЯ ФОККЕРА-ПЛАНКА

Дж.-Х.ХА

Ударные волны часто встречаются в астрофизических средах, и ускорение частиц в астрофизических ударных волнах связано с высокоэнергетическими явлениями. Механизм ускорения и временная эволюция функции распределения частиц тщательно изучены. В этой статье описывается простой аналитический метод с использованием одномерного уравнения Фоккера-Планка в режиме пробных частиц. Основное внимание уделено изучению эволюции функции распределения частиц в ударной волне вверх по потоку, особенно в сценариях, когда частицы могут двигаться к Земле вдоль открытых линий магнитного поля. В работе исследовано поведение аналитического решения в зависимости от различных параметров, характеризующих структуру ударной волны, таких как число Маха ударной волны, бета-плазма, доля инжекции в диффузное ускорение ударной волны и масштаб магнитного поля вверх по потоку. Как и ожидалось, поведение связано с турбулентностью вверх по потоку для диффузионного ускорения ударной волны. Кроме того, предварительно ускоренные частицы могут влиять на временную эволюцию распределения частиц только тогда, когда радиационные или адвективные потери достаточно малы для того, чтобы предварительно ускоренное распределение имело более плоский наклон степенного закона, чем наклон степенного закона, основанный на теории ускорения ударной волны. Кроме того, в статье приводится формула для сферически расширяющейся ударной волны и ее применение для расчета высокоэнергетического излучения в результате адронных взаимодействий. Предположено, что простой аналитический метод может быть эффективно использован для исследования различных типов астрофизических ударных волн, характеризующихся широким диапазоном параметров плазмы.

Ключевые слова: *ускорение частиц: высокоэнергетическое излучение: астрофизические ударные волны: уравнение Фоккера-Планка*

REFERENCES

1. *R.Vainio*, *L.Kocharov*, *T.Laitinen*, Astrophys. J., **528**, 1015, 2000.
2. *T.G.Forbes et al.*, Space Sci. Rev., **123**, 251, 2006.
3. *B.E.Gordon et al.*, Journal of Geophysical Research, **104**, 28263, 1999.
4. *S.P.Reynolds*, Astrophys. Space Sci., **336**, 257, 2011.
5. *G.Morlino*, Nuclear Instruments and Methods in Physics Research Section A: Accelerators, Spectrometers, Detectors and Associated Equipment, **720**, 70, 2013.
6. *A.Bell*, Brazilian Journal of Physics, **44**, 415, 2014.
7. *F.Miniati et al.*, Astrophys. J., **559**, 59, 2001.
8. *D.Ryu et al.*, Astrophys. J., **593**, 599, 2003.
9. *S.E.Hong et al.*, Astrophys. J., **785**, 133, 2014.
10. *J.-H.Ha*, *D.Ryu*, *H.Kang*, Astrophys. J., **857**, 26, 2018.
11. *A.R.Bell*, Mon. Not. Roy. Astron. Soc., **182**, 147, 1978.
12. *R.D.Blandford*, *J.P.Ostriker*, Astrophys. J. Lett., **221**, L29, 1978.
13. *D.Caprioli*, *A.Spitkovsky*, Astrophys. J., **783**, 91, 2014.
14. *J.Park*, *D.Caprioli*, *A.Spitkovsky*, Phys. Rev. Lett., **114**, 085003, 2015.
15. *J.-H.Ha et al.*, Astrophys. J., **864**, 105, 2018.
16. *J.-H.Ha et al.*, Astrophys. J., **915**, 18, 2021.
17. *A.Bodan et al.*, Astrophys. J., **847**, 71, 2017.
18. *R.Xu*, *D.Caprioli*, *A.Spitkovsky*, Astrophys. J. Lett., **897**, L41, 2020.
19. *H.Kang*, *T.W.Jones*, *U.D.J.Gieseler*, Astrophys. J., **579**, 337, 2002.
20. *D.Caprioli et al.*, Mon. Not. Roy. Astron. Soc., **407**, 1773, 2010.
21. *M.A.Malkov*, Astrophys. J., **485**, 638, 1997.
22. *E.Amano*, *P.Blasi*, Mon. Not. Roy. Astron. Soc., **364**, L76, 2005.
23. *H.Kang*, *D.Ryu*, Astrophys. J., **721**, 886, 2010.
24. *J.-H.Ha*, *D.Ryu*, *H.Kang*, Astrophys. J., **892**, 86, 2020.
25. *J.-H.Ha*, *D.Ryu*, *H.Kang*, Astrophys. J., **943**, 119, 2023.
26. *J.-H.Ha*, *D.Ryu*, *H.Kang*, Astrophys. J., **907**, 26, 2021.
27. *E.Peretti et al.*, Mon. Not. Roy. Astron. Soc., **487**, 168, 2019.
28. *E.Peretti et al.*, Mon. Not. Roy. Astron. Soc., 493, 5880, 2020.
29. *M.R.Krumholz et al.*, Mon. Not. Roy. Astron. Soc., **493**, 2817, 2020.
30. *P.H.Yoon*, Physics of Plasmas, **19**, 052301, 2012.
31. *P.H.Yoon*, Journal of Geophysical Research: Space Physics, **119**, 7074, 2014.
32. *V.Pierrard*, *M.Lazar*, S.Stverak, Frontiers in Astron. Space Sci., **9**, 892236, 2022.
33. *R.A.Lopez*, *S.M.Shaaban*, *M.Lazar*, J. Plasma Physics, **87**(3), 905870310, 2021.
34. *M.A.Malkov*, *H.J.Völk*, Advances in Space Research, **21**, 551, 1998.
35. *T.Amano*, *M.Hoshino*, Astrophys. J., **927**, 132, 2022.
36. *A.R.Bell*, Mon. Not. Roy. Astron. Soc., **353**, 550, 2004.
37. *M.A.Riquelme*, *A.Spitkovsky*, Astrophys. J., **694**, 626, 2009.
38. *G.Millward et al.*, Space Weather, **11**, 57, 2013.
39. *H.Kang*, *D.Ryu*, Astrophys. J., **734**, 18, 2011.

40. *P.Mukhopadhyay et al.*, Astrophys. J., **953,** 49, 2023.
41. *F.Acero et al.*, Astrophys. J. Suppl. Ser., **224**, 8, 2016.
42. *A.A.Abdo et al.*, Science, **327**, 1103, 2010.
43. *A.A.Abdo et al.*, Astrophys. J. Lett., **709**, L152, 2010.
44. *S.Abdollahi et al.*, Astrophys. J. Suppl. Ser., **247**, 33, 2020.
45. *A.Abramowski et al.*, Astrophys. J., **757**, 158, 2012.
46. *F.Acero et al.*, Science, **326**, 1080, 2009.
47. *S.R.Kelner*, *F.A.Aharonian*, *V.V.Bugayov*, Phys. Rev. D, **74**, 034018, 2006.

АСТРОФИЗИКА

ТОМ 67 АВГУСТ, 2024 ВЫПУСК 3

DOI: 10.54503/0571-7132-2024.67.3-359

LORENTZIAN CORRECTION FOR THE EVOLUTION OF THE CMB TEMPERATURE

A.NOVAIS, A.L.B.RIBEIRO

Received 26 May 2024
Accepted 26 August 2024

Observational evidence consistently shows that the universe is spatially flat and undergoes Lorentzian time dilation as a function of redshift. In combination, such discoveries suggest that a Minkowskian description of cosmology might be technically viable. The thermal evolution that transpires in a conformal spacetime is herein derived. The description is constrained by the energy conservation of a unified cosmic fluid. The resulting model puts forth a Lorentzian correction for the temperature of the CMB as a function of redshift, which improves current data fitting without adding any free parameter. Furthermore, it sheds light upon the early galaxy formation problem: our model predicts up to 0.86 Gyr older objects within the first two billion years of the structure evolution in the universe.

Keywords: *cosmology: CMB temperature: Minkowski spacetime: early galaxies*

1. *Introduction*. The Cosmic Microwave Background (CMB) indicates that space possesses but a vanishing curvature on cosmological scales [1,2]. Supernovae surveys [3] and recent studies on primordial quasars [4] also bring forth evidence that Lorentzian time dilation is an observable effect at high recession speeds. Such data suggest the possibility of a Minkowskian description of cosmology.

Over the course of the 20th century, cosmological models utilizing the Minkowskian background were developed as attempts at preserving the conformal quality of spacetime. Milne [5] proposed a thought experiment where a distribution of particles endowed with arbitrary velocities $0 < v < c$ around any observer inevitably produces a radial expansion scenario governed by the Hubble law. Infeld and Schild [6] generalized Milne's results, deriving multiple cases of conformal universes embedded in the Minkowskian metric and their respective equations of motion. The authors demonstrated that such cases were geometrically equivalent to Friedmann-Lemaître-Robertson-Walker (FLRW) universes.

Later, Tauber [7] explicitly solved Einstein's equations for the FLRW conformally flat-form metrics and for various types of equation of state. Endean [8] considered transformations of the FLRW metrics in the case of open three-dimensional space curvature, and also for closed three-dimensional space curvature [9]. Subsequently, Endean [10] found a possible solution to cosmological age and redshift-distance difficulties by applying the appropriate conformally flat spacetime coordinates to the standard solution of the field equations in a standard dust model closed universe. Ibison [11] showed that the metrics of all RW models ($k=0, \pm1$) are conformally flat; and Romero et al. [12] showed that any RW cosmological model is totally determined by the Weyl scalar field ϕ while spacetime remains fixed - ϕ may be considered as a gauging function determining the behaviour of clocks and measuring rods in a Minkowski spacetime. Finally, Lombriser [13] presents a formulation of cosmology in Minkowski spacetime, where the cosmological constant problem is absent.

All these results reiterate the relevance of studying cosmology in Minkowski spacetime. The aim of the present work is to develop a Lorentz-invariant description of cosmology, which can be understood as a conformal transformation of the FLRW metric into the Minkowski space with a cosmic fluid undergoing Hubble flow from the perspective of any given inertial observer. This path leads us to a Lorentzian correction for the evolution of the CMB temperature.

2. *Hubble flow in Minkowski space*. The Hubble law defines the proportionality between distance and velocity:

$$v = H_0 r \tag{1}$$

Considering that the resulting Hubble flow is subject to Lorentz transformations, one can determine the contracted length *dx*:

$$dx = dr\sqrt{1-\left(\frac{v}{c}\right)^2}\,. \tag{2}$$

Next, defining the Hubble radius R_H as the distance r where the recession velocity equals the speed of light, one obtains:

$$c = H_0 R_H\,, \tag{3}$$

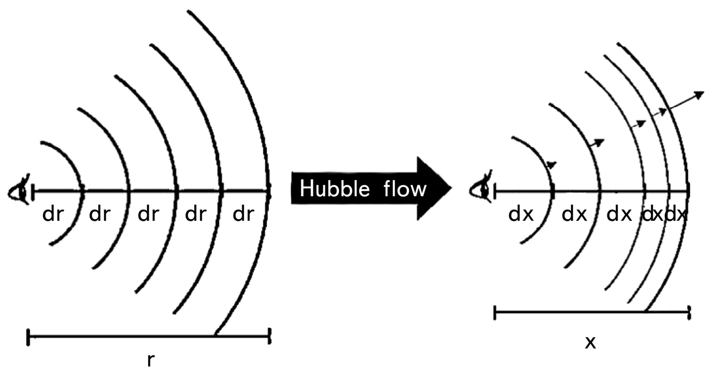

Fig.1. Length contraction of successive sections of the cosmic radius yielding a conformally transformed distance.

$$dx = dr\sqrt{1-\left(\frac{H_0 r}{H_0 R_H}\right)^2}\,, \quad dx = dr\sqrt{1-\left(\frac{r}{R_H}\right)^2}\,. \tag{4}$$

Thus, the transformed segment dx is expressed as a function of r. For simplicity purposes, it is beneficial to define the angle α, such that:

$$\sin\alpha \overset{\Delta}{=} \frac{r}{R_H}\,, \tag{5}$$

and Eq. (4) becomes:

$$dx = dr\sqrt{1-\sin^2\alpha}\,, \quad dx = dr\cos\alpha\,. \tag{6}$$

Finally, the sum of all consecutive segments dx yields the integrated distance x (Fig.1), observed in the expanding Minkowskian substratum:

$$x = \int_0^r dr\cos\alpha\,, \quad x = \frac{R_H}{2}\left(\sin\alpha\cos\alpha + \alpha\right). \tag{7}$$

In this description, the length contraction does not affect the recession velocity, since time dilation is also present in Minkowski spacetime, i.e., as a signal crosses a contracted length, its local time passage dt_L is slowed down by the same factor and the original speed is maintained.

$$\upsilon = \frac{dx}{dt_L} = \frac{dr\cos\alpha}{dt\cos\alpha} = \frac{dr}{dt}\,. \tag{8}$$

Therefore, the signal transmission is always conformal and instant velocities are preserved by the Lorentz transformations. This generates an important con-

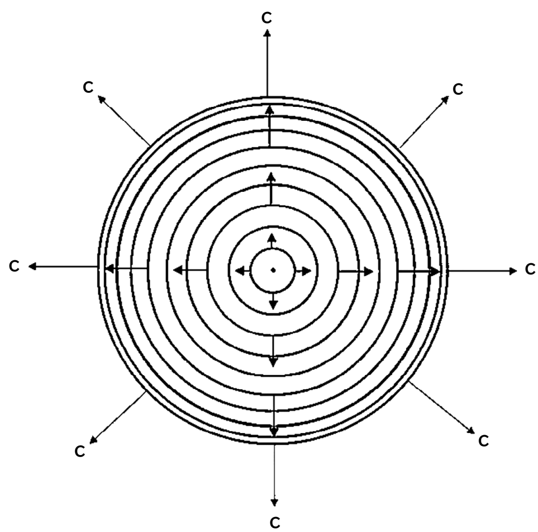

Fig.2. Expanding cosmic fluid in Minkowski space.

sequence for the Hubble flow equation, given that the speeds must be conserved when x replaces r as the observed distance. The result is a Lorentz-corrected Hubble parameter H_L.

The conformal condition equation is:

$$H_0 r = H_L x. \tag{9}$$

Introducing the transformed radius x obtained in (7) and isolating H_L:

$$H_L = H_0 \frac{2r}{R_H(\sin\alpha\cos\alpha + \alpha)}.$$

Finally, using the definition of $\sin\alpha$ given by (5):

$$H_L = H_0 \frac{2\sin\alpha}{(\sin\alpha\cos\alpha + \alpha)}. \tag{10}$$

Such relation determines that, at any given time, the Lorentz-corrected Hubble parameter H_L is not constant for the entire cosmological radius, but gently ascends with the distance, i.e., with α and the proximity to the horizon. H_0, in turn, is a temporal function that continuously declines with the expansion of the universe, as R_H increases, as we can see by rearranging (3):

$$H_0(t) = \frac{c}{R_H(t)}. \tag{11}$$

Moreover, since the Hubble radius always expands at the speed of light:

$$R_H = ct. \tag{12}$$

It is clear from this equation that the Minkowskian description of a unified cosmic fluid (Fig.2) shall carry fundamental similarities to the $R_h = ct$ model put forth by Melia and Shevchuk [14], albeit utilizing different metrics.

Substituting (12) in (11), one gets:

$$H_0 = \frac{1}{t}. \tag{13}$$

Therefore, in this work's description, hereon named ZEUS (Zero-Energy Unified Substratum), the age of the universe measured by the clock of the observer is always equal to the inverse of the Hubble constant H_0 at that epoch. In consonance with the cosmological principle, this fundamental property is equally valid for all inertial observers at any given era, dismissing the need for a cosmic reference frame and resolving the present-time age coincidence problem [15]. Next, we present a new perspective on the early structure formation problem according to ZEUS.

3. *Time dilation and a new perspective on the early galaxy problem*. From the definition of $\sin\alpha$ and H_0, it is straightforward to show that the Hubble flow does not alter the angle α of a receding object over time, which

means that the Lorentz contraction creates a fixed radial gradient in α -space, which persists throughout cosmic expansion history.

$$\frac{d\sin\alpha}{dt} = 0. \tag{14}$$

In Minkowski coordinates, the total time dilation perceived by an observer receiving signals from a receding source is the combination of the Lorentzian γ - here treated as $1/\cos\alpha$ - due to the velocity itself, and an extra factor $(1+\beta)$ - here expressed as $(1+\sin\alpha)$ - due to the continuous increase in separation.

$$\frac{dt_0}{dt_L} = \frac{(1+\sin\alpha)}{\cos\alpha}. \tag{15}$$

One can also express the term $(1+z)$ as a function of α, arriving at the conclusion that the relativistic Doppler redshift is the exact manifestation of the time dilation.

$$1+z = \frac{\sqrt{1+v/c}}{\sqrt{1-v/c}} = \frac{1+\sin\alpha}{\cos\alpha}. \tag{16}$$

Observational evidence supports $(1+z)$ as the time dilation term. Davis and Lineweaver [16] also concluded that a Lorentz-Minkowski type of expansion leads to this term, which is the same as the one given by the FLRW metrics. They proceeded, however, to calculate an incorrect luminosity distance, which was then rectified by Chodorowski [17], who showed that the magnitude-redshift diagram

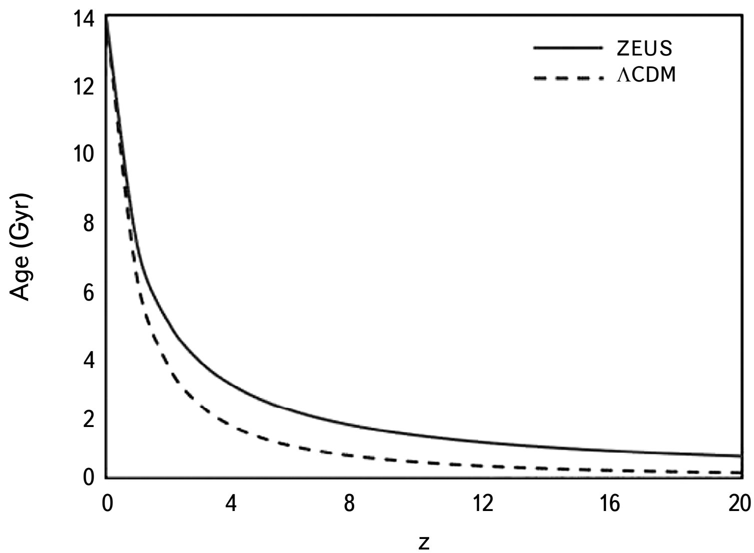

Fig.3. Time available for the evolution of a given source versus its redshift considering the time dilation effect. Solid curve is the ZEUS prediction and dashed curve is the ΛCDM correlation.

of a Minkowskian description is, in fact, remarkably close to the best ΛCDM fit.

A conundrum of crescent notoriety facing current cosmology is the observation of complex structure - quasars and mature galaxies - at precocious epochs of the cosmic evolution. This rapid emergence challenges the known structure formation mechanisms given by hierarchical models and appears to contradict theoretical constraints, such as the Eddington limit for black hole accretion [18-20].

The root of the conflict is the correlation between the redshift and the cosmic age given by the ΛCDM framework, i.e., if another valid cosmological description adjusts the age of the structures at the instant of emission, providing more time for them to have formed at the observed redshifts, the problem may be solved.

In the ZEUS description, since the redshift of a given source is fixed, it constitutes a constant in any time integration, hence this very factor is applicable to vast cosmic eras as well as infinitesimal intervals. Therefore, the age of the object in the ZEUS model is calculated by dividing the current age of the universe, here considered 14 Gyr, by the factor $(1+z)$.

$$\Delta t_{source} = \frac{\Delta t_{observer}}{(1+z)}, \quad Age_{source} = \frac{Age_{localUniverse}}{(1+z)}. \tag{17}$$

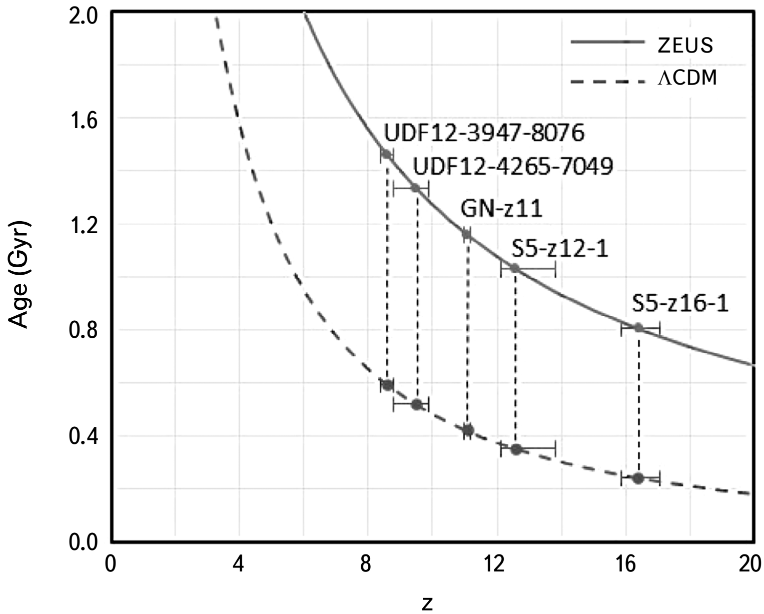

Fig.4. Same as Fig.3 but focusing upon the first two billion years of structure evolution. Observed galaxies from HST ([21,22]) and JWST ([23]), are projected onto ΛCDM and ZEUS timelines.

In contrast, the ΛCDM evolution presents transition phases that render the age-redshift correlation more complex and time-compressed, as shown in Fig.3. Fig.4 then zooms into the first two billion years of the structure evolution in order to highlight the significant difference in the age-versus-redshift curves. We show objects observed by HST and JWST that are 0.56 to 0.86 Gyr older in ZEUS than in the ΛCDM model. The early galaxy formation problem is alleviated within the ZEUS description for it grants more time for the galaxies and quasars to develop.

4. *Energy conservation*. In this section, the dynamics of the ZEUS model is explored. It is based upon the hypothesis that the total energy of the unified cosmic substratum is always zero. It is important to emphasize that the universe is not filled with a single fluid, but the mixture of radiation, baryons, and some manifestation of dark matter and dark energy, evolving under the zero energy condition:

$$\sum \rho_i + 3\sum p_i = 0. \tag{18}$$

This premise is similar to the unified medium with zero active mass and cosmic equation of state $p/\rho = -1/3$ proposed by [14] in the FLRW metric. Here, however, the Lorentzian correction applied to the Hubble flow in Minkowski spacetime leads to an energy density gradient along cosmic distances which is more descriptive of some CMB features, e.g., the high entropy density and the temperature evolution with redshift (see Section V).

First, from a mechanical perspective, the relativistic kinetic energy, written in terms of α, is given by:

$$K = m_0 c^2 \left(\frac{1}{\sqrt{1-(v/c)^2}} - 1 \right) = \frac{m_0 v^2}{\sin^2\alpha} \left(\frac{1}{\cos\alpha} - 1 \right), \quad K = \frac{m_0 v^2}{\cos\alpha (1+\cos\alpha)}. \tag{19}$$

Next, introducing the relativistic potential energy produced by the gravitational field of a sphere centered at the inertial observer with transformed radius x and average energy density ρ:

$$P = -\frac{8\pi G \rho x^2 m_0}{3c^2 \cos\alpha (1+\cos\alpha)}. \tag{20}$$

In agreement with the observed spatial flatness, the total mechanical energy of free particles that move exclusively due to the Hubble flow is considered to be zero:

$$\frac{m_0 v^2}{\cos\alpha(1+\cos\alpha)} - \frac{8\pi G \rho x^2 m_0}{3c^2 \cos\alpha(1+\cos\alpha)} = 0, \quad v^2 = \frac{8\pi G \rho x^2}{3c^2}. \tag{21}$$

Next, expressing the Hubble law:

$$H_L^2 x^2 = \frac{8\pi G \rho x^2}{3c^2}, \quad H_L^2 = \frac{8\pi G \rho}{3c^2}. \tag{22}$$

This result is analogous to the first Friedmann equation for a flat space with total energy density equal to the critical value and vanishing cosmological constant. The key distinction is that the Minkowskian coordinates produce a Lorentz-corrected Hubble parameter H_L, which slightly grows with distance. This means that the average energy density ρ of the cosmic sphere also presents a radial gradient at any given point in time. This can be demonstrated by taking (22) and substituting the H_L obtained in (10):

$$H_0^2 \frac{4\sin^2\alpha}{(\sin\alpha\cos\alpha+\alpha)^2} = \frac{8\pi G\rho}{3c^2}, \quad \rho = \frac{3c^2}{8\pi G} H_0^2 \frac{4\sin^2\alpha}{(\sin\alpha\cos\alpha+\alpha)^2}. \tag{23}$$

At the limit $\alpha \to 0$, where the small-angle approximation ($\sin\alpha \to \alpha$ and $\cos\alpha \to 1$) is applicable, one can calculate the energy density in the spatial vicinity of the observer:

$$\rho_0 = \frac{3c^2}{8\pi G} H_0^2 \tag{24}$$

$$\rho = \rho_0 \frac{4\sin^2\alpha}{(\sin\alpha\cos\alpha+\alpha)^2}. \tag{25}$$

Note that this expression determines the average density of the entire cosmic sphere from $\alpha = 0$ up to an α of interest. The differential energy density ε at α itself is the increment of the total energy of the sphere dU with an increment of the volume dV.

$$V = \frac{4}{3}\pi x^3. \tag{26}$$

Applying the expression of x obtained in (7):

$$V = \frac{\pi}{6} R_H^3 (\sin\alpha\cos\alpha+\alpha)^3, \tag{27}$$

and differentiating with respect to α:

$$\frac{dV}{d\alpha} = \pi R_H^3 \cos^2\alpha (\sin\alpha\cos\alpha+\alpha)^2. \tag{28}$$

Next, defining the internal energy U:

$$U = \rho V. \tag{29}$$

Which can be calculated by employing Eqs. (23) and (27) for ρ and V:

$$U = \frac{2}{3}\pi R_H^3 \rho_0 \sin^2\alpha (\sin\alpha\cos\alpha+\alpha), \tag{30}$$

and differentiating with respect to α:

$$\frac{dU}{d\alpha} = \frac{4}{3}\pi R_H^3 \rho_0 \sin\alpha\cos\alpha (2\sin\alpha\cos\alpha+\alpha). \tag{31}$$

One may finally determine the differential energy density ε at an α of interest:

$$\varepsilon = \frac{dU}{dV} = \frac{dU/d\alpha}{dV/d\alpha} \tag{32}$$

$$\varepsilon = \rho_0 \left[\frac{4}{3} \frac{\sin\alpha\left(2\sin\alpha\cos\alpha + \alpha\right)}{\cos\alpha\left(\sin\alpha\cos\alpha + \alpha\right)^2} \right]. \tag{33}$$

For notation simplicity, the term in square brackets is hereon denoted by ξ:

$$\xi = \frac{4}{3} \frac{\sin\alpha\left(2\sin\alpha\cos\alpha + \alpha\right)}{\cos\alpha\left(\sin\alpha\cos\alpha + \alpha\right)^2} \tag{34}$$

$$\varepsilon = \rho_0 \xi \tag{35}$$

Such gradient may have measurable implications for the temperature of the CMB, as studied in the next section.

5. *Temperature of the CMB*. The linear $T_{CMB}(z)$ is a property of standard adiabatic models that presuppose homogeneity and isotropy, such as ΛCDM.

$$T_{CMB}(z) = T_0(1+z). \tag{36}$$

Such proportionality is not bound to a particular metric theory when assuming that the cosmos expands isotropically, photon has no mass, the CMB radiation is thermal and the first law of thermodynamics is true [24]. However, a departure from linearity would require important and hard to detect distortions in the Planck spectrum of the CMB [25], which could be used to constrain alternative scenarios, e.g., cases where photons are either created or destroyed, as explored by Lima et al. [26], or modifications of gravity via the presence of a scalar field with a multiplicative coupling to the electromagnetic Lagrangian [27]. At present, there appears to be no inconsistency of the $T_{CMB}(z)$ data with the ΛCDM model [e.g. 28]. An extensive program of experiments based on new technologies will be able to detect minimal distortions in the energy spectrum of the CMB in the near future [29].

A different approach to study the evolution of the CMB temperature is to introduce a Lorentzian correction in the $T_{CMB}(z)$ function. In this case, the universe would be strictly flat, with a unified fluid describing its contents at all times. The aim of this work is to show that a Minkowskian description of cosmology, where the thermal evolution takes place in a conformal spacetime, can improve the data fitting of $T_{CMB}(z)$ for current datasets. This has important consequences for flatness tests and the foundations of cosmology.

While each component of the ΛCDM model behaves in a particular manner in terms of $\rho_i(t)$, in the ZEUS description, the energy density of the unified cosmic fluid possesses a universal behavior: it decreases with the square of the proper time ($\rho_0 \propto 1/t^2$). The second difference is the spatial gradient, which we characterized in the previous section with the term ξ.

$$\varepsilon = \rho_0(t)\xi(\alpha), \quad \varepsilon = \frac{3c^2}{8\pi G}\frac{1}{t^2}\xi(\alpha). \tag{37}$$

Equipped with this cosmic energy profile across time and space, one can now tell the story of the CMB from the ZEUS model's perspective, including its interaction with structures at their respective redshifts and the resulting perception of the observer, once time dilation is taken into account.

In the beginning (t ~0), the temperature of the unified cosmic fluid is far too great around the observer (and even greater at higher values of α) for any nucleon to form. One can directly express the temperature as a function of time by invoking the Stefan-Boltzmann law.

$$T = (\sigma\varepsilon)^{1/4}, \quad T = (\sigma\rho_0)^{1/4}\xi^{1/4}, \quad T = T_0\,\xi^{1/4}. \tag{38}$$

where ξ is a spatial function and T_0 is a temporal function:

$$T_0(t) = (\sigma\rho_0)^{1/4} = \left(\sigma\frac{3c^2}{8\pi G}\right)^{1/4}\frac{1}{t^{1/2}}. \tag{39}$$

Therefore, the local temperature decreases monotonically. With time, the local temperature of the cosmic fluid eventually drops sufficiently to enable the primordial nucleosynthesis. Given yet more time, the plasma decoupling also takes place. However, since the universe was far smaller and the photons always travel conformally in Minkowskian coordinates, those first local photons are not the ones received at the present time.

Referring to equation (38), for every value of T_0 there can be found a value of $\xi^{1/4}$ that produces the temperature at which recombination takes place (any arbitrary value is possible, given that ξ tends to infinity at the horizon). As T_0 decreases monotonically over time, this Surface of Last Scattering (SLS) must occupy greater and greater values of ξ, i.e., it advances ever closer to the horizon in α -space.

Next, to understand how the CMB radiation interacts with the intervening galaxies between the SLS and the observer, as well as how the interaction signal is measured, two factors must be considered. First, as discussed in the previous section, the observed energy density of a given region of the cosmic fluid is affected by the total Lorentzian time dilation, which inserts a $1/(1+z)$ factor to each time contribution. Second, in the CMB analysis, the primary emission surface (the SLS) is far out close to the horizon, meaning that any galaxy travels towards the CMB photons as it recedes from the observer, i.e., a blueshift is expected in this interaction when compared to the CMB energy density perceived by the static observer. This blueshift can be readily determined, since it is the inverse of the observed galaxy's redshift. Such mechanism adds yet another $1/(1+z)$ factor to the proper time. Hence, the total ρ_0 time correction now becomes:

$$\rho_{0CMB} \propto \frac{3c^2}{8\pi G}\left[\frac{(1+z)(1+z)}{t}\right]^2 \tag{40}$$

$$\rho_{0CMB} \propto \rho_0(1+z)^4\,, \quad \varepsilon_{CMB} \propto \rho_0(1+z)^4\xi \tag{41}$$

$$T_{CMB} = (\sigma\varepsilon_{CMB})^{1/4}\,, \quad T_{CMB} = (\sigma\rho_0)^{1/4}(1+z)\xi^{1/4}\,, \quad T_{CMB} = T_0(1+z)\xi^{1/4}\,. \tag{42}$$

It is remarkable that alternative perspectives of cosmology, based on different coordinates, timelines, redshift interpretations and photonic histories, provide such similar predictions for the $T_{CMB}(z)$. This reinforces the idea that, in a flat universe, which is clearly endowed with time dilation, the Minkowskian description of cosmological phenomena should be technically viable.

From the observational standpoint, at low redshifts ($0<z<1$), the thermal Sunyaev-Zeldovich (tSZ) effect can be employed as a cosmic thermometer (see [30-32]). Fig.5 shows that the FLRW linear prediction and the ZEUS curve are extremely similar along this range and both are good fits to the presently available datapoints.

As more profound redshifts are probed, different estimation techniques are required. Multiple studies rely upon atomic and molecular fine-structure levels

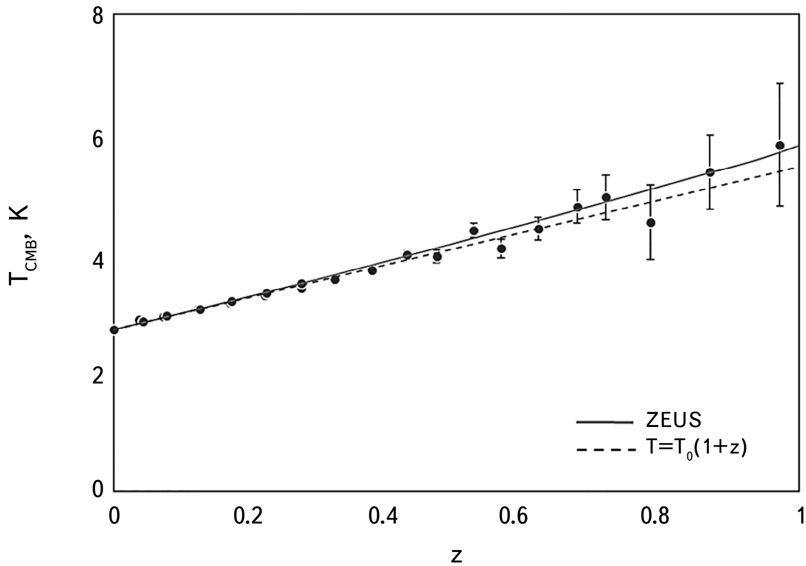

Fig.5. Circles are the results from [33,34] based on Planck map data and SZ effect at $z<1$. Dashed line shows the FLRW linear prediction with $\chi^2_{FLRW}=0.121$. Solid curve is the ZEUS prediction with $\chi^2_{ZEUS}=0.118$.

observed in the absorption spectra of quasars. This method depends upon free parameters associated with local physical conditions, such as kinetic temperature, UV background intensity, gas number density, collisional corrections, etc [e.g. 44].

In order to assess the predictive potential of the ZEUS description, we first gathered in Fig.6 the data sources in the redshift range $2 < z < 3.5$ that utilize atomic carbon fine-structure levels. Despite the large error bars, early signs of a tendency may be observed: at higher redshifts, the datapoints tend to land above the $T_0(1+z)$ line. As a result, the ZEUS fit ($\chi^2 = 0.431$) is even better than the FLRW linear relation ($\chi^2 = 1.636$).

Although the case of CO rotational levels excitation poses a greater statistical challenge, due to the low probability of detection and the ongoing debate on the required corrections, we incorporated the six results originally obtained by [40-42] in Fig.7. The cumulative result shows that the ZEUS fit ($\chi^2 = 1.500$) has good potential when compared with the FLRW fit ($\chi^2 = 1.676$).

It is worth noting that other studies further correct the inferred $T_{CMB}(z)$ for the six CO datapoints, reasserting the sensitivity with respect to the assumptions about local physical conditions. For instance, Klimenko et al. [44] present adjusted temperatures, deriving a fit that is closer to the FLRW linear prediction. Maeder [45] further reduces the T_{CMB} estimates by assuming additional galactic corrections, rendering both FLRW and ZEUS utterly unfit. Clearly, a better grasp on the CO rotational levels methodology must be achieved. This includes a more profound

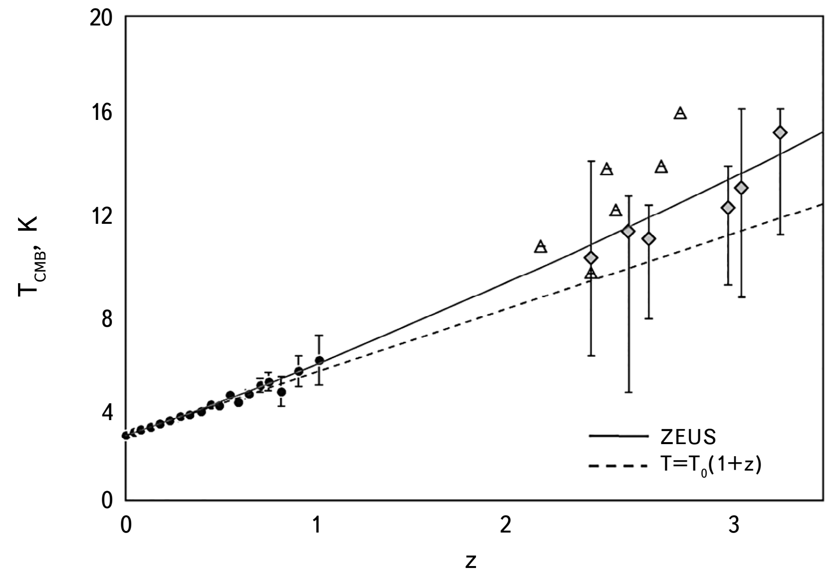

Fig.6. Same as Fig.5 plus literature data based on carbon fine-structure absorption lines represented as diamonds at $2 < z < 3.5$ ([35-39]). Triangles are upper bounds, not taken into account for $\chi^2\chi^2_{FLRW} = 1.636$ and $\chi^2_{ZEUS} = 0.431$.

understanding of local physical conditions as well as the detection of statistically robust samples.

Finally, Riechers et al. [43] reported a 1σ range measurement of the CMB temperature at $z = 6.34$. Using observations of submillimetre line absorption from the H_2O molecule, they arrived at a temperature estimation of 16.4 - 30.2 K. Most of the range lies above the $T_0(1+z)$ line and, as seen in Fig.8, both ZEUS and FLRW curves are able to accommodate the implied temperatures.

Larger datasets and greater refinement are required to expand the study. This work aims to showcase the fitting potential of a valid cosmological description in a developing observational field. The objective is to enrich future discussions, especially when it comes to the model-dependent aspects of the data treatment.

6. *Conclusion*. For over a century, the Minkowskian coordinates have been associated with specific motions of particles on restricted local scales. And correctly so: in a universe filled with energy and a spectrum of density fluctuations, one has no right to postulate *a priori* that a special case of flat space is applicable to cosmological scales. However, the scenario shifts in light of observational evidence, which reveals a vanishing global curvature.

In a coherent development, time dilation at high recession speeds (high z) has been empirically verified. If correctly studied, this temporal transformation is shown to exactly match the Lorentzian type for moving sources.

Put together, such discoveries indicate that a Minkowskian description of

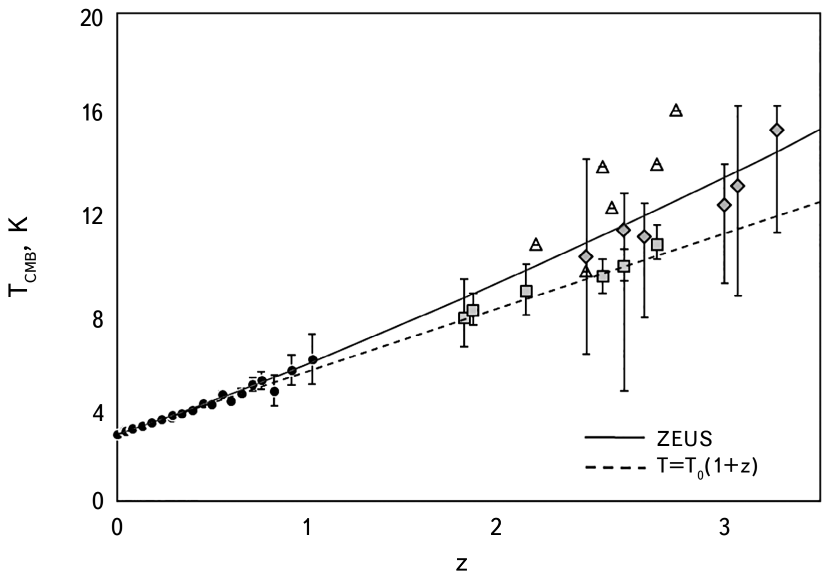

Fig.7. Same as Fig.6 plus literature data based on CO rotation excitation represented as squares [40-42]. $\chi^2_{FLRW} = 1.676$. $\chi^2_{ZEUS} = 1.500$.

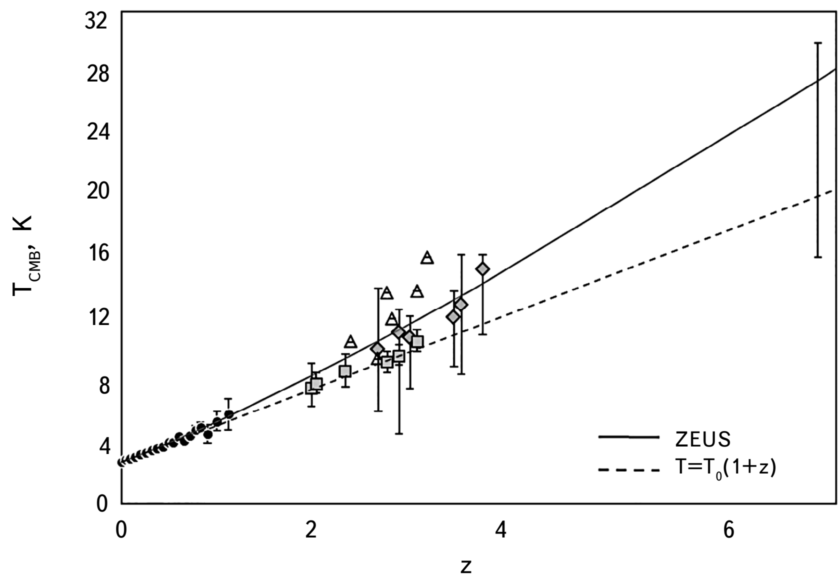

Fig.8. $T_{CMB}(z)$ ($0 < z < 6.5$), including the result obtained by [43] via H_2O absorption line.

cosmological phenomena should be technically viable. The question that remains is: can this description account for the evolution of the universe or is it limited to a kinematic snapshot of instant motions?

In the ZEUS description, the unified dynamics is granted by the postulate of total energy conservation. From this assumption (fully integrated with flatness), the thermal evolution of the universe is derived, and every instant of proper time can be described in a Lorentz-invariant framework.

In this introduction to a novel cosmological description, for pedagogical and conciseness purposes, the focus was set upon two macro-observables: firstly, the widely discussed problem of the early galaxies in ΛCDM emerging from JWST and HST data, which is mitigated by ZEUS. And secondly, the developing observational field of $T_{CMB}(z)$, still less discussed in the literature, and for which this work presents a unique, falsifiable and unprecedented approach with satisfactory fit to the current data, thus enriching the field's dialogue as it grows.

Nonetheless, before declaring the model as viable, a series of tests must be conducted where the current standard cosmology is already successful, e.g., Supernovae and Gamma-ray Bursts studies, Baryonic Acoustic Oscillations tests, structure formation modelling and Big Bang Nucleosynthesis, as well as presenting solutions to current conflicts, such as the Hubble tension, the initial entropy problem and dark sector candidates.

Acknowledgements. The authors are grateful to the referee Olga Sergeevna Sazhina for a detailed and constructive review, which has led to significant improvements in the manuscript. The authors also thank A.Kandus and G.Monerat for the useful suggestions. ALBR thanks CNPq, grant 316317/2021-7 and FAPESB INFRA PIE 0013/2016 for the support.

Laboratório de Astrofísica Teórica e Observacional, Universidade Estadual de Santa Cruz, Rodovia Jorge Amado, Ilheus, 45662-900, Bahia, Brazil, e-mail: arturnovais@gmail.com albr@uesc.com.br

ЛОРЕНЦ-ПОПРАВКА К ЭВОЛЮЦИИ ТЕМПЕРАТУРЫ РЕЛИКТОВОГО ИЗЛУЧЕНИЯ

А.НОВАИС, А.Л.Б.РИБЕЙРУ

Данные наблюдений последовательно показывают, что Вселенная пространственно плоская и испытывает лоренцево замедление времени с красным смещением. Эти результаты позволяют предположить, что описание космологии, данное Минковским, может быть технически жизнеспособным. В данном исследовании мы выводим тепловую эволюцию в конформном пространстве-времени, ограниченную законом сохранения энергии единой космической жидкости. Полученная модель дает поправку Лоренца для температуры космического микроволнового фонового излучения как функцию от красного смещения. Эта коррекция улучшает соответствие текущим данным без добавления свободных параметров. Кроме того, модель проливает свет на проблему раннего формирования галактик, предсказывая существование более старых объектов возрастом до 0.86 миллиарда лет в течение первых двух миллиардов лет структурной эволюции Вселенной.

Ключевые слова: *космология: температура космического микроволнового фонового излучения: пространство-время Минковского: ранние галактики*

REFERENCES

1. *N.Aghanim*, *Y.Akrami*, *M.Ashdown et al.*, Astron. Astrophys., **641**, A5, 2020.
2. *G.Efstathiou*, *S.Gratton*, Mon. Not. Roy. Astron. Soc. Lett., **496**, 91, 2020.

3. *A.G.Riess*, *A.V.Filippenko*, *D.C.Leonard et al.*, Astron. J., **114**, 722, 1997.
4. *G.F.Lewis*, *B.J.Brewer*, Nat. Astron, **7**, 1265, 2023.
5. *E.A.Milne*, Zeitschrift für Astrophysik **6**, 1, 1933.
6. *L.Infeld*, *A.Schild*, Phys. Rev., **68**(11-12), 250, 1945.
7. *G.E.Tauber*, J. Math. Phys., **8**, 118, 1967.
8. *G.Endean*, Astrophys. J., **434**, 397, 1994.
9. *G.Endean*, Mon. Not. Roy. Astron. Soc., **277**, 627, 1995.
10. *G.Endean*, Astrophys. J., **479**, 40, 1997.
11. *M.Ibison*, J. Math. Phys., **48**, 122501, 2007.
12. *C.Romero*, *J.B.Fonseca-Neto*, *M.L.Pucheu*, Foundations of Physics, **42**, 224, 2012.
13. *L.Lombriser*, Classical and Quantum Gravity, **49**, 155005, 2023.
14. *F.Melia*, *A.Shevchuk*, Mon. Not. Roy. Astron. Soc., **419**, 2579, 2012.
15. *M.Kutschera*, *M.A.Dyrda*, Phys. Pol. B, **38**(1), 215, 2007.
16. *T.M.Davis*, *C.H.Lineweaver*, Publ. Astron. Soc. Australia, **21**, 97, 2004.
17. *M.Chodorowski*, Publ. Astron. Soc. Australia, **22**, 287, 2005.
18. *B.Robertson*, Nat Astron, **7**, 611, 2023.
19. *F.Melia*, Astron. J., **147**, 120, 2014.
20. *F.Melia*, *T.M.McClintock*, Proc. R. Soc. A, 2015.
21. *P.A.Oesch*, *G.Brammer*, *P.G.Dokkum et al.*, Astrophys. J., **819**, 129, 2016.
22. *R.S.Ellis*, *R.J.McLure*, *J.S.Dunlop et al.*, Astrophys. J. Lett., **763**(1), 7, 2013.
23. *Y.Harikane*, *M.Ouchi*, *M.Oguri et al.*, Astrophys. J., **265**, 5, 2023.
24. *M.H.Abitbol*, *J.C.Hill*, *J.Chluba*, Astrophys. J., **893**(1), 18, 2020.
25. *J.Chluba*, Mon. Not. Roy. Astron. Soc., **443**(3), 1881, 2014.
26. *J.Lima*, *A.Silva*, *S.Viegas*, Mon. Not. Roy. Astron. Soc., **312**(4), 747, 2000.
27. *A.Hees*, *O.Minazzoli*, *J.Larena*, Phys. Rev. D, **90**(12), 124064, 2014.
28. *R.Arjona*, Journal of Cosmology and Astroparticle Physics, **2020**(08), 2020.
29. *A.Kogut*, *M.Abitbol*, *J.Chluba et al.*, American Astron. Soc., **51**, 2019.
30. *R.A.Sunyaev*, *Y.B.Zeldovich*, Astrophys. Space Sci., **7**(3), 1970.
31. *R.Fabbri*, *F.Melchiorri*, *V.Natale*, Astrophys. Space Sci., **59**, 223, 1978.
32. *Y.Rephaeli*, Astrophys. J., **241**, 858, 1980.
33. *G.Hurier*, *N.Aghanim*, *M.Douspis et al.*, Astron. Astrophys., **561**, 2014.
34. *I.Martino*, *R.Génova-Santos*, *F.Atrio-Barandela et al.*, Astrophys. J., **808**, 128, 2015.
35. *R.Srianand*, *P.Petitjean*, *C.Ledoux*, Nature, **408**, 931, 2000.
36. *P.Molaro*, *S.A.Levshakov*, *M.Dessauges-Zavadsky et al.*, Astron. Astrophys. Lett., **381**, 64, 2002.
37. *S.A.Balashev*, *A.V.Ivanchik*, *D.A.Varshalovich*, Astron. Lett., **36**, 761, 2010.
38. *R.A.Jorgenson*, *A.M.Wolfe*, *J.X.Prochaska*, Astrophys. J., **722**, 460, 2010.
39. *R.Guimaraes*, *P.Noterdaeme*, *P.Petitjean et al.*, Astron. J., **143**, 147, 2012.
40. *R.Srianand*, *P.Noterdaeme*, *C.Ledoux et al.*, Astron. Astrophys., **482**(3), 39, 2008.
41. *P.Noterdaeme*, *P.Petitjean*, *C.Ledoux et al.*, Astron. Astrophys., **523**(A80), 2010.
42. *P.Noterdaeme*, *P.Petitjean*, *R.Srianand et al.*, Astron. Astrophys., **526**(L7), 2011.
43. *D.A.Riechers*, *A.Weiss*, *F.Walter et al.*, Nature, **602**, 58, 2022.
44. *V.Klimenko*, *A.V.Ivanchik*, *P.Petitjean et al.*, Astron. Lett., **46**, 715, 2020.
45. *A.Maeder*, Astrophys. J., **847**(1), 65, 2017.

АСТРОФИЗИКА

ТОМ 67 АВГУСТ, 2024 ВЫПУСК 3

DOI: 10.54503/0571-7132-2024.67.3-375

METHANIMINE IN COOL COSMIC OBJECTS USING ACCURATE COLLISIONAL RATE COEFFICIENTS

S.CHANDRA[1], M.K.SHARMA[2]
Received 18 June 2024
Accepted 26 August 2024

Accurate collisional rate coefficients for collisional transitions between 15 rotational levels of methanimine, colliding with p-H_2 molecule, are available. Methanimine is a planar, asymmetric top molecule having electric dipole moment with components $\mu_a = 1.3396$ Debye and $\mu_b = 1.4461$ Debye, and thus, producing both the *a* and *b* type spectral lines of nearly equal intensities. Therefore, all the rotational levels need to be considered together. Between 15 rotational levels, 105 collisional transitions are considered in an investigation by others. We have discussed that each level is not connected with all others through the collisions, and therefore, there should be 77 instead of 105 collisional transitions between 15 levels of methanimine. With availability of accurate collisional rate coefficients, it is worth to perform the Sobolev analysis of methanimine. We have found six weak MASER transitions, 1_{10}-1_{11}, 2_{11}-2_{12}, 3_{12}-3_{13}, $4_{1.3}$-$4_{1.4}$, 3_{03}-2_{12} and $4_{0.4}$-$3_{1.3}$, and one transition 1_{11}-2_{02}, showing anomalous absorption. These seven lines may play important role for the methanimine.

Keywords: *ISM: molecules: methanimine: MASER action and radiative transfer*

1. *Introduction*. Methanimine (CH_2NH) is an important prebiotic molecules, as it is considered as precursor of glycine (NH_2CH_2COOH) [1,2]

$$CH_2NH \xrightarrow{2H} CH_3NH_2 \xrightarrow{CO_2} CH_2NH_2COOH .$$

According to Strecker's synthesis [3], the methanimine can be produced through the combination of ammonia (NH_3) [4] and formaldehyde (H_2CO) [5], which are well known abundant species in the interstellar medium (ISM):

$$NH_3 + H_2CO \rightarrow CH_2NH + H_2O .$$

Faure et al. [6] have calculated accurate collisional rate coefficients for collisional transitions between 15 rotational levels of methanimine due to collisions with p-H_2 molecule. They [6] have considered 105 collisional transitions between 15 levels, considering that each level is connected to all other levels through collisions. By considering the symmetries, we have discussed that there should be 77 instead of 105 collisional transitions between 15 levels of methanimine.

Gorski et al. [7] have discovered methanimine megamasers toward compact obscured galaxy nuclei at 5.29 GHz through the transition 1_{10}-1_{11}. As the accurate collisional rate coefficients are available, we have performed the Sobolev analysis of methanimine. Six weak MASER transitions, 1_{10}-1_{11}, 2_{11}-2_{12}, 3_{12}-3_{13}, $4_{1.3}$-$4_{1.4}$, 3_{03}-2_{12} and $4_{0.4}$-$3_{1.3}$, and one transition 1_{11}-2_{02}, showing anomalous absorption have been found. These seven lines may be found significant for the investigation of methanimine.

2. *Methanimine (CH_2NH)*. The methanimine is a planar asymmetric top molecule having electric dipole moment with components $\mu_a = 1.3396$ Debye and $\mu_b = 1.4461$ Debye [8]. Thus, it has both *a* and *b* type radiative transitions of nearly equal intensities. Godfrey et al. [9] have reported the first detection of methanimine in gas phase in the molecular cloud Sgr B2 towards the Galactic center. Subsequently, it has been found in Sgr B2 [10-15], in molecular cloud L183 [16], in Orion-KL nebula [17-19], in W51 [17,18], in Ori 3N, G34.3+0.15 [17] in G10.47+0.03, G34.3+0.2, G31.41+0.3, G19.6-0.23, NGC6334F, DR21(OH) [18], in G19.61- 0.23 [20], in IRC+10216 [21], and in ultra-luminous infrared galaxy Arp 220 [22]. Bourgalais et al. [23] have predicted the existence of methanimine in the atmosphere of Titan. The results of Yuen et al. [24] have supported the formation of methanimine in the massive star formation regions.

In the terrestrial laboratories, the methanimine has been analyzed from time to time [25-30]. The rotational and centrifugal distortion constants derived by Motoki et al. [29] are used in the present work for calculation of energies of rotational levels, and radiative transitions probabilities for the radiative transitions between the levels. Sharma et al. [31] have investigated analytically weak MASER action of 1_{10}-1_{11} transition of methanimine. Sil et al. [32] have performed the chemical modeling for prediction of abundances of aldimines and amines in hot cores. Luthra et al. [33] have predicted the gas-phase methanimine abundance in cold cores.

2.1. *Collisional transitions*. The 15 rotational levels considered by Faure et al. [6] and their energies are given in Table 1. The selection rules for the *J* for non-radiative (collisional) transitions are:

$$\Delta J = 0, \pm 1, \pm 2, \pm 3, ...$$

Table 1

LEVELS AND THEIR ENERGIES IN cm^{-1}

No.	Level	Energy	No.	Level	Energy	No.	Level	Energy
1	000	0.00	6	212	11.61	11	404	21.27
2	101	2.13	7	211	12.14	12	414	25.91
3	202	6.40	8	303	12.78	13	413	27.67
4	111	7.52	9	313	17.74	14	221	28.29
5	110	7.69	10	312	18.80	15	220	28.29

Let us consider the collisional transitions only for k_a, k_c levels. Each of the pseudo quantum number, k_a and k_c can independently assume even (e) and odd (o) positive integer values, including zero. When the electric dipole moment is along the a-axis of inertia, the following collisional transitions for k_ak_c are not allowed.

$$(e,o)\leftrightarrow(o,e) \qquad (e,e)\leftrightarrow(o,o) \tag{1}$$

$$(e,o)\leftrightarrow(o,o) \qquad (e,e)\leftrightarrow(o,e). \tag{2}$$

These rules divide the rotational levels into the ortho and para species. The allowed collisional transitions are:

$$(o,e)\leftrightarrow(o,o) \qquad (o,o)\leftrightarrow(o,o) \qquad (o,e)\leftrightarrow(o,e) \qquad (\text{Group I}) \tag{3}$$

$$(e,o)\leftrightarrow(e,e) \qquad (e,o)\leftrightarrow(e,o) \qquad (e,e)\leftrightarrow(e,e) \qquad (\text{Group II}) \tag{4}$$

The above can be verified from the papers published for a-type molecules. When the electric dipole moment is along the b-axis of inertia, the following collisional transitions for k_a, k_c are not allowed.

$$(e,o)\leftrightarrow(e,e) \qquad (o,e)\leftrightarrow(o,o) \tag{5}$$

$$(e,o)\leftrightarrow(o,o) \qquad (o,e)\leftrightarrow(e,e) \tag{6}$$

These rules divide the rotational levels into the ortho and para species. The allowed collisional transitions are:

$$(e,o)\leftrightarrow(o,e) \qquad (e,o)\leftrightarrow(e,o) \qquad (o,e)\leftrightarrow(o,e) \qquad (\text{Group III}) \tag{7}$$

$$(e,e)\leftrightarrow(o,o) \qquad (e,e)\leftrightarrow(e,e) \qquad (o,o)\leftrightarrow(o,o) \qquad (\text{Group IV}). \tag{8}$$

The above can be verified from the papers published for b-type molecules.

The present molecule methanimine has both a and b components of electric dipole moment. Consequently, the transitions (5) are allowed due to b component of dipole moment, and the transitions (1) are allowed due to a component of dipole moment. However, still the transitions (6) and transitions (2) are not allowed. These transitions (6 and 2) are the blank positions in Table 3.

Between these 15 levels, there are 35 radiative transitions (Table 2) and 77 collisional transitions (Table 3). In Tables 2 and 3, the first row indicates the upper level and the first column indicates the lower level of transition. Cross indicates transition between levels corresponding to the row and column of the cross. Table 3 obviously indicates that each level is not connected to other levels through collisions.

3. *Details of model*. For 15 levels, we have constituted 15 steady state statistical equilibrium equations, coupled with 35 equations of radiative transfer. The background of the cosmic object generating the lines is taken as the Cosmic Microwave Background (CMB), which corresponds to the background temperature

of 2.73 K. Hence, no spectral line is supposed to have excitation temperature less than 2.73 K. Further, details of the model is discussed by Chandra & Sharma

Table 2

RADIATIVE TRANSITIONS BETWEEN 15 LOWER ROTATIONAL LEVELS OF METHANIMINE. CROSS INDICATES TRANSITION BETWEEN LEVELS CORRESPONDING TO ROW AND COLUMN OF THE CROSS

	2	3	4	5	6	7	8	9	10	11	12	13	14	15
1	x		x											
2		x		x	x									x
3			x			x	x	x					x	
4				x	x									x
5						x							x	
6						x	x	x					x	
7									x					x
8									x	x	x			x
9									x	x	x			x
10												x	x	
11												x		
12												x		
13														
14														x

Table 3

COLLISIONAL TRANSITIONS BETWEEN 15 LOWER ROTATIONAL LEVELS OF METHANIMINE. CROSS INDICATES TRANSITION BETWEEN LEVELS CORRESPONDING TO ROW AND COLUMN OF THE CROSS

	2	3	4	5	6	7	8	9	10	11	12	13	14	15
1	x	x	x			x	x	x		x		x	x	x
2		x		x	x		x		x	x	x		x	x
3			x			x	x	x		x		x	x	x
4				x	x	x		x	x	x	x	x		x
5					x	x	x	x	x		x	x	x	
6						x	x	x	x		x	x	x	
7								x	x	x	x	x		x
8									x	x	x		x	x
9									x	x	x	x		x
10											x	x	x	
11												x	x	x
12												x	x	
13														x
14														x

[34] and Sharma, Chandra [35,36]. When the excitation temperature of a spectral line is less than 2.73 K, the situation is known as the anomalous absorption, i.e., the absorption against the CMB.

The required input data for the investigation are the radiative transition probabilities (Einstein A and B coefficients) and the collisional rate coefficients for the collisional transitions.

3.1. *Collisional rate coefficients*. Accurate collisional rate coefficients have been calculated under the CoupledStates (CS) approximation by Faure et al. [6]. Though these collisional rate coefficients are available for the kinetic temperature T up to 30 K, but considering the highest value (28.3 cm^{-1}) of energy, we have used their data for $T = 5$, 10, 15 K.

4. *Results and discussion*. On solving the set of statistical equilibrium equations coupled with the equations of radiative transfer (Sobolev analysis), we have obtained nonthermal population densities of the levels as a function of the density of colliding partner p-H_2, n_{H_2}, kinetic temperature T, and parameter $\gamma \left[= n_{mol}/(d\, v_r/dr)\right]$, where n_{mol} denotes the density of the methanimine, and $d\, v_r/dr$ the velocitygradient in the molecular region. The γ is used as a parameter in the investigation.

To make our results applicable to various types of cosmic objects, in the analysis, we have considered wide ranges of physical parameters. The molecular hydrogen density n_{H_2} is taken from 10^2 to 10^6 cm^{-3}; the kinetic temperatures T are taken 5, 10, 15 K. For γ, we have taken two values as 10^{-5} and 10^{-6} cm^{-3} (km/s)$^{-1}$ pc. However, in Fig.1, we have plotted results for $\gamma = 10^{-5}$ cm^{-3} (km/s)$^{-1}$ pc, as the results for the two sets are very close to each other.

The excitation temperature T_{ex} for a line between an upper level u and a lower level l is expressed as

$$T_{ex} = -\frac{\Delta E_{ul}}{k \ln\left(n_u g_l / n_l g_u\right)}.$$

where n denotes the population density, g the statistical weight, k the Boltzmann constant, and ΔE_{ul} the energy difference between the two levels.

For low density in a region, the collisional rates are very small as compared to the radiative transition rates, and the population densities of levels are governed by the radiative transitions. Therefore, the excitation temperature tends to the CMB temperature of 2.73 K.

One transition 1_{11}-2_{02} is found to show anomalous absorption i.e., the absorption against the CMB. Information about this transition is given in Table 4, where we have given the frequency, Einstein A coefficient, energy of upper level of transition, and radiative life-times of upper and lower levels of the transition. For this

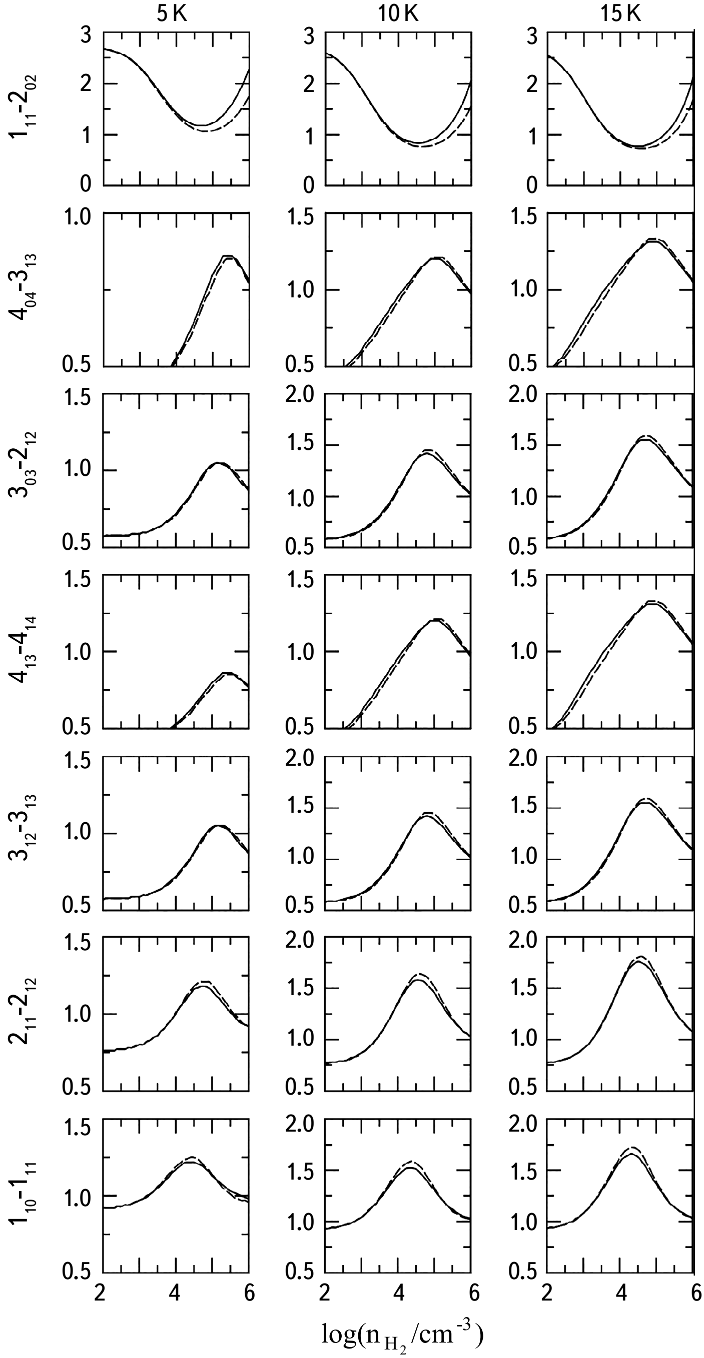

Fig.1 Variation of $n_u g_l/n g_u$ versus molecular hydrogen density n_{H_2} for six transitions 1_{10}-1_{11}, 2_{11}-2_{12}, 3_{12}-3_{13}, $4_{1.3}$-$4_{1.4}$, 3_{03}-2_{12} and $4_{0.4}$-$3_{1.3}$, and variation of excitation temperature T_{ex} (K) versus molecular hydrogen density n_{H_2} for the transition 1_{11}-2_{02}, for kinetic temperatures of 5, 10, 15 K (written at the top) for $\gamma = 10^{-5}$ cm^{-3} (km/s)$^{-1}$ pc. The solid line is for the present investigation. whereas the dotted line is for the transitions considered by [6].

Table 4

FREQUENCY ν, A COEFFICIENT A_{ul}, ENERGY E_u OF UPPER LEVEL, RADIATIVE LIFE-TIME t_u OF UPPER LEVEL AND t_l OF LOWER LEVEL FOR TRANSITIONS OF METHANIMINE

Transition	ν (MHz)	A_{ul} (s^{-1})	E_u (cm^{-1})	t_u (s)	t_l (s)
MASER lines					
$1_{1.0}$-$1_{1.1}$	5290.123	1.546E-09	7.695	1.77E+04	1.07E+04
$2_{1.1}$-$2_{1.2}$	15869.890	1.391E-08	12.137	1.31E+04	5.58E+03
$3_{1.2}$-$3_{1.3}$	31736.418	5.565E-08	18.798	7.56E+03	3.07E+03
$4_{1.3}$-$4_{1.4}$	52880.576	1.546E-07	27.674	4.09E+03	1.81E+03
$3_{0.3}$-$2_{1.2}$	35065.696	1.621E-07	12.777	1.59E+04	5.58E+03
$4_{0.4}$-$3_{1.3}$	105794.062	5.385E-06	21.267	6.31E+03	3.07E+03
Anomalous absorption line					
$1_{1.1}$-$2_{0.2}$	33704.842	1.63E-07	7.52	1.07E+04	5.73E+04

anomalous absorption transition, the variation of excitation temperature T_{ex} (K) versus the molecular hydrogen density n_{H_2} for the kinetic temperatures, written on the top, is shown in Fig.1, uppermost row.

As expected, Fig.1 (uppermost row) shows that with the decrease of density, the excitation temperature tends to the CBM temperature 2.73 K. The trough of the transition is found around $10^{4.5}$ cm^{-3}, which shifts towards the low density with the increase of kinetic temperature, as expected.

For the MASER action, population inversion ($n_u g_l / n_l g_u > 1$) between the upper level u and lower level l is required.

$$\frac{n_u g_l}{n_l g_u} > 1.$$

Further, the condition of larger radiative life-time of upper level as compared to that of the lower level is a favourable condition. In the present work, we have taken $n_u g_l / n_l g_u > 1.2$. It makes a little hard criteria for the MASER action. Six lines, 1_{10}-1_{11}, 2_{11}-2_{12}, 3_{12}-3_{13}, $4_{1.3}$-$4_{1.4}$, 3_{03}-2_{12} and $4_{0.4}$-$_{31.3}$, have been found to show the weak MASER action. Information about these transitions also is given in Table 4.

For these MASER transitions, the variation of $n_u g_l / n_l g_u$ versus molecular hydrogen density n_{H_2} for kinetic temperatures of 5, 10, 15 K, are given in Fig.1. MASER action is in the region having $n_u g_l / n_l g_u$ larger than 1. The peak of MASER line is found shifted towards the low density region with the increase kinetic temperature, as expected. The MASER action is found to decrease with the decrease of kinetic temperature. At large densities, the population inversion is destroyed by the collisions.

In their investigation, Faure et al. [6] considered 31 radiative transitions. They did not take four radiative transitions, 2_{20}-1_{01}, 2_{21}-2_{02}, 2_{20}-2_{21} and 2_{20}-3_{03}. Further, they assumed that each level is connected to all other levels through collisions. Thus, they have 105 collisional transitions, whereas in our investigation, there are 77 collisional transitions. The basis of our 77 collisional transitions is the consideration of the symmetries.

We have repeated our calculations for the transitions (31 radiative and 105 collisional) considered by Faure et al. [6] and the results are shown in Fig.1. comparison of the two sets of results shows a very little variation. This very little variation may be assigned to small values of collisional rates as compared to the Einstein A coefficients. The contribution of four transitions, 2_{20}-1_{01}, 2_{21}-2_{02}, 2_{20}-2_{21} and 2_{20}-3_{03} is not found significant, as they are connecting the highest two levels whose population densities are very low.

The anomalous absorption transition 1_{11}-2_{02} and weak MASER transition 1_{10}-1_{11} have a common level 1_{11}. The appearance of these two anomalous phenomena (anomalous absorption and weak MASER action) simultaneously may be assigned to a large value $0.931 \cdot 10^{-4}$ s^{-1} of Einstein A-coefficient for the transition 1_{11}-0_{00}.

5. *Conclusions*. For 15 rotational levels of methanimine, we have discussed that there should be 77 collisional transitions, instead of 105 taken by Faure et al. [6]. It is also found that Faure et al. [6] have not considered four radiative transitions, 2_{20}-1_{01}, 2_{21}-2_{02}, 2_{20}-2_{21} and 2_{20}-3_{03}. A set of statistical equilibrium equations coupled with the equations of radiative transfer has been solved (Sobolev analysis), for wide ranges of physical parameters. We have found six lines, 1_{10}-1_{11}, 2_{11}-2_{12}, 3_{12}-3_{13}, $4_{1.3}$-$4_{1.4}$, 3_{03}-2_{12} and $4_{0.4}$-31.3, having the weak MASER action and one line, 1_{11}-2_{02} having anomalous absorption. Present results have been found to vary very little when the transitions (radiative and collisional) considered by Faure et al. [6] are taken. It may be because of the relative dominance of radiative transitions over the collisional ones.

The anomalous absorption transition 1_{11}-2_{02} and the weak MASER transition 1_{10}-1_{11}, connecting a common level 1_{11}, may be assigned to the large value $0.931 \cdot 10^{-4}$ s^{-1} of Einstein A coefficient of the transition 1_{11}-0_{00}.

Acknowledgments. We are grateful to learned reviewer for encouraging and constructive comments. We are thankful to Prof. A.Faure for providing data in the tabular form. SC is grateful to Hon'ble Dr. Ashok K.Chauhan, Founder President, Hon'ble Dr. Atul Chauhan, Chancellor, Hon'ble Vice Chancellor Dr. Balvinder Shukla, Amity University for valuable support and encouragements.

Financial assistance from the Indian Space Research Organization, Bengaluru as project No. ISRO/RES/2/426/19-20 is thankfully acknowledged.

[1] Amity Centre for Astronomy & Astrophysics, Amity Institute of Applied Sciences, Amity University Uttar Pradesh, Sector-125, NOIDA 201313, India
e-mail: schandra2@amity.edu suresh492000@yahoo.co.in
[2] Physics Department, Sunder Deep Group of Institutions, NH-24, Delhi-Hapur Road, Dasna 201001, India

МЕТАНИМИН В ХОЛОДНЫХ КОСМИЧЕСКИХ ОБЪЕКТАХ С ИСПОЛЬЗОВАНИЕМ ТОЧНЫХ КОЭФФИЦИЕНТОВ СКОРОСТИ СТОЛКНОВЕНИЙ

С.ЧАНДРА[1], М.К.ШАРМА[2]

Представлены точные коэффициенты скорости столкновений для переходов между 15 вращательными уровнями метанимина, сталкивающегося с молекулой p-H_2. Метанимин представляет собой плоскую асимметричную молекулу с электрическим дипольным моментом, имеющим компоненты $\mu_a = 1.3396$ Дебая и $\mu_b = 1.4461$ Дебая. Это приводит к образованию спектральных линий типа *a* и *b* с почти одинаковой интенсивностью. Следовательно, все вращательные уровни необходимо рассматривать вместе. В исследованиях других авторов первоначально рассматривались в общей сложности 105 переходов между 15 уровнями метанимина. В данной работе учитывалось, что не каждый уровень связан со всеми другими посредством столкновений, и, следовательно, должно быть 77 вместо 105 переходов между 15 уровнями метанимина. При наличии точных коэффициентов скорости столкновений важно выполнить анализ Соболева для метанимина. В ходе анализа были идентифицированы шесть слабых мазерных переходов: 1_{10}-1_{11}, 2_{11}-2_{12}, 3_{12}-3_{13} $4_{1.3}$-$4_{1.4}$, 3_{03}-2_{12} и $4_{0.4}$-$3_{1.3}$, а также один переход 1_{11}-2_{02}, демонстрирующий аномальное поглощение. Эти семь линий могут играть важную роль в поведении метанимина.

Ключевые слова: *МЗС: молекулы: метанимин: мазеры: перенос излучения*

REFERENCES

1. *D.E.Woon*, Astrophys. J. Lett., **571**, L177, 2002.
2. *P.Theule et al.*, Astron. Astrophys., **534**, A64, 2011.
3. *A.Strecker*, Ann. Chem. Pharm., **75**, 27, 1850.
4. *A.C.Cheung*, *D.M.Rank*, *C.H.Townes et al.*, Phys. Rev. Lett., **21**, 1701, 1968.
5. *L.E.Snyder*, *D.Buhl*, *B.Zuckerman et al.*, Phys. Rev. Lett., **22**, 679, 1969.
6. *A.Faure*, *F.Lique*, *A.J.Remijan*, Phys. Chem. Lett., **9**, 3199, 2018.
7. *M.D.Gorski*, *S.Aalto*, *J.Mangum et al.*, Astron. Astrophys., **654**, A110, 2021.
8. *M.Allegrini*, *J.W.C.Johns*, *A.R.W.McKellar*, J. Chem. Phys., **70**, 2829, 1979.
9. *P.D.Godfrey*, *R.D.Brown*, *B.J.Robinson et al.*, Astrophys. Lett., **13**, 119, 1973.
10. *D.T.Halfen*, *V.V.Ilyushin*, *L.M.Ziurys*, Astrophys. J., **767**, 66, 2013.
11. *P.A.Jones et al.*, Mon. Not. Roy. Astron. Soc., **386**, 117, 2008.
12. *P.A.Jones*, *M.G.Burton*, *N.F.H.Tothill et al.*, Mon. Not. Roy. Astron. Soc., **411**, 2293, 2011.
13. *A.Nummelin et al.*, Astrophys. J. Suppl., **117**, 427, 1998.
14. *E.C.Sutton*, *P.A.Jaminet*, *W.C.Danchi et al.*, Astrophys. J. Suppl., **77**, 255, 1991.
15. *B.E.Turner*, Astrophys. J. Suppl., **70**, 539A, 1989.
16. *B.E.Turner*, *R.Terzieve*, *E.Herbst*, Astrophys. J., **518**, 699, 1999.
17. *J.E.Dickens*, *W.M.Irvine*, *C.H.DeVries et al.*, Astrophys. J., **479**, 307, 1997.
18. *T.Suzuki*, *M.Ohishi*, *T.Hirota et al.*, Astrophys. J., **825**, 79, 2016.
19. *G.J.White*, *M.Araki*, *J.S.Greaves et al.*, Astron. Astrophys., **407**, 589A, 2003.
20. *S.L.Qin et al.*, Astrophys. J., **711**, 399, 2010.
21. *E.D.Tenenbaum*, *J.L.Dodd*, *S.N.Milam et al.*, Astrophys. J. Lett., **720**, L102, 2010.
22. *C.J.Salter et al.*, Astron. J., **136**, 389, 2008.
23. *J.Bourgalais*, *N.Carraso*, *L.Vettier et al.*, Low Pressure EUV Photochemical Experiments: Insight on the Ion-Chemistry Occurring in Titan's Atmosphere, /JGR, **124**, 9214, 2019.
24. *C.H.Yuen*, *M.A.Ayouz*, *N.Balucani et al.*, Mon. Not. Roy. Astron. Soc., **484**, 659, 2019.
25. *L.Dore*, *L.Bizzocchi*, *C.Degli Esposti et al.*, J. Mol. Spectrosc., **263**, 44, 2010.
26. *L.Dore*, *L.Bizzocchi*, *C.Degli Esposti*, Astron. Astrophys., **544**, A19, 2012.
27. *L.Halonen*, *G.Duxbury*, J. Chem. Phys., **83**, 2078, 1985.
28. *D.R.Johnson*, *F.J.Lovas*, Chem. Phys. Lett., **15**, 65, 1972.
29. *Y.Motoki*, *F.Isobe*, *H.Ozeki et al.*, Astron. Astrophys., **566**, A28, 2012.
30. *S.Saito*, *S.Yamamoto*, *W.M.Irvine et al.*, Astrophys. J., **334**, L113, 1988.
31. *M.K.Sharma*, *M.Sharma*, *N.Kumar et al.*, Ind. J. Phys., **95**, 2255, 2021.
32. *M.Sil et al.*, Astrophys. J., **853**, 139, 2018.
33. *H.Luthra*, *V.Wakelam*, *M.K.Sharma et al.*, Mon. Not. Roy. Astron. Soc., **521**, 2181, 2023.
34. *S.Chandra*, *M.K.Sharma*, J. Quan. Spec. and Rad. Tran., **251**, 107085, 2020.
35. *M.K.Sharma*, *S.Chandra*, Astrophysics, **64**, 388, 2021.
36. *M.K.Sharma*, *S.Chandra*, Astrophys. Astron., **42**, 112, 2021.

А С Т Р О Ф И З И К А

ТОМ 67 АВГУСТ, 2024 ВЫПУСК 3

DOI: 10.54503/0571-7132-2024.67.3-385

ВЕРОЯТНОСТЬ ВЫХОДА И СРЕДНИЕ ЧИСЛА РАССЕЯНИЯ ФОТОНОВ. II. МОНОХРОМАТИЧЕСКОЕ ИЗОТРОПНОЕ РАССЕЯНИЕ В ОДНОМЕРНОЙ СРЕДЕ И ПЛОСКИХ СРЕДАХ

Д.И.НАГИРНЕР, А.В.ДЕМЕНТЬЕВ, Е.В.ВОЛКОВ

Поступила 24 июня 2024

Принята к печати 26 августа 2024

В качестве примеров применения формул части I рассмотрены рассеяние в одномерной среде, для которой все характеристики поля излучения выражаются через элементарные функции, и (трехмерное) изотропное монохроматическое рассеяние. Изучены некоторые свойства функции Амбарцумяна, а также выведены асимптотики средних чисел рассеяния фотонов в оптически толстом плоском слое.

Ключевые слова: *перенос излучения: средние числа рассеяний фотонов*

1. *Введение*. Во второй части данной работы, формулы, приведенные в первой части [1], конкретизируются для двух важных случаев рассеяния, рассматривавшихся в теории переноса излучения.

В начале развития теории переноса излучения, для выяснения простейших аспектов процесса, принималось, что рассеяние происходит в так называемой одномерной среде, в которой все фотоны могут проходить только вдоль одной прямой [2]. Такая модель может служить приближением в случае очень сильно вытянутых индикатрис, заменяемых игольчатой индикатрисой (рассеяние вперед-назад). Процесс рассеяний в такой среде изучался в работах основоположников [3,4].

Идеализированное рассеяние в одномерной среде представляет еще и тот интерес, что все характеризующие это рассеяние величины могут быть выражены в элементарных функциях. Кроме того, асимптотики величин реального рассеяния в трехмерной среде очень похожи на точные выражения одномерных и позволяют оценить их действие на примере точных формул.

Изотропное рассеяние в трехмерной плоскопараллельной однородной среде с горизонтально симметричным полем излучения представляет простейший случай трехмерного рассеяния и позволяет продвинуться в построении теории переноса в однородных плоских средах наиболее далеко. Большое значение в этой теории имеют как точные, так и различные асимптотические формулы.

Как и в первой части, здесь выводятся асимптотики для больших глубин как полубесконечной среды, так и оптически толстого слоя, а также для рассеяния, близкого к чистому.

2. *Рассеяние в одномерной среде.*

2.1. *Основные формулы.* Ядерная функция при рассеянии в одномерной среде - простая экспонента, а весовая функция в представлении ее в виде (I.2) - дельта-функция (основной промежуток вырождается в точку 1):

$$K(\tau)=e^{-\tau},\quad A(y)=\delta(y-1). \tag{1}$$

Им соответствуют функции (I.3) (двустороннее преобразование Лапласа и преобразование Фурье ядерной функции)

$$\mathcal{V}(p)=\frac{1}{1-p^2},\quad V(u)=\frac{1}{1+u^2} \tag{2}$$

и характеристическое число (решение уравнения (I.52)) $k=\sqrt{1-\lambda}$.

2.2. *Полубесконечная среда.* Поскольку $A(1)=\infty$, во многих общих формулах интегралы обращаются в нуль и остаются только внеинтегральные слагаемые. Так задаются резольвентная функция, интеграл от нее и преобразование Лапласа, то есть H-функция:

$$\Phi(\tau)=(1-k)e^{-k\tau}=C_0e^{-k(\tau+\tau_e)},\quad \Psi(\tau)=\frac{1}{k}\left[1-(1-k)e^{-k\tau}\right],\quad H(p)=\frac{p+1}{p+k}. \tag{3}$$

Величины, входящие в эти функции:

$$\tau_e=\frac{1}{2k}\ln\frac{1+k}{1-k}=\frac{\operatorname{arth}k}{k},\quad C_0=\sqrt{1-k^2}=\sqrt{\lambda}=\frac{1}{\operatorname{ch}k\tau_e}=\frac{k}{\operatorname{sh}k\tau_e}. \tag{4}$$

Простыми формулами определяются даже резольвента полубесконечной среды

$$\begin{gathered}\Gamma(\tau,\tau_1)=\Phi(|\tau-\tau_1|)+\int\limits_0^{\min(\tau,\tau_1)}\Phi(\tau-t)\Phi(\tau_1-t)dt=\\ \frac{1-k^2}{2k}e^{-k|\tau-\tau_1|}-\frac{(1-k)^2}{2k}e^{-k(\tau+\tau_1)}\end{gathered} \tag{5}$$

и вероятность выхода фотона из среды

$$P(\tau)=\frac{\lambda}{2}D(\tau,1)=\frac{\lambda}{2}(1-k)\frac{2}{1-k^2}e^{-k\tau}=(1-k)e^{-k\tau}=\Phi(\tau). \tag{6}$$

Наконец, решение однородного уравнения (задача Милна)

$$\frac{S_M(\tau)}{S_M(0)}=\frac{1+k}{2k}e^{k\tau}-\frac{1-k}{2k}e^{-k\tau}=C_0\frac{\operatorname{sh}k(\tau+\tau_e)}{k}. \tag{7}$$

2.3. *Конечный отрезок*. Простая точная формула получается для резольвентной функции и при конечном τ_0:

$$\Phi(\tau,\tau_0)=\lambda\frac{\operatorname{sh}k(\tau_0-\tau)+k\operatorname{ch}k(\tau_0-\tau)}{(1+k)^2\operatorname{sh}(k\tau_0)+2k\operatorname{ch}(k\tau_0)}=C_0\frac{\operatorname{sh}k(\tau_0-\tau+\tau_e)}{\operatorname{sh}k(\tau_0+2\tau_e)}, \tag{8}$$

$$\Phi(\tau_0,\tau_0)=C_0\frac{\operatorname{sh}k\tau_e}{\operatorname{sh}k(\tau_0+2\tau_e)}=\frac{k}{\operatorname{sh}k(\tau_0+2\tau_e)}. \tag{9}$$

При рассмотрении трехмерных задач рассеяния обычно значения ядерной $K(\tau)$ и резольвентной функций при $\tau=0$ бесконечны, здесь они конечны.

По резольвентной функции находим резольвенту:

$$\Gamma(\tau,\tau_1,\tau_0)=C_0\frac{\operatorname{sh}k(\tau_0-\overline{\tau}+\tau_e)\operatorname{sh}k(\underline{\tau}+\tau_e)}{\operatorname{sh}k(\tau_0+2\tau_e)\operatorname{sh}k\tau_e}, \tag{10}$$

где

$$\underline{\tau}=\frac{\tau+\tau_1-|\tau-\tau_1|}{2}=\min\{\tau,\tau_1\},\quad \overline{\tau}=\frac{\tau+\tau_1+|\tau-\tau_1|}{2}=\max\{\tau,\tau_1\}. \tag{11}$$

Предельные случаи $\tau_1=0$ и $\tau_1=\tau_0$ получаются верными.

Получим еще интеграл от (8). Его можно представить в разных формах. Непосредственное интегрирование (8) дает

$$\Psi(\tau,\tau_0)=1+\int_0^\tau\Phi(\tau,\tau_0)d\tau=1+\frac{C_0}{k}\frac{\operatorname{ch}k(\tau_0+\tau_e)-\operatorname{ch}k(\tau_0-\tau+\tau_e)}{\operatorname{sh}k(\tau_0+2\tau_e)}. \tag{12}$$

Воспользовавшись соотношениями (4) между C_0, k и τ_e, получаем тождество

$$k\operatorname{sh}k(\tau_0+2\tau_e)+C_0\operatorname{ch}k(\tau_0+\tau_e)=\operatorname{ch}k(\tau_0+2\tau_e), \tag{13}$$

а с его помощью - выражение

$$\Psi(\tau,\tau_0)=\frac{\operatorname{cth}k(\tau_0+2\tau_e)}{k}-\frac{C_0}{k}\frac{\operatorname{ch}k(\tau_0-\tau+\tau_e)}{\operatorname{sh}k(\tau_0+2\tau_e)}=\frac{\operatorname{ch}k(\tau_0+2\tau_e)-C_0\operatorname{ch}k(\tau_0-\tau+\tau_e)}{k\operatorname{sh}k(\tau_0+2\tau_e)}. \tag{14}$$

В таком виде точная формула для одномерной среды по форме совпадает с крупномасштабной асимптотикой (I.78).

Приведение (12) к общему знаменателю и преобразование гиперболических функций приводит к еще одному выражению:

$$\Psi(\tau,\tau_0)=\frac{\operatorname{sh}k(\tau_0-\tau/2+2\tau_e)\operatorname{sh}k(\tau/2+\tau_e)+\operatorname{sh}k(\tau_0-\tau/2+\tau_e)\operatorname{sh}k(\tau/2)}{\operatorname{sh}k\tau_e\operatorname{sh}k(\tau_0+2\tau_e)}. \tag{15}$$

Последнее выражение позволяет легко перейти к пределу чистого рассеяния: при $\lambda\to1$ будет $k\to0$ и $\Psi(\tau,\tau_0)\to1+\frac{\tau}{2}\frac{2\tau_0+2-\tau}{\tau_0+2}$.

Крайнее значение интеграла также можно представить по-разному:

$$\Psi(\tau_0,\tau_0)=1+\frac{C_0}{k}\frac{\operatorname{sh}\frac{k\tau_0}{2}}{\operatorname{ch}k\frac{\tau_0+2\tau_e}{2}}=\frac{\operatorname{th}k\frac{\tau_0+2\tau_e}{2}}{k}=\frac{1+\frac{1}{k}\operatorname{th}k\frac{\tau_0}{2}}{1+k\operatorname{th}k\frac{\tau_0}{2}}\to 1+\frac{\tau_0}{2}\quad \text{при}\quad \lambda\to 1. \tag{16}$$

Второе выражение имеет вид общей асимптотики (I.68), если подставить $k=\sqrt{1-\lambda}$. С этим условием совпадают асимптотики при $\tau_0\to\infty$ и вид пределов при $\lambda\to 1$, хотя значения экстраполированной длины у них разные.

В случае одномерной среды вероятность выхода совпадает с резольвентной функцией. Выход фотона из среды может осуществляться через одну из границ и соответствующие вероятности можно разграничить. Для одномерной среды это одна и та же функция от дополняющих друг друга аргументов:

$$P(\tau,\tau_0)=\frac{\lambda}{2}D(\tau,1,\tau_0)=\Phi(\tau,\tau_0)=C_0\frac{\operatorname{sh}k(\tau_0-\tau+\tau_e)}{\operatorname{sh}k(\tau_0+2\tau_e)}, \tag{17}$$

$$P(\tau_0-\tau,\tau_0)=\frac{\lambda}{2}D(\tau,-1,\tau_0)=\Phi(\tau_0-\tau,\tau_0)=C_0\frac{\operatorname{sh}k(\tau+\tau_e)}{\operatorname{sh}k(\tau_0+2\tau_e)}, \tag{18}$$

$$\mathcal{P}(\tau,\tau_0)=P(\tau,\tau_0)+P(\tau_0-\tau,\tau_0)=C_0\frac{\operatorname{ch}k(\tau_0/2-\tau)}{\operatorname{ch}k(\tau_0/2+\tau_e)}. \tag{19}$$

По только что приведенным формулам или по (I.33) находим вероятности выхода фотонов с границ среды:

$$\begin{gathered}P(0,\tau_0)=C_0\frac{\operatorname{sh}k(\tau_0+\tau_e)}{\operatorname{sh}k(\tau_0+2\tau_e)}=1-\frac{k}{\operatorname{th}k(\tau_0+2\tau_e)},\\ P(\tau_0,\tau_0)=C_0\frac{\operatorname{sh}k(\tau_e)}{\operatorname{sh}k(\tau_0+2\tau_e)}=\frac{k}{\operatorname{sh}k(\tau_0+2\tau_e)}.\end{gathered} \tag{20}$$

Полная вероятность выхода с границ отрезка и с его середины

$$\begin{gathered}\mathcal{P}(0,\tau_0)=\mathcal{P}(\tau_0,\tau_0)=C_0\frac{\operatorname{ch}k(\tau_0/2)}{\operatorname{ch}k(\tau_0/2+\tau_e)}=1-k\operatorname{th}k\frac{\tau_0+2\tau_e}{2},\\ \mathcal{P}(\tau_0/2,\tau_0)=\frac{C_0}{\operatorname{ch}k(\tau_0/2+\tau_e)}.\end{gathered} \tag{21}$$

В середине эта вероятность принимает минимальное значение.

При $\tau_0\to\infty$ получается, естественно, $P(\tau,\tau_0)\to P(\tau)=\Phi(\tau)$, $P(\tau_0-\tau,\tau_0)\to 0$. При $\lambda\to 1$

$$\begin{gathered}P(\tau,\tau_0)=\frac{\tau_0-\tau+1}{\tau_0+2},\quad P(\tau_0-\tau,\tau_0)=\frac{\tau+1}{\tau_0+2},\\ \mathcal{P}(\tau,\tau_0)=P(\tau,\tau_0)+P(\tau_0-\tau,\tau_0)=1.\end{gathered} \tag{22}$$

2.4. *Средние числа рассеяний*. Полное число рассеяний фотона, рожденного на расстоянии τ от начала промежутка, легко найти по формуле

(I.38) с использованием (15) и (16):

$$N(\tau,\tau_0)=\frac{1}{k^2}\left[1-C_0\frac{\operatorname{ch}k\left(\dfrac{\tau_0}{2}-\tau\right)}{\operatorname{ch}k\left(\dfrac{\tau_0}{2}+\tau_e\right)}\right]= \tag{23}$$

$$\frac{\operatorname{sh}k\left(\dfrac{\tau_0-\tau}{2}+\tau_e\right)\operatorname{sh}k\left(\dfrac{\tau}{2}+\tau_e\right)+\operatorname{sh}k\dfrac{\tau_0-\tau}{2}\operatorname{sh}k\dfrac{\tau}{2}}{k\operatorname{sh}k\,\tau_e\operatorname{ch}k\left(\dfrac{\tau_0}{2}+\tau_e\right)}.$$

При чистом рассеянии

$$N(\tau,\tau_0)=1+\frac{\tau_0+\tau(\tau_0-\tau)}{2},\quad N(0,\tau_0)=N(\tau_0,\tau_0)=1+\frac{\tau_0}{2},$$
$$N(\tau_0/2,\tau_0)=1+\frac{\tau_0}{2}+\frac{\tau_0^2}{8}. \tag{24}$$

Формулы (19)-(24) были получены В.В.Соболевым [4] без введения τ_e.

Для получения других средних чисел рассеяния требуется находить производные по λ от вероятностей выхода фотонов.

Проще сначала находить производные по числу k, а производные по λ получать, умножая их на $dk/d\lambda$. При этом используем производные

$$\frac{dC_0}{dk}=\frac{d\sqrt{1-k^2}}{dk}=-\frac{k}{C_0},\ \frac{d(k\tau_e)}{dk}=\frac{d}{dk}\left(\frac{1}{2}\ln\frac{1+k}{1-k}\right)=\frac{1}{1-k^2}=\frac{1}{C_0^2}=\frac{1}{\lambda},\ \frac{dk}{d\lambda}=-\frac{1}{2k}. \tag{25}$$

Производная от полной вероятности получается дифференцированием (19):

$$\frac{\partial\mathcal{P}(\tau,\tau_0)}{\partial k}=-\frac{k}{C_0}\frac{\operatorname{ch}k(\tau_0/2-\tau)}{\operatorname{ch}k(\tau_0/2+\tau_e)}+C_0\frac{\operatorname{sh}k(\tau_0/2-\tau)}{\operatorname{ch}k(\tau_0/2+\tau_e)}\left(\frac{\tau_0}{2}-\tau\right)$$
$$-C_0\frac{\operatorname{ch}k(\tau_0/2-\tau)}{\operatorname{ch}^2k(\tau_0/2+\tau_e)}\operatorname{sh}k(\tau_0/2+\tau_e)\left(\frac{\tau_0}{2}+\frac{1}{C_0^2}\right). \tag{26}$$

Некоторые преобразования гиперболических функций приводят к немного отличающемуся выражению. Умножим его на -1/(2k) и получим производную по λ:

$$\frac{\partial\mathcal{P}(\tau,\tau_0)}{\partial\lambda}=\frac{1}{2k}\left[\frac{\operatorname{ch}k(\tau_0/2-\tau)}{\operatorname{ch}^2k(\tau_0/2+\tau_e)}\operatorname{sh}k(\tau_0/2+2\tau_e)\right.$$
$$\left.+\frac{\tau_0}{2}C_0\frac{\operatorname{sh}k(\tau+\tau_e)}{\operatorname{ch}^2k(\tau_0/2+\tau_e)}+C_0\,\tau\frac{\operatorname{sh}k(\tau_0/2-\tau)}{\operatorname{ch}k(\tau_0/2+\tau_e)}\right]. \tag{27}$$

Выражение (26) явно симметрично относительно середины отрезка, симметричность (27) проверяется с использованием равенства

$$\operatorname{sh} k(\tau_0-\tau+\tau_e)-2\operatorname{sh} k\left(\frac{\tau_0}{2}-\tau\right)\operatorname{ch} k\left(\frac{\tau_0}{2}+\tau_e\right)=\operatorname{sh} k(\tau+\tau_e), \tag{28}$$

получающегося в результате перегруппировки аргументов гиперболических функций.

Продифференцируем и односторонние вероятности, сначала по *k*, затем перейдем к производной по λ. После ряда преобразований найдем для выхода вверх, то есть (17):

$$\frac{\partial P(\tau,\tau_0)}{\partial\lambda}=\frac{1}{2k}\left[\frac{\operatorname{sh} k(\tau_0-\tau+2\tau_e)\operatorname{ch} k(\tau_0+2\tau_e)-\operatorname{sh} k(\tau+2\tau_e)}{\operatorname{sh}^2 k(\tau_0+2\tau_e)}\right.$$
$$\left.-\frac{C_0\operatorname{sh} k(\tau+\tau_e)\tau_0}{\operatorname{sh}^2 k(\tau_0+2\tau_e)}+C_0\frac{\operatorname{ch} k(\tau_0-\tau+\tau_e)}{\operatorname{sh} k(\tau_0+2\tau_e)}\tau\right]. \tag{29}$$

Для выхода вниз надо просто сделать замены $\tau_0-\tau\leftrightarrow\tau$. Выкладка с использованием формул с гиперболическими функциями доказывает, что сумма (29) с выражением при указанной замене дает (26).

Все приведенные формулы содержат экстраполированную длину, выражение для которой в (2) достаточно простое и при подстановке его в формулы получаются тоже не очень сложные выражения, которые были найдены ранее [2,4,5]. Удобство выражений с τ_e в их компактности, а также в простоте вычислений и процедуры перехода к чистому рассеянию. Еще одно преимущество формул с τ_e в том, что они похожи на асимптотические формулы для трехмерной среды даже в том общем случае, для которого эти асимптотики были найдены в части I.

2.5. *Средние числа рассеяний при чистом рассеянии*. Для перехода к случаю чистого рассеяния, то есть к пределу при $\lambda\to 1$, $k\to 0$, разложим последовательно интересующие нас величины по степеням *k* с запасом степеней. Начинать надо с разложений гиперболических функций. Разложения синуса и косинуса общеизвестны, а разложения обратных величин содержат числа Бернулли B_n и Эйлера E_n:

$$\frac{1}{\operatorname{ch} x}=\sum_{n=0}^{\infty}E_n\frac{x^{2n}}{(2n)!},\quad \frac{1}{\operatorname{sh} x}=2\sum_{n=0}^{\infty}\frac{(-1)^n\left(2^{2n-1}-1\right)}{(2n)!}B_n x^{2n-1}, \tag{30}$$

$$\operatorname{th} x=\sum_{n=1}^{\infty}\frac{2^{2n}\left(2^{2n-1}-1\right)}{(2n)!}B_{2n}x^{2n-1},\quad \operatorname{cth} x=\sum_{n=0}^{\infty}\frac{2^{2n}}{(2n)!}B_{2n}x^{2n-1}. \tag{31}$$

Экстраполированная длина в данном случае простая функция и ее разложение также широко известно.

Указанные разложения позволяют найти средние при чистом рассеянии. При этом несколько первых степеней *k* сокращаются и для среднего числа рассеяний фотона, возникшего на глубине τ, а вышедшего через верхнюю границу, получается

$$N_+(\tau,\tau_0)=\frac{R(\tau,\tau_0)}{6(\tau_0+2)(\tau_0-\tau+1)}, \tag{32}$$

где

$$R(\tau,\tau_0)=2\tau_0^3(1+\tau)+3\tau_0^2\left(4+2\tau-\tau^2\right)+\tau_0\left(24-9\tau^2+\tau^3\right)+2\left(6-6\tau-3\tau^2+\tau^3\right). \tag{33}$$

Полное число рассеяний выходящих фотонов

$$\begin{aligned} N_E(\tau,\tau_0)&=P(\tau,\tau_0)N_+(\tau,\tau_0)+P(\tau_0-\tau,\tau_0)N_+(\tau_0-\tau,\tau_0)\\ &=1+\frac{\tau_0}{2}+\frac{\tau(\tau_0-\tau)}{2}=N(\tau,\tau_0) \end{aligned} \tag{34}$$

равно полному числу рассеяний, так как фотоны не поглощаются.

Для средних чисел рассеяния фотонов, родившихся на глубинах 0 и τ_0, а вышедших через границу $\tau=0$, получаются следующие значения

$$\begin{aligned} N_+(0,\tau_0)&=N_-(\tau_0,\tau_0)=\frac{2\tau_0^3+12\tau_0^2+24\tau_0+12}{6(\tau_0+2)(\tau_0+1)},\\ N_+(\tau_0,\tau_0)&=N_-(0,\tau_0)=\frac{\tau_0^3+6\tau_0^2+12\tau_0+12}{6(\tau_0+2)}. \end{aligned} \tag{35}$$

Как видно из этих формул, число рассеяний фотона, выходящего через ту же границу, на которой он возник, значительно меньше, чем у фотона, выходящего через противоположную границу. При больших толщинах

$$\begin{aligned} &P(0,\tau_0)\sim 1, \quad N_+(0,\tau_0)\sim\frac{\tau_0}{3}, \quad P(\tau_0,\tau_0)\sim\frac{1}{\tau_0},\\ &N_+(\tau_0,\tau_0)\sim\frac{\tau_0^2}{6}, \quad N_E(0,\tau_0)=N_E(\tau_0,\tau_0)\sim\frac{\tau_0}{2}. \end{aligned} \tag{36}$$

При рождении фотона в середине отрезка

$$P\left(\frac{\tau_0}{2},\tau_0\right)=\frac{1}{2}, \quad N_\pm\left(\frac{\tau_0}{2},\tau_0\right)=N_E\left(\frac{\tau_0}{2},\tau_0\right)=1+\frac{\tau_0}{2}+\frac{\tau_0^2}{8}. \tag{37}$$

2.6. *Графики при $\tau_0 = 10$.* Для иллюстрации приведенных формул построены графики вероятностей выхода (рис.1) и средних чисел рассеяния (рис.2-5) при оптической длине отрезка, в котором происходит рассеяние, равной $\tau_0=10$.

Величина, графики которой приведены на рисунке, указана на том же рисунке. Ввиду малой величины вероятностей на большом протяжении аргумента τ даны их десятичные логарифмы. Графики $P(\tau_0-\tau,\tau_0)$ и $N_-(\tau,\tau_0)=$ $=N_+(\tau_0-\tau,\tau_0)$ не приводятся, так как получаются из приведенных отражением в прямой $\tau=\tau_0/2$. Значения вероятности выживания фотона приведены

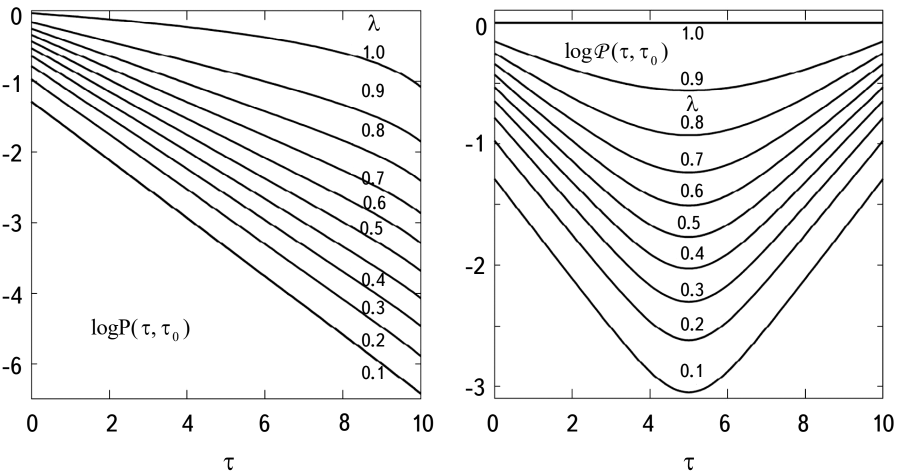

Рис.1. Логарифмы вероятностей выхода фотонов: слева - через верхнюю границу, справа - полные.

около кривых. Из-за большого разброса значений графики чисел рассеяния даются раздельно для $\lambda = 0.1\,(0.1)\,0.8$ и $\lambda = 0.9, 0.92, 0.95, 0.97, 0.99, 1.0$. Графики приведены в разных масштабах для большего заполнения площади рисунков.

Графики демонстрируют сильную зависимость величин от λ при ее приближении к единице, то есть к чистому рассеянию. На рис.1 это не так сильно выражено, так как приведены логарифмы, выравнивающие значения функций.

2.7. *Некоторые интегралы*. Часто при приложениях теории переноса источники излучения аппроксимируются степенной функцией оптической

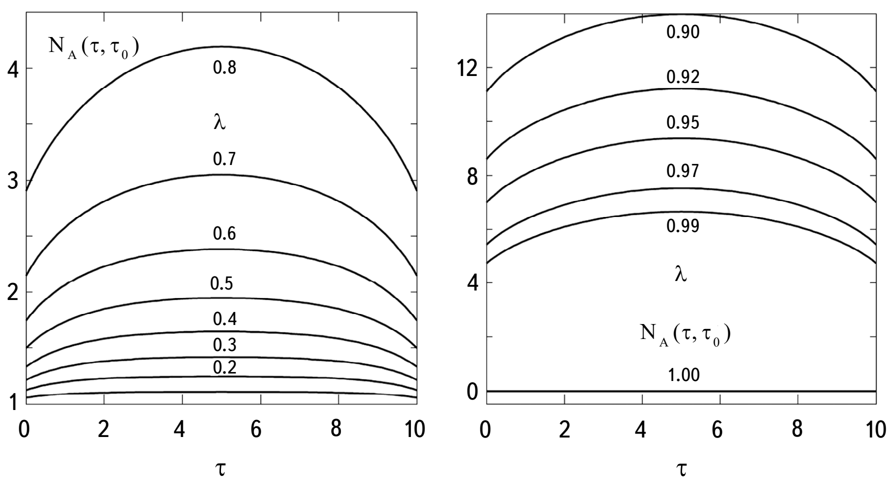

Рис.2. Средние числа рассеяний поглощенных фотонов.

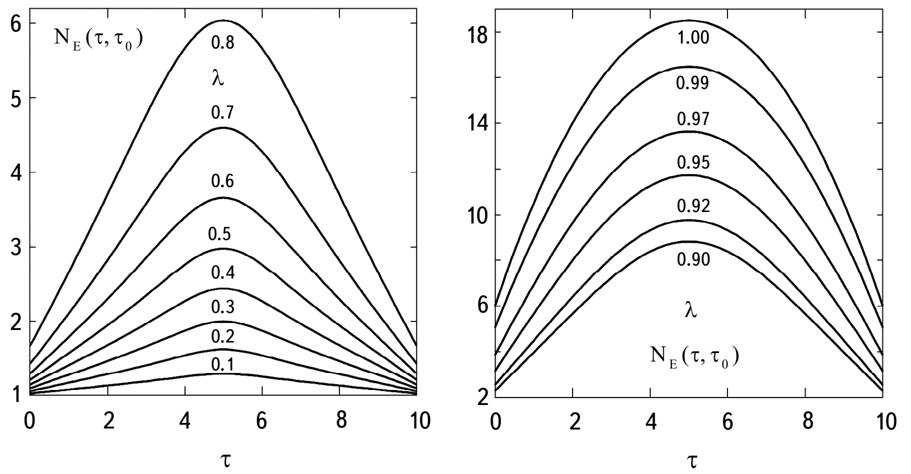

Рис.3. Средние числа рассеяний вышедших фотонов.

глубины. Рассмотрим такое распределение.

Пусть первичные источники описываются формулой $S_0(\tau) = \tau^n$. Для получения усредненных по такому распределению величин, требуется найти интегралы от произведений степеней τ и гиперболических функций с аргументами $k(\tau + \tau_e)$, $k(\tau_0 - \tau + \tau_e)$ и $k(\tau_0/2 - \tau)$.

Начнем с

$$h_n^{(s)}(\tau_0) = \int_0^{\tau_0} \tau^n \operatorname{sh} k(\tau + \tau_e)\, d\tau, \quad h_0^{(s)}(\tau_0) = \frac{2}{k} \operatorname{sh} k \frac{\tau_0}{2} \operatorname{sh} k\left(\frac{\tau_0}{2} + \tau_e\right), \tag{38}$$

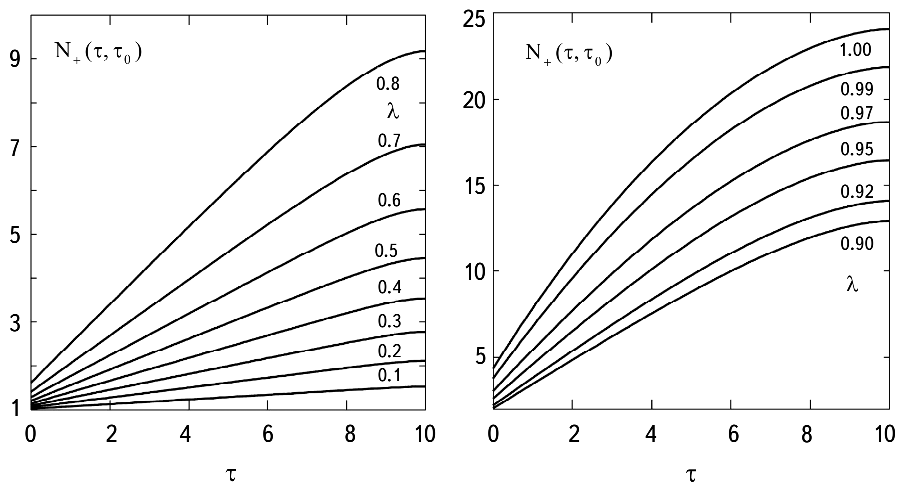

Рис.4. Средние числа рассеяний фотонов, вышедших через верхнюю границу.

$$h_1^{(s)}(\tau_0)=\frac{\tau_0}{k}\operatorname{ch}k(\tau_0+\tau_e)-\frac{2}{k^2}\operatorname{sh}k\frac{\tau_0}{2}\operatorname{ch}k\left(\frac{\tau_0}{2}+\tau_e\right). \tag{39}$$

Дважды интегрируя по частям, приходим к рекуррентному соотношению

$$h_n^{(s)}(\tau_0)=\frac{\tau_0^n}{k}\operatorname{ch}k(\tau_0+\tau_e)-n\frac{\tau_0^{n-1}}{k^2}\operatorname{sh}k(\tau_0+\tau_e)+\frac{n(n-1)}{k^2}h_{n-2}^{(s)}(\tau_0). \tag{40}$$

Аналогично для:

$$h_n^{(c)}(\tau_0)=\int_0^{\tau_0}\tau^n\operatorname{ch}k(\tau+\tau_e)d\tau,\quad h_0^{(c)}(\tau_0)=\frac{2}{k}\operatorname{sh}k\frac{\tau_0}{2}\operatorname{ch}k\left(\frac{\tau_0}{2}+\tau_e\right), \tag{41}$$

$$h_1^{(c)}(\tau_0)=\frac{\tau_0}{k}\operatorname{sh}k(\tau_0+\tau_e)-\frac{2}{k^2}\operatorname{sh}k\frac{\tau_0}{2}\operatorname{sh}k\left(\frac{\tau_0}{2}+\tau_e\right), \tag{42}$$

$$h_n^{(c)}(\tau_0)=\frac{\operatorname{sh}k(\tau_0+\tau_e)}{k}-n\frac{\tau_0^{n-1}}{k}\operatorname{ch}k(\tau_0+\tau_e)+\frac{n(n-1)}{k^2}h_{n-2}^{(c)}(\tau_0). \tag{43}$$

Следующие два интеграла

$$f_n^{(c)}(\tau_0)=\int_0^{\tau_0}\tau^n\operatorname{ch}k\left(\frac{\tau_0}{2}-\tau\right)d\tau,\quad f_0^{(c)}(\tau_0)=\frac{2}{k}\operatorname{sh}k\frac{\tau_0}{2},\quad f_1^{(c)}(\tau_0)=\frac{\tau_0}{k}\operatorname{sh}k\frac{\tau_0}{2}, \tag{44}$$

$$f_n^{(s)}(\tau_0)=\int_0^{\tau_0}\tau^n\operatorname{sh}k\left(\frac{\tau_0}{2}-\tau\right)d\tau,\ f_0^{(s)}(\tau_0)=0,\ f_1^{(s)}(\tau_0)=-\frac{\tau_0}{k}\operatorname{ch}k\frac{\tau_0}{2}+\frac{2}{k^2}\operatorname{sh}k\frac{\tau_0}{2}. \tag{45}$$

При $n\geq 2$

$$f_n^{(c)}(\tau_0)=\frac{\tau_0^n}{k}\operatorname{sh}k\frac{\tau_0}{2}-\frac{n}{k^2}\left[\tau_0^{n-1}\operatorname{ch}k\frac{\tau_0}{2}-(n-1)f_{n-2}^{(c)}\right], \tag{46}$$

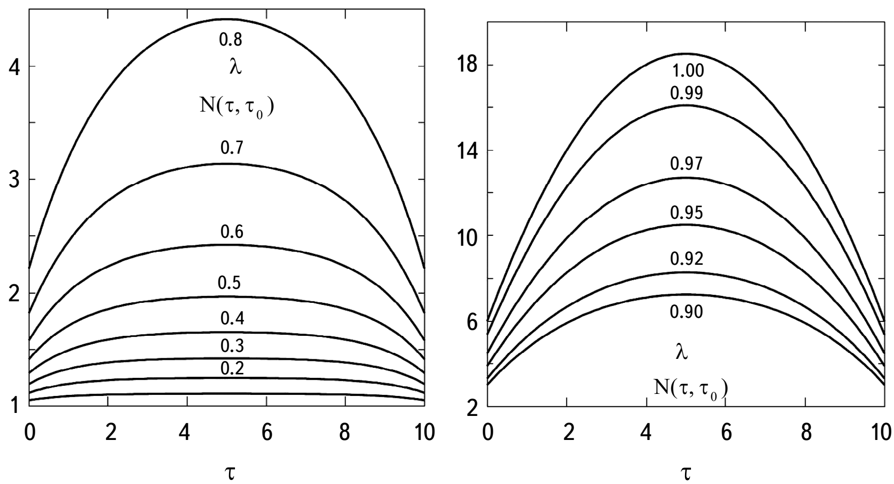

Рис.5. Полные средние числа рассеяний фотонов.

$$f_n^{(s)}(\tau_0) = -\frac{\tau_0^n}{k}\operatorname{ch} k\frac{\tau_0}{2} + \frac{n}{k^2}\left[\tau_0^{n-1}\operatorname{sh} k\frac{\tau_0}{2} + (n-1) f_{n-2}^{(s)}(\tau_0)\right]. \tag{47}$$

Еще два интеграла выражаются через (38) и (41):

$$\widetilde{h}_n^{(s)}(\tau_0) = \int_0^{\tau_0} \tau^n \operatorname{sh} k(\tau_0 - \tau + \tau_e)\, d\tau = \int_0^{\tau_0} (\tau_0 - \tau)^n \operatorname{sh} k(\tau + \tau_e)\, d\tau = \sum_{l=0}^{n} \frac{(-1)^l\, n!}{l!(n-l)!} \tau_0^{n-l}\, h_l^{(s)}(\tau_0), \tag{48}$$

$$\widetilde{h}_n^{(c)}(\tau_0) = \int_0^{\tau_0} \tau^n \operatorname{ch} k(\tau_0 - \tau + \tau_e)\, d\tau = \int_0^{\tau_0} (\tau_0 - \tau)^n \operatorname{ch} k(\tau + \tau_e)\, d\tau = \sum_{l=0}^{n} \frac{(-1)^l\, n!}{l!(n-l)!} \tau_0^{n-l}\, h_l^{(c)}(\tau_0). \tag{49}$$

Между тремя парами интегралов имеются связи:

$$\begin{aligned} \widetilde{h}_n^{(s)}(\tau_0) + h_n^{(s)}(\tau_0) &= 2\operatorname{sh} k\left(\frac{\tau_0}{2} + \tau_e\right) f_n^{(c)}(\tau_0), \\ \widetilde{h}_n^{(c)}(\tau_0) + h_n^{(c)}(\tau_0) &= 2\operatorname{ch} k\left(\frac{\tau_0}{2} + \tau_e\right) f_n^{(c)}(\tau_0), \end{aligned} \tag{50}$$

$$\begin{aligned} \widetilde{h}_n^{(s)}(\tau_0) - h_n^{(s)}(\tau_0) &= 2\operatorname{ch} k\left(\frac{\tau_0}{2} + \tau_e\right) f_n^{(s)}(\tau_0), \\ \widetilde{h}_n^{(c)}(\tau_0) - h_n^{(c)}(\tau_0) &= 2\operatorname{sh} k\left(\frac{\tau_0}{2} + \tau_e\right) f_n^{(s)}(\tau_0). \end{aligned} \tag{51}$$

2.8. *Вероятности выхода и числа рассеяний при степенных источниках*. Усредненные вероятности выхода через границы

$$\overline{P}_n(\tau_0) = \frac{\int_0^{\tau_0} \tau^n\, P(\tau, \tau_0)\, d\tau}{\int_0^{\tau_0} \tau^n\, d\tau} = \frac{C_0(n+1)}{\operatorname{sh} k(\tau_0 + 2\tau_e)} \frac{\widetilde{h}_n^{(s)}(\tau_0)}{\tau_0^{n+1}}, \tag{52}$$

$$\overline{\overline{P}}_m(\tau_0) = \frac{\int_0^{\tau_0} \tau^n\, P(\tau_0 - \tau, \tau_0)\, d\tau}{\int_0^{\tau_0} \tau^n\, d\tau} = \frac{C_0(n+1)}{\operatorname{sh} k(\tau_0 + 2\tau_e)} \frac{h_n^{(s)}(\tau_0)}{\tau_0^{n+1}}. \tag{53}$$

Усредненная вероятность выхода через обе границы выражается через $f_n^{(c)}(\tau_0)$ и равна, естественно, сумме

$$\overline{\mathcal{P}}_n(\tau_0) = \overline{P}_n(\tau_0) + \overline{\overline{P}}_n(\tau_0) = \frac{C_0(n+1)}{\operatorname{sh} k(\tau_0 + 2\tau_e)} \frac{h_n^{(s)}(\tau_0) + \widetilde{h}_n^{(s)}}{\tau_0^{n+1}} = \frac{C_0(n+1)}{\tau_0^{n+1}} \frac{f_n^{(c)}(\tau_0)}{\operatorname{ch} k(\tau_0/2 + \tau_e)}. \tag{54}$$

При чистом рассеянии предельные выражения усредненных вероятностей выхода

$$\overline{P}_n(\tau_0) = \frac{\tau_0 + n + 2}{(n+2)(\tau_0 + 2)}, \quad \overline{\overline{P}}_n(\tau_0) = \frac{(n+1)\tau_0 + n + 2}{(n+2)(\tau_0 + 2)}. \tag{55}$$

Сумма этих величин равна точно единице, так как усреднение единицы оставляет ее неизменной.

Полное число рассеяний фотона на отрезке при степенном распределении источников, если $0<\lambda<1$ и $\lambda=1$, равно соответственно

$$\overline{N}_n(\tau_0)=\frac{1}{k^2}\left[1-C_0\frac{f_n(\tau_0)}{\operatorname{ch}k(\tau_0/2+\tau_e)}\right]\to 1+\frac{\tau_0}{2}+\frac{n+1}{2(n+2)(n+3)}\tau_0^2 \quad \text{при} \quad \lambda\to 1. \tag{56}$$

Для получения других усредненных чисел рассеяния надо подобно формулам (I.46) и (I.48) результаты усреднения производных поделить на усредненные вероятности выхода. Поскольку операции дифференцирования по λ и интегрирования по τ перестановочны, получаем последовательно

$$\begin{aligned}\frac{\partial\overline{P}_n(\tau_0)}{\partial\lambda}&=-\frac{k}{C_0}\frac{\widetilde{h}_n^{(s)}(\tau_0)}{\operatorname{sh}k(\tau_0+2\tau_e)}+C_0\frac{\widetilde{h}_n^{(c)}(\tau_0)}{\operatorname{sh}k(\tau_0+2\tau_e)}\left(\tau_0+\frac{1}{C_0^2}\right)\\ &-C_0\frac{\widetilde{h}_{n+1}^{(c)}(\tau_0)}{\operatorname{sh}k(\tau_0+2\tau_e)}-C_0\frac{\operatorname{ch}k(\tau_0+2\tau_e)}{\operatorname{sh}^2k(\tau_0+2\tau_e)}\widetilde{h}_n^{(s)}(\tau_0)\left(\tau_0+\frac{1}{C_0^2}\right),\end{aligned} \tag{57}$$

$$\begin{aligned}\frac{\partial\overline{\overline{P}}_n(\tau_0)}{\partial\lambda}&=-\frac{k}{C_0}\frac{h_n^{(s)}(\tau_0)}{\operatorname{sh}k(\tau_0+2\tau_e)}+\frac{1}{C_0}\frac{h_n^{(c)}(\tau_0)}{\operatorname{sh}k(\tau_0+2\tau_e)}\\ &+C_0\frac{h_{n+1}^{(c)}(\tau_0)}{\operatorname{sh}k(\tau_0+2\tau_e)}-C_0\frac{\operatorname{ch}k(\tau_0+2\tau_e)}{\operatorname{sh}^2k(\tau_0+2\tau_e)}h_n^{(s)}(\tau_0)\left(\tau_0+\frac{2}{C_0^2}\right).\end{aligned} \tag{58}$$

По приведенным формулам средние можно находить, последовательно увеличивая степени *n*.

3. *Изотропное монохроматическое рассеяние в трехмерных средах.*

3.1. *Основные формулы*. Этот вид рассеяния как в полубесконечной среде, так и в конечном слое, исследовался всеми, кто обращался к проблемам переноса излучения. Монографии и учебники были указаны в первой части.

Все общие формулы разделов 2-5 части I годятся для этого рассеяния. При этом введенные там обозначения сохраняются почти для всех функций кроме тех, которые характеризуют выходящее излучение, то есть вместо Чандрасекаровских *H*-функций и функций *X* и *Y* [6] следует использовать введенные В.А.Амбарцумяном $\varphi(\eta)=H(1/\eta)$, $\varphi(\eta,\tau_0)=X(1/\eta,\tau_0)$, $\psi(\eta,\tau_0)=Y(1/\eta,\tau_0)$ [7,8] (см. также [9]).

Так как для этого рассеяния существует характеристическое число, то и все асимптотики к нему тоже применимы.

В этом разделе приведем более подробные формулы для основных величин, общих для полубесконечной среды и слоя.

Для этого вида рассеяния

$$K(\tau)=E_1(\tau)=\int_0^1 e^{-\tau/\eta}\frac{d\eta}{\eta}=\int_1^\infty e^{-y\tau}\frac{dy}{y}, \quad a=1, \quad b=\infty, \quad A(y)=\frac{1}{y}, \tag{59}$$

$$\mathcal{V}(p)=\frac{1}{2p}\ln\frac{1+p}{1-p}, \quad \mathcal{V}(y)=\frac{1}{2y}\ln\frac{y+1}{y-1}, \quad V(u)=\frac{\operatorname{arctg}u}{u}. \tag{60}$$

Параметр $y=1/\eta$ при $\eta\le 1$ имеет смысл обратного косинуса полярного угла. Например, вероятность, что поглощенный на глубине τ фотон выйдет из слоя под углом к границе $\tau=0$, косинус которого η, в телесном угле $2\pi d\eta$, равна $(\lambda/2)D(\tau,1/\eta,\tau_0)d\eta$. Но допускаются и другие значения *y*.

В асимптотики всех функций входят характеристическое число k и экстраполированная длина τ_e. Здесь подробно исследуются эти величины для изотропного рассеяния.

Уравнение для нахождения *k*, полученное еще Хвольсоном [10], имеет вид (напишем его и в удобной для нас форме)

$$\frac{\lambda}{2k}\ln\frac{1+k}{1-k}=1, \quad \frac{k}{\lambda}=\frac{1}{2}\ln\frac{1+k}{1-k}. \tag{61}$$

Экстраполированная длина (I.55)

$$\tau_e(\lambda)=\frac{1}{\lambda}-\frac{1}{\pi}\int_0^1 \operatorname{arcctg}\mathcal{X}\left(\frac{1}{\eta},\lambda\right)\frac{d\eta}{1-k^2\eta^2}, \quad \mathcal{X}\left(\frac{1}{\eta},\lambda\right)=\frac{\dfrac{1}{\lambda}-\dfrac{\eta}{2}\ln\dfrac{1+\eta}{1-\eta}}{\dfrac{\pi\eta}{2}}. \tag{62}$$

3.2. *Производные от характеристического числа и экстраполированной длины по* λ. Продифференцировав обе части второго равенства в (61), найдем

$$\frac{dk}{d\lambda}=-\frac{k}{\lambda}\frac{1+k^2}{\lambda-1+k^2}. \tag{63}$$

Эта производная отрицательна, так как с ростом λ число k уменьшается.

Продифференцируем и экстраполированную длину (62). Ее производная

$$\frac{d\tau_e(\lambda)}{d\lambda}=-\frac{1}{\lambda^2}-\frac{1}{\lambda\pi}\int_0^1 d\eta\left[\mathcal{A}(\eta,\lambda)-\frac{\operatorname{arcctg}\mathcal{X}(1/\eta,\lambda)}{\left(1-k^2\eta^2\right)^2}k^2\frac{1-k^2}{\lambda-1+k^2}\right],$$
$$\mathcal{A}(\eta,\lambda)=\frac{2}{\lambda}\mathcal{R}\left(\frac{1}{\eta},\lambda\right). \tag{64}$$

Эти формулы точные.

Значение производной экстраполированной длины (64) при $\lambda=1$

$$\tau_e'(1)=\left.\frac{d\,\tau_e(\lambda)}{d\,\lambda}\right|_{\lambda=1}=-1-\frac{1}{\pi}\int_0^1 d\,\eta\left[\frac{1}{\mathcal{A}(\eta,1)}-\frac{3}{2}\operatorname{arcctg}\mathcal{X}(1/\eta,1)\right]$$
$$=\frac{1}{2}-\frac{3}{2}\tau_e(1)-\frac{1}{\pi}\int_0^1\frac{d\,\eta}{\mathcal{A}(\eta,1)}. \tag{65}$$

Вычисления дают

$$\int_0^1\frac{d\,\eta}{\mathcal{A}(\eta,1)}=\frac{4}{5},\quad \tau_e(1)=0.7104460898,\quad \tau_e'(1)=-0.8203170. \tag{66}$$

$\tau_e(1)$ известно с очень большим числом знаков (до 60, см. [11]).

3.3. *Связи между* λ *и* k *при почти чистом рассеянии.* Для рассеяния, близкого к чистому, сначала получим разложения $\varepsilon=1-\lambda$ по степеням k и обратные.

Общеизвестно разложение

$$\frac{1}{\lambda}=\frac{1}{1-\varepsilon}=\frac{1}{2k}\ln\frac{1+k}{1-k}=\sum_{n=0}^{\infty}\frac{k^{2n}}{2n+1}. \tag{67}$$

Обратим этот ряд, то есть найдем разложение

$$\lambda=1-\varepsilon=\sum_{l=0}^{\infty}a_l k^{2l}\,. \tag{68}$$

Приравняв произведение рядов к единице, получим рекуррентное соотношение

$$\sum_{n=0}^{s}\frac{a_{s-n}}{2n+1}=0\,, \tag{69}$$

из которого найдем

$$a_0=1,\quad a_1=-\frac{1}{3},\quad a_2=-\frac{4}{45},\quad a_3=-\frac{44}{945},\quad a_4=-\frac{428}{14175},$$
$$a_5=-\frac{10196}{467775},\quad a_2=-\frac{10719068}{638512875}. \tag{70}$$

Представив k^2 разложением с неопределенными коэффициентами и подставив его в (68), получим с той же точностью

$$k^2\sim 3\varepsilon\left(1-\frac{4}{5}\varepsilon+\frac{4}{175}\varepsilon^2+\frac{4}{175}\varepsilon^3+\frac{7556}{336875}\varepsilon^4+\frac{471844}{21896875}\varepsilon^5\right). \tag{71}$$

Наконец, извлекая корни, находим

$$k\sim\sqrt{3\varepsilon}\left(1-\frac{2}{5}\varepsilon-\frac{12}{175}\varepsilon^2-\frac{2}{125}\varepsilon^3+\frac{166}{67375}\varepsilon^4+\frac{33354}{3128125}\varepsilon^5\right), \tag{72}$$

$$\sqrt{\varepsilon}\sim\frac{k}{\sqrt{3}}\left(1+\frac{2}{15}k^2+\frac{32}{525}k^4+\frac{878}{23625}k^6+\frac{1130}{43659}k^8+\frac{11508074}{591215625}k^{10}\right), \tag{73}$$

$$\frac{1}{\sqrt{\varepsilon}} \sim \frac{\sqrt{3}}{k}\left(1-\frac{2}{15}k^2-\frac{68}{1575}k^4-\frac{22}{945}k^6-\frac{82906}{5457375}k^8-\frac{8334902}{760134375}k^{10}\right). \tag{74}$$

Найдем еще разложения производных. Сначала производную λ по k

$$\frac{d\lambda}{dk}=2k\sum_{l=0}^{\infty}a_{l+1}(l+1)k^{2l} \sim$$
$$-\frac{2}{3}k\left(1+\frac{8}{15}k^2+\frac{44}{105}k^4+\frac{1712}{4725}k^6+\frac{10196}{31185}k^8+\frac{21438136}{70945875}k^{10}\right), \tag{75}$$

затем обратную производную

$$\frac{dk}{d\lambda} \sim -\frac{3}{2}\frac{1}{k}\left(1-\frac{8}{15}k^2-\frac{212}{1575}k^4-\frac{176}{2625}k^6-\frac{13996}{336875}k^8-\frac{17013224}{591215625}k^{10}\right). \tag{76}$$

3.4. *Слабое рассеяние*. В противоположном предельном случае малых λ число k очень близко к единице. Удобно его представить в виде разложения

$$k=1-2y\sum_{n=0}^{\infty}(-1)^n y^n \sum_{m=0}^{n}(-1)^m b_{nm}x^m,$$
$$x=\frac{2}{\lambda},\quad y=e^{-x},\ b_{n0}=1. \tag{77}$$

Характеристическое уравнение представляется в виде

$$(1-k)x=\ln\left(1-\frac{1-k}{2}\right)-\ln\left(1+\frac{1-k-2y}{2y}\right). \tag{78}$$

Разложение логарифмов по степеням малых добавок к единице в их аргументах дает возможность последовательно находить коэффициенты b_{nm}. Первые из них

$$b_{11}=2,\quad b_{21}=b_{22}=6,\quad b_{31}=12,\quad b_{32}=32,\quad b_{33}=\frac{64}{3},$$
$$b_{41}=20,\quad b_{42}=100,\quad b_{43}=\frac{500}{3},\quad b_{44}=\frac{250}{3}, \tag{79}$$

$$b_{51}=30,\quad b_{52}=240,\quad b_{53}=720,\quad b_{54}=864,\quad b_{55}=\frac{1728}{5}, \tag{80}$$

$$b_{61}=42,\quad b_{62}=490,\quad b_{63}=\frac{6860}{3},\quad b_{64}=4802,\quad b_{65}=\frac{67228}{15},\quad b_{66}=\frac{67228}{45}, \tag{81}$$

$$b_{71}=56,\quad b_{72}=896,\quad b_{73}=\frac{17920}{3},\quad b_{74}=\frac{57344}{3},$$
$$b_{75}=\frac{458752}{15},\quad b_{76}=\frac{1048576}{45},\quad b_{77}=\frac{2097152}{315}. \tag{82}$$

При $\lambda=0.3$ последовательные слагаемые в разложении после единицы по модулю меньше, соответственно, $2.6\cdot10^{-3}$, $2.0\cdot10^{-5}$, $1.1\cdot10^{-5}$, $3.2\cdot10^{-7}$, $1.1\cdot10^{-8}$,

$3.0 \cdot 10^{-10}$ и $1.2 \cdot 10^{-11}$. Казалось бы, что с уменьшением вероятности выживания фотона точность разложения должна расти. Однако при малых значениях λ последовательные степени экспоненты быстро уменьшаются, но при них растут коэффициенты, которые являются многочленами той же степени от $2/\lambda$, что и степень экспоненты.

Первые два слагаемых в разложении (77) приведены в [12,13].

Составленная программа, включившая и разложения пунктов 3 и 4, обеспечивает получение значений k с точностью не менее 10 значащих цифр. Более подробные сведения о характеристическом числе и программа его вычисления помещены на сайте www.astro.spbu.ru.

4. *Полубесконечная среда.*

4.1. ***Функция Амбарцумяна.*** Функция, характеризующая отраженное от полубесконечной среды излучение, для изотропного рассеяния была введена Амбарцумяном [7], обозначена им $\varphi(\eta)$ и называется функцией Амбарцумяна. Аргумент $0 \le \eta \le 1$ обозначал косинус угла отражения. Здесь будем рассматривать эту функцию при любых неотрицательных аргументах z и отразим явно ее зависимость от вероятности выхода фотона λ, то есть - $\varphi(z,\lambda)$.

Функция была определена Амбарцумяном нелинейным уравнением, которому также присвоено имя его автора и которое может быть записано в двух формах:

$$\varphi(z,\lambda) = 1 + \frac{\lambda}{2} z\,\varphi(z,\lambda)\int_0^1 \frac{\varphi(z',\lambda)dz'}{z+z'}, \quad \frac{1}{\varphi(z,\lambda)} = \sqrt{1-\lambda} + \int_0^1 \frac{\varphi(z',\lambda)z'dz'}{z+z'}. \tag{83}$$

Путем численного решения этого уравнения многие авторы вычисляли функцию $\varphi(\eta,\lambda)$. Достаточно ее найти для $\eta \le 1$, для других значений z она может быть найдена с помощью того же уравнения. Наиболее точные значения получены в [14].

Явное выражение для этой функции было найдено Фоком [15]:

$$\ln\varphi(z,\lambda) = \ln H(1/\eta) = -\frac{z}{\pi}\int_0^\infty \ln(1-\lambda V(u))\frac{du}{1+z^2u^2}, \tag{84}$$

где вместо $V(u)$ надо подставить последнюю формулу из (60) (формула (84) написана в общем виде, справедливом для многих видов рассеяния). По этой формуле функция может быть вычислена при любых положительных z. Программа вычисления с описанием выложена на сайте www.astro.spbu.ru.

Графики функции при некоторых значениях λ даются на рис.6. Аргумент $z > 1$ заменен по формуле $z = 1/(2-\tilde{z})$. На том же рисунке изображена зависимость функции от $z = 1/k(\lambda) \ge 1$ с той же заменой, то есть приведены значения для $\tilde{z} = 2 - k$.

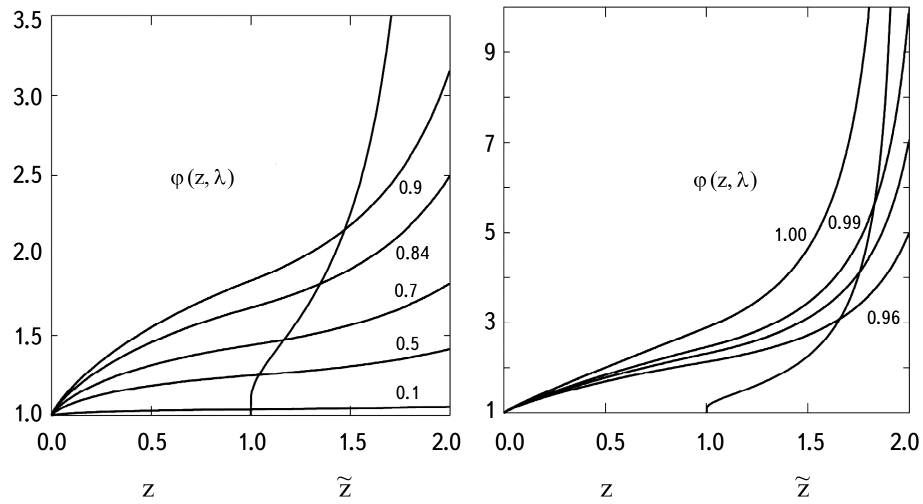

Рис.6. Графики функции $\varphi(z,\lambda)$ при некоторых λ (указаны около кривых, кроме 0.98). При $z>1$ дается зависимость от $\tilde{z}=2-1/z$. Кривая $\varphi(1/k,\lambda)$ ($k=2-\tilde{z}$) пересекает все кривые при $\lambda<1$.

4.2. *Моменты функции Амбарцумяна.* Представляют интерес моменты целого порядка

$$\alpha_n(\lambda)=\int_0^1 \varphi(z,\lambda)z^n dz. \tag{85}$$

Аналитические выражения известны для нулевого и регуляризованного минус-первого моментов (см., например, [12]):

$$\alpha_0(\lambda)=\frac{2}{\lambda}\left(1-\sqrt{1-\lambda}\right),\quad \alpha_{-1}(\lambda)=\int_0^1 \frac{\varphi(z,\lambda)-1}{z}dz=2\ln\varphi(1,\lambda). \tag{86}$$

При переходе от первой формы уравнения в (83) ко второй использовано выражение для $\alpha_0(\lambda)$.

На рис.7 представлены графики моментов от минус первого до десятого в зависимости от величины λ. Кривая минус-первого момента пересекает все остальные кривые.

Моменты являются коэффициентами в разложении при $z>1$:

$$\frac{1}{\varphi(z,\lambda)}=\sqrt{1-\lambda}+\frac{\lambda}{2}\frac{1}{z}\sum_{l=0}^{\infty}\frac{(-1)^l}{z^l}\alpha_{l+1}(\lambda). \tag{87}$$

По этому разложению можно вычислять функцию при достаточно больших z.

4.3. *Поведение при слабом рассеянии.* Если рассеяние отсутствует, то есть $\lambda=0$, то тождественно $\varphi(z,0)=1$. При малых $\lambda \ll 1$ должно выполняться разложение

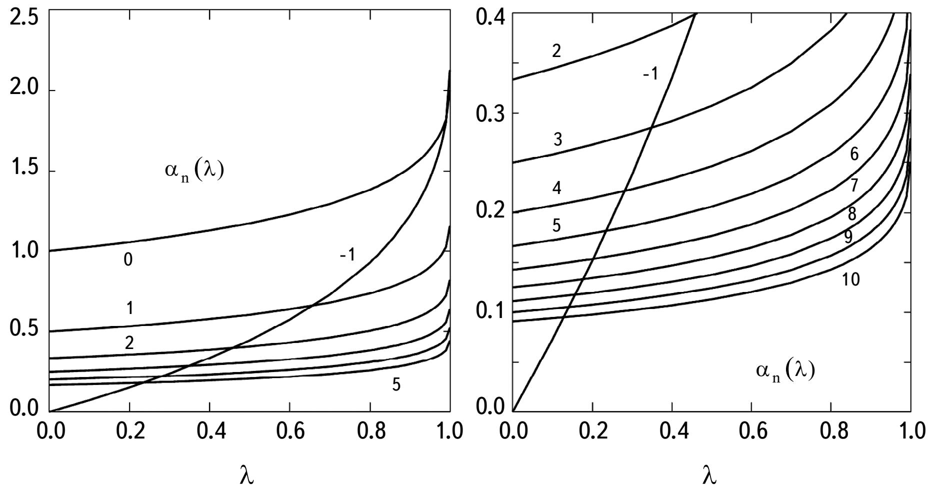

Рис.7. Моменты $\alpha_n(\lambda)$ как функции λ (номера, кроме 3 и 4, указаны около кривых).

$$\varphi(z,\lambda)=\sum_{l=0}^{\infty} a_l(z)\lambda^l = 1 + a_1(z)\lambda + a_2(z)\lambda^2 + ..., a_0(z)=1. \tag{88}$$

Подставив это разложение в нелинейное уравнение, получим рекуррентное соотношение

$$a_l(z)=\delta_{l,0}+\frac{z}{2}\sum_{l'=0}^{l-1} a_{l'}(z)\int_0^1 \frac{dz'}{z+z'}a_{l-1-l'}(z'). \tag{89}$$

Легко находятся значения всех коэффициентов на бесконечности:

$$a_l(\infty)=\frac{(2l-1)!!}{(2l)!!},\quad a_1(\infty)=\frac{1}{2},\quad a_2(\infty)=\frac{3}{8},\quad a_3(\infty)=\frac{5}{16},\quad a_4(\infty)=\frac{35}{128},... \tag{90}$$

Введем для удобства обозначения для интеграла, его значения в нуле и предела:

$$\overline{a}_l(z)=\frac{1}{2}\int_0^1 \frac{dz'}{z+z'}a_{l-1}(z'),\quad \overline{a}_l(0)=\frac{1}{2}\int_0^1 dz\frac{a_{l-1}(z)}{z},\quad \lim_{z\to\infty} z\overline{a}_l(z)=\widetilde{a}_l=\frac{1}{2}\int_0^1 dz a_{l-1}(z). \tag{91}$$

Только первый коэффициент находится явно:

$$a_1(z)=\frac{z}{2}\int_0^1 \frac{dz'}{z+z'}=\frac{z}{2}\ln\frac{1+z}{z}. \tag{92}$$

Все остальные приходится находить численно, хотя при выделенных значениях z удается найти точные значения, как и на бесконечности.

Второй коэффициент, как и все последующие, содержит интеграл от предыдущего коэффициента:

$$a_2(z)=\frac{z}{2}\left[\int_0^1 a_1(z')\frac{dz'}{z+z'}+a_1(z)\int_0^1\frac{dz'}{z+z'}\right]=z\left[\overline{a}_2(z)+z\overline{a}_1^2(z)\right]. \tag{93}$$

Однако при $z=1$ оба коэффициента вычисляются: $a_1(1)=\ln 2/2$,

$$a_2(1)=\overline{a}_2(1)+\frac{\ln^2 2}{4}=\frac{\ln^2 2}{8}+\frac{\ln 2}{2}-\frac{\pi^2}{48}. \tag{94}$$

По рекуррентной формуле

$$a_3(z)=\frac{z}{2}\left[a_0\int_0^1\frac{dz'}{z+z'}a_2(z')+a_1(z)\int_0^1\frac{dz'}{z+z'}a_1(z')+a_2(z)\int_0^1\frac{dz'}{z+z'}\right]. \tag{95}$$

Последние два интеграла уже известны, остается вычислить один интеграл:

$$a_3(z)=z\overline{a}_3(z)+a_1(z)\left[2a_2(z)-a_1^2(z)\right]=z\overline{a}_3(z)+z^2\overline{a}_1(z)\left[2\overline{a}_2(z)+z\overline{a}_1^2(z)\right]. \tag{96}$$

Аналогично третьему

$$a_4(z)=\frac{z}{2}\int_0^1\frac{dz'}{z+z'}a_3(z')+2a_1(z)a_3(z)-3a_1^2(z)a_2(z)+a_2^2(z)+a_1^4(z). \tag{97}$$

Как видно из выражений для коэффициентов, внеинтегральные суммы состоят из слагаемых, у которых суммы индексов сомножителей равны номерам коэффициентов.

Графики зависимости первых четырех коэффициентов приведены на рис.8.

Коэффициенты при $z=1$ можно использовать для легкого определения значений $\varphi(1/k(\lambda))$ при небольших λ, так как при таких λ значения $k(\lambda)$

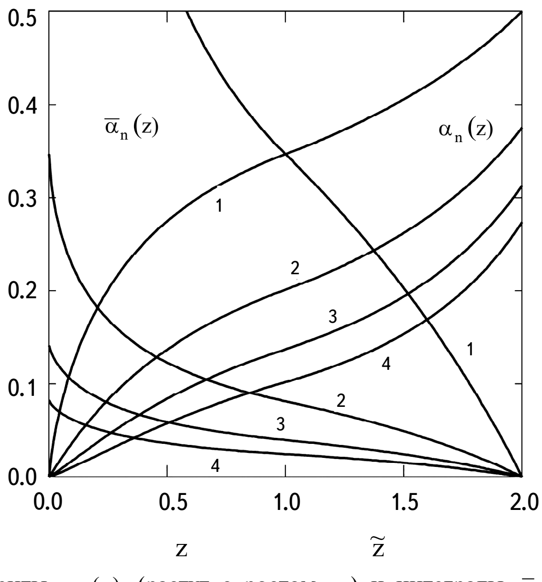

Рис.8, Коэффициенты $\alpha_n(z)$ (растут с ростом z) и интегралы $\overline{a}_n(z)$ (убывают) при $n=1$, 2, 3, 4 (указаны около кривых). При $z>1$, как и на рис.6, сделана замена $z=1/(2-\widetilde{z})$.

очень близки к единице. С точностью до четвертой степени λ

$$\varphi_{apr}\left(\frac{1}{k(\lambda)}\right)=1+\lambda\, a_1(1)+\lambda^2\, a_2(1)+\lambda^3\, a_3(1)+\lambda^4\, a_4(1). \tag{98}$$

При $\lambda<0.3$ формула дает не меньше четырех верных знаков, при $\lambda<0.5$ - не меньше трех.

4.4. *Другие функции*. Приведем выражение для резольвентной функции:

$$\Phi(\tau)=C_0 e^{-k(\tau+\tau_e)}+\frac{\lambda}{2}\int_0^1 \frac{\exp(-\tau/\eta)}{\left[1-\frac{\lambda}{2}\eta\ln\frac{1+\eta}{1-\eta}\right]^2+\left[\frac{\lambda\pi}{2}\eta\right]^2}\frac{d\eta}{\varphi(\eta,\lambda)\eta},\quad C_0=\sqrt{2k^2\frac{1-k^2}{\lambda-1+k^2}}. \tag{99}$$

Эти функции исследовались многими авторами (см., например, [12,16]). Они заслуживают нового подробного рассмотрения в отдельной статье.

Здесь отметим, что очень просто получить асимптотики для чистого рассеяния ($\lambda\to 1$, $\tau>>1$ подразумевается). Достаточно в формулы части I подставить приведенные выше разложения. Например, по формуле (I.78)

$$\Psi(\tau)\sim\frac{1}{\sqrt{1-\lambda}}-\frac{C_0}{k}e^{-k(\tau+\tau_e)}\sim\sqrt{3}(\tau+\tau_e(1))+k\sqrt{3}\left[\frac{3}{10}-\frac{(\tau+\tau_e(1))^2}{2}\right]. \tag{100}$$

Через $\tau_e(1)=0.710446$ можно записать асимптотическую формулу для функции $\varphi(z,\lambda)$ при больших z и близких к единице λ:

$$\frac{1}{\varphi(z,\lambda)}\sim\frac{1+kz}{z\sqrt{3}}\left[1-\frac{\tau_e(1)}{z}+\frac{2}{15}k^2-\left(\frac{3}{10}+\frac{\tau_e^2(1)}{2z^2}\right)\right]. \tag{101}$$

Формула объединяет (7.26) и (7.27) из [12,13].

5. *Изотропное монохроматическое рассеяние в оптически толстом слое.*

5.1. *Асимптотики чисел рассеяния.* Все общие формулы части I справедливы, достаточно использовать приведенные выше разложения. Приведем для примера асимптотики чисел рассеяния фотонов, рожденных на границах слоя. Они выражаются согласно формулам (I.48) через логарифмические производные от вероятностей выхода фотонов до вероятности их выживания при каждом рассеянии.

Отметим особенности обозначений. Вероятность выхода $P(\tau,\tau_0)$ предполагает выход фотона через границу $\tau=0$, так что полная вероятность (через обе границы) равна сумме $\mathcal{P}(\tau,\tau_0)=P(\tau,\tau_0)+P(\tau_0-\tau,\tau_0)$. Число же рассеяний $N(\tau,\tau_0)$ - через обе границы. Различие границ для числа рассеяний отражается дополнительными значками $\pm$: $N_+(\tau,\tau_0)$ - выход фотона, рожденного на глубине τ, через верхнюю границу, а $N_-(\tau,\tau_0)$ - через нижнюю. Очевидны соотношения $\mathcal{P}(\tau,\tau_0)=\mathcal{P}(\tau_0-\tau,\tau_0)$, $N_+(\tau,\tau_0)=N_-(\tau_0-\tau,\tau_0)$.

Найдем производные по λ от асимптотик (I.70) и (I.71):

$$P(0,\tau_0)\sim 1-\sqrt{1-\lambda}\,\mathrm{cth}\,k(\tau_0+2\tau_e),\quad P(\tau_0,\tau_0)\sim\frac{\sqrt{1-\lambda}}{\mathrm{sh}\,k(\tau_0+2\tau_e)}. \tag{102}$$

Сначала для нижней границы

$$\frac{\partial P(\tau_0,\tau_0)}{\partial\lambda}=-\frac{1}{2}\frac{1}{\sqrt{1-\lambda}}\frac{1}{\mathrm{sh}\,k(\tau_0+2\tau_e)}-\sqrt{1-\lambda}\,\frac{\mathrm{ch}\,k(\tau_0+2\tau_e)}{\mathrm{sh}^2\,k(\tau_0+2\tau_e)}\mathcal{D}(\lambda,\tau_0), \tag{103}$$

где (отрицательный множитель (I.91))

$$\mathcal{D}(\lambda,\tau_0)=\frac{dk}{d\lambda}(\tau_0+2\tau_e)+2k\frac{d\tau_e}{d\lambda}. \tag{104}$$

Затем для верхней

$$\frac{\partial P(0,\tau_0)}{\partial\lambda}=\frac{1}{2}\frac{1}{\sqrt{1-\lambda}}\mathrm{cth}\,k(\tau_0+2\tau_e)+\frac{\sqrt{1-\lambda}}{\mathrm{sh}^2\,k(\tau_0+2\tau_e)}\mathcal{D}(\lambda,\tau_0). \tag{105}$$

По этим производным находим асимптотики средних чисел рассеяния:

$$N(\tau_0,\tau_0)=\frac{\lambda}{P(\tau_0,\tau_0)}\frac{\partial P(\tau_0,\tau_0)}{\partial\lambda}=-\frac{1}{2}\frac{1}{1-\lambda}-\mathrm{cth}\,k(\tau_0+2\tau_e)\mathcal{D}(\lambda,\tau_0), \tag{106}$$

$$N(0,\tau_0)=\frac{\lambda}{P(0,\tau_0)}\frac{\partial P(0,\tau_0)}{\lambda}. \tag{107}$$

Последнее выражение не упрощается при подстановке асимптотики вероятности.

5.2. *Разложения по степеням k и асимптотики при чистом рассеянии*. Получим разложения величин по степеням k, используя, в частности,

$$\tau_e\sim\tau_e(1)+\tau_e'(1)(\lambda-1)\sim\tau_e(1)-\tau_e'(1)\frac{k^2}{3}. \tag{108}$$

Затем разложение

$$\mathcal{D}(\lambda,\tau_0)\sim-\frac{3}{2}\frac{1}{k}\left[[\tau_0+2\tau_e(1)]\left(1-\frac{8}{15}k^2\right)-2\tau_e'(1)k^2\right]. \tag{109}$$

С их помощью получаем разложения вероятностей выхода с границ и полную вероятность:

$$P(\tau_0,\tau_0)\sim\frac{1}{\sqrt{3}[\tau_0+2\tau_e(1)]}\left[1+\frac{k^2}{3}\left(\frac{2}{5}-\frac{[\tau_0+2\tau_e(1)]^2}{2}+2\frac{\tau_e'(1)}{\tau_0+2\tau_e(1)}\right)\right], \tag{110}$$

$$P(0,\tau_0)\sim 1-\frac{1}{\sqrt{3}[\tau_0+2\tau_e(1)]}\left[1+\frac{k^2}{3}\left([\tau_0+2\tau_e(1)]^2+\frac{2}{5}+2\frac{\tau_e'(1)}{\tau_0+2\tau_e(1)}\right)\right], \tag{111}$$

$$\mathcal{P}(\tau_0) \sim 1 - \frac{k^2}{2\sqrt{3}}\left[\tau_0 + 2\tau_e(1)\right]. \tag{112}$$

Асимптотики верны, если $k\tau_0 \ll 1$.

Дифференцирование асимптотик по λ выполняется очень просто, так что при чистом рассеянии

$$\frac{dP(\tau_0,\tau_0)}{d\lambda} = \frac{\sqrt{3}}{6}\left[\tau_0 + 2\tau_e(1)\right]\left(1 - \frac{4}{5}\frac{1}{\left[\tau_0 + 2\tau_e(1)\right]^2} - \frac{4\tau_e'(1)}{\left[\tau_0 + 2\tau_e(1)\right]^3}\right), \tag{113}$$

$$\frac{dP(0,\tau_0)}{d\lambda} = \frac{\sqrt{3}}{3}\left[\tau_0 + 2\tau_e(1)\right]\left(1 + \frac{2}{5}\frac{1}{\left[\tau_0 + 2\tau_e(1)\right]^2} + \frac{2\tau_e'(1)}{\left[\tau_0 + 2\tau_e(1)\right]^3}\right), \tag{114}$$

$$\frac{d\mathcal{P}(\tau_0)}{d\lambda} = \frac{\sqrt{3}}{2}\left[\tau_0 + 2\tau_e(1)\right]. \tag{115}$$

Для средних чисел рассеяния получается

$$N_+(\tau_0,\tau_0) = \frac{\left[\tau_0 + 2\tau_e(1)\right]^2}{2}\left(1 - \frac{4}{5}\frac{1}{\left[\tau_0 + 2\tau_e(1)\right]^2} - \frac{4\tau_e'(1)}{\left[\tau_0 + 2\tau_e(1)\right]^3}\right), \tag{116}$$

$$N_+(0,\tau_0) = \frac{\sqrt{3}}{3}\frac{\left[\tau_0 + 2\tau_e(1)\right]}{1 - \dfrac{1}{\sqrt{3}\left[\tau_0 + 2\tau_e(1)\right]}}\left(1 + \frac{2}{5}\frac{1}{\left[\tau_0 + 2\tau_e(1)\right]^2} + \frac{2\tau_e'(1)}{\left[\tau_0 + 2\tau_e(1)\right]^3}\right), \tag{117}$$

$$N(0,\tau_0) = P(0,\tau_0)N_+(0,\tau_0) + P(\tau_0,\tau_0)N_+(\tau_0,\tau_0) = \frac{\sqrt{3}}{2}\left[\tau_0 + 2\tau_e(1)\right]. \tag{118}$$

Все поправки к приведенным асимптотикам имеют порядок $e^{-\tau_0}$.

Получению асимптотик при переходе к чистому рассеянию было посвящено несколько статей разных авторов (см., например, [17,18]). Здесь разделены фотоны, выходящие через определенные границы, и систематически использована экстраполированная длина.

6. *Заключение*. В статье получены точные выражения для всех значимых характеристик изотропного рассеяния в одномерной среде, полубесконечной и конечной, включая резольвенты основных интегральных уравнений. При этом известные ранее формулы представлены в новой форме: они содержат экстраполированную длину. Это позволило очень просто перейти к пределу чистого рассеяния. Приведены точные аналитические выражения для вероятностей выхода и средних чисел рассеяния фотонов в конечной среде, выходящих через одну или другую границы. Продемонстрировано, что асимптотические формулы для характеристик полей излучения в трехмерной среде по виду совпадают с точными формулами для тех же характеристик одномерной

среды. Формулы применяются для случая степенных источников излучения.

Для изотропного рассеяния в трехмерных средах приведены основные функции и константы, входящие в характеристики излучения: ядро интегрального уравнения, характеристическое число k, экстраполированная длина τ_e, разложения k при близких к единице и малых λ, производные по λ от этих же констант. Затем приводятся графики функции Амбарцумяна $\varphi(z,\lambda)$ и ее моментов, а также первых четырех коэффициентов разложения этой функции по степеням λ при $\lambda \ll 1$.

Для рассеяния в оптически толстом плоском слое получены асимптотики средних чисел рассеяния фотонов, возникших на одной из границ и вышедших из слоя через ту же или другую границы, при чистом рассеянии и близком к нему.

Санкт-Петербургский государственный университет,
e-mail: dinagirner@gmail.com

THE ESCAPE PROBABILITY AND MEAN NUMBERS OF SCATTERINGS OF PHOTONS. II. MONOCHROMATIC ISOTROPIC SCATTERING IN ONE-DIMENSIONAL MEDIUM AND PLANE MEDIA

D.I.NAGIRNER, A.V.DEMENTYEV, E.V.VOLKOV

As examples of application of formulas of the part I the scattering in one-dimensional medium is considered for which all characteristics of radiation field are expressed in elementary functions. Isotropic monochromatic photon scattering in three-dimensional media is considered as well. Some features of the Ambartsumian function are studied and the asymptotics of the mean photon scattering numbers in optically thick layer are derived.

Keywords: *radiation transfer: mean numbers of scatterings of photons*

ЛИТЕРАТУРА

1. *Д.И.Нагирнер*, *Ю.В.Миланова*, *А.В.Дементьев и др.*, Астрофизика, **65**, 587, 2022, (Astrophysics, **65**, 560, 2022).
2. *В.В.Соболев*, "Перенос лучистой энергии в атмосферах звезд и планет", М., ГИТТЛ, 1956.
3. *В.А.Амбарцумян*, ДАН Арм. ССР, **8**, 101, 1948.
4. *В.В.Соболев*, Астрофизика, **2**, 135, 1966, (Astrophysics, **2**, 69, 1966).
5. *М.Л.Тер-Микаелян*, ДАН Арм. ССР, **8**, 149, 1948.
6. *С.Чандрасекар*, "Перенос лучистой энергии", М., ИЛ, 1953, ("Radiative transfer", Oxford: Clarendon Press, 1950).
7. *В.А.Амбарцумян*, ЖЭТФ, **12**, 323, 1943.
8. *В.А.Амбарцумян*, Астрон. ж., **19**, 30, 1942.
9. *В.А.Амбарцумян*, "Научные труды. Том I", Ереван, АН Армении, 1960.
10. *О.Д.Хвольсон*, Ж. Русск. физ.-хим. об-ва, **22**, 1, 1890.
11. *T.Viik*, Astrophys. Space Sci., **127**, 285, 1986.
12. *В.В.Иванов*, "Перенос излучения и спектры небесных тел", М., Наука, 1969.
13. *V.V.Ivanov*, "Transfer of Radiation in Spectral Lines", NBS, 1973.
14. *K.Kawabata*, Astrophys. Space Sci., **363**, 17, 2018.
15. *В.А.Фок*, Мат. сборник, **14**, 3, 1944.
16. *D.I.Nagirner*, Astrophys. Space Phys. Rev., **13**, 1, 2006.
17. *В.В.Соболев*, Астрон. ж., **41**, 97, 1964.
18. *В.В.Соболев*, "Рассеяние света в атмосферах планет", М., Наука, 1972. ("Light Scattring in Planetary Atmospheres", Oxford: Pergamon Press; 1975).

А С Т Р О Ф И З И К А

ТОМ 67 АВГУСТ, 2024 ВЫПУСК 3

DOI: 10.54503/0571-7132-2024.67.3-409

PLANE SYMMETRIC GRAVITATIONAL FIELDS IN (D+1)-DIMENSIONAL GENERAL RELATIVITY

R.M.AVAGYAN[1,2], T.A.PETROSYAN[1], A.A.SAHARIAN[1,2], G.H.HARUTYUNYAN[1]

Received 19 June 2024

We consider plane symmetric gravitational fields within the framework of General Relativity in (D+1)-dimensional spacetime. Two classes of vacuum solutions correspond to higher-dimensional generalizations of the Rindler and Taub spacetimes. The general solutions are presented for a positive and negative cosmological constant as the only source of the gravity. Matching conditions on a planar boundary between two regions with distinct plane symmetric metric tensors are discussed. An example is considered with Rindler and Taub geometries in neighboring half-spaces. As another example, we discuss a finite thickness cosmological constant slab embedded into the Minkowski, Rindler and Taub spacetimes. The corresponding surface energy-momentum tensor is found required for matching the exterior and interior geometries.

Keywords: *plane symmetric gravitational fields: Taub's solution: Rindler's spacetime: cosmological constant*

1. *Introduction*. Exact solutions of Einstein's equations for the gravitational field are available only in geometries with relatively high symmetry (for reviews see [1,2]). In particular, they include spherical, axial and planar symmetric configurations. Another classes of solutions with maximally symmetric subspaces are used in cosmology. Despite their apparent simplicity, plane symmetric solutions remain an active subject of research. The investigations are motivated by interesting geometrical properties of those solutions and by their applications in different areas of gravitational physics. The latter include the domain wall type topological defects in field theories [3] and branes in string theory and in braneworld models with extra dimensions [4-6].

The static plane-symmetric vacuum solutions of Einstein's equations were already known in the early days of the development of the General Relativity [7] and were rediscovered later in [8]. Two classes of solutions are present. The first one corresponds to the Rindler spacetime and describes a flat geometry. It approximates the gravitational field near the black hole horizon and is among the most popular geometries in quantum field theory on backgrounds with horizons (see, for example, [9]). The second class of single parameter solutions corresponds to the Taub geometry. The characteristic feature of the latter is the presence of a curvature singularity on a plane with a fixed value of the coordinate along which the geometry is inhomogeneous. The test particle is repelled by the singularity. The nature of the singularity, the other properties of the Taub solution and its generalizations in the presence of the matter sources have been widely discussed in the literature (see, e.g., [10-34] and references therein). In the present paper we discuss several aspects of plane-symmetric static solutions in (D+1)-dimensional General Relativity. Higher dimensional gravitational configurations with planar symmetry appear in a number of models including braneworld scenarios, Anti-de Sitter/Conformal field theory (AdS/CFT) correspondence and fundamental branes in string theories and supergravity.

The organization of the paper is as follows. In the next section, the background geometry, gravitational field equations and the matching conditions in problems with different metric tensors in separate regions are presented. In Section 3 two classes of vacuum solutions corresponding to the Rindler and Taub spacetimes are considered. The solutions with a cosmological constant (CC) as the only source in the gravitational field equations are discussed in Section 4. In Section 5 we consider a slab with CC interior and with different exterior geometries. The corresponding surface energy-momentum tensors required by the matching conditions on the slab boundaries are given.

2. *Background geometry, the field equations and matching conditions*. We consider a plane symmetric (D+1)-dimensional spacetime with the line element

$$ds^2 = e^{2u_0}dt^2 - e^{2u_1}dx^2 - e^{2u_2}\sum_{i=2}^{D}\left(dx^i\right)^2, \tag{1}$$

where $x^1 = x$, $u_l = u_l(x)$, $l = 0,\ 1,\ 2$. The nonzero components of the Ricci tensor are given by the expressions

$$\begin{aligned} R_0^0 &= e^{-2u_1}\left[u_0'' + u_0'^2 - u_0'u_1' + (D-1)u_0'u_2'\right], \\ R_1^2 &= e^{-2u_1}\left[u_0'' + u_0'^2 - u_1'u_0' - (D-1)\left(u_2'' + u_2'^2 - u_0'u_2'\right)\right], \\ R_2^2 &= e^{-2u_1}\left[u_2'' + u_0'u_2' - u_1'u_2' + (D-1)u_2'^2\right], \end{aligned} \tag{2}$$

and (no summation over i) $R_i^i = R_2^2$ for $i = 3,\ \ldots,\ D$. Here, the prime stands for the derivative with respect to the coordinate x. The Ricci scalar is expressed as

$$R = 2e^{-2u_1}\left[u_0'' + u_0'^2 - u_0'u_1' + (D-1)\left(u_2'' + u_0'u_2' - u_1'u_2' + \frac{D}{2}u_2'^2\right)\right]. \tag{3}$$

For discussion of geodesic motion one needs also to have the Christoffel symbols. The expressions for the corresponding nonzero components read (no summation over $i = 2,\ 3,\ \ldots,\ D$)

$$\Gamma^0_{01} = \Gamma^0_{10} = u'_0\,, \quad \Gamma^1_{00} = e^{2(u_0-u_1)}u'_0\,, \quad \Gamma^1_{11} = u'_1\,,$$
$$\Gamma^1_{ii} = -e^{2(u_2-u_1)}u'_2\,, \quad \Gamma^i_{1i} = \Gamma^i_{i1} = u'_2\,. \tag{4}$$

The i th component of the acceleration for a test particle is given by $a^i = -\Gamma^i_{kl}\, w^k w^l$ with $w^i = dx^i/ds$ being the (D+1)-velocity. For a test particle at rest one has $w^i = \delta^i_0\, e^{-u_0}$ and the acceleration is directed along the x-axis with $a^i = d^2x^i/ds^2 = -\delta^i_1\, e^{-2u_1} u'_0$.

For the gravitational field equations $R^k_i - \delta^k_i\, R/2 = 8\pi G T^k_i$, with T^k_i being the metric energy-momentum tensor, we get

$$-\frac{8\pi G T^0_0 e^{2u_1}}{D-1} = u''_2 + \frac{D}{2}u'^2_2 - u'_1 u'_2\,, \quad -\frac{8\pi G T^1_1 e^{2u_1}}{D-1} = u'_2\left(u'_0 + \frac{D-2}{2}u'_2\right),$$
$$-8\pi G T^2_2 e^{2u_1} = u''_0 + u'^2_0 - u'_0 u'_1 + (D-2)\left(u''_2 + u'_0 u'_2 - u'_1 u'_2 + \frac{D-1}{2}u'^2_2\right). \tag{5}$$

In accordance with the problem symmetry one has (no summation over i) $T^i_i = T^2_2$ for $i=3, \ldots, D$. Note that the quantity $-T^i_i$, $i=1, 2, \ldots, D$, presents the effective pressure along the i th spatial dimension. From the covariant conservation equation $\nabla_k T^k_i = 0$ one finds

$$T^{1'}_1 + \left(T^1_1 - T^0_0\right)u'_0 + (D-1)\left(T^1_1 - T^2_2\right)u'_2 = 0\,. \tag{6}$$

This equation does not contain the function $u_1(x)$. For a source with barotropic equation of state, $T^i_i = -w_i T^0_0$ with constants w_i, we get

$$T^1_1 = \mathrm{const}\cdot\exp\left[-\left(\frac{1}{w_1}+1\right)u_0 + (D-1)\left(\frac{w_2}{w_1}-1\right)u_2\right]. \tag{7}$$

In this case the components of the energy-momentum tensor, as functions of the coordinate x, do not change the sign.

The function $u_1(x)$ in (1) can be fixed by the choice of the coordinate x. The field equations are essentially simplified taking

$$u_1(x) = 0\,. \tag{8}$$

This gives

$$-\frac{8\pi G T^0_0}{D-1} = u''_2 + \frac{D}{2}u'^2_2, \quad -\frac{8\pi G T^1_1}{D-1} = u'_2\left(u'_0 + \frac{D-2}{2}u'_2\right),$$
$$-8\pi G T^2_2 = u''_0 + u'^2_0 + (D-2)\left(u''_2 + u'_0 u'_2 + \frac{D-1}{2}u'^2_2\right). \tag{9}$$

From these equations the following relations can be obtained:

$$\left[u_0' e^{u_0+(D-1)u_2}\right]' = \frac{8\pi G}{D-1}\left[(D-2)T_0^0 - T_1^1 - (D-1)T_2^2\right] e^{u_0+(D-1)u_2} ,$$
$$\left[u_0' e^{u_0+(D-1)u_2}\right]' = -\frac{8\pi G}{D-1}\left(T_0^0 + T_1^1\right) e^{u_0+(D-1)u_2} . \tag{10}$$

Note that $e^{u_0+(D-1)u_2} = \sqrt{|g|}$ with g being the determinant of the metric tensor g_{ik}. Additionally, by combining the equations (10) we get

$$\left[e^{u_0+(D-1)u_2}\right]'' = -\frac{8\pi G}{D-1}\left[T_0^0 + DT_1^1 + (D-1)T_2^2\right] e^{u_0+(D-1)u_2} . \tag{11}$$

The integration of relations (10) and (11) give conditions for the energy-momentum tensor to be compatible with given solutions for $u_0(x)$ and $u_2(x)$.

By using the set of equations (9) we can derive the matching conditions for the components of the metric tensor in problems where the geometry is described by two distinct metric tensors in regions separated by a planar boundary. As a separating boundary we take a hyperplane $x = L$. The energy-momentum tensor is decomposed into two contributions:

$$T_i^k = T_{(v)i}^k + T_{(s)i}^k , \quad T_{(s)i}^k = \tau_i^k \delta(x - L). \tag{12}$$

Here, $T_{(v)i}^k$ is the volume part and $T_{(s)i}^k$ corresponds to the surface energy-momentum tensor localized on the interface $x = L$. Generally, the volume part is different in the regions $x < L$ and $x > L$. Assuming that the metric tensor is continuous at $x = L$, the discontinuities in its first order derivatives are found by integrating the equations (9) in the region $[L-\varepsilon, L+\varepsilon]$, $\varepsilon > 0$, and then taking the limit $\varepsilon \to 0$. The continuity conditions for the metric tensor read

$$u_0\big|_{L_-}^{L_+} = \lim_{\varepsilon\to 0}\left[u_0(L+\varepsilon) - u_0(L-\varepsilon)\right] = 0 , \quad u_2\big|_{L_-}^{L_+} = 0 . \tag{13}$$

Under these conditions, by taking into account that $\lim_{\varepsilon\to 0}\int_{L-\varepsilon}^{L+\varepsilon} dx u_l'^2 = 0$ and $\lim_{\varepsilon\to 0}\int_{L-\varepsilon}^{L+\varepsilon} dx u_0' u_2' = 0$, for the first order derivatives we get

$$u_0'\big|_{L_-}^{L_+} = 8\pi G\left(\frac{D-2}{D-1}\tau_0^0 - \tau_2^2\right), \quad u_2'\big|_{L_-}^{L_+} = -\frac{8\pi G}{D-1}\tau_0^0 , \quad \tau_1^1 = 0 . \tag{14}$$

The discontinuities in the derivatives of the metric tensor are completely determined by the surface energy-momentum tensor. The corresponding conditions can also be obtained from the Israel matching conditions in terms of the extrinsic curvature tensor of the separating boundary.

3. *Vacuum solutions*. We start with the vacuum solutions of the set of equations (9). For them one has $T_i^k = 0$. By having the coordinate x fixed by the condition (8), we have two possibilities. For the first one $u_2' = 0$ and the first and second equations in (9) are satisfied identically. From the last equation we

get $u_0''+u_0'^2=0$. The solution $u_0'=0$ corresponds to a flat spacetime in the Minkowskian coordinates. The solution for $u_0'\neq 0$ is obtained after a simple integration: $e^{2u_0}=(x+C)^2$. Taking $C=0$ we get the line element

$$ds_R^2=x^2dt_R^2-dx^2-\sum_{i=2}^{D}\left(dx^i\right)^2, \tag{15}$$

which corresponds to the Rindler spacetime. Note that in the representation (15) the Rindler time coordinate t_R is dimensionless. Introducing new coordinates (T, X) in accordance with $T=x\sinh t_R$, $X=\mathrm{sgn}(X)x\cosh t_R$, the line element (15) takes the Minkowskian form. The coordinates ($t_R, x, x^2, \ldots, x^D$) cover the Rindler wedges $|X|>|T|$ of the Minkowski spacetime. The worldline with fixed ($x, x^2, \ldots, x^D$) describes a uniformly accelerated observer having the proper acceleration $1/x$. The hypersurface $x=0$ corresponds to the Rindler horizon.

For the second class of the vacuum solutions we have $u_2'\neq 0$ and from the first equation in (9) we find $e^{2u_2}=\mathrm{const}\cdot|x+C|^{4/D}$. With this function $u_2(x)$, the second equation gives $e^{2u_0}=\mathrm{const}\cdot|x+C|^{-2(D-2)/D}$. For these expressions of $u_0(x)$ and $u_2(x)$ the last equation in (9) is obeyed identically. Specifying the constants, the solution is presented in the Taub form:

$$ds_T^2=|1-\sigma x|^{-2(2-D)/D}dt^2-dx^2-|1-\sigma x|^{4/D}\sum_{i=2}^{D}\left(dx^i\right)^2, \tag{16}$$

where σ is another constant. This solution has a singularity at $x=1/\sigma$. For $D=3$ it is reduced to the Taub solution in General Relativity. The higher dimensional generalization of the Taub solution has also been considered in [27]. For a test particle at rest with the coordinate x, the acceleration in the geometry (16) is expressed as $a^i=\delta_1^i(1-2/D)/(x-1/\sigma)$. This corresponds to the repulsion from the wall at $x=1/\sigma$ in both regions $x<1/\sigma$ and $x>1/\sigma$. Introducing the notations

$$n_D=2\frac{D-1}{D},\quad \sigma'=n_D^{(D-2)/2(D-1)}\sigma, \tag{17}$$

and new coordinates x'^i in accordance with

$$t'=n_D^{(2-D)/2(D-1)}t,\quad 1-\sigma' x'=\frac{(1-\sigma x)^{n_D}}{n_D},\quad x'^i=n_D^{1/(D-1)}x^i,\quad i=2,\ldots,D, \tag{18}$$

the line element is written in the form

$$ds_T^2=|1-\sigma' x'|^{(2-D)/(D-1)}\left(dt'^2-dx'^2\right)-|1-\sigma' x'|^{2/(D-1)}\sum_{i=2}\left(dx'^i\right)^2. \tag{19}$$

As a simple example with two different metric tensors in the regions $x>0$ and $x<0$, we take $ds^2=ds_T^2$ in the region $x<0$ (given by (16) with $\sigma>0$) and

$$ds_R^2 = (1 + x/b)^2\, dt^2 - dx^2 - \sum_{i=2}^{D} (dx^i)^2 , \tag{20}$$

in the region $x > 0$. The latter corresponds to the Rindler spacetime and is obtained from (15) redefining $x \to x + b$ and passing to a new time coordinate $t = bt_R$. For both regions $T_{(v)i}^k = 0$ and the metric tensor is regular. From (14) one gets the surface energy-momentum tensor required by the matching conditions:

$$8\pi G \tau_0^0 = -2\sigma \frac{D-1}{D}, \quad \tau_1^1 = 0, \quad 8\pi G \tau_2^2 = -\frac{1}{b} - \sigma \frac{D-2}{D}. \tag{21}$$

Note that the corresponding energy density is negative. In the special case $\sigma = 1/b$ we obtain $\tau_2^2 = \tau_0^0$ and τ_i^k describes a CC-type source localized on the plane $x = 0$.

4. *Solutions with cosmological constant*. In this section we consider the solutions of the gravitational field equations (9) with the CC Λ as the only source. For the corresponding energy-momentum tensor one has

$$T_i^k = T_{(\Lambda)i}^k = \frac{\Lambda}{8\pi G} \delta_i^k . \tag{22}$$

4.1. *AdS spacetime*. For a negative CC from the first equation we have a special solution

$$u_2' = \pm \frac{1}{a}, \quad a = \sqrt{\frac{D(D-1)}{2|\Lambda|}} . \tag{23}$$

With this solution, the second equation in (9) gives $u_0' = \pm 1/a$. The third equation is automatically satisfied. Fixing the integration constants, the line element corresponding to this solution takes the form

$$ds^2 = e^{\pm 2x/a} \left[dt^2 - \sum_{i=2}^{D} (dx^i)^2 \right] - dx^2 . \tag{24}$$

This line element describes AdS spacetime in Poincaré coordinates. Introducing a new coordinate $z = \mp a e^{\mp x/a}$, $-\infty < \pm z < 0$, the line element is written in a conformally flat form

$$ds^2 = \frac{a^2}{z^2} \left[dt^2 - \sum_{i=2}^{D} (dx^i)^2 - dz^2 \right]. \tag{25}$$

Here, the hypersurfaces $z = \mp\infty$ and $z = 0$ correspond to the AdS horizon and boundary, respectively. The acceleration of a test particle in the geometry (24) is given by $a^i = \mp \delta_1^i / a$ and it does not depend on the location of the particle. The latter property is a consequence of the maximal symmetry of the AdS spacetime. The acceleration is directed towards of the AdS horizon.

In the D-dimensional generalization of the Randall-Sundrum 1-brane model

[35] the background line element reads

$$ds^2 = e^{-2|x|/a}\left[dt^2 - \sum_{i=2}^{D}\left(dx^i\right)^2\right] - dx^2 , \tag{26}$$

and the brane is located at $x=0$. By taking into account that the volume energy-momentum tensor is given by (22) in both regions $x<0$ and $x>0$, from the matching conditions (14) we get

$$\tau_0^0 = \tau_2^2 = \frac{D-1}{4\pi Ga}, \quad \tau_1^1 = 0. \tag{27}$$

This correspond to a positive CC localized on the brane.

4.2. *General solution for negative CC.* For a negative cosmological constant the first integral of the first equation in (9) is given by

$$u_2' = \frac{1}{a}\tanh w, \quad w \equiv \frac{D(x-x_0)}{2a}, \tag{28}$$

with x_0 being an integration constant. Substituting this in the second equation we get

$$u_0' = \frac{1}{2a}\left[D\coth w - (D-2)\tanh w\right]. \tag{29}$$

Now it can be checked that with these solutions for u_0' and u_2' the third equation in (9) is obeyed identically. The simple integration of (28) and (29) gives the functions $u_0(x)$ and $u_2(x)$. The corresponding line element reads

$$ds^2 = \frac{\sinh^2 w}{(\cosh w)^{2(D-2)/D}}dt^2 - dx^2 - (\cosh w)^{4/D}\sum_{i=2}^{D}\left(dx^i\right)^2 . \tag{30}$$

Let us consider the asymptotic of the line element (30) for small and large values of $|w|$. For $|w| << 1$, keeping the leading terms we get

$$ds^2 \approx x'^2 dt'^2 - dx'^2 - \sum_{i=2}^{D}\left(dx^i\right)^2 , \tag{31}$$

where $x' = x - x_0$ and $t' = Dt/2a$. The right-hand side of (31) is the line element for the Rindler spacetime (compare with (15)). For large values of $|w|$, $|w| >> 1$, keeping the leading terms we get

$$ds^2 \approx e^{\pm 2x/a}\left[dt'^2 - \sum_{i=2}^{D}\left(dx'^i\right)^2\right] - dx^2 , \tag{32}$$

with $t' = 2^{-2/D}e^{\mp x_0/a}t$ and $x'^i = 2^{-2/D}e^{\mp x_0/a}x^i$. Here, the upper and lower signs correspond to the cases $w>0$ and $w<0$, respectively. Hence, in this limit the asymptotic geometry corresponds to the AdS spacetime.

For the acceleration of a test particle at rest one has $a^i = -\delta_1^i u_0'$ with u_0' given by (29). It is positive in the region $w<0$ and negative in the region $w>0$ and, hence, the acceleration is directed towards the hyperplane $w=0$ which corresponds to the Rindler horizon. At large distances from the horizon, corresponding to $|w|>>1$, we get $a^i \approx -\delta_1^i \operatorname{sgn}(w)/a$. Near the horizon the leading term in the asymptotic expansion is given by $a^i \approx \delta_1^i/(x_0 - x)$. This term does not depend on the value of CC.

4.3. *General solution for positive CC*. We turn to the case of $\Lambda > 0$. By steps similar to those described in the previous subsection we can show that

$$u_0' = \frac{1}{2a}\left[D\cot w + (D-2)\tan w\right], \quad u_2' = -\frac{1}{a}\tan w. \tag{33}$$

The further integrations of these relations lead to the line element

$$ds^2 = \frac{\sin^2 w}{|\cos w|^{2(D-2)/D}}dt^2 - dx^2 - |\cos w|^{4/D}\sum_{i=2}(dx^i)^2. \tag{34}$$

In this case the metric is a periodic function of w with the period equal to π. This corresponds to the periodicity with respect to the coordinate x with the period equal to $2\pi a/D$. The asymptotic of the line element near the point $w=0$ is described by the Rindler line element (31). Near the point $w=\pi/2$ the line element is approximated by the Taub solution:

$$ds^2 \approx \frac{dt^2}{|w-\pi/2|^{2(D-2)/D}} - dx^2 - |w-\pi/2|^{4/D}\sum_{i=2}(dx^i)^2. \tag{35}$$

Note that in this point we have a singularity.

By taking into account that the metric tensor is periodic, let us consider the acceleration of the test particle, given as $a^i = -\delta_1^i u_0'$, in the region $-\pi/2 < w < \pi/2$. It is positive for $-\pi/2 < w < 0$ and negative for $0 < w < \pi/2$. This means that, similar to the case of negative CC, the acceleration is directed towards the Rindler horizon $w=0$ with the near horizon asymptotic $a^i \approx \delta_1^i/(x_0 - x)$. The singular walls $w = \pm\pi/2$ are repulsive and near of them the asymptoic of the acceleration is given by $a^i \approx \delta_1^i(2-D)\operatorname{sgn}(w)/[a(\pi - 2|w|)]$.

5. *CC slab with finite thickness*. As an application of the matching procedure and of the solutions described above, here we consider a finite thickness slab with the CC energy-momentum tensor (22) in the region $-L \le x \le L$. Different geometries in the exterior regions $x < -L$ and $x > L$ will be discussed. Assuming a symmetric configuration with respect to the plane $x=0$, firstly we consider the interior line element (30) with $x_0 = 0$, corresponding to a negative cosmological constant Λ. We have $ds^2 = g_{ik}^{(\Lambda)}dx^i dx^k$ with the metric tensor

$$g_{ik}^{(\Lambda)}(x) = \operatorname{diag}\left(\frac{\sinh^2 w}{(\cosh w)^{2(D-2)/D}}, -1, -\cosh^{4/D} w, \ldots, -\cosh^{4/D} w\right), \tag{36}$$

in the region $|x| \le L$ and $w = Dx/2a$. Rescaling the time and spatial coordinates x^i, $i = 2, \ldots, D$, the interior line element can be written in the form

$$ds^2 = g_{ik}(x) dx^i dx^k, \quad g_{ik}(x) = \frac{g_{ik}^{(\Lambda)}(x)}{\left|g_{ik}^{(\Lambda)}(L)\right|}, \quad |x| \le L. \tag{37}$$

With this normalization $g_{ik}(L) = \mathrm{diag}(1, -1, \ldots, -1)$. This normalization is convenient in the consideration of the matching conditions discussed below.

5.1. *Minkowski exterior*. We start the discussion by the Minkowskian geometry in the exterior regions:

$$ds_M^2 = dt^2 - dx^2 - \sum_{i=2}^{D} \left(dx^i\right)^2, \quad |x| > L. \tag{38}$$

With the choice (37) for the interior line element, the metric tensor is continuous on the boundaries $x = \pm L$. The surface energy-momentum tensor is determined by the matching conditions (14). By taking into account that

$$u_0' = \frac{1}{2a}\left[D \coth w - (D-2)\tanh w\right], \quad u_2' = \frac{1}{a}\tanh w, \tag{39}$$

in the region $|x| < L$ and $u_0' = u_2' = 0$ for $|x| > L$, from (14) we get

$$\tau_0^0 = \frac{D-1}{8\pi Ga}\tanh w_L, \quad \tau_1^1 = 0, \quad \tau_2^2 = \frac{D-2}{D-1}\frac{\tau_0^0}{2} + \frac{D\coth w_L}{16\pi Ga}, \tag{40}$$

where $w_L = DL/(2a)$. The surface energy density and the stresses (no summation over i) $\tau_i^i = \tau_2^2$, $i = 2, \ldots, D$, are positive. Note that the effective pressure along the i th spatial direction is given by $-\tau_i^i$ and in the example under consideration it is negative.

5.2. *Rindler exterior*. For the exterior Rindler geometry the line element is given by (15) in the regions $|x| > L$ and for the interior geometry we have (37). Introducing a new Rindler time coordinate t in accordance with $t = Lt_R$, we see that the metric tensor is continuous on the boundaries $x = \pm L$. The derivatives in the matching conditions are given by (39) in the region $|x| < L$ and by $u_0' = 1/x$, $u_2' = 0$ in the region $|x| > L$. From (14) one finds

$$\tau_0^0 = \frac{D-1}{8\pi Ga}\tanh w_L, \quad \tau_1^1 = 0, \quad \tau_2^2 = \frac{D-2}{D-1}\frac{\tau_0^0}{2} + D\frac{\coth w_L - 1/w_L}{16\pi Ga}. \tag{41}$$

The surface energy density is the same as that for the Minkowski exterior, whereas the stresses are different. Note that, depending on the value of the parameter w_L, the effective pressure $-\tau_2^2$ can be either negative or positive.

5.3. *Taub exterior*. The exterior geometry is described by the line element (16). Redefining the coordinates and the constant σ, we rewrite it in the form

$$ds_T^2 = \left(\frac{1+\sigma|x|}{1+\sigma L}\right)^{2(D-2)/D} dt^2 - dx^2 - \left(\frac{1+\sigma|x|}{1+\sigma L}\right)^{4/D} \sum_{i=2}^{D} \left(dx^i\right)^2 . \tag{42}$$

For $\sigma > 0$ the metric tensor is regular. With this line element in the region $|x| > L$ and with the line element (37) for $|x| < L$, the metric tensor is continuous at $x = \pm L$. By taking into account that

$$u_0' = \frac{2-D}{D}\frac{\sigma \operatorname{sgn}(x)}{1+\sigma|x|}, \quad u_2' = \frac{2}{D}\frac{\sigma \operatorname{sgn}(x)}{1+\sigma|x|}, \tag{43}$$

for $|x| > L$, the matching conditions at $x = L$ give

$$\tau_0^0 = \frac{D-1}{8\pi G a}\left(\tanh w_L - \frac{2}{D}\frac{\sigma a}{1+\sigma L}\right), \quad \tau_2^2 = \frac{D-2}{D-1}\frac{\tau_0^0}{2} + D\frac{\coth w_L}{16\pi G a}, \tag{44}$$

and $\tau_1^1 = 0$. Note that for the Taub exterior, depending on the relative values of a and L, the surface energy density can be either positive or negative.

5.4. *Slab with positive CC.* Now we turn to the slab with positive CC. The interior line element is given by (34) with the metric tensor

$$g_{ik}^{(\Lambda)}(x) = \operatorname{diag}\left(\frac{\sin^2 w}{|\cos w|^{2(D-2)/D}}, -1, -|\cos w|^{4/D}, \ldots, -|\cos w|^{4/D}\right), \tag{45}$$

where $w = Dx/(2a)$. Again, rescaling the coordinates the line element is presented in the form (37) with $g_{ik}^{(\Lambda)}(L) = \operatorname{diag}(1, -1, \ldots, -1)$. We will assume that $L < \pi a/D$. In this case the metric tensor is regular inside the slab. The derivatives of the functions $u_0(x)$ and $u_2(x)$ in the region $|x| < L$ are given by (33). For the case of $\Lambda > 0$, the components of the surface energy-momentum tensor for the exterior Minkowski, Rindler and Taub geometries are obtained from the formulas given above for $\Lambda < 0$ by the replacements

$$\tanh w_L \to -\tan w_L , \quad \coth w_L \to \cot w_L . \tag{46}$$

The surface energy density is negative for all those geometries.

6. *Conclusion.* We have considered plane symmetric solutions of General Relativity for general number of spatial dimensions. For the metric tensor given by (1), the field equations are presented in the form (5) and the covariant continuity equation for the energy-momentum tensor is reduced to (6). The set of gravitational equations is simplified by the choice of the coordinate x in accordance with (8). By using those equations one can derive the matching conditions for the metric tensor in the problems where the geometry is described by two distinct line elements in neighboring half-spaces. The metric tensor is continuous on the separating boundary and the discontinuity of its first order

derivative is given by (14), where τ_i^k is the surface energy-momentum tensor.

Two classes of the vacuum solutions of the gravitational field equation are presented. The first one corresponds to the Rindler spacetime and the second one is a higher-dimensional generalization of the well known Taub solution. By an appropriate choice of the integration constants the latter is given by (16) (see also [27]). It has a singularity at $x = 1/\sigma$ that presents a repulsive wall for test particles. As a simple example of geometry with two distinct metric tensors in two different regions we have considered the combination of the Rindler and Taub geometries separated by a planar boundary. The components of the corresponding surface energy-momentum tensor are expressed by (21).

As an example of the source in gravitational field equations we have considered the CC Λ. For negative CC there is a special solution that corresponds to $(D+1)$-dimensional AdS spacetime. In Poincaré coordinates the line element has the form (24). In the Randall-Sundrum 1-brane model two copies of the AdS half-space are combined in the form of Eq. (26). The surface energy-momentum tensor on the separating brane is given by (27). The general solutions of the field equations for negative and positive CC are given by (30) and (34), respectively. In the case of a negative CC the geometry is non-singular. For small and large values of the variable $|w|$ it is approximated by the Rindler and AdS spacetimes, respectively. For a positive CC the metric tensor is a periodic function of x with the period $2\pi a/D$. In this case one has singularities at the points corresponding to $w = (n+1/2)\pi$. Near these points the geometry is approximated by the Taub solution. For both solutions with negative and positive CC the hyperplane $w = 0$ $(x = x_0)$ corresponds to a horizon that is the analog of the Rindler horizon. The acceleration of a test particle at rest is directed towards the horizon.

By using the solutions with a CC we have constructed a simple model of a finite thickness slab symmetric with respect to the central plane. The volume energy-momentum tensor inside the slab is given by (22) and in the exterior regions we have used the vacuum solutions of the field equations. Three different cases have been considered with the Minkowski, Rindler and Taub geometries. For the latter geometry the singularity-free Taub solution is employed. The corresponding surface energy-momentum tensors are expressed by (40), (41) and (44), respectively. For a slab with positive CC the interior geometry is non-singular for the half-thickness obeying the condition $L < \pi a/D$.

The setup considered in the present paper can be used for the investigation of the backreaction effects of the vacuum polarization of quantum fields induced by boundaries with $x = \mathrm{const}$. The boundary conditions imposed on quantum fields lead to the modification of the spectrum for vacuum fluctuations and, as a consequence, the vacuum expectation values of physical observables are changed.

In particular, the vacuum energy-momentum tensor for planar boundaries has been widely considered in the literature. The simplest example is the Casimir effect (see, for example, [36]) for perfectly conducting parallel plates in the Minkowski spacetime. Already in that simple example the vacuum stresses are anisotropic. The planar boundaries in the Rindler spacetime, corresponding to uniformly accelerated plates in the Fulling-Rinlder vacuum, have been considered in [37-40]. The references for the corresponding investigations in the AdS bulk can be found in [41].

Acknowledgments. The work was supported by the grant No. 21AG-1C047 of the Higher Education and Science Committee of the Ministry of Education, Science, Culture and Sport RA.

[1] Institute of Physics, Yerevan State University,
Armenia, e-mail: saharian@ysu.am
[2] Institute of Applied Problems of Physics NAS RA, Yerevan, Armenia

ПЛОСКО-СИММЕТРИЧНЫЕ ГРАВИТАЦИОННЫЕ ПОЛЯ В (D+1)-МЕРНОЙ ОБЩЕЙ ТЕОРИИ ОТНОСИТЕЛЬНОСТИ

Р.М.АВАКЯН, Т.А.ПЕТРОСЯН, А.А.СААРЯН, Г.Г.АРУТЮНЯН

Рассмотрены плоско-симметричные гравитационные поля в рамках общей теории относительности в (D+1)-мерном пространстве-времени. Два класса вакуумных решений соответствуют многомерным обобщениям пространства-времени Риндлера и Тауба. Представлены общие решения для положительной и отрицательной космологической постоянной в качестве единственного источника гравитации. Обсуждаются условия сшивки на плоской границе двух областей с различными плоско-симметричными метрическими тензорами. Рассмотрен пример с геометриями Риндлера и Тауба в соседних полупространствах. В качестве другого примера обсуждается плоско-параллельная пластина конечной толщины с космологической постоянной, погруженная в пространство-время Минковского, Риндлера и Тауба. Найден соответствующий поверхностный тензор энергии-импульса, необходимый для согласования внешней и внутренней геометрии.

Ключевые слова: *плоско-симметричные гравитационные поля: решение Тауба: пространство-время Риндлера: космологическая постоянная*

REFERENCES

1. *H.Stephani*, *D.Kramer*, *M.Maccallum et al.*, Exact Solutions of Einstein's Field Equations, Cambridge University Press, Cambridge, U.K., 2003.
2. *J.B.Griffiths*, *J.Podolský*, Exact Space-Times in Einstein's General Relativity, Cambridge University Press, Cambridge, U.K., 2009.
3. *A.Vilenkin*, *E.P.S.Shellard*, Cosmic strings and other topological defects, Cambridge University Press, Cambridge, U.K., 1994.
4. *C.V.Johnson*, D-branes, Cambridge University Press, Cambridge, U.K., 2009.
5. *P.West*, Strings and Branes, Cambridge University Press, Cambridge, U.K., 2012.
6. *R.Maartens*, *K.Koyama*, Living Rev. Relativity, **13**, 5, 2010.
7. *T.Levi-Civita*, Atti Accad. Naz. Rend., **27**, 240, 1918.
8. *A.H.Taub*, Ann. Math., **53**, 472, 1951.
9. *N.D.Birrell*, *P.C.W.Davies*, Quantum Fields in Curved Space, Cambridge University Press, Cambridge, U.K., 1982.
10. *A.H.Taub*, Phys. Rev., **103**, 454, 1956.
11. *R.Tabensky*, *A.H.Taub*, Commun. Math. Phys., **29**, 61, 1973.
12. *R.M.Avakyan*, *J.Horský*, Astrophysics, **11**, 454, 1975.
13. *J.Horský*, E.V.Chubaryan, V.V.Papoyan, Bull. Astron. Inst. Czech., **27**, 115, 1976.
14. *J.Horský*, *E.V.Chubaryan*, Bull. Astron. Inst. Czech., **27**, 133, 1976.
15. *G.G.Arutyunyan*, *Ya.Gorskii*, *E.V.Chubaryan*, Astrophysics, **12**, 77, 1976.
16. *P.A.Amundsen*, *Ø.Grøn*, Phys. Rev. D, **27**, 1731, 1983.
17. *J.Ipser*, *P.Sikivie*, Phys. Rev. D, **30**, 712, 1984.
18. *J.Novotný*, *J.Kuéera*, *J.Horský*, Gen. Rel. Grav., **19**, 1195, 1987.
19. *A.D.Dolgov*, *I.B.Khriplovich*, Gen. Rel. Grav., **21**, 13, 1989.
20. *W.B.Bonnor*, Gen. Rel. Grav., **24**, 551, 1992.
21. *M.L.Bedran*, *M.O.Calvão*, *F.M.Paiva et al.*, Phys. Rev. D, **55**, 3431, 1997.
22. *R.M.Avakyan*, *E.V.Chubaryan*, *A.H.Yeranyan*, arXiv:gr-qc/0102030.
23. *R.E.Gamboa Saraví*, Class. Quantum Grav., **25**, 045005, 2008.
24. *H.Zhang*, *H.Noha*, *Z.-H.Zhu*, Phys. Lett. B, **663**, 291, 2008.
25. *P.Jones*, *G.Muńoz*, *M.Ragsdale et al.*, Am. J. Phys., **76**, 73, 2008.
26. *R.E.Gamboa Saraví*, Gen. Relativ. Grav., **41**, 1459, 2009.
27. *R.E.Gamboa Saraví*, Gen. Relativ. Grav., **44**, 1769, 2012.
28. *R.E.Gamboa Saraví*, Int. J. Theor. Phys., **51**, 3062, 2012.
29. *S.A.Fulling*, *J.D.Bouas*, *H.B.Carter*, Phys. Scr., **90**, 088006, 2015.
30. *A.J.Silenko*, *Yu.A.Tsalkou*, Int. J. Mod. Phys. A, **34**, 1950228, 2019.
31. *A.Yu.Kamenshchik*, *T.Vardanyan*, Phys. Lett. B, **792**, 430, 2019.
32. *A.Yu.Kamenshchik*, *T.Vardanyan*, JETP Lett., **111**, 306, 2020.
33. *R.M.Avagyan*, *A.A.Saharian*, *S.S.Jibilyan*, Astrophysics, **66**, 411, 2023.
34. *M.Halilsoy*, *V.Memari*, Int. J. Theor. Phys., **62**, 219, 2023.
35. *L.Randall*, *R.Sundrum*, Phys. Rev. Lett., **83**, 3370, 1999.

36. *M.Bordag*, *G.L.Klimchitskaya*, *U.Mohideen et al.*, Advances in the Casimir Effect, Oxford University Press, New York, 2009.
37. *P.Candelas*, *D.Deutsch*, Proc. R. Soc. London, **A354**, 79, 1977.
38. *A.A.Saharian*, Class. Quantum Grav., **19**, 5039, 2002.
39. *R.M.Avagyan*, *A.A.Saharian*, *A.H.Yeranyan*, Phys. Rev. D, **66**, 085023, 2002.
40. *A.A.Saharian*, *R.S.Davtyan*, *A.H.Yeranyan*, Phys. Rev. D, **69**, 085002, 2004.
41. *A.A.Saharian*, *A.S.Kotanjyan*, *H.G.Sargsyan*, Phys. Rev. D, **102**, 105014, 2020.

АСТРОФИЗИКА

ТОМ 67 АВГУСТ, 2024 ВЫПУСК 3

DOI: 10.54503/0571-7132-2024.67.3-423

ТЕРМОДИФФУЗИОННЫЙ УНИПОЛЯРНЫЙ ЭЛЕКТРОГЕНЕРАТОР

Г.С.БИСНОВАТЫЙ-КОГАН[1,2], М.В.ГЛУШИХИНА[1]

Поступила 30 июля 2024

Рассмотрена модель проводящего цилиндра с радиальным температурным градиентом, который создает в окружающем вакууме растущее во времени электрическое поле. Указаны условия, при которых такая модель функционирует. Генерация электрического поля происходит в том числе и при наличии магнитного поля вдоль оси цилиндра. В статье обсуждаются взаимодействия теплового потока, магнитного поля и распределения заряда. Рассмотрены четыре модели с различными условиями снабжения электронами от центрального источника и возможностью либо захватывать электроны внутри цилиндра, либо позволять им свободно покидать его через внешнюю границу.

Ключевые слова: *проводящий цилиндр: электрическое поле: термодиффузия: униполярная индукция*

1. *Введение*. Генерация электрического поля вращающимся униполярным индуктором - хорошо известный классический электродинамический эффект [1]. В космических объектах он наблюдался астрономами с середины прошлого века. Идея ускорения заряженных частиц вращающимися намагниченными звездами в качестве униполярных индукторов была впервые предложена Терлецким в 1945г. [2]. Позднее несколько авторов рассматривали возможность ускорения заряженных частиц униполярным индукционным полем Солнца и звезд для объяснения происхождения космических лучей [3-7].

После открытия радиопульсаров Голдрайх и Джулиан [8] применили этот механизм для описания процессов в магнитосфере пульсара. В настоящее время этот механизм рассматривается как один из наиболее важных для ускорения электронов и протонов, потери энергии вращения намагниченных нейтронных звезд и формирования туманностей пульсарного ветра (PWN).

Униполярная индукция рассматривалась как эффективный механизм извлечения энергии вращения из вращающейся керровской черной дыры, окруженной сильно замагниченной плазмой. Авторы предлагали различные названия этому эффекту: динамо-машина черной дыры [9], униполярная индукционная батарея [10], поверхностная батарея [11]. Проблемы, возникающие при применении механизма униполярной индукции в замагниченной плазме, окружающей керровскую черную дыру, обсуждались в статье Окамото [12].

Действие униполярного механизма на спутнике Юпитера Ио было рассмотрено Голдрайхом и Линденом-Беллом в 1969г. [13]. Они предположили, что ускоренный этим механизмом поток электронов от Ио вызывает наблюдаемые всплески декаметрового излучения Юпитера при взаимодействия с его ионосферой.

Магнитное поле линейного тока, окруженного идеально проводящим цилиндром с зазором, было рассмотрено Леонтовичем [14]. Свойства плазменного цилиндра для различных условий были исследованы Таммом [15]. Эти работы были выполнены в связи с началом работ над созданием термоядерного реактора, который еще находится на стадии строительства.

В данной статье мы предлагаем механизм униполярной индукции, в котором рассматривается проводящий цилиндр с радиальным градиентом температуры, выполняющим роль вращающегося замагниченного цилиндра [1]. Рассматривая упрощенную цилиндрическую модель в однородном магнитном поле и без него, мы исследуем взаимодействие теплового потока, магнитного поля и распределения заряда в этой модели. Наибольшее внимание уделено варианту с растущим электрическим полем в вакууме.

Наличие радиального теплового потока, приводящего к созданию радиального электрического тока за счет эффекта термодиффузии, а также наличие азимутального магнитного поля, создаваемого возможным электрическим током вдоль оси, не нарушает цилиндрическую симметрию. В лаборатории появления электрического тока вдоль оси цилиндра можно избежать, используя два одинаковых потока электронов, движущихся противоположно. В дальнейшем изложении везде принимается отсутствие продольного тока от внешних источников $j_z = 0$, а также пренебрегается инерцией электронов в макроскопических явлениях.

2. *Магнитные поля и электрические токи в проводящем цилиндре.* Рассмотрим цилиндр, предположительно, с невырожденной, нерелятивистской плазмой, с нулевой скоростью вещества, с градиентом температуры, направленном вдоль радиуса, с возможным однородным магнитным полем B вдоль оси Z. Предполагается, что единственный источник тепла и электронов расположен вблизи оси цилиндра и представлен равномерно нагретым цилиндром с радиусом $R_1 << R_0$, где R_0 - внешний радиус цилиндра, R_1 - радиус внутреннего цилиндра, внутренней "струны".

Коэффициенты переноса, определяющие тепловой поток и диффузию в плазме, имеют тензорную структуру в магнитном поле. Это означает, что направление теплового и диффузионного потоков не совпадает с направлением соответствующих векторов электрического поля **E** и градиента температуры $\nabla\mathbf{T}$, ответственных за формирование этих потоков. Часть вектора электрического тока **j** связана с вектором электрического поля **E**, составляющим основную часть вектора диффузии **d**, с помощью тензора электропроводности $\overleftrightarrow{\sigma}_E$. Другая часть **j** связана с вектором температурного градиента **T** тензором $\overleftrightarrow{\sigma}_T$.

В работах [16-18] были рассчитаны компоненты четырех тензоров кинетических коэффициентов - теплопроводности, диффузии, термодиффузии и диффузионного термоэффекта для различных условий, включая сильно вырожденную плазму.

Соотношения для теплового потока q_i и скорости диффузии υ_i записываются в следующем виде:

$$q_i = q_i^{(T)} + q_i^{(D)} = -\left(\lambda^{(1)}\delta_{ij} - \lambda^{(2)}\varepsilon_{ijk}\,B_k + \lambda^{(3)}\,B_iB_j\right)\frac{\partial T}{\partial x_j} - \frac{en_e}{kT}\left(\nu^{(1)}\delta_{ij} - \nu^{(2)}\varepsilon_{ijk}\,B_k + \nu^{(3)}\,B_iB_j\right)E_j\,, \tag{1}$$

$$\left\langle \upsilon_i \right\rangle = \left\langle \upsilon_i^{(D)} \right\rangle + \left\langle \upsilon_i^{(T)} \right\rangle = -\frac{en_e}{kT}\left(\eta^{(1)}\delta_{ij} - \eta^{(2)}\varepsilon_{ijk}\,B_k + \eta^{(3)}\,B_iB_j\right)E_j - \left(\mu^{(1)}\delta_{ij} - \mu^{(2)}\varepsilon_{ijk}\,B_k + \mu^{(3)}\,B_iB_j\right)\frac{\partial T}{\partial x_j}. \tag{2}$$

Индексы (T) и (D) соответствуют тепловому потоку и скорости диффузии электронов, определяемых градиентом температуры $\partial T/\partial x_j$ и электрическим полем E_i (как части вектора диффузии) соответственно.

Кинетические коэффициенты $\lambda^{(i)}$, $\mu^{(i)}$, $\eta^{(i)}$ и $\nu^{(i)}$ определяют тепловые и диффузионные потоки в следующих направлениях. Верхние индексы $^{(1)}$ определяют вышеупомянутые потоки вдоль температурного градиента $\partial T/\partial x_j$, или вектора диффузии d_i. Верхние индексы $^{(3)}$ связаны с направлением вдоль магнитного поля; а верхние индексы $^{(2)}$ определяют потоки, перпендикулярные плоскости, определяемой вектором магнитного поля B_i и любым из векторов $\partial T/\partial x_j$ или d_i. Эти потоки называются холловскими q_{Hall} и j_{Hall}.

Плазма в оболочках нейтронных звезд является столкновительной из-за высокой плотности. Газ электронов там находится в кристаллической решетке тяжелых ядер, с которыми сталкиваются электроны.

Один из первых расчетов кинетических коэффициентов в замагниченной плазме путем решения уравнения Больцмана с использованием метода Чепмена-Энскога [19] был выполнен Брагинским [20,21]. Кинетические коэффициенты для полностью ионизированной намагниченной плазмы были рассчитаны путем прямого численного расчета уравнения Фоккера-Планка в работе [22]. В работах [16,18] аналитические выражения для четырех тензорных кинетических коэффициентов в намагниченной плазме были получены путем решения уравнения Больцмана в трехполиномиальном приближении, уточнив двухполиномиальные результаты [20,21].

Мы используем кинетические коэффициенты, полученные в приближении Лоренца [19]. В этом приближении кинетические коэффициенты в отсутствии магнитного поля рассчитываются из точного решения линеаризованного уравнения Больцмана [19,23,24]. Погрешности результатов в приближении Лоренца не превышают 50%, что достаточно для качественного описания процессов в рассматриваемой задаче.

При цилиндрической симметрии $\partial/\partial z = \partial/\partial\phi = 0$, единственными ненулевыми величинами остаются: q_r, q_ϕ, j_r, j_ϕ, B_z, E_r. Для невырожденных электронов из (1), (2), используя определения плотности электрического тока:

$$j_i = -n_e e\langle \upsilon_i \rangle, \tag{3}$$

в присутствии магнитного поля вдоль оси цилиндра имеем следующие соотношения:

$$q_r = -\lambda^{(1)}\frac{dT}{dr} - \frac{en_e}{kT}\nu^{(1)}E_r, \quad q_\phi = -B_z\left(\lambda^{(2)}\frac{dT}{dr} + \frac{en_e}{kT}\nu^{(2)}E_r\right), \tag{4}$$

$$\upsilon_r = -\mu^{(1)}\frac{dT}{dr} - \frac{en_e}{kT}\eta^{(1)}E_r, \quad \upsilon_\phi = -B_z\left(\mu^{(2)}\frac{dT}{dr} + \frac{en_e}{kT}\eta^{(2)}E_r\right), \tag{5}$$

$$j_r = en_e\left(\mu^{(1)}\frac{dT}{dr} + \frac{en_e}{kT}\eta^{(1)}E_r\right), \quad j_\phi = B_z en_e\left(\mu^{(2)}\frac{dT}{dr} + \frac{en_e}{kT}\eta^{(2)}E_r\right). \tag{6}$$

Коэффициенты теплопроводности и термодиффузии, рассчитанные в приближении Лоренца для случая нулевого магнитного поля, записываются в виде:

$$\tilde{\lambda}_T = \frac{320}{3\pi}\frac{k^2 T n_e}{m_e}\tau_e, \tag{7}$$

$$\mu^{(1)} = \frac{16k}{m_e\pi}\tau_e \equiv \frac{\sigma_T}{en_e}. \tag{8}$$

Из выражения для плотности электрического тока, можно записать его часть, связанную с градиентом температуры, используя коэффициент термодиффузии, в виде:

$$j_r^T = -n_e e\langle \upsilon_r^T \rangle = -n_e e\left(-\mu^{(1)}\frac{dT}{dr}\right) = \sigma_T\frac{dT}{dr}. \tag{9}$$

Здесь и далее используются следующие параметры плазмы: ларморовская частота электрона $\omega_B = eB/m_e c$, время между eN столкновениями

$\tau_e = \frac{3}{4}\sqrt{\frac{m_e}{2\pi}}\frac{(kT)^{3/2}}{Z^2 e^4 n_N \Lambda}$, коэффициент тепловой электропроводности σ_T, который в приближении невырожденного газа Лоренца определен в [24]; n_e, n_N - концентрации электронов и ядер с атомным номером Z, Λ - кулоновский логарифм.

Коэффициенты электропроводности σ_E и диффузионного термоэффекта λ_E записываются в виде

$$\sigma_E = n_e \eta^{(1)} = \frac{32}{3\pi}\frac{e^2 n_e}{m_e}\tau_e, \quad \lambda_E = n_e \nu^{(1)} = \frac{128}{3\pi}\frac{ekTn_e}{m_e}\tau_e. \tag{10}$$

Таким образом, тепловой поток q_i и электрический ток j_i в незамагниченной плазме записываются в виде:

$$q_r = -\tilde{\lambda}_T \frac{dT}{dr} - \lambda_E E_r, \quad j_r = \sigma_T \frac{dT}{dr} + \sigma_E E_r. \tag{11}$$

При наличии магнитного поля вдоль оси цилиндра нам нужно использовать одно из уравнений Максвелла для расчета дополнительного магнитного поля B_z, создаваемого азимутальным электрическим током, возникающим из-за эффекта Холла [25]. В отсутствии продольного тока, запишем необходимые нам компоненты в следующем виде:

$$\mathrm{rot}\mathbf{B} = \frac{4\pi}{c}\mathbf{j}, \quad \frac{dB_r}{dz} - \frac{dB_z}{dr} = \frac{4\pi}{c} j_\phi, \quad \frac{1}{r}\frac{d}{dr}(rB_\phi) - \frac{1}{r}\frac{dB_r}{d\phi} = \frac{4\pi}{c} j_z. \tag{12}$$

При этом надо различать сторонние электродвижущие силы, связанные с градиентом температуры, и электрические силы, действующие внутри проводящей среды, см. обсуждение этого вопроса в книге Тамма [1]. Ненулевые составляющие вектора плотности электрического тока j_i в цилиндре определяются следующим образом [19],

$$j_r = \frac{\sigma_T (\nabla T)_r + \sigma_E E_r}{1 + \omega_B^2 \tau_e^2}, \quad j_\varphi = \frac{(\sigma_T (\nabla T)_r + \sigma_E E_r)\omega_B \tau_e}{1 + \omega_B^2 \tau_e^2}, \quad j_z = 0. \tag{13}$$

Принимая во внимание симметрию цилиндра, стационарность нашей модели и уравнения (12) и (13), записываем уравнения Максвелла (12) как:

$$B_r = B_\varphi = 0, \quad \frac{c}{4\pi}\frac{dB_z}{dr} = \frac{(\sigma_T (\nabla T)_r + \sigma_E E_r)\omega_B \tau_e}{1 + \omega_B^2 \tau_e^2}. \tag{14}$$

Определяемая таким образом "холловская" компонента магнитного поля B_z является добавкой (предположительно малой) к исходному продольному магнитному полю, которое определяет ларморовскую частоту ω_B. Основной целью данной работы является построение модели генератора электрического поля в плазменном или металлическом цилиндре с радиальным градиентом температуры. Использовано приближение Лоренца для кинетических коэффициентов. Отклонения от более точных формул в плазме составляют около нескольких десятков процентов, но, используя их, мы получаем простое аналитическое решение уравнения. В оболочке нейтронной звезды, где материя находится в состоянии кулоновского кристалла, результаты приближения Лоренца почти точны.

Связь векторов **j** и **B**, определяемая уравнением Максвелла, рассматривается для двух различных условий на внутренней и внешней границах цилиндра.

I. Электроны пересекают внешнюю границу без какой-либо подачи электронов из центра. Стационарное состояние устанавливается при положительном заряде цилиндра, нулевом электрическом токе и ненулевом радиальном электрическом поле $E_r(r)$, как внутри, так и вне цилиндра. Эта модель рассмотрена в разделе 3.1, см. рис.1.

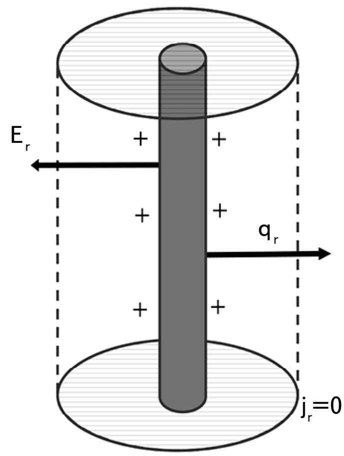

Рис.1. Модель цилиндра со свободной внешней границей без подачи электронов из центра. Цилиндр переходит в стационарное состояние, приобретая положительный электрический заряд, который создает внутреннее и внешнее радиальное электрическое поле и обнуляет электрический ток. Тепловой поток за пределами цилиндра определяется диффузией фотонов. Рисунки здесь и далее приведены для случая нулевого магнитного поля.

II. Электроны поступают из центра, но не могут пересечь внешнюю границу. Стационарное состояние не устанавливается. Электрическое поле внутри цилиндра не создается, а электрический ток поддерживается температурным градиентом, как и в случае I. Отрицательный заряд на внешней границе со временем увеличивается, создавая растущее электрическое поле $E_r(t)$ за пределами цилиндра. Эта модель рассмотрена в разделе 3.2, см. рис.2.

III. Электроны не могут пересечь никакой границы, общий электрический заряд цилиндра с радиальным тепловым потоком остается равным нулю, но образуется внутреннее электрическое поле, которое сводит на нет электрический ток. Процессы в таком цилиндре рассмотрены в разделе 3.3, см. рис.3.

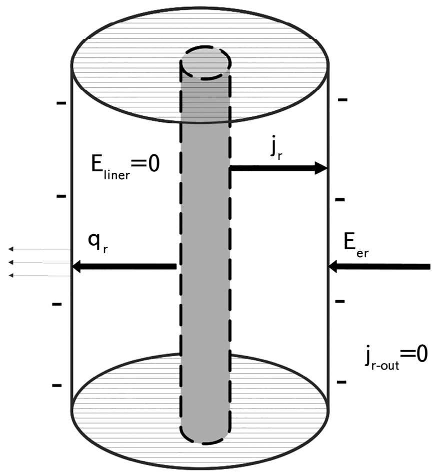

Рис.2. Модель цилиндра с непрерывной подачей свободных электронов от центрального источника и без пересечения ими внешней границы. На внешней границе образуется отрицательный заряд, внешнее электрическое поле E_r со временем увеличивается из-за увеличения поверхностного отрицательного заряда, но внутреннее электрическое поле остается равным нулю. Тепловой поток за пределами цилиндра определяется диффузией фотонов.

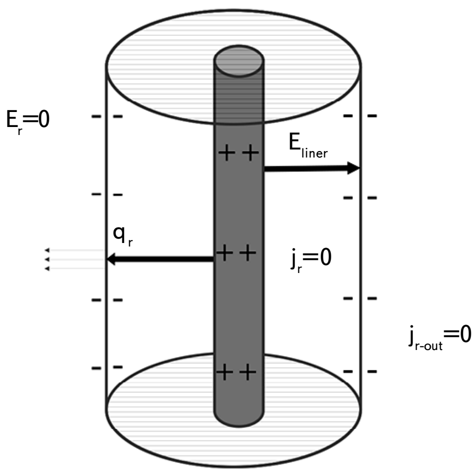

Рис.3. Модель цилиндра без снабжения электронами из центрального источника и без проникновения через внешнюю границу. Положительный центральный заряд образуется на оси, а отрицательный - на внешней границе. В стационарном состоянии внешнее электрическое поле равно нулю, как и электрический ток, из-за нулевого общего электрического заряда цилиндра и уравновешивания действия теплового потока и электрического поля внутри него. Тепловой поток снаружи цилиндра определяется диффузией фотонов.

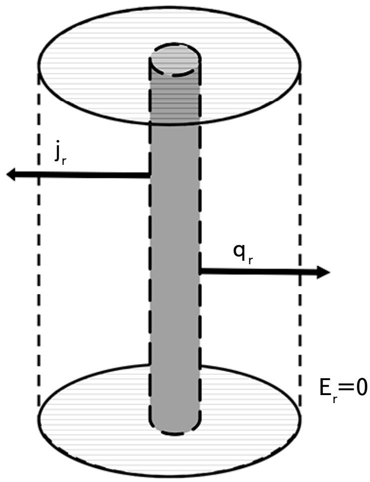

Рис.4. Модель цилиндра со свободной внешней границей и свободным поступлением электронов от центрального источника из [25]. Полный радиальный тепловой поток внутри цилиндра Q считается постоянной величиной, электрическое поле E_r равно нулю. Тепловой поток за пределами цилиндра определяется диффузией фотонов и потоком электронов.

IV. Электроны свободно пересекают внешнюю и внутреннюю границы цилиндра таким образом, что радиальное электрическое поле не создается, и можно считать, что $E_r = 0$ везде. В этом случае нужна непрерывная подача электронов вблизи оси цилиндра. В нашей упрощенной модели это выглядит искусственным, но в более сложной модели с нейтронной звездой могло бы реализоваться нечто похожее. Идеализированная одномерная модель рассмотрена в разделе 3.4, см. рис.4.

Тепловой поток вне цилиндра полностью определяется фотонным излучением с поверхности на рис.2, 3 и частично на рис.1, 4.

3. *Модели с открытыми и закрытыми границами.*

3.1. *Модель I. Электроны свободно пересекают внешнюю границу цилиндра без поступления электронов из центра.* Электроны пересекают внешний радиус цилиндра под действием радиального теплового потока, увеличивая положительный заряд цилиндра. В этом случае электроны вылетают через внешнюю границу до того момента, когда действие положительного электрического заряда, сформированного на внутреннем цилиндре, не уравновесит действие теплового потока, см. рис.1. Величина такого электрического поля определяется из условия $j_r = 0$ в (11) при магнитном поле равном нулю. Используя для учета влияния магнитного поля приближение лоренцевого газа (13), получаем при $j_r = 0$ такую же связь электрического поля с градиентом температуры. Стационарный тепловой поток в этой модели определяется из соотношений:

$$j_r = j_\varphi = 0\,, \quad E_r = -\frac{\sigma_T}{\sigma_E}\frac{dT}{dr}\,,$$
$$q_r = -\left(\widetilde{\lambda}_T - \lambda_E \frac{\sigma_T}{\sigma_E}\right)\frac{dT/dr}{1+(\omega_B\tau_e)^2} = -\frac{2}{5}\frac{\widetilde{\lambda}_T\, dT/dr}{1+(\omega_B\tau_e)^2}\,, \quad q_\varphi = q_r\,\omega_B\tau_e\,. \tag{15}$$

Здесь Q - постоянный радиальный тепловой поток, выходящий из единицы длины цилиндра. Радиальный тепловой потока на единицу площади равен $q_r = Q/(2\pi r)$. Распределение температуры и электрического поля по радиусу цилиндра записываются в виде:

$$\frac{dT}{dr} = -\frac{5}{2\widetilde{\lambda}_T}\left[1+(\omega_B\tau_e)^2\right]q_r\,,$$
$$E_r = \frac{\sigma_T}{\sigma_E}\frac{5}{2\widetilde{\lambda}_T}\left[1+(\omega_B\tau_e)^2\right]q_r = \frac{5\sigma_T}{2\sigma_E\widetilde{\lambda}_T}\left[1+(\omega_B\tau_e)^2\right]\frac{Q}{2\pi r}\,. \tag{16}$$

При постоянных физических параметрах по радиусу σ_T, λ_E, $\widetilde{\lambda}_T$, $\omega_B\tau$ такое распределение электрического поля создается линейной плотностью положительного заряда ρ_e на оси цилиндра с

$$\rho_e = \frac{5\sigma_T}{2\sigma_E\widetilde{\lambda}_T}\left[1+(\omega_B\tau_e)^2\right]\frac{Q}{2\pi}\,, \tag{17}$$

и нулевой плотностью электрического заряда в самом цилиндре. Считаем, что центральный цилиндр имеет очень малый, но конечный радиус.

3.2. *Модель II. Электроны непрерывно поступают из центральной области, но не пересекают внешнюю границу цилиндра.* В этом случае предполагается, что электроны могут проникать в цилиндр вблизи центральной оси, из центрального цилиндра очень малого радиуса.

Стационарное состояние в этом случае не устанавливается. Электрическое поле внутри цилиндра не создается, а электрический ток поддерживается температурным градиентом, как и в случае I. Отрицательный заряд накапливается на внешней границе, увеличивается со временем, создавая растущее электрическое поле $E_r(t)$ за пределами цилиндра, см. рис.2. Очевидно, что отрицательный заряд граничной окружности единичной длины ρ_{eb} и напряженность внешнего электрического поля вокруг цилиндра линейно растут со временем, и при нулевом магнитном поле определяются соотношениями:

$$\rho_{eb} = -\frac{\sigma_T\, Q}{\widetilde{\lambda}_T}t\,, \quad E_{er} = -2\frac{\rho_{eb}}{r}\,, \tag{18}$$

при $r \geq R$:

3.3. *Модель III. Электроны не пересекают никаких границ цилиндра, общий электрический заряд остается нулевым.* В этом случае электроны собираются вблизи внешней границы цилиндра, а сам цилиндр приобретает положительный заряд, создавая внутреннее электрическое поле, которое в стационарном состоянии останавливает электрический ток, см. рис.3. Это электрическое поле определяется из условия $j_i = 0$, см. (11) для нулевого магнитного поля. При наличии продольного магнитного поля возникает электрическое поле той же величины, как следует из упрощенного учета влияния магнитного поля в модели газа Лоренца (13). Тепловой поток при этом определяется соотношениями (15). Отличие от случая II заключается в нулевом значении общего электрического заряда цилиндра в неподвижном состоянии. В этом случае он не заряжен, в отличие от случая I, когда цилиндр приобретает общий положительный электрический заряд на внутренней струне, в соответствии с (17). Отметим, что в отсутствии электрического тока в среде с градиентом температуры, коэффициент теплопроводности λ_T в 2.5 раза меньше коэффициента $\widetilde{\lambda}_T$ из (7), (11), в котором не наложено условие отсутствия электрического тока. Так как в большинстве стационарных объектов электрический ток и другие диффузионные движения отсутствуют, в литературе принято называть коэффициентом теплопроводности именно величину $\lambda_T = 2/5\widetilde{\lambda}_T$ [19].

3.4. *Модель IV, со свободными выходящими и входящими электронами.* В этом случае электроны свободно пересекают границу цилиндра и получают приток электронов из центральной области. Плотность электрического заряда не возникает, и мы получаем E_i=0, см. рис.4. Процессы, происходящие в такой модели, были подробно проанализированы в статье [25], где рассматривалась роль токов Холла в формировании результирующего магнитного поля в проводящем намагниченном цилиндре. Аналитические решения и численные расчеты были получены для условий, близких к параметрам плазмы в коре нейтронных звезд, и для плазмы в лаборатории.

4. *Обсуждение.* Модель электрического генератора в виде цилиндра с радиальным тепловым потоком, могла бы быть сконструирована в лаборатории, с использованием металлического или плазменного цилиндра с сильно нагретой осью.

Специфической особенностью данной модели электрогенератора является возможность создания устройства, в котором электрическое поле нарастает с течением времени при сохранении параметров модели. Физический предел напряженности генерируемого поля достигается, когда напряженность наведенного поля становится равной порогу выброса электронов. Это поле становится стационарным и не меняется со временем.

Аналогичная ситуация может возникнуть в нейтронной звезде после ее рождения. Некоторые слои нейтронной звезды могут стать электрически заряженными, и при аккреции, в результате поступления внешних электронов и из-за выброса электронов электрическим полем нейтронная звезда может приобрести ненулевой электрический заряд. Применение этой модели для получения реалистичных параметров нейтронной звезды требует дальнейшего рассмотрения.

Такие модели необходимы для изучения магнитотепловой эволюции магнитного и электрического полей в нейтронных звездах и белых карликах с учетом анизотропных потоков тепла и электрического тока, обусловленных магнитными полями и холловскими членами в коэффициентах переноса.

Работа выполнена при поддержке темы "Звезды" ИКИ РАН.

[1] Институт космических исследований РАН, e-mail: gkogan@cosmos.ru
[2] НИЯУ МИФИ

THERMODIFFUSION UNIPOLAR ELECTRIC GENERATOR

G.S.BISNOVATYI-KOGAN[1,2], M.V.GLUSHIKHINA[1]

The model of a conductive cylinder with a radial temperature gradient that creates an electric field growing over the time in the surrounding vacuum is considered. The conditions under which such a model exists are discussed. The generation of an electric field also occurs in the presence of a magnetic field along the axis of the cylinder. The article discusses the interactions of heat flux, magnetic field and charge distribution. Four models are considered with different conditions for the supply of electrons from a central source and the ability to either capture electrons inside the cylinder, or to allow them to leave freely through the outer boundary.

Keywords: *conducting cylinder: electrical field: thermodiffusion: unipolar induction*

ЛИТЕРАТУРА

1. *И.Е.Тамм*, Основы теории электричества, М. Наука, 1976.
2. *Я.П.Терлецкий*, ДАН СССР, **47**, 104, 1945.
3. *Я.П.Терлецкий*, ЖЭТФ, **16**, 403, 1946.
4. *L.Davis*, Phys. Rev., **72**, 632, 1947.
5. *Я.П.Терлецкий*, Вестник Московского Университета, Серия 3: Физика, Астрономия, **1**, 75, 1948.
6. *Я.П.Терлецкий*, ЖЭТФ, **19**, 1059, 1949.
7. *W.L.Ginzburg*, *H.Vogel*, Fortschritte der Physik, **1**, 659, 1953.
8. *P.Goldreich*, *W.H.Julian*, Astrophys. J., **157**, 869, 1969.
9. *R.L.Znajek*, Mon. Not. Roy. Astron. Soc., **185**, 833, 1978.
10. *E.S.Phinney*, Astrophysical Jets; D. Reidel Publishing Company, 1982.
11. *К.Торн*, *Р.Прайс*, *Д.Макдональд*, Черные дыры мембранный подход; Мир, 1988.
12. *I.Okamoto*, Publ. Astron. Soc. Japan, **67**, 5, 2015.
13. *P.Goldreich*, *D.Lynden-Bell*, Astrophys. J., **156**, 59, 1969.
14. *М.А.Леонтович*, Физика плазмы и проблема управляемых термоядерных реакций, **1**, 222, 1958.
15. *И.Е.Тамм*, Физика плазмы и проблема управляемых термоядерных реакций, **1**, 30, 1958.
16. *G.S.Bisnovatyi-Kogan*, *M.V.Glushikhina*, Plasma Phys. Rep., **44**, 405, 2018.
17. *Г.С.Бисноватый-Коган*, *М.В.Глушихина*, Физика Плазмы, **44**, 1, 2018.
18. *М.В.Глушихина*, Физика Плазмы, **46**, 121, 2020.
19. *С.Чепмен*, *Т.Каулинг*, Математическая теория неоднородных газов, М., Изд. Иностранной Литературы, 1960.
20. *С.И.Брагинский*, ЖЭТФ, **33**, 459, 1957.
21. *С.И.Брагинский*, Вопросы теории плазмы, ред. М.А.Леонтович, Госатомиздат, М., **1**, 183, 1963.
22. *E.M.Epperlein*, *M.G.Haines*, Phys. Fluids, **29**, 1029, 1986.
23. *E.Schatzman*, White dwarfs; North-Holland Publishing Company, 1958.
24. *G.Bisnovatyi-Kogan*, Stellar Physics I: Fundamental Concepts and Stellar Equilibrium, Springer, 2001.
25. *G.Bisnovatyi-Kogan*, *M.Glushikhina*, J. Plasma Phys., **90**, 905900112, 2024.

ПРАВИЛА ДЛЯ АВТОРОВ

1. Рукописи могут быть представлены в печатном виде (hard copies) в двух экземплярах, отпечатанные на одной стороне листа формата А4, вместе с соответствующей электронной версией. Один из экземпляров должен быть подписан всеми авторами. Указываются сведения об авторах: фамилия, имя, отчество, название учреждения, электронный адрес.

2. *Рукопись* может быть набрана в виде файла с расширениями .doc, .docx, .rtf, через 1.5 интервала, используя Font 12pt.

3. *Рисунки* должны быть выполнены предельно аккуратно с разборчивыми надписями. Необходимые объяснения даются в подписях к рисункам, которые не должны повторяться в тексте. Рисунки необходимо отправить в виде .jpg, .bmp, .wmf, .eps файлов. С учетом формата журнала размеры рисунков редакцией могут быть изменены. В тексте рисунки нумеруются в порядке очередности (рис.1, рис.2, и т.д.). Если рисунок, состоит из двух или более панелей, то возможны обозначения типа рис.1а или рис.1а, b.

4. *Таблицы* должны иметь номера и информативные названия. Примечания должны быть сведены к минимуму и пронумерованы надстрочными арабскими цифрами.

5. *Цитирование литературы.* Цитируемая литература дается порядковым номером в строчку в квадратных скобках (например, [5]) и соответствует номеру в списке литературы. Список литературы должен быть оформлен следующим образом:

а) Для журнальных статей указываются инициалы и фамилии авторов курсивным шрифтом (в оригинальной транскрипции), название журнала в принятом сокращении (сокращения для некоторых наиболее часто встречаемых журналов, применяемых в "Астрофизике", дается в сайте журнала), номер тома жирным шрифтом, номер первой страницы, год издания. Для русскоязычных журналов, которые переводятся на английский язык, в скобках приводятся соответствующее название журнала на английском, том, страница и год публикации.

б) Для книг следует указывать инициалы и фамилию автора курсивом, место и год издания.

6. *Оформление рукописи.* На первой странице дается название статьи (по возможности кратко и информативно), инициалы, фамилия каждого автора и аннотация на русском языке. На второй странице приводятся название статьи, инициалы, фамилия каждого автора и текст аннотации на английском языке, который должен полностью соответствовать русскому. В аннотации должны быть изложены главные результаты работы без ссылок на литературу. Максимальный объем аннотации не должен превышать 5% основного текста. Таблицы, список литературы, рисунки и надписи к рисункам печатаются на отдельных страницах. Расположение таблиц и рисунков отмечается на полях основного текста. Аннотации, основной текст, список литературы и таблицы должны иметь одну общую нумерацию страниц. Суммарный объем не должен превышать 16 стандартных страниц. Объем краткого сообщения - не более 4 страниц.

Статья состоит из пронумерованных разделов, начиная с "1. *Введение*". Названия разделов печатаются курсивом в строке, они должны быть краткими и содержательными. Подразделы могут быть пронумерованы как 2.1, 2.2 и т.д. Необходимые сокращения терминов или названий могут быть использованы во всей статье, однако их объяснение дается лишь один раз при первом упоминании.

7. В случае представления двух или более статей одновременно необходимо указать желательный порядок их публикации.

8. Рукописи авторам не возвращаются.

9. Авторам статьи (независимо от их количества) представляется 10 оттисков бесплатно.